



# Optical properties of InAs/InP nanowire heterostructures

Roman Anufriev

## ► To cite this version:

Roman Anufriev. Optical properties of InAs/InP nanowire heterostructures. Micro and nanotechnologies/Microelectronics. INSA de Lyon, 2013. English. NNT : 2013ISAL0133 . tel-01127210

**HAL Id: tel-01127210**

<https://theses.hal.science/tel-01127210>

Submitted on 7 Mar 2015

**HAL** is a multi-disciplinary open access archive for the deposit and dissemination of scientific research documents, whether they are published or not. The documents may come from teaching and research institutions in France or abroad, or from public or private research centers.

L'archive ouverte pluridisciplinaire **HAL**, est destinée au dépôt et à la diffusion de documents scientifiques de niveau recherche, publiés ou non, émanant des établissements d'enseignement et de recherche français ou étrangers, des laboratoires publics ou privés.

## THESE

# Optical Properties of InAs/InP nanowire heterostructures

Présentée devant

L'institut national des sciences appliquées de Lyon

Pour obtenir

Le grade de docteur

École doctorale EEA

Par

Roman Anufriev

Soutenue le 22 novembre 2013 devant la commission d'examen

## Jury

---

Anna Fontcuberta i Morral	Professeur (EPFL)	<i>Rapporteur</i>
Jean-Christophe Harmand	Directeur de Recherche CNRS (LPN)	<i>Rapporteur</i>
Valery Zwiller	Professeur (TU Delft)	<i>Président</i>
Michel Gendry	Directeur de recherche CNRS (INL)	<i>Examinateur</i>
Catherine Bru-Chevallier	Directeur de recherche CNRS (INL)	<i>Directeur</i>
Nicolas Chauvin	Chargé de Recherche CNRS (INL)	<i>Co-directeur</i>

---

Cette thèse a été préparée à l'Institut des Nanotechnologies de Lyon de l'INSA de Lyon

Contact e-mail: anufrievroman@yandex.ru

---

# **Optical Properties of InAs/InP Nanowire Heterostructures**

---

Roman Anufriev

Supervised by

Catherine Bru-Chevallier and Nicolas Chauvin

*This thesis is dedicated to my mother,  
for her kindness and devotion*

# Acknowledgments

---

First and foremost, I sincerely thank my thesis advisors Catherine Bru-Chevallier and Nicolas Chauvin, whose trust and constant care, patient guidance and useful advices made this whole work possible. My very great appreciation goes to Nicolas Chauvin for the countless useful discussions with valuable and constructive suggestions during these years.

My deep gratitude to the “Heteroepitaxy and Nanostructures” group of INL namely to Khalid Naji, Hammadi Khmissi and Michel Gendry for their excellent work in nanowire sample fabrication and to Gilles Patriarche from the Laboratoire de Photonique et de Nanostructures in Marcoussis for all the scanning transmission electron microscopy images.

Moreover, I would like to extend my thanks to all the technicians in our laboratory. Warm thanks go to Philippe Girard and Robert Perrin for their help. I also thank Joëlle Grégoire, Khaled Ayadi and Armel Descamps from NanoLyon team for their assistance.



# Abstract

---

The field of semiconductor nanowires (NWs) has been developed very rapidly during the last ten years. Advances in epitaxial growth technology together with unique properties of NWs, make this nanomaterial interesting for many potential applications. In this context, this thesis is devoted to experimental investigation of the optical properties of InAs/InP NW heterostructures by means of photoluminescence (PL) spectroscopy.

First, it was demonstrated that the transfer of NWs (in our case, InP NWs) onto new host-substrates can affect the optical properties of these NWs. This is interpreted as a consequence of a strain induced in the InP NWs, due to a difference in the thermal expansion coefficients of the NWs and the host-substrate. Next, the optical properties of NW heterostructures, such as quantum rod (QRod) and radial quantum well (QWell) NWs, were investigated. The experimental results are interpreted using theoretical simulation of similar NW heterostructures.

The polarization properties of single InP NWs, InAs/InP QWell-NWs, InAs/InP QRod-NWs and an ensemble of well ordered NWs were studied at different temperatures. It was demonstrated that the polarization properties of the single NWs, being independent on temperature, are in agreement with theoretical predictions. Due to the knowledge of NW orientations on as-grown substrates, the polarization properties of a NW ensemble can be correlated with the properties of the single NWs. Furthermore, using this approach, the polarization anisotropy of the NWs was investigated as a function of excitation wavelength and temperature on the NW ensemble.

Moreover, we report on the evidences of the strain-induced piezoelectric field in WZ InAs/InP QRod-NWs. This electric field, caused by the lattice mismatch between InAs and InP, results in a quantum confined Stark effect and, as a consequence, affects the optical properties of the structure. It was shown that this piezoelectric field could be screened by photogenerated carriers or its impact could be removed by increasing temperature. In addition, the piezoelectric effect was theoretically demonstrated by simulations of WZ InAs/InP QRod-NW structures.

Finally, PL quantum efficiency of NW heterostructures and their planar analogues were measured by means of a PL setup coupled to an integrating sphere.

**Keywords:** Nanowires, III-V semiconductors, Photoluminescence, Piezoelectricity, Quantum efficiency, Polarization, Quantum confinement, Heterostructure, InAs/InP.

# Contents

---

<b>Chapter I. Semiconductor nanowires.....</b>	<b>3</b>
1.1 Introduction.....	4
1.2 Nanowire growth.....	5
1.3 Types of nanowire heterostructures.....	8
1.4 Crystallographic structure of nanowires.....	9
1.5 Energy band structure.....	11
1.6 InAs/InP material pair for nanowire heterostructures.....	13
1.7 III-V Nanowires on silicon emitting in telecom wavelength.....	14
1.8 References.....	15
<b>Chapter II. InAs/InP nanowire samples. Growth and characterization.....</b>	<b>23</b>
2.1 Introduction.....	24
2.2 InP nanowires.....	25
2.3 InAs/InP radial quantum well nanowires.....	29
2.4 InAs/InP quantum rod nanowires.....	32
2.5 Conclusions.....	35
2.6 References.....	36
<b>Chapter III. Experimental techniques and sample preparation.....</b>	<b>38</b>
3.1 Introduction.....	39
3.2 Photoluminescence technique.....	40
3.3 Micro-Photoluminescence technique.....	41
3.4 Photoluminescence with integrating sphere.....	43
3.5 Experimental setup calibration.....	45
3.6 Nanowire transfer and sample preparation.....	46
3.7 References.....	48
<b>Chapter IV. Optical properties of InP nanowires.....</b>	<b>49</b>
4.1 Introduction.....	50
4.2 PL characterization of InP nanowires.....	52
4.3 Phenomenon of substrate-induced strain.....	55
4.4 Theory of substrate-induced strain and its impact on the optical properties.....	56
4.5 Experimental observation of substrate-induced strain.....	58
4.6 Impact of surface charges.....	64
4.7 Conclusions.....	67
4.8 References.....	68

<b>Chapter V. Spectroscopy of NW heterostructures.....</b>	72
5.1 Introduction.....	73
5.2 Spectroscopy of QWell-NWs.....	74
5.3 Simulation of QWell-NWs.....	78
5.4 Spectroscopy of QRod-NWs.....	82
5.5 Simulation of QRod-NWs.....	86
5.6 Conclusions.....	91
5.7 Table of constants for InP and InAs of wurtzite type.....	92
5.8 References.....	94
<b>Chapter VI. Polarization properties of nanowires.....</b>	97
6.1 Introduction.....	98
6.2 State of the art.....	99
6.3 Mechanisms responsible for polarization anisotropy.....	101
6.4 Polarization properties of InP nanowires.....	105
6.5 Polarization properties of QWell nanowires.....	106
6.6 Polarization properties of single QRod nanowires.....	108
6.7 Polarization anisotropy of nanowire ensembles.....	112
6.8 Ensemble polarization model.....	115
6.9 Wavelength and temperature dependences of polarization anisotropy.....	119
6.10 Conclusions .....	122
6.11 References.....	123
<b>Chapter VII. Piezoelectricity of wurtzite nanowire heterostructures.....</b>	126
7.1 Introduction.....	127
7.2 Experimental results: piezoelectric field observation.....	128
7.3 Experimental results: impact of temperature.....	131
7.4 Simulation of piezoelectric field in nanowire heterostructures.....	133
7.5 Simulation results.....	136
7.6 Conclusions.....	141
7.7 References.....	142
<b>Chapter VIII. Quantum efficiency of nanowire heterostructures.....</b>	144
8.1 Introduction.....	145
8.2 Sample description.....	146
8.3 Experimental method.....	147
8.4 Results and discussion.....	149
8.5 Conclusions.....	153
8.6 References.....	154
<b>General conclusions.....</b>	156
<b>List of publications.....</b>	160
<b>Appendix: Résumé détaillé de la thèse en français.....</b>	161

# Chapter I

---

## Semiconductor nanowires

- 1.1 Introduction.
- 1.2 Nanowire growth.
- 1.3 Types of nanowire heterostructures.
- 1.3 Crystallographic structure of nanowires.
- 1.4 Energy band structure.
- 1.6 InAs/InP material pair for nanowire heterostructures.
- 1.7 III-V Nanowires on silicon emitting in telecom wavelength.
- 1.8 References.

## 1.1 Introduction.

The field of semiconductor nanowires (NWs) has during the last ten years developed very rapidly. Advances in epitaxial growth technology provide possibilities of NW growth with well controlled dimensions, position [1.1] and crystal structure [1.2]. Together with unique properties of NWs, this makes them interesting for many potential applications. In recent years, a number of simple devices has been demonstrated, showing the possibilities that may be available in the future. It was shown that semiconductor NWs can be used in such nanodevices as field-effect transistors (FETs) [1.3 – 1.8], solar cells [1.9 – 1.12], complementary metal oxide semiconductor (CMOS) [1.13], sensors [1.14, 1.15], superlattices [1.16], lasers [1.17, 1.18], detectors [1.15], [1.19], logic gates, computation circuits and memories [1.20 – 1.22]. P-n junctions have been demonstrated both within a single NW [1.5, 1.23, 1.24] and between NWs in contact [1.25]. Memory devices based on NW superlattices, demonstrated enhanced write-speeds compared to conventional flash memory [1.26]. It was shown that NWs can also be used for the piezo-mechanical applications [1.27 – 1.29]. The unique NW feature of polarization anisotropy of absorption and emission is very promising for making polarization-sensitive photo-detectors. NW heterostructures are also promising materials for fabrication of nanolasers, because a NW itself has possibility to be both waveguide and gain media at the same time, while the end facets of the NWs provide natural optical reflectors. In this context NWs have significant advantages of one-dimensional geometry, high-quality single-crystalline, high refractive index and strong photon confinement as compared to their thin-film analogues. Optically pumped laser emission from NWs has been reported number of times [1.17, 1.18, 1.30 – 1.33]. Another advantage of NWs is the possibility to tune the band gap controlling the NW diameter [1.34, 1.35]. NW based LEDs emitting with different wavelengths have been demonstrated [1.36 – 1.38]. Furthermore, III-V NWs can be grown epitaxially on Si, which enables III-V NW based devices to be integrated with established Si microelectronics technology. All that makes NWs promising building blocks for the future optoelectronic devices at nanoscale.

## 1.2 Nanowire growth.

A variety of techniques has been developed for one-dimensional structure fabrication. The formation of one-dimensional structures mostly depends on the enhancement of the crystal growth rate in one dimension and/or suppression of the growth in the other dimensions. In general, there are two main categories of NW growth techniques: template-directed and freestanding. The template-directed method suggests that the shape of the crystals is pre-defined by the template, so the suppressing of the growth in other dimensions is realized simply by physical confinement. For instance, the preferential nucleation may be set along the height of the template (Figure 1.1.a) [1.39], or along the length [1.40], as in v-groove templated NW growth (Figure 1.1.b).

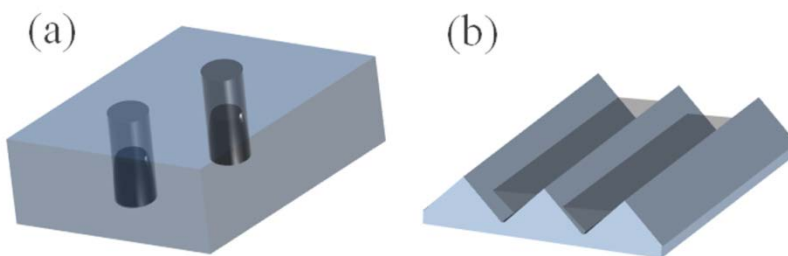


**Figure 1.1:** Template-directed NW growth techniques. (a) Nanowire growth directed by a template. (b) V-groove template-directed growth.

Template-directed NW growth techniques have certain advantages, such as existing lithographic technologies and possibility to be scaled with potential for high throughput, as well as natural integration into existing device structures, but, on the other hand, the resulting structures are necessarily confined to the surface on which they are grown.

The freestanding approach usually suggests the growth from a single nucleation point, with confinement only due to the relative growth rates of the different dimensions. NWs grown with this method have shown exceptional versatility in terms of material options, can be grown on a variety of surfaces (or without a surface at all) and readily transferred to other surfaces/media after the growth, and typically can be produced down to smaller sizes than those grown with template-directed approach.

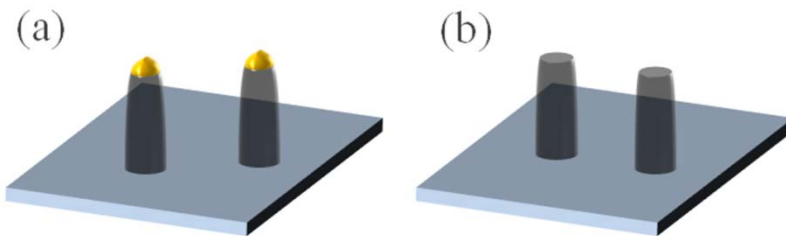


**Figure 1.2:** Freestanding NW growth techniques. (a) Particle-assisted freestanding nanowire growth. (b) Particle-free (self-assembled) freestanding nanowire growth.

The main approach in the growth of freestanding NWs is to use small seed particles of a foreign material (Figure 1.2.a). These particles promote the growth, increasing the growth rate in one dimension. This method is the oldest and most studied of the NW fabrication techniques. The foreign metal seed particle (typically Au; often called the catalyst) acts as a collector for the growth species in an MBE or MOVPE system or their derivatives. Growth species are collected in the metal droplet (seed particle) by direct impingement, by diffusion after impingement on the surrounding substrate surface or by diffusion after impingement on the nanowire sidewall surfaces (following initial formation of the NW). Supersaturation of the seed particle by the growth species results in the nucleation and epitaxial growth of NW material under each seed particle [1.41]. The earliest model explaining this phenomenon was named the Vapor-Liquid-Solid (VLS) model [1.42]. Such particle-assisted freestanding NWs can be grown from vapor or solution, with or without a substrate, with a very large range of potential particle materials in liquid or solid state, so the VLS method is used to grow almost all III–V compound semiconductors including phosphides, arsenides, antimonides and even some ternary alloy compounds. Nevertheless, the growth of freestanding NWs does not necessarily require a seed particle (Figure 1.2.b). One of the common techniques of particle-free growth is oxide-assisted growth. In this technique a mobile oxide layer on the surface acts to passivate side facets while enhancing one-dimensional growth [1.43]. Another technique suggests the use of a template to define the nucleation centers, while tailoring growth rates to suppress growth on certain crystalline facets, which form the side facets of the NWs. This technique is optimized to produce highly regular areas of nanowires over large areas [1.44, 1.45].

However, in the present work the particle-assisted approach is used to obtain NW samples. Particle-assisted methods for growth of freestanding III–V NWs include Metal Organic Chemical

Vapor Deposition (MOCVD) [1.46, 1.47], Molecular Beam Epitaxy (MBE) [1.48], and Chemical Beam Epitaxy (CBE) [1.49]. Samples described in Chapter 2 were grown on Si substrates by VLS assisted solid source MBE (VLS-MBE) on Si substrates with the assistance of Au-In particles. Axial and radial heterostructures are achieved by switching of species during the growth. In MBE, the NW morphology and the type of the grown heterostructures (radial or axial) are determined by the diffusivity of the growth species which can be controlled by growth conditions (temperature, impingement rate, V/III flux ratio) [1.41, 1.50 – 1.54]. Next we will consider the types of NW heterostructures that may be realized in freestanding NWs.

### 1.3 Types of nanowire heterostructures.

As far as NW heterostructures are concerned, the possibility to grow heterostructures in two different directions (axial and radial) is one of the advantages of semiconductor NWs as compared to planar heterostructures. For instance, such 2D quantum structure as quantum well (QWell) may be formed as radial QWell (usually referred as core-shell [1.55 – 1.58] and core-multishell [1.59 – 1.62]) or axial QWell (sometimes referred as quantum disk) [1.63 – 1.65]. In case of radial heterostructures even highly mismatched material systems are allowed due to the radial strain release [1.66]. Limitation of radial growth allows forming 0D quantum structures such as quantum dots (QDots) [1.38, 1.67 – 1.69] and 1D quantum structures such as quantum rods (QRods – elongated QDots) [1.70, 1.71] also known as quantum wires. Different types of NW heterostructures are summarized in Figure 1.3.

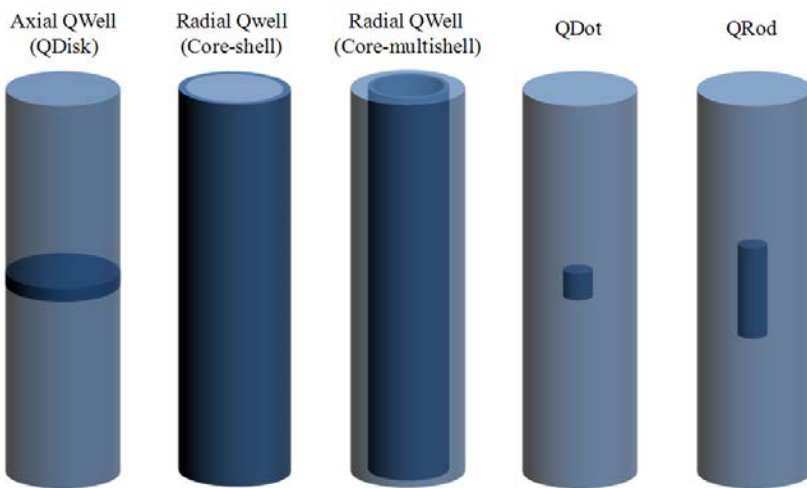


**Figure 1.3:** Schematic illustrations of the main types of NW heterostructures.

Beside of these simple configurations, fabrication of NW heterostructures containing multiple quantum structures has also been reported. As an example, radial [1.37] and axial [1.2, 1.72] multi QWell have been demonstrated. Moreover, the possibility to grow multiple QDots on the facets of NWs has also been shown [1.73]. A detailed review on the different types of NW heterostructures may be found elsewhere [1.74]. However, in this thesis we will mostly focus on QRod and radial QWell NW heterostructures obtained by VLS-MBE technique.

## 1.4 Crystallographic structure of nanowires.

Another important aspect of NW growth technology is the crystallographic structure of NWs. There are two main crystallographic structures found in III-V compounds: cubic zinc-blende (ZB) and hexagonal wurtzite (WZ) lattice structures. Although usually bulk III-V materials demonstrate the ZB cubic structure, with the exception of III-nitride compounds exhibiting WZ hexagonal structure, III-V NWs commonly display ZB and WZ polymorphism, in pure WZ phase [1.75 – 1.77] and sometimes in pure ZB phase [1.78].

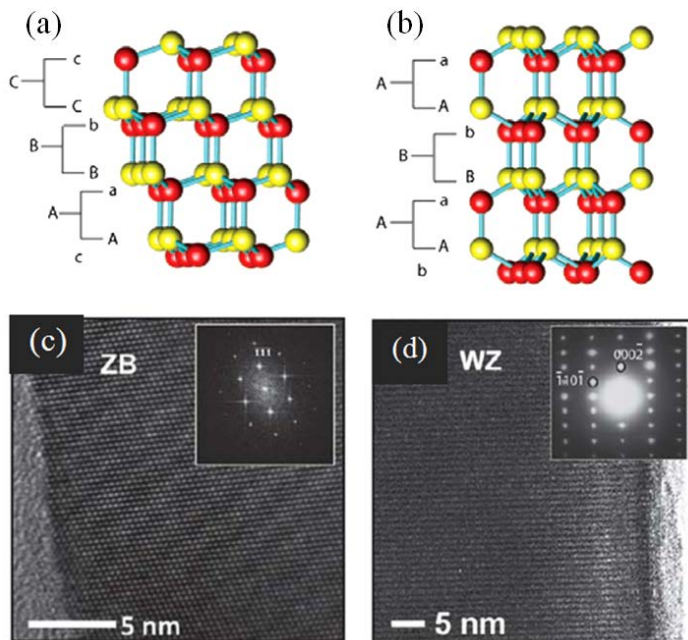


**Figure 1.4:** Schemes of atomic arrangement in ZB(a) and WZ(b) structures along the  $<111>$  and  $<0001>$  growth directions correspondingly [1.77, 1.79].

Scheme of atomic arrangement in ZB and WZ structures along the  $<111>$  and  $<0001>$  growth directions are shown in Figure 1.4. The ZB structure results from the stacking of monoatomic layers in the sequence of “cAaBbCcA” in the  $<111>$  direction. The WZ structure shows a stacking sequence of “bAaBbA” in the  $<0001>$  direction. There are certain types of planar defects which commonly occur in NWs: stacking faults and twin planes. The former appears when, due to the similarity of the two layer sequences, misplacement of an “Aa” plane with a “Cc” plane leads to the appearance of small ZB segments in WZ, while the latter leads to the introduction of two sequential twin planes which results in appearance of small WZ segments in ZB [1.75, 1.77]. The fraction of these “faulty” segments within the primary phase is often

regarded as the likelihood of nucleating seeds and growing single crystal NWs in either of the two phases [1.48, 1.75, 1.79 – 1.82]. The nucleation is believed to occur at the vapor-liquid-solid interface [1.83]. It is known that both the supersaturation of the liquid nanoparticle and the interface energies at the triple phase boundary have strong influence on the nucleation process and the resulting crystallographic phase [1.84]. Therefore, the appearance of a certain structure can be controlled by tuning temperature and V/III ratio parameters of VLS growth. The surface energy of WZ lateral facets is usually lower than those of ZB for the most of material systems and crystal orientations. So in the NWs, where surface-to-volume ratio is high, the appearance of WZ phase is favored [1.77, 1.84, 1.85]. Moreover, it is also known that the Gibbs–Thomson effect may also favor the formation of WZ structure in NWs of small radius [1.86, 1.87]. It is generally accepted that high supersaturation favors the appearance of a WZ phase [1.84, 1.87]. Thus, growth temperature is probably an effective parameter to control the NW crystallographic structure. Indeed, for a given precursor molar fraction, supersaturation increases at higher temperatures promoting WZ [1.47, 1.77, 1.88]. V/III ratio parameter is known to affect supersaturation, together with surface and interfacial energies, which in turn affect the formation of twins at the triple phase contact line [1.82]. Therefore, structure can be tuned by different precursor molar fractions with a fixed V/III ratio [1.89, 1.90] or varying the V/III ratio by changing group V or group III molar fractions independently [1.48, 1.82]. Decrease of the V/III ratio is usually increasing supersaturation and favoring the WZ phase. Hence, small V/III ratios and small group V molar flows results in formation of large WZ segments. It is important to note, that beside the other materials, these trends are also experimentally shown for InAs [1.47] and InP [1.77, 1.81, 1.91] materials grown on Si substrates. However it is worth mentioning that InAs seems to be an exception to this general trend, where the decrease of the growth temperature was found to increase the proportion of WZ phase [1.75, 1.86]. These remarkable advances in controlling the crystallographic properties of III-V NWs by the VLS mechanism made possible the fabrication of axial periodic structures. For instance, the formation of twinning superlattices were studied in the MOCVD growth of InAs [1.75] and InP [1.89] NWs. A more detailed review of NW crystal structure is provided in [1.77]. In the present work, growth conditions are chosen to favor the formation of the WZ phase, so the studied NWs and NW heterostructures have purely WZ crystallographic structure.

## 1.5 Energy band structure.

Since semiconductor NWs may be formed in the different crystallographic phases, it is important to note that optoelectronic properties of III-V crystals in the ZB and WZ phase are significantly different [1.92]. Theoretical calculations of the band structure of the most common III-V binary compounds predict the persistence of the direct character of the energy gap situated at the  $\Gamma$  point [1.93]. Scheme of energy band structures of ZB and WZ semiconductors at the  $\Gamma$  points is illustrated in Figure 1.5.

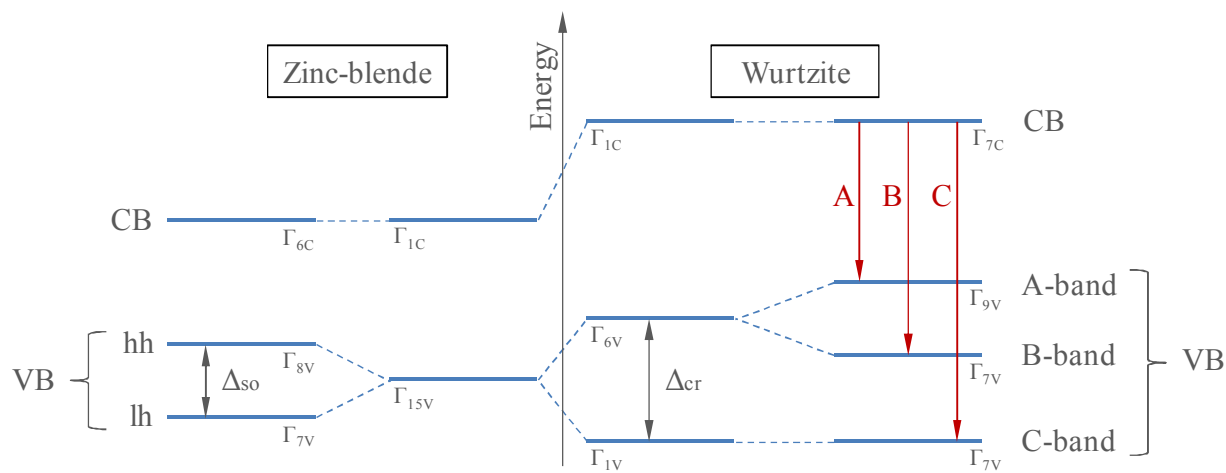


**Figure 1.5:** Scheme of energy band structures of ZB and WZ semiconductors.

At the highly symmetric  $\Gamma$  point, each band has numerous possible symmetries for the wavefunction. Without spin-orbit interaction, the transition from ZB to WZ structure causes the valence band to split at the  $\Gamma$  point, with a crystal-field splitting denoted by  $\Delta_{\text{cr}}$ . When spin-orbit interaction is concerned, the spin-orbit coupling  $\Delta_{\text{so}}$ , results in the splitting of  $\Gamma_{6v}$  valence band in WZ into a higher ( $\Gamma_{9v}$ ) energy band (known as A-band) and a lower ( $\Gamma_{7v}$ ) energy band (known as B-band). Therefore three different transitions (A, B and C) are possible. In general, under the quasicubic approximation, the energy differences between the valence bands induced by spin-orbit interaction in the WZ structure are given by [1.92]:

$$\Delta E = E(\Gamma_{7v}^{1,2}) - E(\Gamma_{9v}) = \frac{\Delta_{\text{so}} + \Delta_{\text{cr}}}{2} \pm \frac{\sqrt{(\Delta_{\text{so}} + \Delta_{\text{cr}})^2 - u^{-1}\Delta_{\text{so}}\Delta_{\text{cr}}}}{2} \quad (1.1)$$

where  $u$  is related to the lattice constants by  $u = (a / c)^2$ . In case of ZB structure the  $\Gamma_{15v}$  valence band also splits into higher ( $\Gamma_{8v}$ ) and lower ( $\Gamma_{7v}$ ) energy bands, known as heavy and light holes, making two different transitions possible.

Another important difference in optoelectronic properties of ZB and WZ consists in polarization of different transition. The symmetry of the crystalline structure may affect such optical properties as the dielectric function or the absorption coefficient. These parameters are generally represented by a second order tensor, where the number of components depends on the crystalline structure [1.93]. ZB structure does not cause any anisotropy in optical transitions [1.94], hence the tensor has only one component, whereas in WZ structure the tensor has two components that depend on the polarization state being either parallel or orthogonal to the z-axis, so the orientation of the crystal affects the oscillator strength of a direct transition. As far as spin-orbit interaction is concerned, calculations show that A-band transition is expected to be orthogonal to z axis of WZ crystal, while the B and C band transitions have a parallel and an orthogonal components [1.92, 1.94]. This effect is known as the “selection rule” of WZ material. However, there are other mechanisms which may affect polarization of NWs, making the selection rule negligible. These mechanisms will be considered in Chapter 6.2.

## 1.6 InAs/InP material pair for nanowire heterostructures.

At present, III-V compound semiconductors provide a materials basis for a number of well-established commercial applications, including high-electron-mobility and heterostructure bipolar transistors, diode lasers, light-emitting diodes, photodetectors, electro-optic modulators, and frequency-mixing components. Since ternary and quaternary alloys may be included in addition to the binary compounds, and the materials may be designed in an almost endless variety of configurations. InAs has assumed increasing importance in recent years as the electron quantum well/dot material for the optoelectronic devices emitting at telecom wavelength [1.95, 1.96]. Lasers containing InAs or InGaAs QDots embedded in GaAs or AlGaAs matrix have been successfully demonstrated and showing some improved characteristics [1.97, 1.98]. However, the longest wavelength emission for GaInAs/GaAs QDot lasers is 1.3  $\mu\text{m}$ , which considerably restricts applications in optical fiber communication systems [1.99]. In order to achieve the emission within the spectral window of optical telecommunication interest, the growth of InAs QDs on InP substrates has been proposed [1.100 – 1.102]. Furthermore, it was shown that precise tuning of the emitting wavelength can be realized on InAs/InP binary compound [1.95, 1.96, 1.103]. Therefore, InAs/InP material pair is a promising candidate for light emitting and detecting devices at telecommunication wavelength. For these reasons, despite the lattice mismatch between InAs and InP, this pair is chosen as a material basis for this work.

## 1.7 III-V Nanowires on silicon emitting in telecom wavelength.

This thesis mainly takes place in the frame of the French Agence Nationale pour la Recherche (ANR) “INSCOOP” project. This project proposes an original strategy of compact optical sources integration on Si wafer for on-chip interconnects. The link consists of a Si optical waveguide fabricated from a SOI (Si on insulator) substrate. The compact source will operate in the telecommunication window and will be fabricated directly on the Si waveguide. This source is based on an array of III-V nanowires grown selectively on the Si surface on top of the waveguide (Figure 1.6).

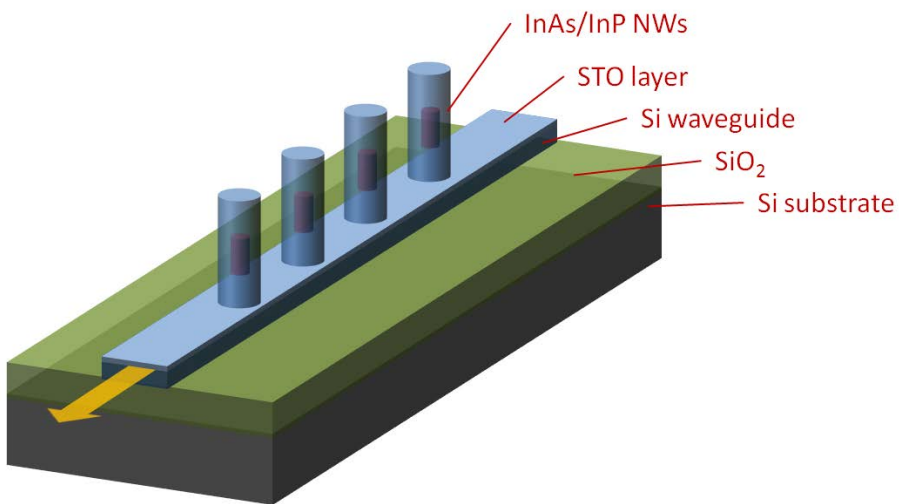


**Figure 1.6:** Scheme of the compact NW light source able to emit photons in the Si waveguide.

The emitter should consist of an InAs or InAsP segment (QRod) embedded in an InP NW. To be able to couple the light emitted by the nanowires into the Si waveguide, the geometry of the NW array must be optimized to obtain a photonic structure with optical modes able to couple with the modes of the Si waveguide. The project aims to demonstrate that under optical pumping, hybrid Bloch modes can be amplified in the III-V NW array and propagate in the passive Si waveguide. This demonstration will pave the way to fully integrated photonic links on Si chips. As far as the optical spectroscopy is concerned, this work requires a good understanding of the emission properties of InAs(P)/InP NWs.

## 1.8 References

- [1.1] T. Mårtensson, M. T. Borgström, L. Samuelson, W. Seifert, and B. J. Ohlsson, "Fabrication of individually seeded nanowire arrays by vapour–liquid–solid", *Nanotechnology*, vol. 14, p. 1255, 2003.
- [1.2] A. Fuhrer, L. E. Fröberg, J. N. Pedersen, M. W. Larsson, A. Wacker, M.-E. Pistol, and L. Samuelson, "Few electron double quantum dots in InAs/InP nanowire heterostructures", *Nano letters*, vol. 7, p. 243, 2007.
- [1.3] J. Xiang, W. Lu, Y. Hu, Y. Wu, H. Yan, and C. M. Lieber, "Ge/Si nanowire heterostructures as high-performance field-effect transistors", *Nature*, vol. 441, p. 489, 2006.
- [1.4] Y. Cui, Z. Zhong, D. Wang, W. U. Wang, and C. M. Lieber, "High performance silicon nanowire field effect transistors", *Nano letters*, vol. 3, p. 149, 2003.
- [1.5] Y. Li, F. Qian, J. Xiang, and C. M. Lieber, "Nanowire electronic and optoelectronic devices Electronic and optoelectronic devices impact many areas of society , from", *Materialstoday*, vol. 9, p. 18, 2006.
- [1.6] H.-Y. Cha, H. Wu, M. Chandrashekhar, Y. C. Choi, S. Chae, G. Koley, and M. G. Spencer, "Fabrication and characterization of pre-aligned gallium nitride nanowire field-effect transistors", *Nanotechnology*, vol. 17, p. 1264, 2006.
- [1.7] S. A. Dayeh, D. P. R. Aplin, X. Zhou, P. K. L. Yu, E. T. Yu, and D. Wang, "High electron mobility InAs nanowire field-effect transistors", *Small*, vol. 3, p. 326, 2007.
- [1.8] J. Goldberger, A. I. Hochbaum, R. Fan, and P. Yang, "Transistors, Silicon Vertically Integrated Nanowire Field Effect", *Nano letters*, vol. 6, p. 973, 2006.
- [1.9] B. Tian, X. Zheng, T. J. Kempa, Y. Fang, N. Yu, G. Yu, J. Huang, and C. M. Lieber, "Coaxial silicon nanowires as solar cells and nanoelectronic power sources", *Nature*, vol. 449, p. 885, 2007.
- [1.10] F. Boxberg, N. Søndergaard, and H. Q. Xu, "Photovoltaics with piezoelectric core-shell nanowires", *Nano letters*, vol. 10, p. 1108, 2010.
- [1.11] M. Law, L. E. Greene, J. C. Johnson, R. Saykally, and P. Yang, "Nanowire dye-sensitized solar cells", *Nature Materials*, vol. 4, p. 455, 2005.
- [1.12] C. Colombo, M. Heiß, M. Gratzel, and A. Fontcuberta i Morral, "Gallium arsenide p-i-n radial structures for photovoltaic applications", *Applied Physics Letters*, vol. 94, p. 173108, 2009.
- [1.13] E. Stern, J. F. Klemic, D. A. Routenberg, P. N. Wyrembak, D. B. Turner-Evans, A. D. Hamilton, D. A. LaVan, T. M. Fahmy, and M. A. Reed, "Label-free immunodetection with CMOS-compatible semiconducting nanowires", *Nature*, vol. 445, p. 519, 2007.

- [1.14] M. C. McAlpine, H. Ahmad, D. Wang, and J. R. Heath, "Highly ordered nanowire arrays on plastic substrates for ultrasensitive flexible chemical sensors", *Nature Materials*, vol. 6, p. 379, 2007.
- [1.15] G. Zheng, F. Patolsky, Y. Cui, W. U. Wang, and C. M. Lieber, "Multiplexed electrical detection of cancer markers with nanowire sensor arrays", *Nature Biotechnology*, vol. 23, p. 1294, 2005.
- [1.16] C. M. Lieber, "Nanowire superlattice", *Nano letters*, vol. 2, p. 81, 2002.
- [1.17] X. Duan, Y. Huang, R. Agarwa, and C. M. Lieber, "Single-nanowire electrically driven lasers", *Nature*, vol. 421, p. 241, 2003.
- [1.18] M. H. Huang, S. Mao, H. Feic, H. Yan, Y. Wu, H. Kind, E. Weber, R. Russo, and P. Yang, "Room-temperature ultraviolet nanowire nanolasers", *Science*, vol. 292, p. 1897, 2001.
- [1.19] K. M. Rosfjord, J. K. W. Yang, E. A. Dauler, A. J. Kerman, V. Anant, B. M. Voronov, G. N. Goltsman, and K. K. Berggren, "Nanowire single-photon detector with an integrated optical cavity and anti-reflection coating", *Optics Express*, vol. 14, p. 527, 2006.
- [1.20] M. Lee, J. Im, B. Y. Lee, S. Myung, J. Kang, L. Huang, Y. K. Kwon, and S. Hong, "Linker-free directed assembly of high-performance integrated devices based on nanotubes and nanowires", *Nature Nanotechnology*, vol. 1, p. 66, 2006.
- [1.21] R. S. Friedman, M. C. McAlpine, D. S. Ricketts, D. Ham, and C. M. Lieber, "Nanotechnology: high-speed integrated nanowire circuits", *Nature*, vol. 434, p. 1085, 2005.
- [1.22] H. Kind, H. Yan, B. Messer, M. Law, and P. Yang, "Nanowire ultraviolet photodetectors and optical switches", *Advanced materials*, vol. 14, p. 158, 2002.
- [1.23] K. Haraguchi, T. Katsuyama, K. Hiruma, and K. Ogawa, "GaAs p-n junction formed in quantum wire crystals", *Applied Physics Letters*, vol. 60, p. 745, 1992.
- [1.24] E. Tutuc, J. Appenzeller, M. C. Reuter, and S. Guha, "Realization of a Linear Germanium Nanowire p–n Junction", *Nano letters*, vol. 6, p. 2070, 2006.
- [1.25] X. Duan, Y. Huang, Y. Cui, J. Wang, and C. M. Lieber, "Indium phosphide nanowires as building blocks for nanoscale electronic and optoelectronic devices", *Nature*, vol. 409, p. 66, 2001.
- [1.26] C. Thelander, H. A. Nilsson, L. E. Jensen, and L. Samuelson, "Nanowire Single-Electron Memory", *Nano letters*, vol. 5, p. 635, 2005.
- [1.27] Y. Qin, X. Wang, and Z. L. Wang, "Microfibre–nanowire hybrid structure for energy scavenging", *Nature*, vol. 451, p. 809, 2008.
- [1.28] X. Wang, K. Kim, Y. Wang, M. Stadermann, A. Noy, A. V Hamza, J. Yang, and D. J. Sirbuly, "Matrix-Assisted Energy Conversion in Nanostructured Piezoelectric Arrays", *Nano letters*, vol. 10, p. 4901, 2010.

- [1.29] Z. Wang, J. Hu, A. P. Suryavanshi, K. Yum, and M.-F. Yu, "Voltage generation from individual BaTiO(3) nanowires under periodic tensile mechanical load", *Nano letters*, vol. 7, p. 2966, 2007.
- [1.30] A. L. Pan, W. Zhou, E. S. P. Leong, R. Liu, A. H. Chin, B. Zou, and C. Z. Ning, "Continuous alloycomposition spatial grading and superbroad wavelength-tunable nanowire lasers on a single chip", *Nano letters*, vol. 9, p. 784, 2009.
- [1.31] A. H. Chin, S. Vaddiraju, A. V. Maslov, C. Z. Ning, M. K. Sunkara, and M. Meyyappan, "Near-infrared semiconductor subwavelength-wire lasers", *Applied Physics Letters*, vol. 88, p. 163115, 2006.
- [1.32] Y. Xiao, C. Meng, P. Wang, Y. Ye, H. Yu, S. Wang, F. Gu, L. Dai, and L. Tong, "Single-Nanowire Single-Mode Laser", *Nano letters*, vol. 11, p. 1122, 2011.
- [1.33] R. Chen, T. D. Tran, K. W. Ng, W. S. Ko, L. C. Chuang, F. G. Sedgwick, and C. Chang-Hasnain, "Nanolasers grown on silicon", *Nature Photonics*, vol. 5, p. 170, 2007.
- [1.34] A. R. Guichard, D. N. Barsic, S. Sharma, T. I. Kamins, and M. L. Brongersma, "Tunable Light Emission from Quantum-Confining Excitons in TiSi<sub>2</sub>-Catalyzed Silicon Nanowires", *Nano letters*, vol. 6, p. 2140, 2006.
- [1.35] L. Yang, J. Motohisa, J. Takeda, K. Tomioka, and T. Fukui, "Size-dependent photoluminescence of hexagonal nanopillars with single InGaAs/GaAs quantum wells fabricated by selective-area metal organic vapor phase epitaxy", *Applied Physics Letters*, vol. 89, p. 203110, 2006.
- [1.36] J. Bao, M. A. Zimmler, and F. Capasso, "Broadband ZnO Single-Nanowire Light-Emitting Diode", *Nano letters*, vol. 6, p. 1719, 2006.
- [1.37] F. Qian, S. Gradečak, Y. Li, C.-Y. Wen, and C. M. Lieber, "Core/Multishell Nanowire Heterostructures as Multicolor, High-Efficiency Light-Emitting Diodes", *Nano letters*, vol. 5, p. 2287, 2005.
- [1.38] E. D. Minot, F. Kelkensberg, M. van Kouwen, J. A. van Dam, L. P. Kouwenhoven, V. Zwiller, M. T. Borgström, O. Wunnicke, M. A. Verheijen, and E. P. a M. Bakkers, "Single quantum dot nanowire LEDs", *Nano letters*, vol. 7, p. 367, 2007.
- [1.39] R. Adelung, O. C. Aktas, J. Franc, A. Biswas, R. Kunz, M. Elbahri, J. Kanzow, U. Schurmann, and F. Faupel, "Strain-controlled growth of nanowires within thin-film cracks", *Nature Materials*, vol. 3, p. 375, 20004.
- [1.40] A. Gustafsson, F. Reinhardt, G. Biasiol, and E. Kapon, "Low pressure organometallic chemical vapor deposition of quantum wires on V-grooved substrates", *Applied Physics Letters*, vol. 67, p. 3673, 1995.
- [1.41] R. R. LaPierre, A. C. E. Chia, S. J. Gibson, C. M. Haapamaki, J. Boulanger, R. Yee, P. Kuyanov, J. Zhang, N. Tajik, N. Jewell, and K. M. A. Rahman, "III-V nanowire photovoltaics: Review of design for high efficiency", *Physica Status Solidi (RRL)*, vol. 16, 2013.

- [1.42] R. S. Wagner and W. C. Ellis, "Vapor-Liquid-Solid Mechanism of Single Crystal Growth", *Applied Physics Letters*, vol. 4, p. 89, 1964.
- [1.43] W. Shi, Y. Zheng, N. Wang, C.-S. Lee, and S.-T. Lee, "A general synthetic route to III-V compound semiconductor nanowires", *Advanced materials*, vol. 13, p. 591, 2001.
- [1.44] J. Noborisaka, J. Motohisa, S. Hara, and T. Fukui, "Fabrication and characterization of freestanding GaAs/AlGaAs core-shell nanowires and AlGaAs nanotubes by using selective-area metalorganic vapor phase epitaxy", *Applied Physics Letters*, vol. 87, p. 093109, 2005.
- [1.45] S. D. Hersee, X. Sun, and X. Wang, "The Controlled Growth of GaN Nanowires", *Nano letters*, vol. 6, p. 1808, 2006.
- [1.46] C. Soci, X.-Y. Bao, D. P. R. Aplin, and D. Wang, "A Systematic Study on the Growth of GaAs Nanowires by Metal-Organic Chemical Vapor Deposition", *Nano letters*, vol. 8, p. 4275, 2008.
- [1.47] H. J. Joyce, J. Wong-Leung, Q. Gao, H. H. Tan, and C. Jagadish, "Phase Perfection in Zinc Blende and Wurtzite III-V Nanowires Using Basic Growth Parameters", *Nano letters*, vol. 10, p. 908, 2010.
- [1.48] D. Spirkoska, J. Arbiol, A. Gustafsson, S. Conesa-Boj, F. Glas, I. Zardo, M. Heigoldt, M. H. Gass, A. L. Bleloch, S. Estrade, M. Kaniber, J. Rossler, F. Peiro, J. R. Morante, G. Abstreiter, L. Samuelson, and A. Fontcuberta i Morral, "Structural and optical properties of high quality zinc-blende/wurtzite GaAs nanowire heterostructures", *Physical Review B*, vol. 80, p. 245325, 2009.
- [1.49] A. I. Persson, B. J. Ohlsson, S. Jeppesen, and L. Samuelson, "Growth mechanisms for GaAs nanowires grown in CBE", *Journal of Crystal Growth*, vol. 272, p. 167, 2004.
- [1.50] V. G. Dubrovskii, M. A. Timofeeva, M. Tchernycheva, and A. D. Bolshakov, "Lateral growth and shape of semiconductor nanowires", *Semiconductors*, vol. 47, p. 50, 2013.
- [1.51] V. Dubrovskii, N. Sibirev, G. Cirlin, I. Soshnikov, W. H. Chen, R. Larde, E. Cadel, P. Pareige, T. Xu, B. Grandidier, J.-P. Nys, D. Stievenard, M. Moewe, L. Chuang, and C. Chang-Hasnain, "Gibbs-Thomson and diffusion-induced contributions to the growth rate of Si, InP, and GaAs nanowires", *Physical Review B*, vol. 79, p. 205316, 2009.
- [1.52] N. V. Sibirev, V. G. Dubrovskii, G. E. Cirlin, V. A. Egorov, Y. B. Samsonenko, and V. M. Ustinov, "Deposition-rate dependence of the height of GaAs-nanowires", *Semiconductors*, vol. 42, p. 1259, 2009.
- [1.53] V. G. Dubrovskii, N. V. Sibirev, G. E. Cirlin, M. Tchernycheva, J. C. Harmand, and V. M. Ustinov, "Shape modification of III-V nanowires: The role of nucleation on sidewalls", *Physical Review E*, vol. 77, p. 031606, 2008.
- [1.54] J.-C. Harmand, F. Glas, and G. Patriarche, "Growth kinetics of a single  $\text{InP}_{(1-x)}\text{As}_{(x)}$  nanowire", *Physical Review B*, vol. 81, p. 235436, 2010.

- [1.55] Z. Zanolli, B. a Wacaser, M.-E. Pistol, K. Deppert, and L. Samuelson, "Core-shell InP-CdS nanowires: fabrication and study", *Journal of physics: Condensed matter*, vol. 19, p. 295218, 2007.
- [1.56] Z. Zanolli, M.-E. Pistol, L. E. Fröberg, and L. Samuelson, "Quantum-confinement effects in InAs-InP core-shell nanowires.", *Journal of physics: Condensed matter*, vol. 19, p. 295219, 2007.
- [1.57] L. V. Titova, T. B. Hoang, H. E. Jackson, L. M. Smith, J. M. Yarrison-Rice, Y. Kim, H. J. Joyce, H. H. Tan, and C. Jagadish, "Temperature dependence of photoluminescence from single core-shell GaAs-AlGaAs nanowires", *Applied Physics Letters*, vol. 89, p. 173126, 2006.
- [1.58] G. Jacopin, L. Rigutti, S. Bellei, P. Lavenus, F. H. Julien, a V Davydov, D. Tsvetkov, K. A. Bertness, N. a Sanford, J. B. Schlager, and M. Tchernycheva, "Photoluminescence polarization in strained GaN/AlGaN core/shell nanowires", *Nanotechnology*, vol. 23, p. 325701, 2012.
- [1.59] Y. Masumoto, Y. Hirata, P. Mohan, J. Motohisa, and T. Fukui, "Polarized photoluminescence from single wurtzite InP/InAs/InP core-multishell nanowires", *Applied Physics Letters*, vol. 98, p. 211902, 2011.
- [1.60] B. Pal, K. Goto, M. Ikezawa, Y. Masumoto, P. Mohan, J. Motohisa, and T. Fukui, "Type-II behavior in wurtzite InP/InAs/InP core-multishell nanowires", *Applied Physics Letters*, vol. 93, p. 073105, 2008.
- [1.61] P. Mohan, J. Motohisa, and T. Fukui, "Fabrication of InP/InAs/InP core-multishell heterostructure nanowires by selective area metalorganic vapor phase epitaxy", *Applied Physics Letters*, vol. 88, p. 133105, 2006.
- [1.62] H. Khmissi, K. Naji, M. H. Hadj Alouane, N. Chauvin, C. Bru-Chevallier, B. Ilahi, G. Patriarche, and M. Gendry, "InAs/InP nanowires grown by catalyst assisted molecular beam epitaxy on silicon substrates", *Journal of Crystal Growth*, vol. 344, p. 45, 2012.
- [1.63] R. Armitage and K. Tsubaki, "Multicolour luminescence from InGaN quantum wells grown over GaN nanowire arrays by molecular-beam epitaxy.", *Nanotechnology*, vol. 21, p. 195202, 2010.
- [1.64] M. Wölz, V. M. Kaganer, O. Brandt, L. Geelhaar, and H. Riechert, "Analyzing the growth of  $In_xGa_{1-x}N/GaN$  superlattices in self-induced GaN nanowires by x-ray diffraction", *Applied Physics Letters*, vol. 98, p. 261907, 2011.
- [1.65] J. Lähnemann, O. Brandt, C. Pfüller, T. Flissikowski, U. Jahn, E. Luna, M. Hanke, M. Knelangen, A. Trampert, and H. T. Grahn, "Coexistence of quantum-confined Stark effect and localized states in an  $(In,Ga)N/GaN$  nanowire heterostructure", *Physical Review B*, vol. 84, p. 155303, 2011.
- [1.66] F. Glas, "Critical dimensions for the plastic relaxation of strained axial heterostructures in free-standing nanowires", *Physical Review B*, vol. 74, p. 121302, 2006.
- [1.67] N. Panev, A. I. Persson, N. Skold, and L. Samuelson, "Sharp exciton emission from single InAs quantum dots in GaAs nanowires", *Applied Physics Letters*, vol. 83, p. 2238, 2003.

- [1.68] M. H. M. van Weert, N. Akopian, F. Kelkensberg, U. Perinetti, M. P. van Kouwen, J. G. Rivas, M. T. Borgström, R. E. Algra, M. a Verheijen, E. P. a M. Bakkers, L. P. Kouwenhoven, and V. Zwiller, "Orientation-dependent optical-polarization properties of single quantum dots in nanowires", *Small*, vol. 5, p. 2134, 2009.
- [1.69] M. Tchernycheva, G. E. Cirlin, G. Patriarche, L. Travers, V. Zwiller, U. Perinetti, and J.-C. Harmand, "Growth and characterization of InP nanowires with InAsP insertions", *Nano letters*, vol. 7, p. 1500, 2007.
- [1.70] A. Sitt, A. Salant, G. Menagen, and U. Banin, "Highly emissive nano rod-in-rod heterostructures with strong linear polarization", *Nano letters*, vol. 11, p. 2054, 2011.
- [1.71] M. T. Borgström, V. Zwiller, E. Müller, and A. Imamoglu, "Optically bright quantum dots in single Nanowires.", *Nano letters*, vol. 5, p. 1439, 2005.
- [1.72] F. Furtmayr, J. Teubert, P. Becker, S. Conesa-Boj, J. R. Morante, A. Chernikov, S. Schäfer, S. Chatterjee, J. Arbiol, and M. Eickhoff, "Carrier confinement in GaN/Al<sub>(x)</sub>Ga<sub>(1-x)</sub>N nanowire heterostructures", *Physical Review B*, vol. 84, p. 205303, 2011.
- [1.73] E. Uccelli, J. Arbiol, J. R. Morante, and A. Fontcuberta i Morral, "InAs Quantum Dot Arrays Decorating the Facets of GaAs Nanowires", *ACS nano*, vol. 4, p. 5985, 2010.
- [1.74] M. D. La Mata, X. Zhou, F. Furtmayr, J. Teubert, S. Gradečák, M. Eickhoff, A. Fontcuberta i Morral, and J. Arbiol, "A review of MBE grown 0D, 1D and 2D quantum structures in a nanowire", *Journal of Materials Chemistry C*, vol. 1, p. 4300, 2013.
- [1.75] P. Caroff, K. A. Dick, J. Johansson, M. E. Messing, K. Deppert, and L. Samuelson, "Controlled polytypic and twin-plane superlattices in III–V nanowires", *Nature Nanotechnology*, vol. 4, p. 50, 2009.
- [1.76] S. A. Dayeh, C. Soci, X.-Y. Bao, and D. Wang, "Advances in the synthesis of InAs and GaAs nanowires for electronic applications", *Nano Today*, vol. 4, p. 347, 2009.
- [1.77] K. A. Dick, P. Caroff, J. Bolinsson, M. E. Messing, J. Johansson, K. Deppert, L. R. Wallenberg, and L. Samuelson, "Control of III–V nanowire crystal structure by growth parameter tuning", *Semiconductor Science and Technology*, vol. 25, p. 024009, 2010.
- [1.78] T. T. T. Vu, T. Zehender, M. a Verheijen, S. R. Plissard, G. W. G. Immink, J. E. M. Haverkort, and E. P. a M. Bakkers, "High optical quality single crystal phase wurtzite and zincblende InP nanowires.", *Nanotechnology*, vol. 24, p. 115705, 2013.
- [1.79] C. Wilhelm, A. Larrue, X. Dai, D. Migasd, and C. Soci, "Anisotropic photonic properties of III–V nanowires in the zinc-blende and wurtzite phase", *Nanoscale*, vol. 4, p. 1446, 2012.
- [1.80] K. Ikejiri, Y. Kitauchi, K. Tomioka, J. Motohisa, and T. Fukui, "Zinc Blende and Wurtzite Crystal Phase Mixing and Transition in Indium Phosphide Nanowires", *Nano letters*, vol. 11, p. 4314, 2011.

- [1.81] S. Paiman, Q. Gao, H. H. Tan, C. Jagadish, K. Pemasiri, M. Montazeri, H. E. Jackson, L. M. Smith, J. M. Yarrison-Rice, X. Zhang, and J. Zou, "The effect of V/III ratio and catalyst particle size on the crystal structure and optical properties of InP nanowires", *Nanotechnology*, vol. 20, p. 225606, 2009.
- [1.82] H. J. Joyce, Q. Gao, H. H. Tan, C. Jagadish, Y. Kim, M. a. Fickenscher, S. Perera, T. B. Hoang, L. M. Smith, H. E. Jackson, J. M. Yarrison-Rice, X. Zhang, and J. Zou, "High Purity GaAs Nanowires Free of Planar Defects: Growth and Characterization", *Advanced Functional Materials*, vol. 18, p. 3794, 2008.
- [1.83] J. Johansson, L. S. Karlsson, C. P. T. Svensson, T. Mårtensson, B. A. Wacaser, K. Deppert, L. Samuelson, and W. Seifert, "Structural properties of left fence 111 right fence B -oriented III-V nanowires", *Nature Materials*, vol. 5, p. 574, 2006.
- [1.84] F. Glas, J.-C. Harmand, and G. Patriarche, "Why Does Wurtzite Form in Nanowires of III-V Zinc Blende Semiconductors?", *Physical Review Letters*, vol. 99, p. 146101, 2007.
- [1.85] V. Dubrovskii, N. Sibirev, G. Cirlin, J. Harmand, and V. Ustinov, "Theoretical analysis of the vapor-liquid-solid mechanism of nanowire growth during molecular beam epitaxy", *Physical Review E*, vol. 73, p. 021603, 2006.
- [1.86] J. Johansson, K. A. Dick, P. Caroff, M. E. Messing, J. Bolinsson, K. Deppert, and L. Samuelson, "Diameter Dependence of the Wurtzite–Zinc Blende Transition in InAs Nanowires", *Journal of Physical Chemistry*, vol. 114, p. 3837, 2010.
- [1.87] V. G. Dubrovskii and N. V. Sibirev, "Growth thermodynamics of nanowires and its application to polytypism of zinc blende III-V nanowires", *Physical Review B*, vol. 77, p. 035414, 2008.
- [1.88] V. G. Dubrovskii, N. V. Sibirev, J. C. Harmand, and F. Glas, "Growth kinetics and crystal structure of semiconductor nanowires", *Physical Review B*, vol. 78, p. 235301, 2008.
- [1.89] R. E. Algra, M. A. Verheijen, L.-F. Feiner, G. G. W. Immink, W. J. P. van Enckevort, E. Vlieg, and E. P. A. M. Bakkers, "The Role of Surface Energies and Chemical Potential during Nanowire Growth", *Nano letters*, vol. 11, p. 259, 2011.
- [1.90] H. J. Joyce, Q. Gao, H. H. Tan, C. Jagadish, Y. Kim, M. A. Fickenscher, S. Perera, T. B. Hoang, L. M. Smith, H. E. Jackson, J. M. Yarrison-Rice, X. Zhang, and J. Zou, "Unexpected Benefits of Rapid Growth Rate for III–V Nanowires", *Nano letters*, vol. 9, p. 695, 2009.
- [1.91] S. Paiman, Q. Gao, H. J. Joyce, Y. Kim, H. H. Tan, C. Jagadish, X. Zhang, Y. Guo, and J. Zou, "Growth temperature and V/III ratio effects on the morphology and crystal structure of InP nanowires", *Journal of Physics D: Applied Physics*, vol. 43, p. 445402, 2010.
- [1.92] S. Chuang and C. Chang, "K-P Method for Strained Wurtzite Semiconductors", *Physical Review B*, vol. 54, p. 2491, 1996.
- [1.93] C. Wilhelm, A. Larrue, X. Dai, D. Migas, and C. Soci, "Anisotropic photonic properties of III-V nanowires in the zinc-blende and wurtzite phase", *Nanoscale*, vol. 4, p. 1446, 2012.

- [1.94] J. L. Birman, "Polarization of Fluorescence in CdS and ZnS Single Crystals", *Physical Review Letters*, vol. 2, p. 157, 1959.
- [1.95] L. Seravalli, G. Trevisi, P. Frigeri, D. Rivas, G. Muñoz-Matutano, I. Suárez, B. Alén, J. Canet, and J. P. Martínez-Pastor, "Single quantum dot emission at telecom wavelengths from metamorphic InAs/InGaAs nanostructures grown on GaAs substrates", *Applied Physics Letters*, vol. 98, p. 173112, 2011.
- [1.96] S. Fréchengues, N. Bertru, V. Drouot, B. Lambert, S. Robinet, S. Loualiche, D. Lacombe, and a. Ponchet, "Wavelength tuning of InAs quantum dots grown on (311)B InP", *Applied Physics Letters*, vol. 74, p. 3356, 1999.
- [1.97] N. Kirstaedter, N. N. Ledentsov, M. Grundmann, and D. Bimberg, "Low threshold, large To injection laser emission from (InGa)As quantum dots", *Electronics Letters*, vol. 30, p. 1416, 1994.
- [1.98] K. Kamath, P. Bhattacharya, T. Sosnowski, T. Norris, and J. Phillips, "Room-temperature operation of In(0.4)Ga(0.6)As/GaAs self-organised quantum dot lasers", *Electronics Letters*, vol. 32, p. 1374, 1996.
- [1.99] D. L. Huffaker and D. G. Deppe, "Electroluminescence efficiency of 1.3  $\mu\text{m}$  wavelength InGaAs/GaAs quantum dots", *Applied Physics Letters*, vol. 73, p. 520, 1998.
- [1.100] A. Ponchet, A. Le Corre, H. L'Haridon, B. Lambert, and S. Salaun, "Relationship between self-organization and size of InAs islands on InP(001) grown by gas-source molecular beam epitaxy", *Applied Physics Letters*, vol. 67, p. 1850, 1995.
- [1.101] H. Marchand, P. Desjardins, S. Guillon, J.-E. Paultre, Z. Bougrioua, R. Y.-F. Yip, and R. a. Masut, "Metalorganic vapor phase epitaxy of coherent self-assembled InAs nanometer-sized islands in InP(001)", *Applied Physics Letters*, vol. 71, p. 527, 1997.
- [1.102] N. Lebouché-Girard, A. Rudra, and E. Kapon, "Growth and transformation of ultra-thin InAs / InP layers obtained by chemical beam epitaxy", *Journal of Crystal Growth*, vol. 175, p. 1210, 1997.
- [1.103] A. Michon, G. Saint-Girons, G. Beaudoin, I. Sagnes, L. Largeau, and G. Patriarche, "InAs/InP(001) quantum dots emitting at 1.55  $\mu\text{m}$  grown by low-pressure metalorganic vapor-phase epitaxy", *Applied Physics Letters*, vol. 87, p. 253114, 2005.

# **Chapter II**

---

## InAs/InP nanowire samples. Growth and characterization

- 2.1 Introduction
- 2.2 InP nanowires.
- 2.3 InAs/InP radial quantum well nanowires.
- 2.4 InAs/InP quantum rod nanowires.
- 2.5 Conclusions.
- 2.6 References.

## **2.1 Introduction.**

The present chapter is devoted to step by step optimization of growth parameters in order to obtain InAs/InP quantum dot/rod NW heterostructures of high quality. The high quality of NWs presupposes pure WZ crystallographic structure with no defects or ZB insertions. To achieve this first step the growth conditions for the formation of pure WZ NWs are to be studied in the first place. Once the pure WZ NWs are obtained, the second step is to develop the growth technique for the formation of heterostructures. This technique involves interruptions of the growth in order to switch the phosphorus flux to arsenic flux and back. This aspect should be investigated so as to prevent the catalyst crystallization. Finally, once the growth procedure for the growth of NW heterostructures is obtained, we need to optimize the growth parameters to avoid the formation of parasitic heterostructures such as radial quantum well. These steps were successfully completed in “Heteroepitaxy and Nanostructures” group of Lyon Institute of Nanotechnology (INL) by Khalid Naji, Hammadi Khmissi and Michel Gendry, and are described in the present chapter. All the scanning transmission electron microscopy images have been performed by Gilles Patriarche from the Laboratoire de Photonique et de Nanostructures in Marcoussis.

## 2.2 InP nanowires.

The first step on the way to InAs/InP NW heterostructures of high quality is to find the optimal conditions for pure WZ InP NW growth. The main problem that one has to solve is the formation of ZB insertions. It is known that the NW crystal structure, grown by the VLS mechanism, is governed by growth parameters such as the growth temperature and group V/III precursor flow ratio [2.1 – 2.3]. So to obtain the growth conditions for the growth of pure WZ crystal phase, the effects of the V/III beam equivalent pressure (BEP) ratio has been studied in the first place [2.4]. For this purpose, the first set of NW samples was grown on Si(001) substrate by solid source molecular beam epitaxy (ssMBE) using VSL method. Here and elsewhere Au-In particles obtained by dewetting of an Au-In film at 700° C were used as the catalyst. The growth was carried out for 20 min at temperature of 380° C with an indium BEP of  $8 \cdot 10^{-7}$  torr and with varying V/III BEP ratio: 6, 10, 14 and 19.

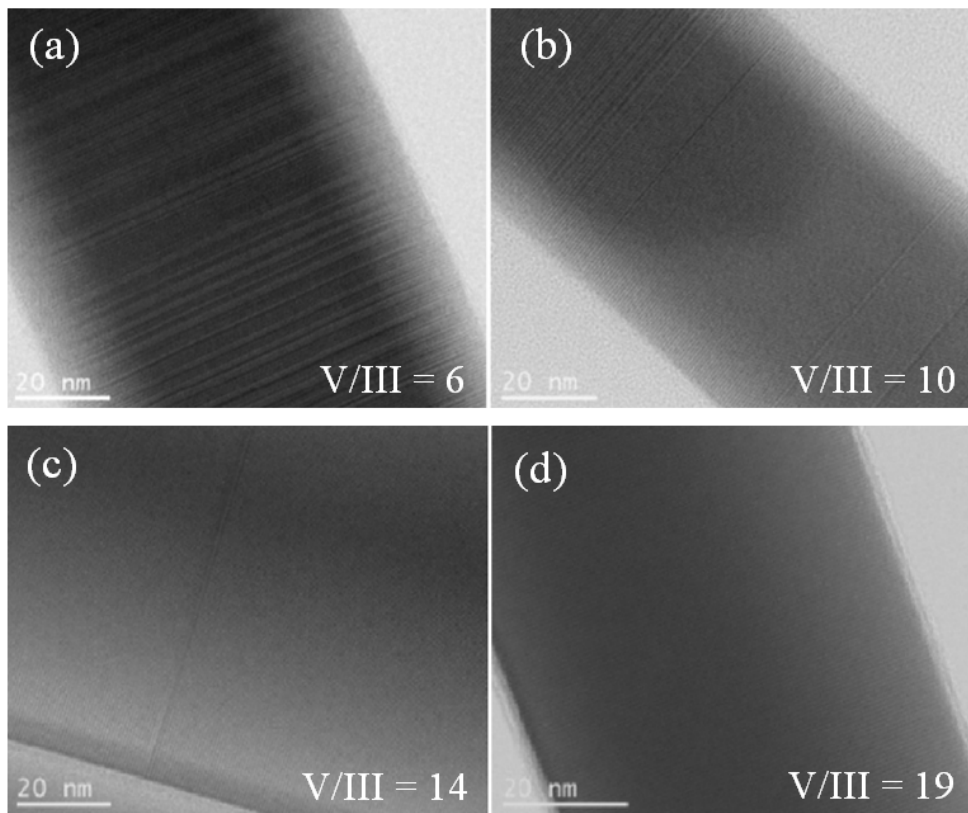


**Figure 2.1:** Bright-field STEM images of InP NWs grown with a V/III BEP ratio of 6 (a), 10 (b), 14 (c) and 19 (d).

To control the crystal structure, bright-field scanning transmission electron microscopy (STEM) was carried out on the obtained InP NWs grown with various V/III BEP ratios. To obtain the STEM images, the NWs were removed from the as-grown substrate and transferred onto a Cu grid with a lacey carbon film. Then the NWs were analyzed in a JEOL 2200FS microscope operating at 200 kV and equipped with a spherical aberration corrector for the probe (aberration-corrected STEM). As evidenced by the Fourier transform pattern, the crystal structure of the NWs is dominated by the WZ phase with the [0001] axis along the growth direction. The bright-field STEM images show that the density of ZB segments is strongly reduced for high V/III BEP ratios (Figure 2.1). Therefore, we may conclude that a high V/III BEP ratio (higher than 15) is required to obtain WZ InP NWs. The axial growth rate increases with increase of V/III ratio and consequently decreases the density of ZB segments. Theoretical investigations have shown that the supersaturation of the liquid must be high enough to obtain a WZ phase and not a ZB phase [2.5, 2.6]. Our experimental results can be understood if we assume that the number V element, i.e. the phosphorus, is the key element to achieve a high III-V supersaturation. That is also in agreement with the experimental results of [2.2] where a high flow of the group V creates high supersaturation growth conditions, which can result in WZ growth.

To study the impact of growth temperature to the crystal purity a second set of NW samples has been produced [2.4, 2.7], with a high V/III BEP ratio equal to 19 and varying the growth temperature: 340°C, 380°C, 420°C, 460°C and 500°C. STEM images of the NWs from this second set of samples reveal that the ZB segment density also depends on the growth temperature. The samples grown at 340° C and 460° C demonstrate medium density of ZB segments in the range of 10 – 100  $\mu\text{m}^{-1}$  (Figure 2.2.a), while the samples grown at 380° C and 420° C have very low density in the range of 0 – 5  $\mu\text{m}^{-1}$  (Figure 2.2.b). The sample grown at 500° C has the highest density of ZB segments in the 150 – 500  $\mu\text{m}^{-1}$  range (Figure 2.2.c). The density of ZB segments as a function of the growth temperature is shown in Figure 2.2.d.

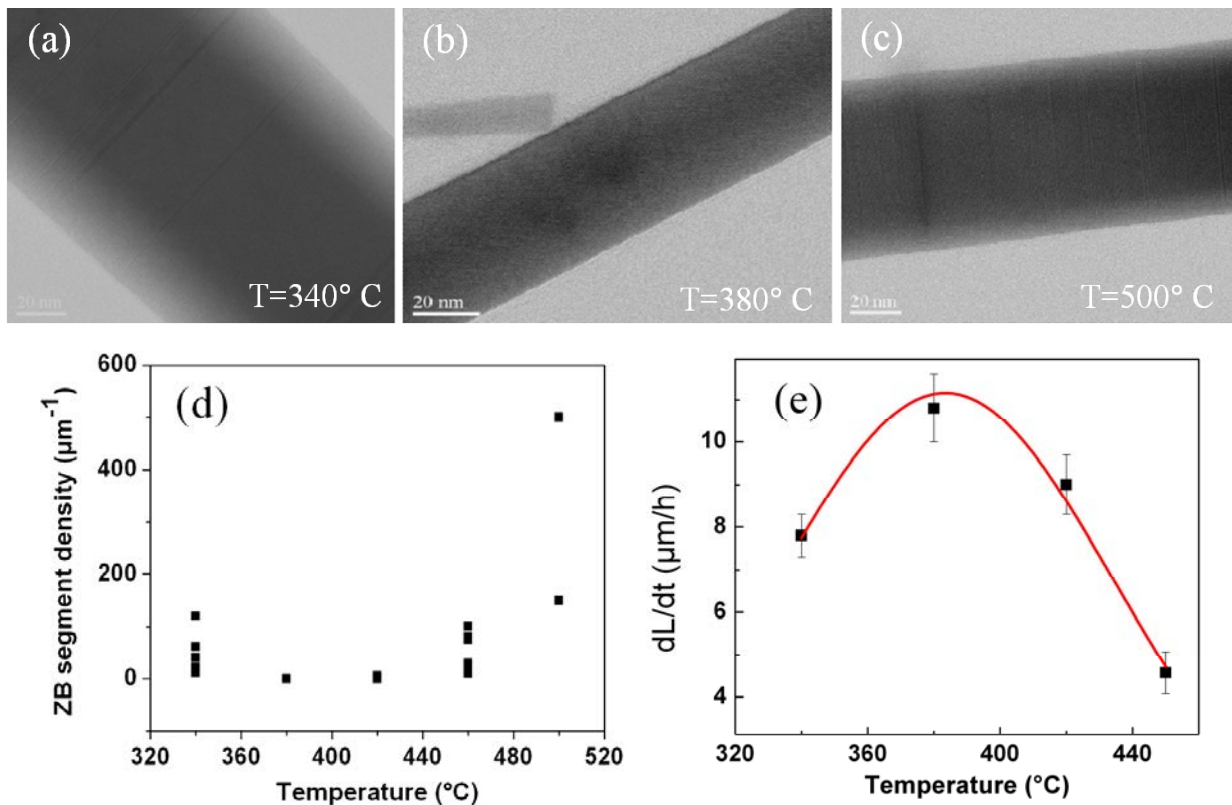


**Figure 2.2:** Bright-field STEM images of InP NWs grown at 340° C (a), 380° C (b) and 500° C (c). (d) ZB segment density and (e) axial growth rate as a function of the growth temperature.

Experimental studies performed using MOVPE growth methods have reported a decrease of the number of ZB insertions as temperature is increased [2.2]. This phenomenon is a consequence of the exponentially increasing decomposition of the precursors with growth temperature, which increases the supersaturation for fixed precursor molar fractions [2.2, 2.8]. However, this explanation is irrelevant for MBE growth. From the STEM images and the dependence of the NW axial growth rate shown on Figure 2.2.e, we have to assume that a maximal supersaturation is reached around 400°C. The maximal axial growth rate around 380°C confirms, once again, that increasing axial growth rate decreases ZB segment density. The presence of such optimum for the axial growth rate is in agreement with theoretical works [2.5]. Therefore, we may conclude that the optimal conditions for the pure WZ InP NW growth would be V/III BEP ratio of 19 and growth temperature in the 380 – 420° C range. These conditions were used to obtain the samples used in this work: the growth of the InP NW samples used for all

the micro-photoluminescence studies in Chapter 4 was carried out for 20 min at temperature of  $420^{\circ}\text{C}$  with fixed indium beam equivalent pressure (BEP) of  $8 \cdot 10^{-7}$  torr and phosphorus BEP of  $1.5 \cdot 10^{-5}$  torr.

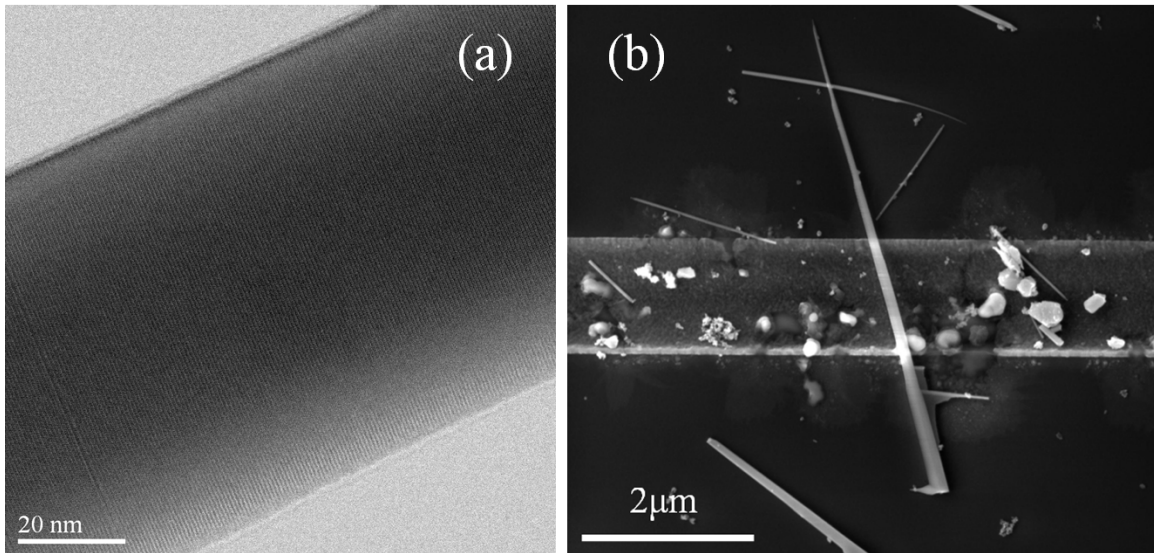


**Figure 2.3:** Transmission electron microscopy (STEM) (a) and scanning electron microscopy (SEM) (b) images of InP NWs.

Finally, the morphology and structural properties of the obtained WZ InP NWs have been investigated by means of High-angle annular dark field STEM (HAADF-STEM) and Scanning electron microscopy (SEM). HAADF-STEM images demonstrated that two morphologies of WZ InP NWs are present in each sample, first looking like a needle with tapered shape and second looking like a column. The two types of NWs have a wurtzite crystal structure with [0001] growth axis (Figure 2.3).

## 2.3 InAs/InP radial quantum well nanowires.

The next step was to obtain InP NWs containing InAs insertions. This can be realized by switching the V element flux twice, from phosphorus to arsenide and back. These switches can be done either with or without stopping the indium flux. To find the best technique, the two procedures were tested for InAs growth time of 10 s [2.9].

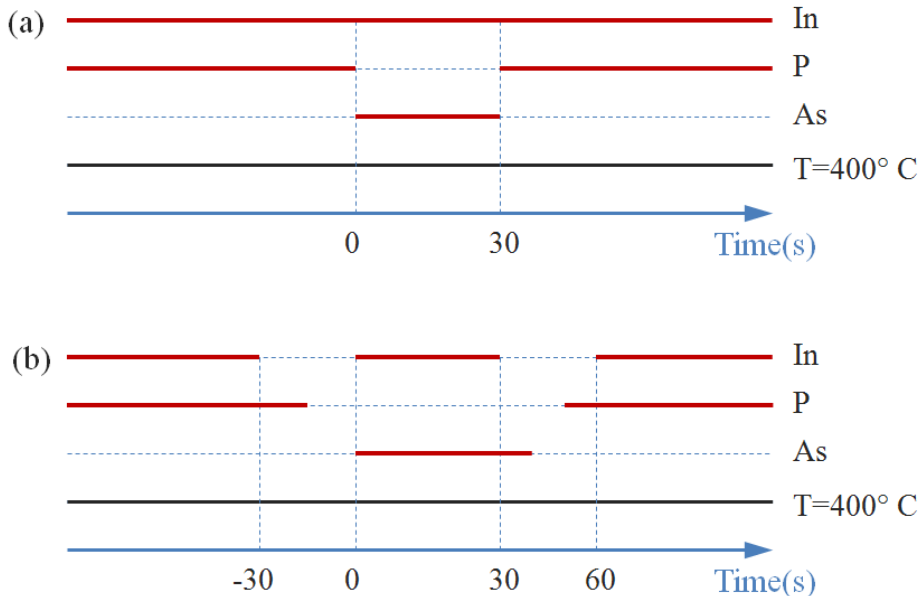


**Figure 2.4:** Schemes of the growth procedures without (a) and with (b) In flux interruption.

VLS ssMBE with Au-In particles as a catalyst were used, to grow the NWs at 400 °C with a V/III BEP ratio of 16 on Si(001) substrate. Schemes of growth procedures with and without interruption of indium flux are illustrated in Figure 2.4. In the case of the growth without In flux interruption, the phenomenon of catalyst droplet crystallization takes place, as evidenced by the SEM observation (Figure 2.5.a). The second procedure included 30 s In flux interruption for the element V flux switching. Figure 2.5.b shows that stopping the indium flux for P/As and As/P flux switching is an efficient procedure to prevent the catalyst crystallization. More details on the matter can be found in [2.9].

Finally, to obtain the sample involved in the present work the following optimized procedure was used. The growth begins with 10 min of InP growth. A growth interruption of 10 s

is realized by closing the indium shutter. During this interruption, the phosphorus flux is switched to the arsenic flux.

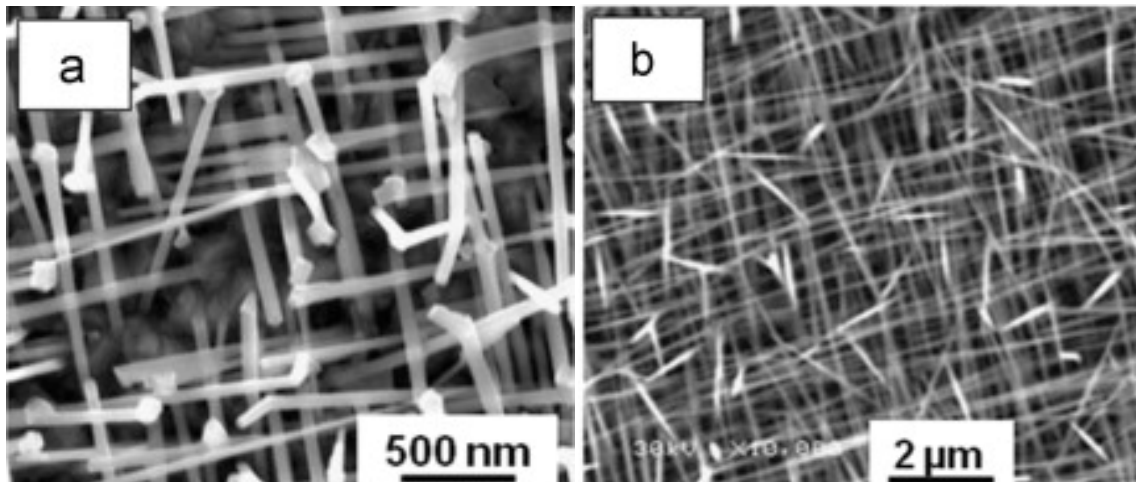


**Figure 2.5:** SEM images of InAs/InP NWs grown without (a) and with (b) interruption of indium flux.

Then, the indium shutter has been open for the growth time of 20 s to grow the InAs insertion. After another 10 s growth interruption for the arsenic/phosphorus flux switching, the structure is completed with 10 min of InP.

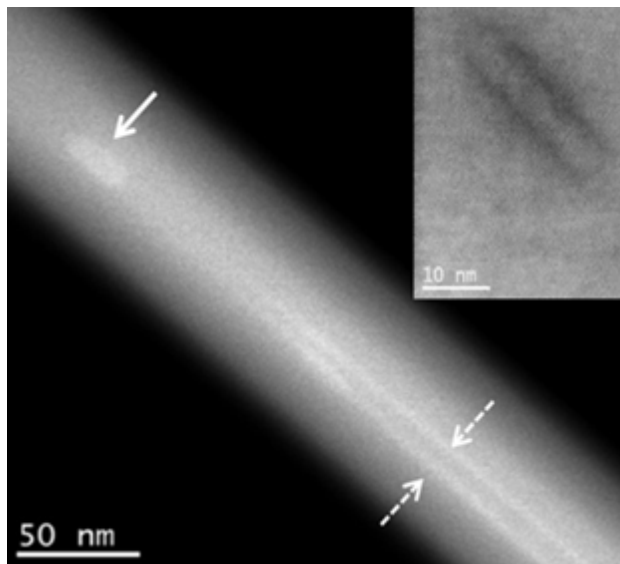


**Figure 2.6:** HAADF-STEM image of an InAs/InP NW containing an InAs insertion (solid arrow) and an InAs radial QWell (dashed arrow). Inset: close-up view of the InAs segment.

HAADF-STEM imaging was carried out on the obtained NWs (Figure 2.6). HAADF-STEM measurements reveal that the NWs have 80 nm diameter, 2 – 4  $\mu\text{m}$  length and an hexagonal cross section with mainly {11-20} facets (so called a-plane). It is known that a- and m-planes are stable facets due to their low surface energy. The fact that a-planes are favoured in these core-shell NWs could be a consequence of the strain generated by the radial growth of WZ InAs QWell into the WZ InP NWs. Due to the high V/III BEP ratio we have used, no stacking faults or cubic segments were observed in the NWs. STEM images demonstrate the formation of a thin radial InAs QWell of few monolayers thick (marked with dashed arrows). This radial QWell is surrounded by an inner 7 nm thick InP core and an outer 30 nm thick InP shell formed during the subsequent InP growth. A similar observation has already been reported by Mohan *et al* [2.10] on InP/InAs/InP core-multishell NWs grown by selective area MOVPE on patterned InP(111) substrates. In addition, due to the axial growth of InAs at the 400° C growth temperature, an inserted InAs segment (marked with a solid arrow) of about 20 nm in length, has been observed. In the InAs segment, the central region has a uniform As content but it gradually drops towards the InP interface. As evidenced by the selected area electron diffraction (SAED) patterns, the NWs have WZ structure with the [0001] axis along the growth direction for both InP and InAs materials, as often observed for VLS grown III-V NWs [2.1, 2.11, 2.12]. In conclusion, a sufficient procedure of InAs/InP NW growth was found and a sample of radial quantum well InAs/InP NWs (QWell-NWs) was obtained. However, since the radial quantum well is not the main goal of this work, the problem of undesirable radial growth is yet to be solved.

## 2.4 InAs/InP quantum rod nanowires.

As we have seen, the first attempt to grow InP NWs with InAs insertions, such as QRods, led to the formation of undesired InAs radial QWell. Presence of such parasitic heterostructures often observed in MBE growth of NW heterostructures and complicates the optical investigation of the QRods [2.13 – 2.15]. Few solutions were proposed to avoid this problem: the use of a post growth heat treatment [2.13], or an increase of the growth temperature [2.14] to favor the axial growth rate over the radial one. However, none of them solved the problem completely. In the present work another approach was developed. As shown in Figure 2.6, due to the diffusion, the formation of the parasitic radial QWell takes place only 50 – 80 nm below the QRod. This fact provides an opportunity to prevent appearance of the radial QWell by growing QRods at the very bottom of NWs, so that the atom diffusion would lead to QRod formation only. Moreover, it is known that the rate of radial growth depends on growth temperature and V/III BEP ratio [2.3], so to avoid the radial growth, higher growth temperature and lower V/III BEP ratio should be used. Scheme of the optimized growth procedure is shown in Figure 2.7.

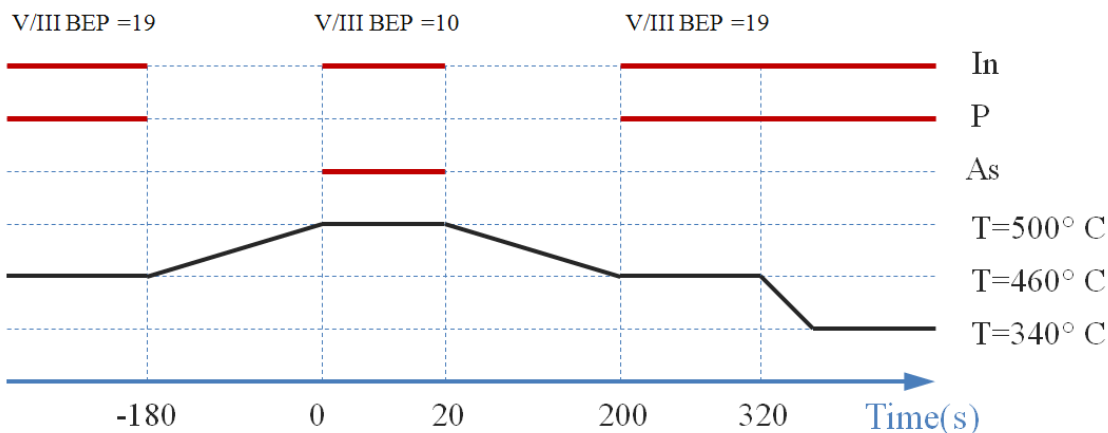


**Figure 2.7:** Scheme of the InAs/InP QRod-NW growth procedure.

The NW growth begins with 2 min of InP growth at 460° C. A growth interruption of 3 min is realized by closing the general shutter. During this interruption, the temperature of the sample is increased to 500° C, in order to avoid the radial growth, and the phosphorus flux is switched to arsenic flux. Then, the growth of the InAs insertion is done by opening the general shutter for the InAs growth time of 20 s at 500° C. The second growth interruption of 3 min is necessary to decrease temperature of the sample to 460° C and to switch from the arsenic to the phosphorus

flux. The growth of the NWs is then continued with InP by opening the general shutter for growth time of 2 min at 460° C. Finally, the structure is completed with 10 min of InP growth at 340° C to favor the InP radial growth. InP and InAs materials are grown with a V/III BEP ratio of 19 and 10, respectively.

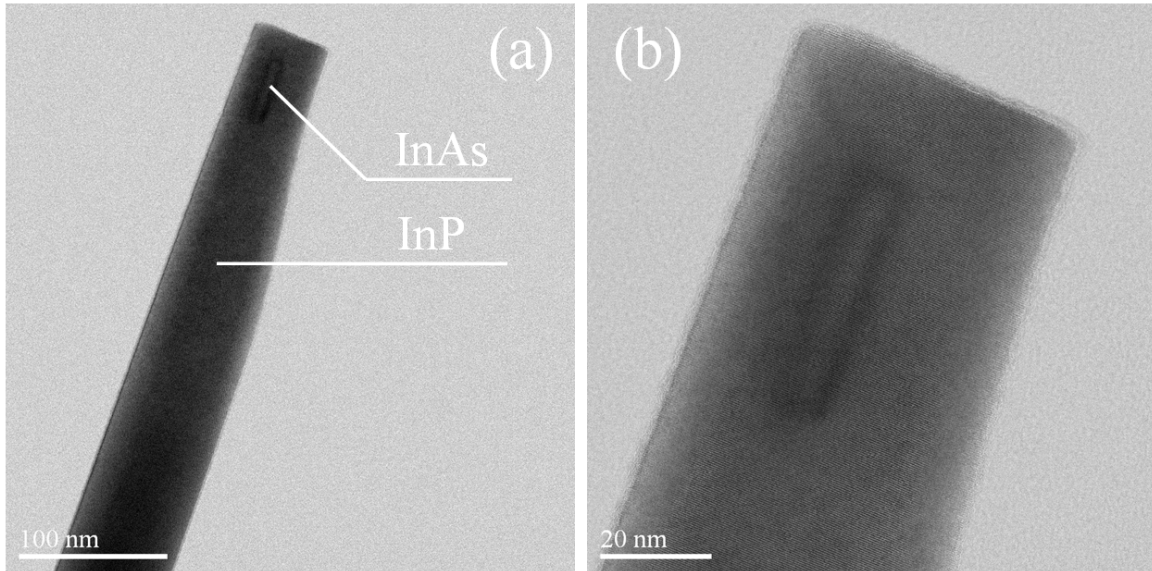


**Figure 2.8:** (a) HAADF-STEM images of an InAs/InP QRod-NW showing an InAs QRod at the bottom part of the NW (the images are upside-down). (b) Close-up view of the InAs QRod.

Figure 2.8 shows HAADF-STEM images of obtained QRod-NWs. The diameter and the length of the InAs QRod, measured by HAADF-STEM imaging on a dozen of different NWs, range from 8 to 11 nm and from 40 to 135 nm, respectively, while the diameter and the length of the QRod-NWs range from 60 to 100 nm and from 2 to 4  $\mu$ m, respectively, depending on the diameter of the catalyst droplet. As it is evidenced by the selected area electron diffraction (SAED) patterns, the NWs have the usual WZ structure with the [0001] axis along the NW growth direction for both InP and InAs materials. Due to the high V/III BEP ratio used for the InP growth, no stacking faults or cubic segments are observed in the NWs.

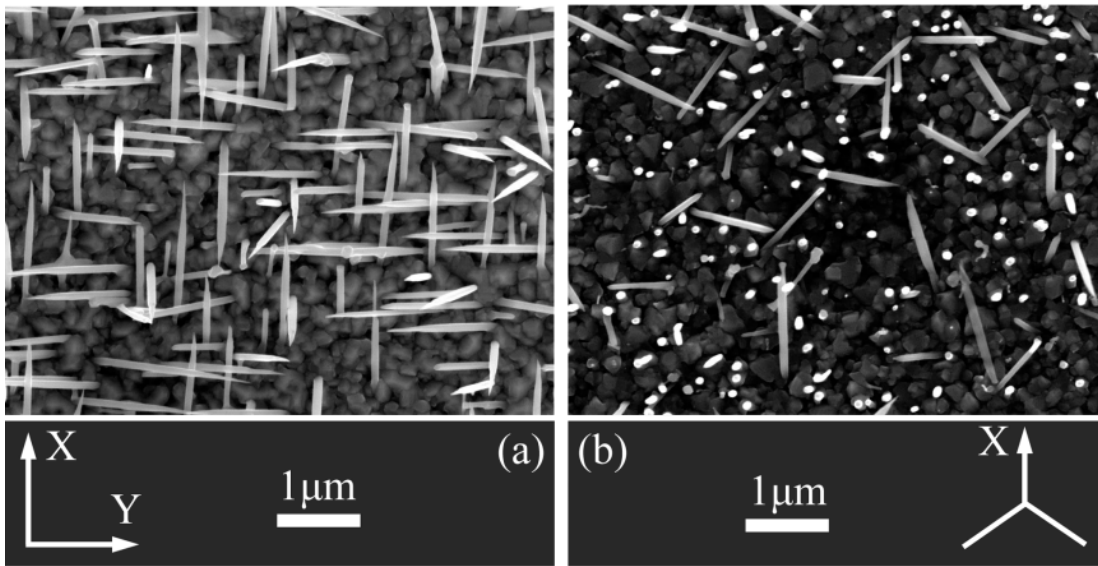


**Figure 2.9:** SEM images of the QR-NWs grown on (001) (a) and (111) (b) oriented Si substrates.

To perform polarization measurements on NW ensembles, QRod-NWs were grown on both (001) and (111) oriented Si substrates. Figure 2.9 demonstrates that the NWs grown on Si(001) substrate are mainly oriented along X and Y axes, while NWs grown on the Si(111) substrate are oriented vertically and in three different directions. More details on the orientation of NWs on the substrate will be presented in Chapter 6.

## 2.5 Conclusions.

In conclusion, first growth conditions were optimized to obtain InP NWs of pure WZ crystallographic structure. Then, growth technique has been modified adding growth interruption for flux switching in order to obtain NW heterostructures. Once the proper procedure of growth interruption had been found, growth conditions were optimized so as to obtain QRod-NWs with no parasitic heterostructures, such as radial QWell.

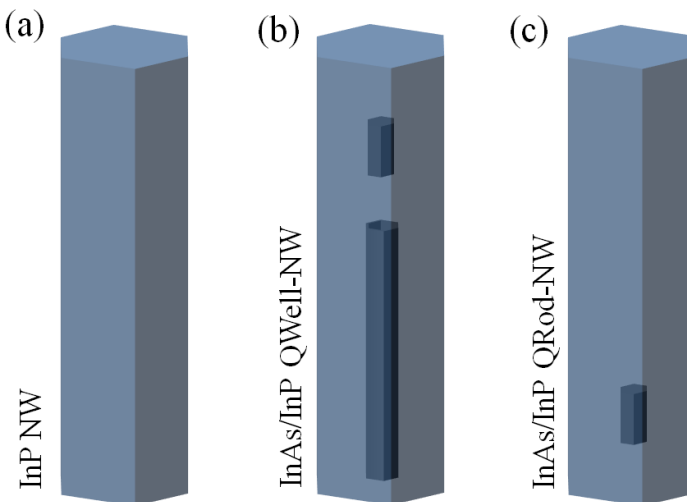


**Figure 2.10:** Schemes of the obtained samples. Pure WZ InP NWs (a), WZ InAs/InP radial QWell-NWs (b) and WZ InAs/InP QRod-NWs (c).

Finally, three types of NW samples have been obtained: pure WZ InP NWs (Figure 2.10.a), WZ InAs/InP radial QWell-NWs (Figure 2.10.b) and WZ InAs/InP QRod-NWs (Figure 2.10.c).

## 2.6 References.

- [2.1] M. Mattila, T. Hakkarainen, M. Mulot, and H. Lipsanen, "Crystal-structure-dependent photoluminescence from InP nanowires", *Nanotechnology*, vol. 17, p. 1580, 2006.
- [2.2] S. Paiman, Q. Gao, H. H. Tan, C. Jagadish, K. Pemasiri, M. Montazeri, H. E. Jackson, L. M. Smith, J. M. Yarrison-Rice, X. Zhang, and J. Zou, "The effect of V/III ratio and catalyst particle size on the crystal structure and optical properties of InP nanowires", *Nanotechnology*, vol. 20, p. 225606, 2009.
- [2.3] S. A. Dayeh, E. T. Yu, and D. Wang, "III-V Nanowire Growth Mechanism: V/III Ratio and Temperature Effects", *Nano letters*, vol. 7, p. 2486, 2007.
- [2.4] M. H. Hadj Alouane, N. Chauvin, H. Khmissi, K. Naji, B. Ilahi, H. Maaref, G. Patriarche, M. Gendry, and C. Bru-Chevallier, "Excitonic properties of wurtzite InP nanowires grown on silicon substrate", *Nanotechnology*, vol. 24, p. 035704, 2013.
- [2.5] V. G. Dubrovskii, N. V. Sibirev, J. C. Harmand, and F. Glas, "Growth kinetics and crystal structure of semiconductor nanowires", *Physical Review B*, vol. 78, p. 235301, 2008.
- [2.6] F. Glas, J.-C. Harmand, and G. Patriarche, "Why Does Wurtzite Form in Nanowires of III-V Zinc Blende Semiconductors?", *Physical Review Letters*, vol. 99, p. 146101, 2007.
- [2.7] N. Chauvin, M. H. Hadj Alouane, R. Anufriev, H. Khmissi, K. Naji, G. Patriarche, C. Bru-Chevallier, and M. Gendry, "Growth temperature dependence of exciton lifetime in wurtzite InP nanowires grown on silicon substrates", *Applied Physics Letters*, vol. 100, p. 011906, 2012.
- [2.8] K. A. Dick, P. Caroff, J. Bolinsson, M. E. Messing, J. Johansson, K. Deppert, L. R. Wallenberg, and L. Samuelson, "Control of III-V nanowire crystal structure by growth parameter tuning", *Semiconductor Science and Technology*, vol. 25, p. 024009, 2010.
- [2.9] H. Khmissi, K. Naji, M. H. Hadj Alouane, N. Chauvin, C. Bru-Chevallier, B. Ilahi, G. Patriarche, and M. Gendry, "InAs/InP nanowires grown by catalyst assisted molecular beam epitaxy on silicon substrates", *Journal of Crystal Growth*, vol. 344, p. 45, 2012.
- [2.10] P. Mohan, J. Motohisa, and T. Fukui, "Fabrication of InP/InAs/InP core-multishell heterostructure nanowires by selective area metalorganic vapor phase epitaxy", *Applied Physics Letters*, vol. 88, p. 133105, 2006.
- [2.11] M. Tchernycheva, G. E. Cirlin, G. Patriarche, L. Travers, V. Zwiller, U. Perinetti, and J.-C. Harmand, "Growth and characterization of InP nanowires with InAsP insertions", *Nano letters*, vol. 7, p. 1500, 2007.
- [2.12] E. D. Minot, F. Kelkensberg, M. van Kouwen, J. A. van Dam, L. P. Kouwenhoven, V. Zwiller, M. T. Borgström, O. Wunnicke, M. A. Verheijen, and E. P. a M. Bakkers, "Single quantum dot nanowire LEDs", *Nano letters*, vol. 7, p. 367, 2007.

- [2.13] G. E. Cirlin, M. Tchernycheva, G. Patriarche, and J.-C. Harmand, "Effect of postgrowth heat treatment on the structural and optical properties of InP/InAsP/InP nanowires", *Semiconductors*, vol. 46, p. 175, 2012.
- [2.14] J.-C. Harmand, F. Jabeen, L. Liu, G. Patriarche, K. Gauthron, P. Senellart, D. Elvira, and A. Beveratos, " $\text{InP}_{(1-x)}\text{As}_{(x)}$  quantum dots in InP nanowires: A route for single photon emitters", *Journal of Crystal Growth*, vol. n/a, p. n/a, 2013.
- [2.15] M. H. H. Alouane, R. Anufriev, N. Chauvin, H. Khmissi, K. Naji, B. Ilahi, H. Maaref, G. Patriarche, M. Gendry, and C. Bru-Chevallier, "Wurtzite InP/InAs/InP core-shell nanowires emitting at telecommunication wavelengths on Si substrate", *Nanotechnology*, vol. 22, p. 405702, 2011.

# **Chapter III**

---

## Experimental techniques and sample preparation

- 3.1 Introduction.
- 3.2 Photoluminescence technique.
- 3.3 Micro-Photoluminescence technique.
- 3.4 Photoluminescence with integrating sphere.
- 3.5 Experimental setup calibration.
- 3.6 Nanowire transfer and sample preparation.
- 3.7 References.

### 3.1 Introduction.

Photoluminescence spectroscopy is a powerful method to investigate semiconductor properties. The term photoluminescence (PL) describes a phenomenon of light emission from any form of matter after the absorption of photons. In a typical PL experiment (Figure 3.1), a semiconductor sample is excited with a light source which provides photons with the energy ( $h\nu_1$ ) higher than the bandgap energy (non-resonant excitation). Once the photons are absorbed (red arrow), electrons and holes are formed with finite momentum in the conduction and valence bands, respectively. Then the carriers are relaxing towards the band gap minimum (dashed arrows). Typical mechanisms of the relaxation are Coulomb scattering and the interaction with phonons. Finally, the electrons recombine with holes (blue arrow) emitting photons with energy ( $h\nu_2$ ) lower than that of absorbed photons ( $h\nu_2 < h\nu_1$ ).

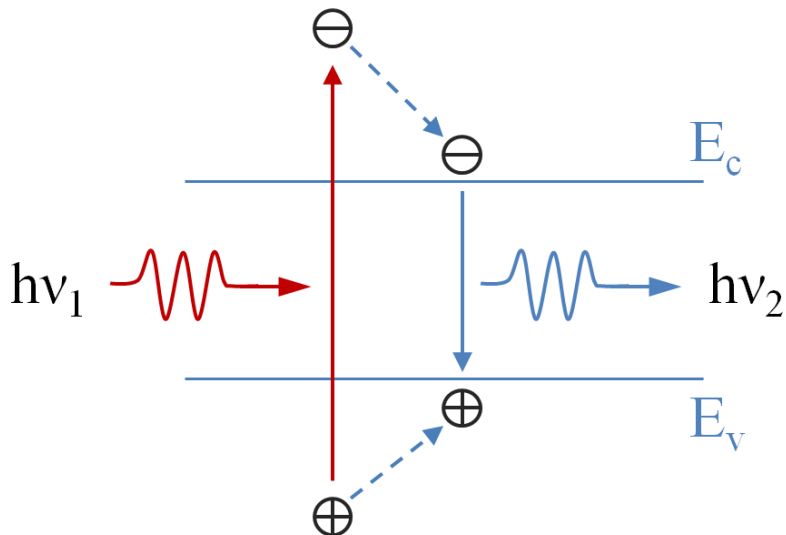


**Figure 3.1:** Scheme of the photoluminescence phenomenon.

The spectrum and decay time of emitted photons may provide information about the material quality, carrier population at the energy levels and many other aspects of semiconductor electronic structure, as it will be shown in the following chapters. This basic principle of PL lies at the root of several PL techniques, such as micro-PL, PL excitation, time-resolved PL and others. The present chapter is devoted to the detailed descriptions of the PL techniques and setups used in this work.

### 3.2 Photoluminescence technique.

To begin, the standard setup for PL measurements should be introduced. In a typical PL setup, the sample is directly excited by a laser with the energy above the band gap. The emitted photons are collected by the detection system and sent to the monochromator equipped with a photodetector.

In the present work, to perform PL experiments on ensembles of NWs, the PL setup schematically illustrated in the Figure 3.2, was used.

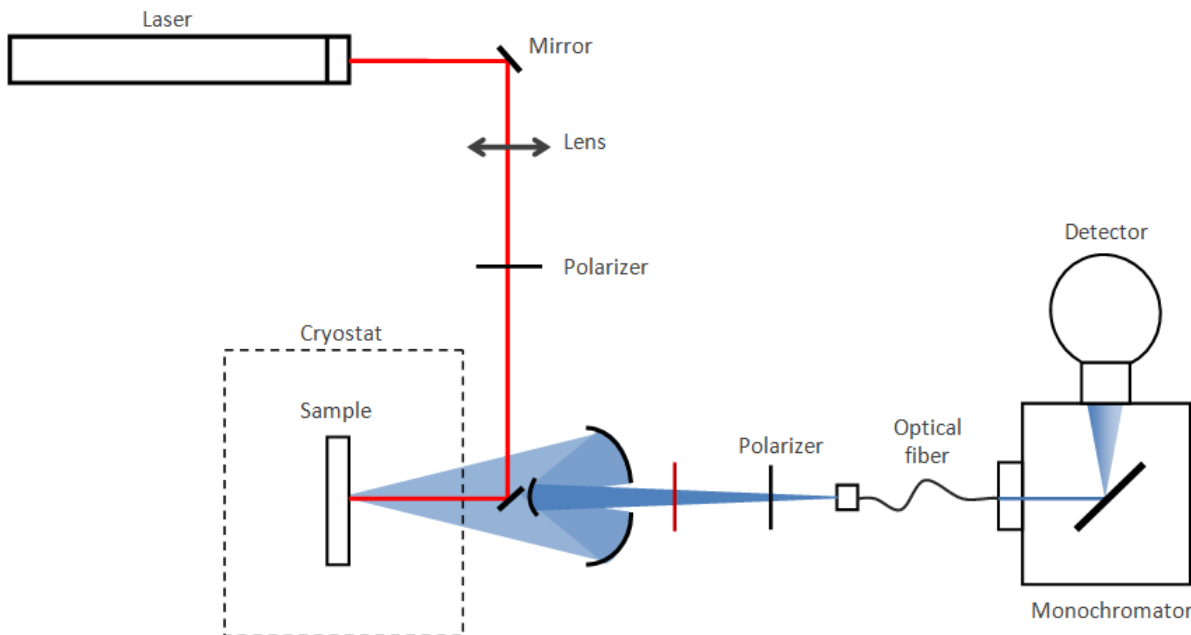


**Figure 3.2:** Scheme of the PL setup.

The sample is placed in a closed-cycle He flow cryostat, with the possibility to work in the 10 – 300 K temperature range. The emitted light is collected by a spherical mirror system and focused on the entrance hall of an optical fiber, which leads the emitted photons to a monochromator equipped with a diffraction grating, and coupled to a liquid nitrogen cooled InGaAs (or Si) photodiode array detector. The reflected laser light is filtered off by a long-pass filter. Polarizers for excitation or collection can be added if needed.

### 3.3 Micro-Photoluminescence technique.

To study single NWs micro-PL ( $\mu$ PL) technique is widely used. The main difference between the  $\mu$ PL setup and the classical PL setup consists in the presence of an optical objective that is focusing the laser beam in a spot of few  $\mu\text{m}$  in diameter.

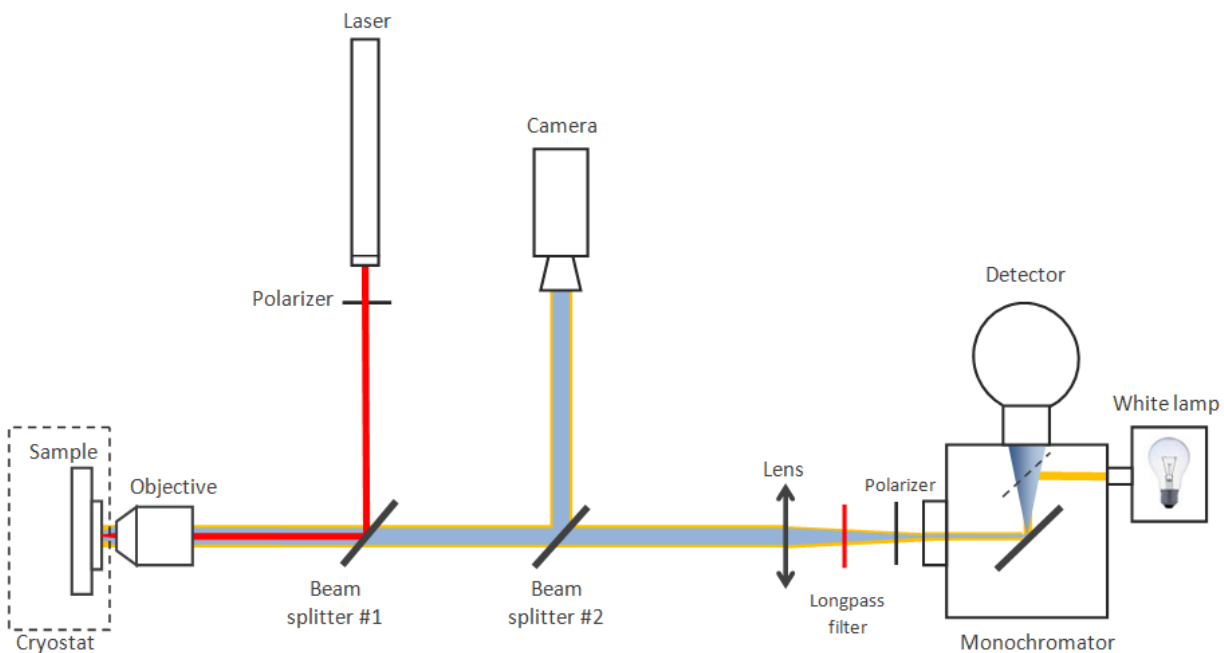


**Figure 3.3:** Scheme of the  $\mu$ PL setup.

The configuration of the  $\mu$ PL setup used in this work is schematically illustrated in Figure 3.3. The beam of a laser (typically He-Ne laser 632 nm) is reflected by a dichroic beam splitter (#1), and focused by an optical objective (20x/0.4) on the sample, which can be placed into a continuous flow liquid He cryostat when necessary. The diameter of the laser spot is about of 2 – 5  $\mu\text{m}$ . To be able to see the surface of the sample on the monitor, a white lamp coupled with monochromator is used. The use of the monochromator allow us to choose a required wavelength (typically near infrared), so that the camera may detect the reflected light in the range far away from laser wavelength. The emitted light together with the reflected light of the white lamp are passing back through the objective, turning into a parallel beam, and passing through the first beam splitter, reflecting from the second beam splitter toward the infrared camera. So, having the information about the surface and the laser beam position on it, we are able to focus the laser beam at a certain point. After the focusing, the mirror inside the monochromator (dashed line) is

switched to the position when the emitted light passes to the detector and the white lamp is turned off. The beam splitter #2 is removed in order to avoid a loss of signal. In this position, the PL emission can be focused at the entrance of the monochromator, inside of which, the diffraction grating splits the beam into a spectrum and reflects it to the liquid nitrogen cooled InGaAs photodiode array detector.

In order to conduct the experiments with various excitation wavelengths, the setup can be modified by replacement of the laser by a second monochromator coupled with a white lamp. In this configuration it is possible to excite the sample using a chosen wavelength.

Here and elsewhere a polarizer for visible range is used to polarize the laser beam, which, however, is not totally non-polarized, and thus angular function of laser intensity is used to correct all polarization dependent results. To analyze polarization of the emitted luminescence a polarizer for infrared range is used.

Summarizing, the  $\mu$ PL technique provides a possibility to study PL emission spectra, their polarization anisotropy and dependence on excitation wavelength and its polarization of single nanoobjects that can be precisely chosen on the sample surface.

### 3.4 Photoluminescence with integrating sphere.

A standard technique for measuring PL quantum efficiency (QE) involves the use of an integrating sphere [3.1 – 3.4]. In the integrating sphere, light is isotropically redistributed over the sphere surface, due to a high reflectance material of the internal surface, so that the possible angular anisotropy of emission does not affect the results. The principal scheme of the PL setup with an integrating sphere is illustrated in Figure 3.4.

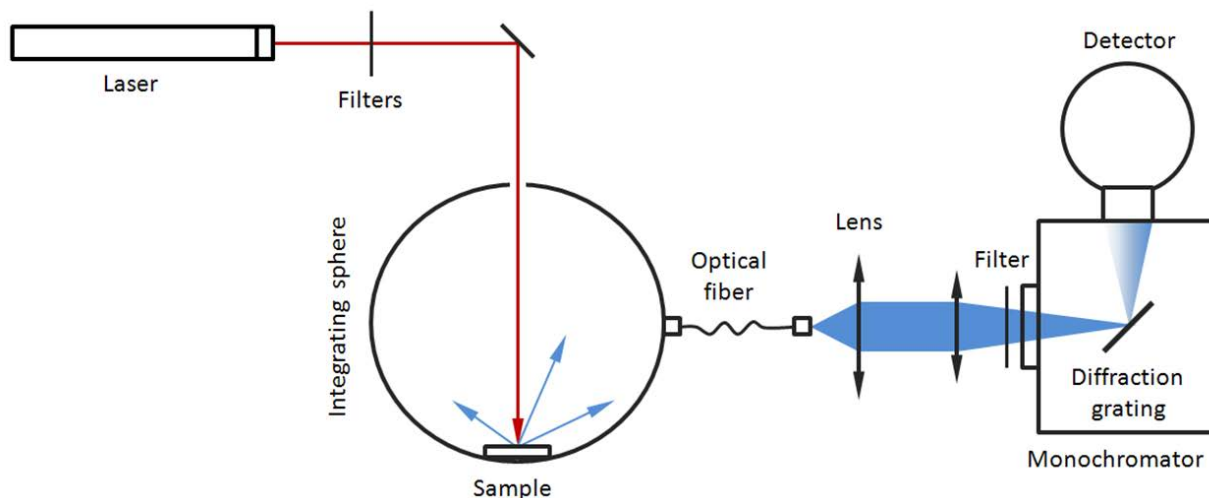


**Figure 3.4:** Scheme of PL setup for quantum efficiency measurements.

In the present work a RTC-060-SL integrating sphere from Labsphere is used. The high reflectance material “Spectralon” (99 % reflectance in the 0.8 – 1.9 eV range) is mounted on the internal surface of the integrating sphere. The laser beam ( $\lambda = 671$  nm), passing through the neutral density filters, is directly introduced into the integrating sphere and aimed to the sample. The scattered laser light and emission of the sample are collected through an optical fiber, plugged to the sphere. To prevent the luminescence from reaching the optical fiber entrance hole directly, diffusely reflecting baffles are installed in the sphere. The collected photons are sent to the monochromator equipped with a nitrogen cooled InGaAs photodiode array detector. To prevent the laser light from reaching the detector a long-pass filter can be installed at the entrance of the monochromator if necessary.

Typically, for the PL QE measurements the method based on that developed by de Mello *et al* [3.2] is used. In this case, experiments in three different configurations are required (Figure 3.5).

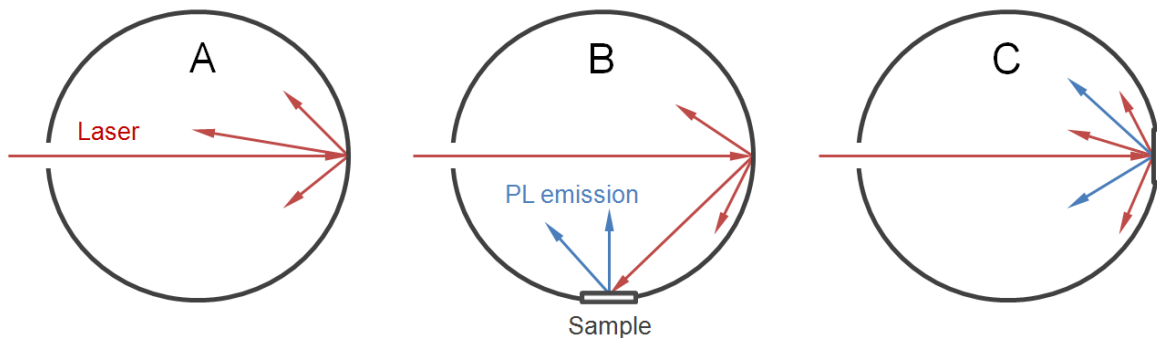


**Figure 3.5:** Schemes illustrating three configurations of the sphere typically used for the QE measurement: (a) empty sphere; (b) laser beam is focused on a wall and the sample is excited indirectly; (c) the sample is excited directly.

The first experiment (Configuration A) with an empty sphere to measure the entire laser intensity ( $L_a$ ). The second (Configuration B) to measure the scattered laser intensity ( $L_b$ ) and emission of the sample ( $P_b$ ) in case of indirect excitation. And the third experiment (Configuration C) to measure the intensity of scattered laser light ( $L_c$ ) and emission of the sample ( $P_c$ ) under the direct excitation. Then, the QE of the sample can be calculated as follows [3.2]:

$$\eta = \frac{P_c - (1-A)P_b}{L_a A} \quad (3.1)$$

where  $A = 1 - L_c / L_b$  is absorption coefficient of the sample. In our case of very small (0.03% of the sphere surface) and weakly emitting samples, the results of the experiments in A and B configurations are indistinguishable (i.e.  $P_b = 0$  and  $L_a = L_b$ ). For this reason, in the present study we only use A and C configurations. In this case the Eq. 3.1 can be simplified as:

$$\eta = P_c / L_a A \quad (3.2)$$

where  $A = 1 - L_c / L_a$  is absorption coefficient.

### 3.5 Experimental setup calibration.

However, the signal obtained from the detector does not represent the real amount of counts as a function of wavelength. Therefore all the results obtained using the PL setups described above should be corrected by so called transmission functions of each component of the collection system (filters, lenses, monochromator etc). The transmission functions have been measured using a calibrated white lamp, which has been measured through the collection system of each setup.

In the case of quantum efficiency measurements, when proper correction plays a crucial role, the collected spectra have been corrected by the spectral response of both the detection system (optical fiber, filters, monochromator and detector) and the integrating sphere, using commercial tungsten white lamp with well known spectral dependence of intensity.

Moreover, the transmission function also depends on the polarization of the light. To obtain the polarization response function, the measurements with the white lamp have been performed with both vertical ( $\phi = 0^\circ$ ) and horizontal ( $\phi = 90^\circ$ ) positions of the polarizer at the collection. Then, since it is known that the maximum of polarization anisotropy is in  $90^\circ$  position, we may obtain transmission function for any angle of polarization of collection using a simple formula:

$$T(\phi) = T(0^\circ) \cos^2(\phi) + T(90^\circ) \sin^2(\phi) \quad (3.3)$$

To obtain polarization anisotropy of the lasers we used an InAs QWell as a sample assuming that the light emitted by this QWell is non-polarized. Therefore, using no polarization selection at the collection, but changing the polarization of excitation, we may obtain the ratio of the emission intensities in cases of vertically and horizontally polarized excitation. This ratio was used to correct results of measurements when the polarization of excitation is concerned.

### 3.6 Nanowire transfer and sample preparation.

To perform  $\mu$ PL measurements, a sample with a low density of NWs on the surface is required, in order to focus the laser beam spot ( $d = 5 \mu\text{m}$ ) at only one single NW. There are few ways to transfer NWs from an as-grown substrate onto another surface (host-substrate). At the beginning of the present work a mechanical transfer was used. In this approach, a piece of clean paper is used to tip on the surface of the as-grown sample. Then, being attached to this paper, the NWs can be transferred by touching a host-substrate [3.5 – 3.7]. This method has been found to be rather rough, because of the high probability of breaking the NWs in half. Moreover, the NWs tend to get stuck together (Figure 3.6.a) and may be mistaken for a single NW using optical microscopy, while lonely lying NWs are rarely observed after such transfer.

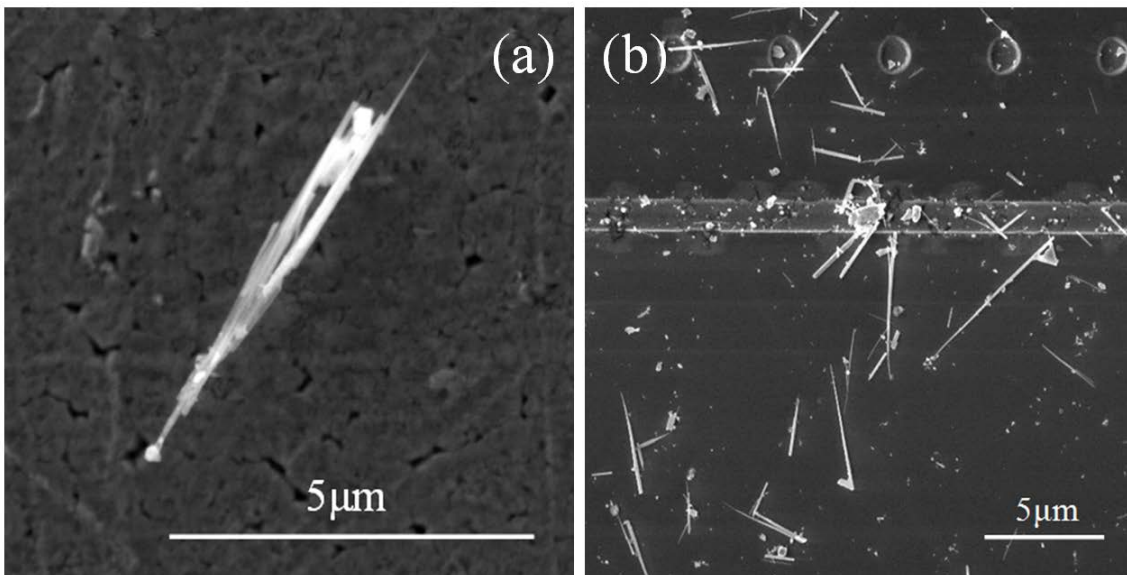


**Figure 3.6:** SEM images of NWs stuck together after the mechanical transfer (a) and NWs spread on the surface after the liquid transfer (b).

To improve the NW dispersion and their quality after the transfer, another approach has been used. This method suggests that NWs are delivered onto the host-substrate in a droplet of liquid (water, methanol or isopropanol), which may thereafter be dried out [3.8]. This method is notable for well randomization and separation of NWs (Figure 3.6.b). There are at least two ways to transfer the NWs into the liquid from as-grown substrate. In the first of them, the as-grown substrate is immersed into a vial with isopropanol, and transferred to liquid nitrogen, where the NWs break from the base, due to the difference in thermal expansion coefficients of NWs and the

substrate. Then, melting the isopropanol, a vial containing a solution with NWs may be obtained [3.9]. The second approach suggests that an as-grown substrate is immersed inside a cuvette with liquid (water, ethanol, methanol), where the NWs are dispersed by ultra-sonification [3.10, 3.11]. This, second method with ethanol as a transfer media was used in the present work in case of liquid transfer.

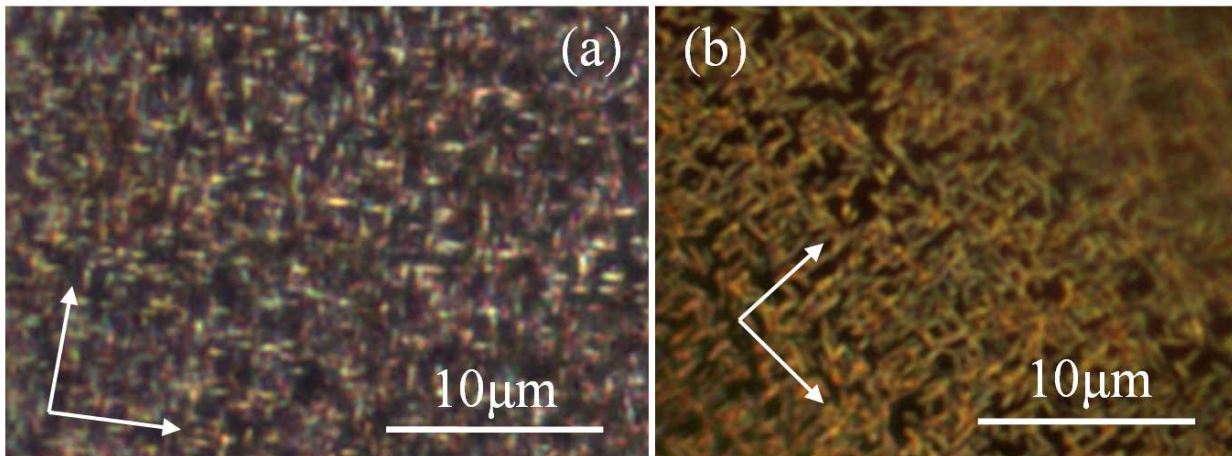


**Figure 3.7:** Optical microscopy image of NWs on as-grown substrate (a) and NWs transferred onto a sticky tape (b) with the similar density and orientation.

The samples for quantum efficiency measurements required specific preparation. To calculate the quantum efficiency, it is important to know the absorption of the incident laser beam by the sample. In this case, the as-grown substrate or the host-substrate will pose a problem of undesirable absorption. Moreover, the presence of a substrate may affect the absorption in NWs [3.12]. To avoid these problems, the NWs were transferred onto a sticky tape, transparent for both laser light and NW emission, and emitting no light in considered range of wavelengths. To transfer NWs, the sticky tape was put upon the as-grown substrate and then lifted up. Figure 3.7 shows NWs on as-grown substrate and NWs transferred onto sticky tape. As it can be seen, careful transfer provides a possibility to obtain similar density and orientation of NWs on the tape.

### 3.7 References

- [3.1] D. Braun, E. G. J. Staring, R. C. J. E. Demandt, G. L. J. Rikken, Y. A. R. R. Kessener, and A. H. J. Venhuizen, "Photo- and electroluminescence efficiency in poly(dialkoxy-p-phenylenevinylene)", *Synthetic Metals*, vol. 66, p. 75, 1994.
- [3.2] J. C. de Mello, H. F. Wittmann, and R. H. Friend, "An Improved Experimental Determination of External Photoluminescence Quantum Efficiency", *Advanced materials*, vol. 9, p. 230, 1997.
- [3.3] N. C. Greenham, I. D. W. Samuel, G. R. Hayes, R. T. Phillips, A. B. Holmes, and R. H. Friend, "Measurement of absolute photoluminescence quantum efficiencies in conjugated polymers", *Chemical Physics Letters*, vol. 241, p. 89, 1995.
- [3.4] H. Mattossi, H. Murata, C. D. Merritt, Y. Iizumi, J. Kido, and Z. H. Kafafi, "Photoluminescence quantum yield of pure and molecularly doped organic solid films", *Journal of Applied Physics*, vol. 86, p. 2642, 1999.
- [3.5] E. G. Gadret, G. O. Dias, L. C. O. Dacal, M. M. de Lima, C. V. R. S. Ruffo, F. Iikawa, M. J. S. P. Brasil, T. Chiaramonte, M. a. Cotta, L. H. G. Tizei, D. Ugarte, and a. Cantarero, "Valence-band splitting energies in wurtzite InP nanowires: Photoluminescence spectroscopy and ab initio calculations", *Physical Review B*, vol. 82, p. 125327, 2010.
- [3.6] Z. Zanolli, M.-E. Pistol, L. E. Fröberg, and L. Samuelson, "Quantum-confinement effects in InAs-InP core-shell nanowires.", *Journal of physics: Condensed matter*, vol. 19, p. 295219, 2007.
- [3.7] H. Khmissi, K. Naji, M. H. Hadj Alouane, N. Chauvin, C. Bru-Chevallier, B. Ilahi, G. Patriarche, and M. Gendry, "InAs/InP nanowires grown by catalyst assisted molecular beam epitaxy on silicon substrates", *Journal of Crystal Growth*, vol. 344, p. 45, 2012.
- [3.8] J. Wang, M. S. Gudiksen, X. Duan, Y. Cui, and C. M. Lieber, "Highly polarized photoluminescence and photodetection from single indium phosphide nanowires", *Science*, vol. 293, p. 1455, 2001.
- [3.9] J. Treffers, "Optical properties of single indium phosphide nanowires on flat surfaces and metallic gratings", 2007.
- [3.10] A. Mishra, L. V. Titova, T. B. Hoang, H. E. Jackson, L. M. Smith, J. M. Yarrison-Rice, Y. Kim, H. J. Joyce, Q. Gao, H. H. Tan, and C. Jagadish, "Polarization and temperature dependence of photoluminescence from zincblende and wurtzite InP nanowires", *Applied Physics Letters*, vol. 91, p. 263104, 2007.
- [3.11] L. K. Van Vugt, "Optical Properties of Semiconducting Nanowires", Condensed Matter and Interfaces, Debye Instituut, 2007.
- [3.12] M. Heiss and A. Fontcuberta i Morral, "Fundamental limits in the external quantum efficiency of single nanowire solar cells", *Applied Physics Letters*, vol. 99, p. 263102, 2011.

# **Chapter IV**

---

## **Optical properties of InP nanowires**

- 4.1 Introduction.
- 4.2 PL characterization of InP nanowires.
- 4.3 Phenomenon of substrate-induced strain.
- 4.4 Theory of substrate-induced strain and its impact on the optical properties.
- 4.5 Experimental observation of substrate-induced strain.
- 4.6 Impact of surface charges.
- 4.7 Conclusions.
- 4.8 References.

## 4.1 Introduction.

We begin the experimental investigation of optical properties of NWs with a study of InP NWs. In recent years, optical properties of InP NWs have been studied in a number of works [4.1 – 4.10]. As we have learned from the preceding chapters, InP NWs may grow in ZB and WZ forms, or contain insertions of one phase in another. In this context, the optical emission of the different crystallographic phases became one of the most important issues in the recent works on the matter. Low temperature emission energy of pure ZB and WZ InP NWs is reported to be in 1.41 – 1.42 eV and 1.48 – 1.5 eV range, respectively [4.1 – 4.4, 4.7, 4.9, 4.10]. The situation is more complex when these two crystallographic phases exist in one NW. In such case, the band alignment between the WZ and ZB phases is usually a type II alignment. The scheme of this mechanism is illustrated in Figure 4.1, where we assume a ZB insertion in a WZ NW. In this case, carriers of one sign located in WZ segment are thought to be able to recombine with the carriers of the opposite sign located in ZB segment, so that the energy of emitted photons turns out to be lower than the band gap of WZ material.

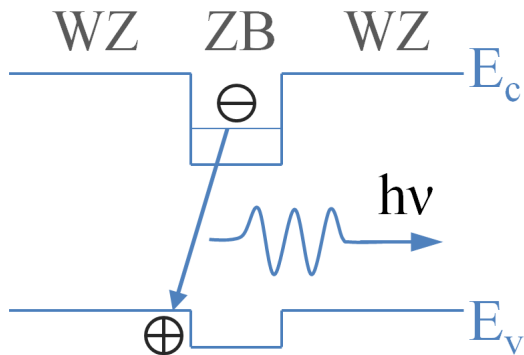


**Figure 4.1:** Principle scheme of type II recombination mechanism.

As far as InP NWs are concerned, this phenomenon results in additional PL emission peaks in the 1.41 – 1.5 eV range [4.3 – 4.5, 4.10]. In this case the holes are confined in WZ material, while the electrons are confined in ZB segments, resulting in significantly longer recombination lifetimes for the lowest-lying electron and hole states which are spatially separated [4.10, 4.11]. In the literature the lifetimes in 0.12 – 7.5 ns range have been reported for WZ InP NWs at low temperature [4.6, 4.10, 4.12, 4.13]. The fact that the nonradiative recombination rate depends

both on the quality of the surface (i.e. the surface recombination velocity) and the diameter of NWs [4.14] could explain the discrepancy in the measured values. The PL emission of InP NWs is often, at least partially, attributed to excitonic recombination [4.1, 4.4, 4.12, 4.13, 4.15] with exciton binding energy of  $\approx 5$  meV [4.1].

Emission energy of WZ NWs varies not only from one work to another but may be different on different NWs on the same substrate [4.9]. Moreover, despite that no shift of emission energy is observed in PL measurements on as-grown samples as the excitation power is increased [4.10, 4.12, 4.15], a blueshift [4.2, 4.9, 4.15] and redshift [4.13] of  $\mu$ PL emission energy are observed on single InP NWs. Another important characteristic of PL emission is the full width at half maximum (FWHM) of the PL emission peak. The best values of FWHW reported on InP NW emission are in 2 – 4 meV range [4.4, 4.6, 4.13].

Possible integration of NWs in electronic, photonic or electromechanical systems at nanoscale requires detailed knowledge of their electronic and optical properties as well as possible impacts of the surface on these properties. Despite its importance, only few works have been published on the optical properties of mechanically strained NWs, though strain effects can play an important role in electronic and optical characteristics. In this context we study the basic optical properties of InP NWs and possible impacts of the surface of host-substrate on these properties. The beginning of the present chapter is devoted to the origin of PL emission from WZ InP NWs, grown at different temperatures, and its basic characteristics (emission energy and FWHM). Next, we aim to demonstrate the possible impacts of the host-substrate on these basic characteristic, both by substrate-induced strain and by presence of surface charges.

## 4.2 PL characterization of InP nanowires.

As was demonstrated in Chapter 2, the WZ InP NWs may contain ZB segments of various density, which strongly depends on the growth temperature. To understand the impact of these segments on the optical properties of the InP NWs, the samples, grown at different temperatures, were studied by means of PL spectroscopy. Figure 4.2 shows bright field STEM images of the InP NWs grown at different temperatures and corresponding PL spectra of these NWs measured on as-grown samples using PL setup, described in Chapter 3.2, at temperature of 14 K [4.12]. All the spectra demonstrate a clear peak at 1.494 eV. This peak is generally attributed to emission of WZ InP [4.2, 4.16, 4.17]. However, an additional low energy peak was observed on NWs grown at 340°, 380°, 460° and 500° C.

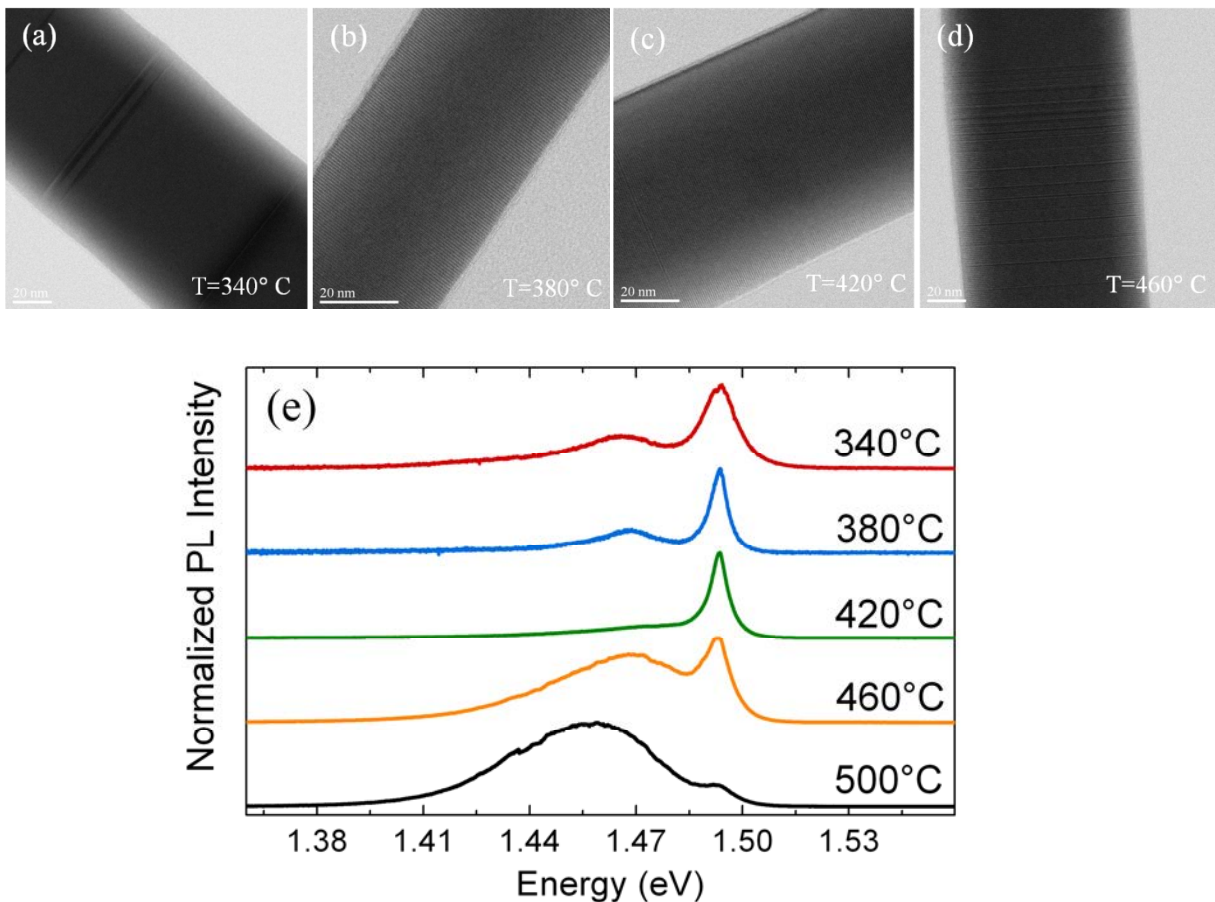


**Figure 4.2:** Bright-field STEM images of InP NWs grown at 340° (a), 380° (b), 420° (c) and 460° C (c). (d) PL spectra of these NWs. Excitation power is 5 mW and temperature is 14 K.

In the literature, this peak is usually attributed either to the type II recombination at the interface between WZ and ZB segments [4.5, 4.18] or to impurity-related emission [4.17]. In the present case, the presence of ZB segments is confirmed by STEM images, and thus, the peak at lower energy is interpreted as the type II recombination. This assumption is also confirmed by the blueshift of emission energy as the excitation power is increased, in agreement with the type II alignment, and longer lifetime as compared to the lifetime measured for the WZ peak [4.10]. As far as the sample grown at 500° C is concerned, due to the high density of ZB insertion, the WZ peak is very weak as compared to the emission of type II recombination around 1.46 eV.

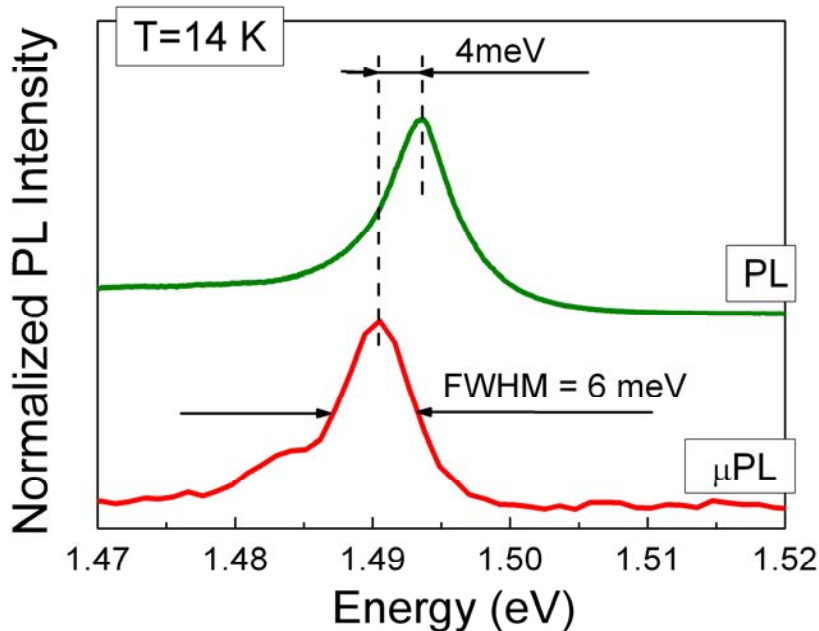


**Figure 4.3:** PL spectrum of NWs grown at 420° C and a micro-PL spectrum on of single NW from this sample.

For the low excitation power, FWHM of 5.3 meV and 5.7 meV are observed for the WZ peak on the samples grown at 380° and 420° C, respectively. These measured values of FWHM are relatively close to the best values reported on single InP NWs at low temperature (2 – 4.7 meV) [4.4, 4.6], despite the fact, that in our experiment the PL spectra were recorded on a population of NWs. Indeed, from  $3 \cdot 10^4$  to  $3 \cdot 10^5$  NWs were excited depending on the studied sample (assuming a spot size of 0.2 mm), which means that the FWHM could be broader than that of a single NW, due to the superposition of emission from many different NWs.

To precise the value of FWHM, the NWs grown at 420° C were removed from the as-grown substrate and transferred onto a clean Si host-substrate as described in Chapter 3.6. Then the setup described in Chapter 3.3 was used to perform  $\mu$ PL spectroscopy measurements on single InP NWs. Figure 4.3 shows the  $\mu$ PL spectrum of a single NW at low excitation power and PL spectrum of the as-grown sample. The WZ peak of the NW is observed at 1.49 eV with a FWHM of about 6 meV in both cases, which confirms that the inhomogeneous broadening is negligible as compared to the homogeneous broadening in our sample. This result can be explained by the fact that diameter of the NWs at the base is in 60 – 80 nm range which is 6 – 8 times bigger than the Bohr radius in bulk InP ( $\sim$  9 nm). In this case the quantum confinement effect is not expected and so is the inhomogeneous broadening.

On top of that, a clear difference of 4 meV in emission energy of PL and micro-PL spectra has been observed (Figure 4.3). The amplitude of this shift differs from one NW to another, but very few of them demonstrate no shift at all. Since all the NWs on the as-grown sample seem to emit at the same energy (1.494 eV), as evidenced by FWHM of emission, we may conclude that the shift is a consequence of the transfer to the host-substrate. In the following investigation we will try to demonstrate how the surface of host-substrates may affect the optical properties on NWs.

### 4.3 Phenomenon of substrate-induced strain.

In general, NW transfer on a host-substrate is a common approach to obtain low density NW samples where a laser beam may be focused on a single NW. For this purpose, materials such as quartz [4.19, 4.8], silicon [4.1, 4.2, 4.12, 4.20, 4.21] silicon oxide [4.9] and few others [4.15, 4.17, 4.22, 4.23] are typically used as the host-substrate. Typical transfer procedures are described in Chapter 3.6. Despite of the numerous advantages of this approach, a potential problem was reported few years ago by J. B. Schlager *et.al.* [4.24]. It was noticed that a tensile strain could be induced on GaN NWs dispersed and bonded to a quartz substrate which led to a redshift of the PL emission peak at low temperature (Figure 4.4.a). This tensile strain was interpreted as a consequence of the difference in the linear thermal expansion coefficients (LTEC) of the substrate and the NW. That is being relaxed at room temperature, the NWs are strained during the cooling of the sample (Figure 4.4.b).

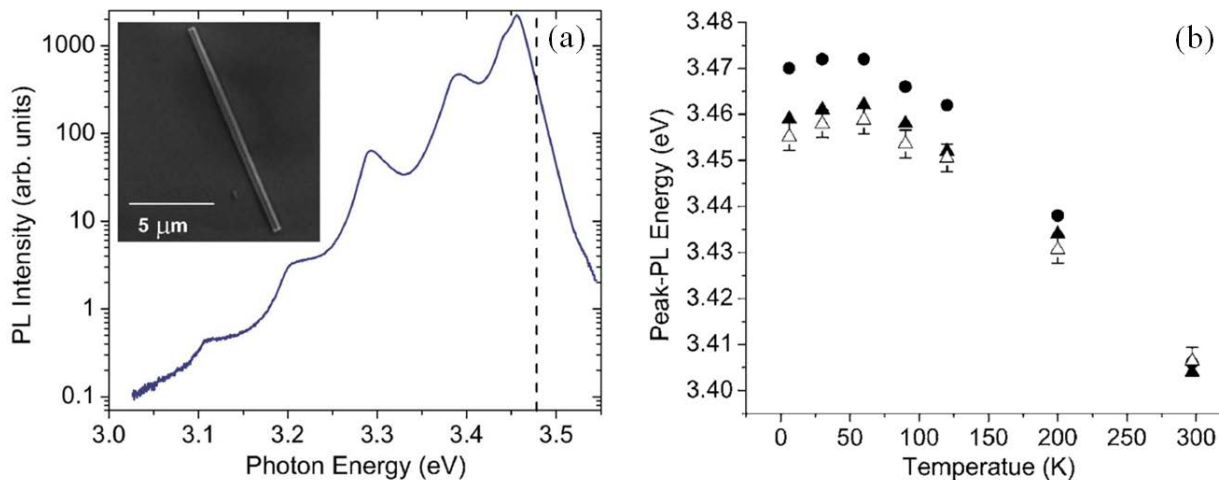


**Figure 4.4:** Images from [4.24]. (a) Low-temperature PL spectrum of a GaN nanowire (12.7  $\mu\text{m}$  length and 425 nm diameter) dispersed on a fused silica substrate. The vertical dashed line indicates the strain-free position of the peak. (b) The emission energies as a function of temperature. Triangles and circles represent strained and strain-free NWs, respectively.

The following study will be focused on the detailed investigation of this phenomenon and the role of a host-substrate in the optical properties of InP NWs. Our aim is to demonstrate that the NW PL emission energy can be related to the choice of the host-substrate, and from this point of view, some results of the recently published works can be explained.

#### 4.4 Theory of substrate-induced strain and its impact on the optical properties.

Basically, the possibility to strain a NW by a host-substrate is related to the static friction per unit area: the shear strength. The maximum axial strain that a NW can accommodate is equal to [4.25]:

$$|\varepsilon_{\max}| = \frac{\tau w L_0}{2EA} = \frac{\tau L_0}{3\sqrt{3}Ew} \quad (4.1)$$

where  $A = 3\sqrt{3}w^2/2$  is the cross sectional area of a hexagonal NW,  $L_0$  is its length,  $w$  is the contact width between the NW and the substrate,  $\tau$  is the shear force and  $E$  is the Young's modulus. Despite the fact that the Young's modulus depends on the NW diameter, for the diameters in the 60 – 100 nm range the value is expected to be close to that of bulk material [4.26]. Approximating the value of Young's modulus for bulk WZ InP with that for ZB InP(111), which is equal to 112.7 GPa [4.27], using a typical value of the shear force for NWs on the substrate (1 – 5 MPa) [4.28], and the dimensions of our NWs ( $w = 30$  nm,  $L = 4$  μm), we can estimate the maximum strain, which can be applied to a NW by the substrate, in the  $10^{-4}$  –  $10^{-3}$  range. Here it is important to note that this phenomenon is a direct consequence of the one dimensional nature of the NWs: without this anisotropic shape, the maximal strain would be in the order of  $\tau / E$ , that is in the order of  $10^{-5}$ .

Let us now consider the impact of the strain on the emission energy of a NW lying on a substrate. Using the temperature dependences of LTECs, represented by  $\alpha(T)$ , the fractional length changes expected with a temperature change may be calculated. Then, assuming a perfect bond (possibly due to van der Waals force) between the substrate and the NWs, the strain can be calculated as follows [4.24]:

$$\varepsilon_{zz} = \int_{T_{\text{cryo}}}^{RT} \alpha_{\text{NF Wz}}^c(T) dT - \int_{T_{\text{cryo}}}^{RT} \alpha_{\text{Sub}}(T) dT \quad (4.2.a)$$

$$\varepsilon_{xx} = \int_{T_{\text{cryo}}}^{RT} \alpha_{\text{NF Wz}}^a(T) dT - \int_{T_{\text{cryo}}}^{RT} \alpha_{\text{Sub}}(T) dT \quad (4.2.b)$$

where  $T_{\text{cryo}}$  and  $RT$  are temperature of the cryostat and room temperature, respectively. Indexes “a” and “c” represent crystallographic axes of WZ material. The strain along the y-axis is

calculated assuming zero stress along this axis and that the NW is lying on one of its m-plane facets:

$$\varepsilon_{yy} = -\frac{C_{12}}{C_{11}}\varepsilon_{xx} - \frac{C_{13}}{C_{11}}\varepsilon_{zz} \quad (4.3)$$

where,  $C_{12}$ ,  $C_{11}$  and  $C_{13}$  are the elastic constants of WZ InP.

We will consider now the band gap of strained WZ materials. Due to the small value of the substrate induced strain, only terms of the first order in the strain are taken into account [4.29]. So the strain dependence of the A exciton energy ( $E$ ) is given by:

$$E = E_0 + a_1\varepsilon_{zz} + a_2(\varepsilon_{xx} + \varepsilon_{yy}) - D_3\varepsilon_{zz} - D_4(\varepsilon_{xx} + \varepsilon_{yy}) \quad (4.4)$$

where  $E_0$  is the unstrained band gap,  $a_1$ ,  $a_2$  are the hydrostatic interband deformation potentials and  $D_3$ ,  $D_4$  are the valence band deformation potentials of the WZ material. Unfortunately, the elastic constants and deformation potentials of the WZ crystal phase of InP material are not well known. So for the following calculation we will use average values of the elastic constants calculated from constants obtained in [4.30] and values calculated in quasi cubic approximation [4.31, 4.32]:  $C_{11} = 125.7$  GPa,  $C_{12} = 51.8$  GPa and  $C_{13} = 39.6$  GPa. Moreover, when the quasi cubic approximation is used, we have the following relations:

$$a_1 - a_2 = D_3$$

$$D_3 = -2D_4$$

and  $D_3 = -1.732 \cdot d = 8.7$  eV (where  $d$  is the shear deformation potential of ZB InP [4.33, 4.34]), so the Eq. 4.2 may simplified as:

$$E = E_0 + (0.68a_1 - 7.3)\varepsilon_{zz} + (0.68a_1 - 2.5)\varepsilon_{xx} \quad (4.5)$$

Therefore, the band gap of NWs may be affected by the strain, and a shift of emission energy, depending of the sign of the strain, should be observed.

## 4.5 Experimental observation of substrate-induced strain.

To study this effect experimentally, InP NWs were transferred onto few host-substrates made of different materials. The identical procedures of the liquid transfer were used to transfer the InP NWs from the as-growth substrate onto clean Si, InP and SrTiO<sub>3</sub> (STO) substrates and onto a copper TEM grid. The choice of the substrates is explained by their LTECs and illustrated in Figure 4.5. While Si has a low LTEC and consequently the NWs should be under a tensile strain on this substrate, the SrTiO<sub>3</sub> substrate and the copper TEM grid have LTECs higher than that of InP, so the NWs are expected to be under a compressive strain [4.35, 4.36]. On the other hand, the NWs transferred on the InP substrate are assumed to be nearly unstrained due to an expected similarity of the LTEC of WZ and ZB InP. On top of that, the as-grown sample, where NWs are free standing and unstrained, will be used as a reference.

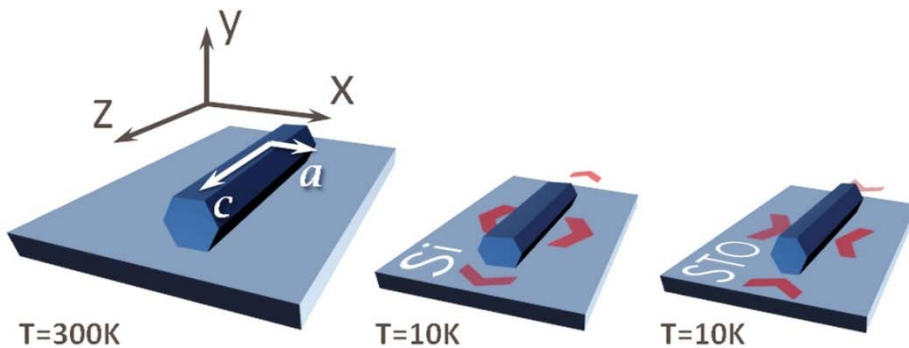


**Figure 4.5:** Scheme of the substrate-induced strain. A NW unstrained at room temperature, becomes either stretched or squeezed, depending on the substrate, silicon (Si) or SrTiO<sub>3</sub> (STO), as temperature is decreased.

To begin, we measured the room temperature micro-PL spectra of the NWs on different host-substrates. Figure 4.6 demonstrates that the typical spectra at room temperature contain two peaks at 1.44 eV and 1.47 eV. Since the energy distance between the peaks is about 30 meV, we attribute these peaks to the A and B bands of WZ InP. This value is in agreement with that calculated from Eq. 1.1. These room temperature measurements aim to show that no difference in A-band emission energy on different host-substrates has been observed at room temperature. This fact is in agreement with hypothesis of temperature dependent substrate-induced strain.

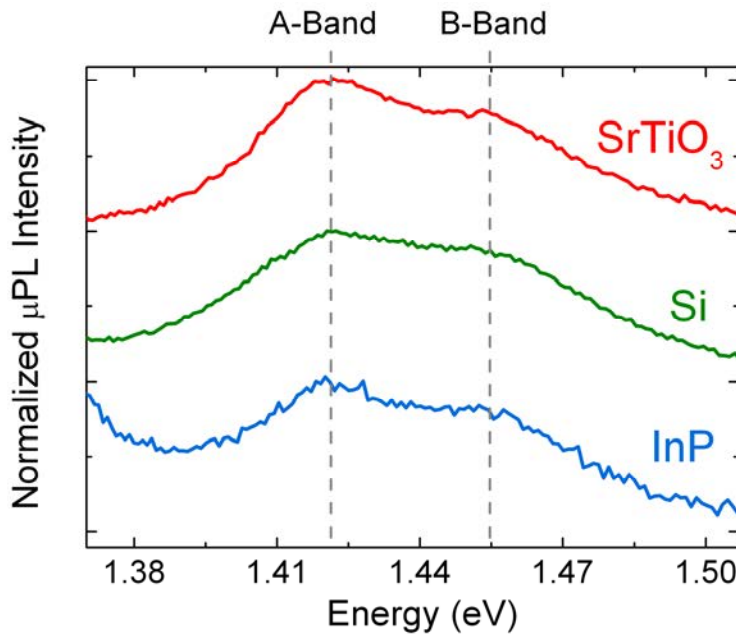


**Figure 4.6:** Room temperature  $\mu$ PL emission of the NWs transferred on different substrates.

Then the samples were placed in the cryostat and studied at low temperature. Figure 4.7 shows the typical low temperature (10 K)  $\mu$ PL emission spectra of InP NWs transferred on different host-substrates. This experimental result appears to be in agreement with the theory explained above. The redshift (shift to lower energies), observed for the NWs transferred on the Si substrate, and the blueshift (shift to higher energies), observed for the NWs transferred on the  $\text{SrTiO}_3$  substrate, are in agreement with the sign of the expected strain induced by the host-substrates. On the other hand, the WZ InP NWs transferred on ZB InP substrate have nearly the same emission energy as the as-grown sample (dashed line), which leads to the expected conclusion that NWs on this substrate are nearly unstrained. Specifically, this means that  $\alpha_{\text{WZ InP}}^c$  and  $\alpha_{\text{WZ InP}}^a$  are either close to  $\alpha_{\text{ZB InP}}$  or compensate each other, because the WZ coefficients, as compared to corresponding coefficient of ZB materials, can be lower and higher, respectively [4.37].

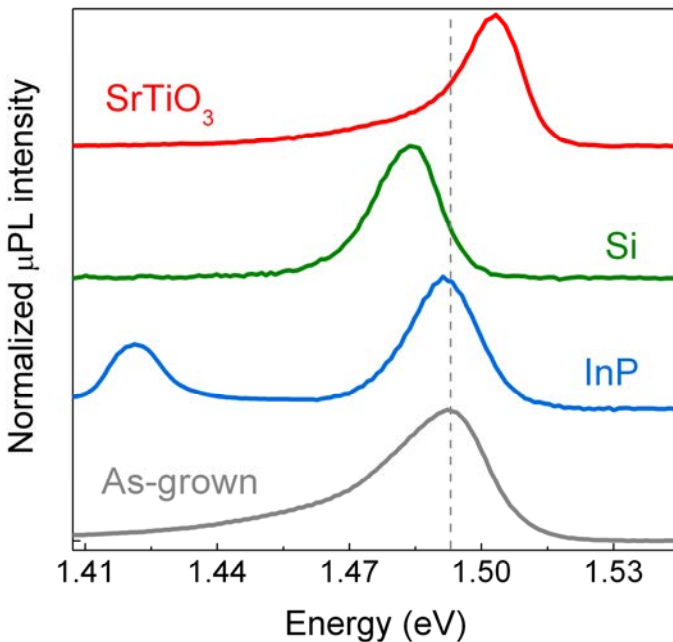


**Figure 4.7:** Low temperature (10K)  $\mu$ PL emission peak shift for the NWs transferred on different substrates (excitation power  $\approx$  5mW).

To make the matter certain, a dozen of NWs was studied on each substrate and few on the TEM grid. Figure 4.8 shows the statistical distribution of the peak position in the spectra of all the measured NWs. The dashed line represents the emission energy of the as-grown sample. Wide distribution over 10 meV is observed on both Si and  $\text{SrTiO}_3$  substrates, whereas the distribution is much narrower on the InP substrate, where more than 75% of the studied NWs emit at the same energy. Thus, we assume that the observed distribution is a consequence of the strain and that the NWs transferred on a given substrate are not all strained identically. This can be explained by the fact that different NWs may have different values of  $|\epsilon_{\max}|$  due to difference in the NW morphology (length, diameter) or due to different shear strength values from one NW to another [4.28]. We also observe that the maximum PL emission redshift on the Si substrate is comparable to the blueshift observed on the  $\text{SrTiO}_3$  substrate. This result contradicts the fact, that due to the significant difference in the thermal expansion coefficients [4.34 – 4.36], the PL blueshift on the  $\text{SrTiO}_3$  substrate should be much more significant than the PL redshift on Si.

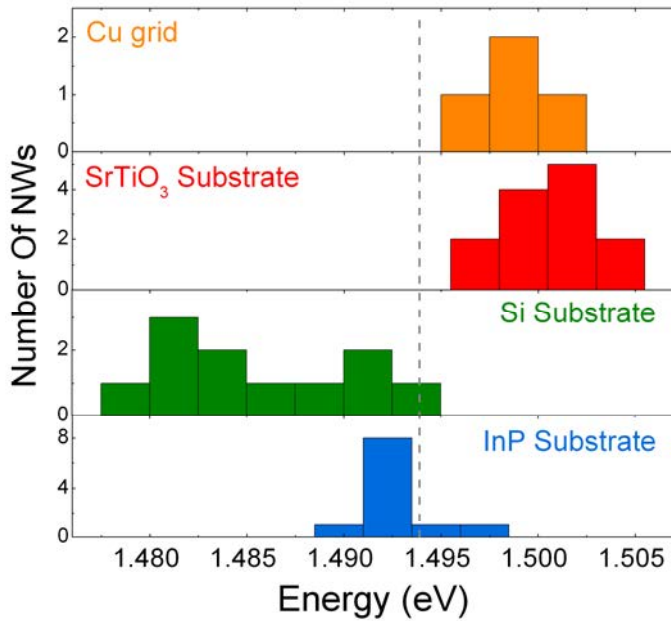


**Figure 4.8:** Statistical distribution of the  $\mu$ PL emission peak position of InP NWs on different substrates at low temperature (10 K).

This discrepancy may be resolved within the assumption that the force created by the strain becomes stronger than the bonding force, at some points, and that the NWs can not be strained anymore. Such maximal strain is comparable to the strain expected on a NW on a Si substrate from Eq. 4.1, but is smaller than that expected on the SrTiO<sub>3</sub> substrate. Consequently, the strain on the SrTiO<sub>3</sub> substrate is assumed to be partly relaxed down to the maximum affordable strain, leading to an energy shift of the same order of magnitude as the shift on Si substrate.

To improve our understanding of the substrate-induced strain phenomenon, NWs transferred onto the SrTiO<sub>3</sub> substrate have also been investigated by cathodoluminescence (CL) microscopy at 10 K. These measurements have been performed using the cathodoluminescence setup from Attolight AG. 27 NWs have been investigated by CL. The investigation was focused only on NWs that are not in contact with other NWs to avoid any unexpected interaction. The obtained distribution is shown in Figure 4.9.a. A blueshift of the CL emission energy is observed on the majority of NWs emitting in the 1.495 – 1.505 eV range, which confirms the result obtained previously.

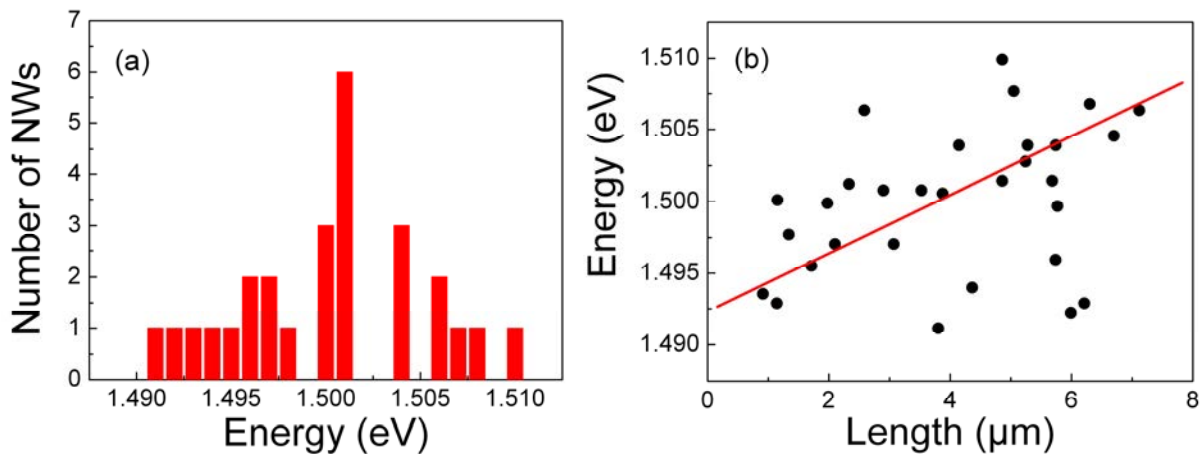


**Figure 4.9:** Results of CL measurements. (a) Statistical distribution of the emission energy for NWs transferred on the  $\text{SrTiO}_3$  substrate. (b) Emission energy of these NWs as a function of their length. The red line is a guide for the eyes.

The CL setup, allows to measure the length of the investigated NWs. Figure 4.9.b shows the CL peak position of the NWs as a function of their length. A trend seems to emerge between the emission energy and the length of the NW in agreement with Eq. 4.1: longer NW can accommodate a bigger strain. However, few long NWs (length between 4 and 6  $\mu\text{m}$ ) are not strained despite the fact they seem to lie directly on the substrate. This may be explained if we assume a strong fluctuation of the shear strength from one NW to another regardless the size. Such strong fluctuation has already been reported for InAs NWs on  $\text{Si}_3\text{N}_4$  [4.38].

To confirm the impact of the sample cooling on the substrate-induced strain, the temperature dependence of the phenomenon has been studied. For this purpose, the emission energy of NWs transferred on InP host-substrate was compared to that of NWs transferred on the  $\text{SrTiO}_3$  substrate. The PL setup is used for this experiment, so the emission of many NWs was detected. Figure 4.10 demonstrates nearly no shift at room temperature, in agreement with hypothesis of substrate-induced strain. As temperature is decreased, the value of blueshift is increasing. At 125K the blueshift seems to reach a limit and stays relatively constant below that temperature. This can be explained by the assumption that the NWs reached the maximum strain they can accommodate ( $\varepsilon_{\max}$ ) at this temperature.

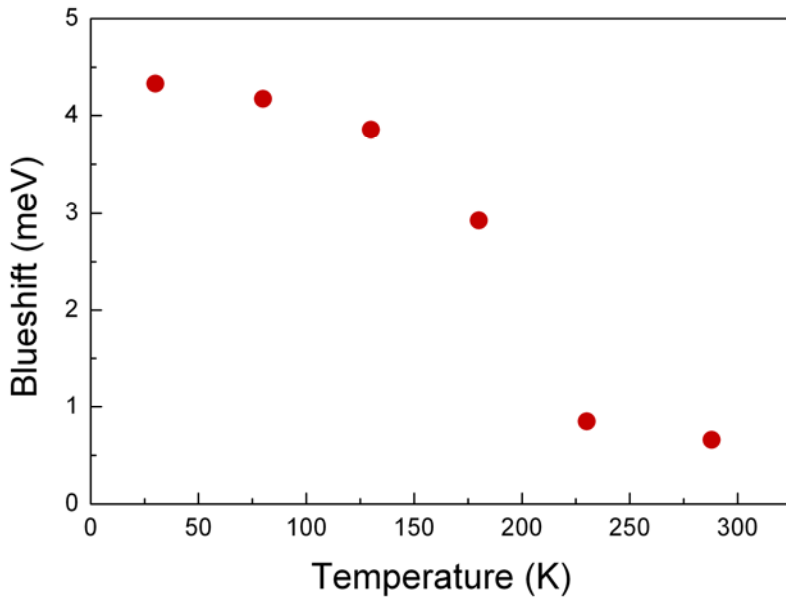


**Figure 4.10:** PL emission blueshift for NWs transferred on the SrTiO<sub>3</sub> host-substrate as compared to NWs transferred on the InP host-substrate as a function of temperature.

The measurements of the optical emission as a function of the strain can be used to estimate deformation potentials of the WZ InP. For instance, the hydrostatic interband deformation potential  $a_1$  can be estimated assuming that the NWs on Si substrate with the biggest redshift are strained completely. In this case, the expected emission peak shift between NWs transferred on Si and on InP substrates is calculated from Eq. 4.2 to discard the unknown LTECs of WZ InP:

$$E_{\text{Si}} - E_{\text{InP}} = (1.36 a_1 - 9.8) \left( \int_{T_{\text{cryo}}}^{RT} \alpha_{\text{Sub}}^{\text{InP}}(T) dT - \int_{T_{\text{cryo}}}^{RT} \alpha_{\text{Sub}}^{\text{Si}}(T) dT \right)$$

Using the LTECs from [4.35] and [4.29], integrated from 10 K (temperature of the cryostat) to 300 K, the value of 12.7 eV is estimated for  $a_1$ , which is twice as much as the hydrostatic potential of ZB InP [4.33].

## 4.6 Impact of surface charges.

It is known, that strain applied to a WZ material may cause a piezoelectric field that would bend the energy bands and affect the optical properties [4.39, 4.40]. In order to check the impact of this phenomenon, the  $\mu$ PL emission of different samples has also been studied as a function of the excitation power. Figure 4.11 shows typical excitation power dependences of the emission energy from various NWs measured on different substrates and the as-grown sample in different days (solid or dashed lines). Each line represents the behavior of several similar NWs.

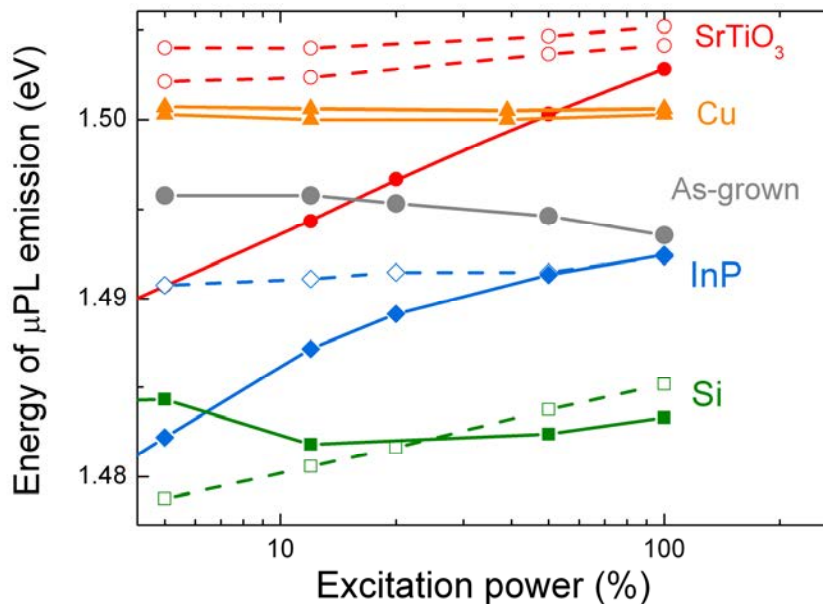


**Figure 4.11:** Energy of  $\mu$ PL emission as a function of the excitation power (100% = 5 mW). Solid and dashed lines hold for records performed on different days.

Although on some NWs a blueshift is observed as the excitation power is increased, its magnitude differs from one host-substrate to another, and is not consistent with the piezoelectric field caused by the strain, because the blueshift is observed even on the unstrained InP NWs. Moreover, in contrast to the blueshift recorded in case of single NWs, a small redshift is observed on the as-grown sample. These results lead to the conclusion that though the magnitude of the blueshift does not depend on the strain, yet it may be related to the presence of the host-substrate material. Moreover, we observed that for a given host-substrate at high excitation power the NWs, presenting the blueshift, have emission energy close to that of the NWs that are not blueshifting (for instance as shown in Figure 4.11 for SrTiO<sub>3</sub> and InP substrates). From these

results, we make the assumption that the blueshift could be the consequence of surface effects, such as surface charges at the host-substrate generating a band bending [4.41]. Indeed, under the low excitation power, the created charge carriers will be separated in space so that one type of the carriers will be confined at the interface, while the other type will be accumulated away from the surface. In this case, the recombination between these carriers may take place at the energy lower than the band gap. As the excitation power is increased, more charge carriers are generated, reducing the band bending due to a partial or complete screening, so the emission energy is increased. This assumption would also explain the difference in the shifts observed on different substrates and in different days, suggesting different conditions on the surface.

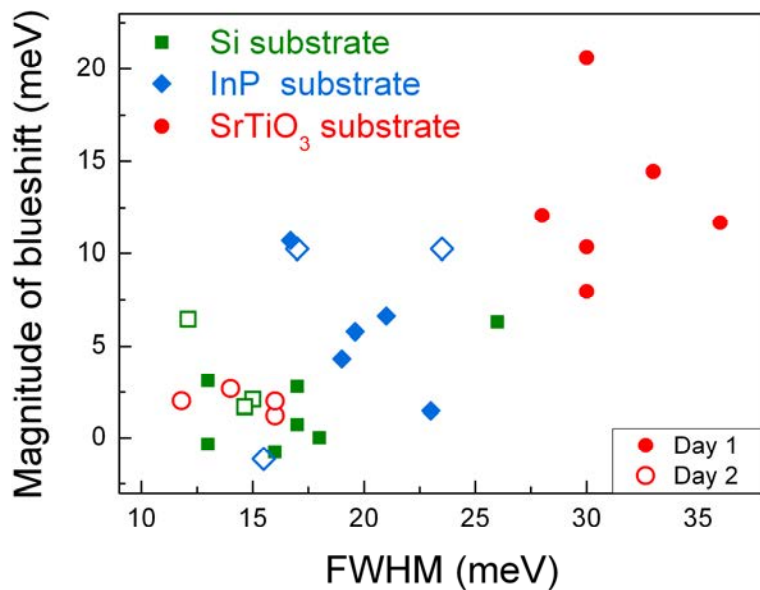


**Figure 4.12:** Correlation between the magnitude of the blueshift as the excitation power is increased and FWHM of PL emission peak at high excitation power. Shaded and open symbols represent data recorded on different days.

To conclude this issue, FWHM of the NWs on different substrates has been studied at high excitation power (5 mW) and values in the 12 – 35 meV range have been observed. In addition, a clear correlation between the FWHM at high excitation power and the magnitude of the blueshift when the excitation power is increased from 0.1 to 5 mW has been noted (Figure 4.12).

Figure 4.13 reflects our interpretation of this correlation. At low excitation power, the emission of a NW is redshifted (i.e. takes place at lower energy) as compared to the band gap.

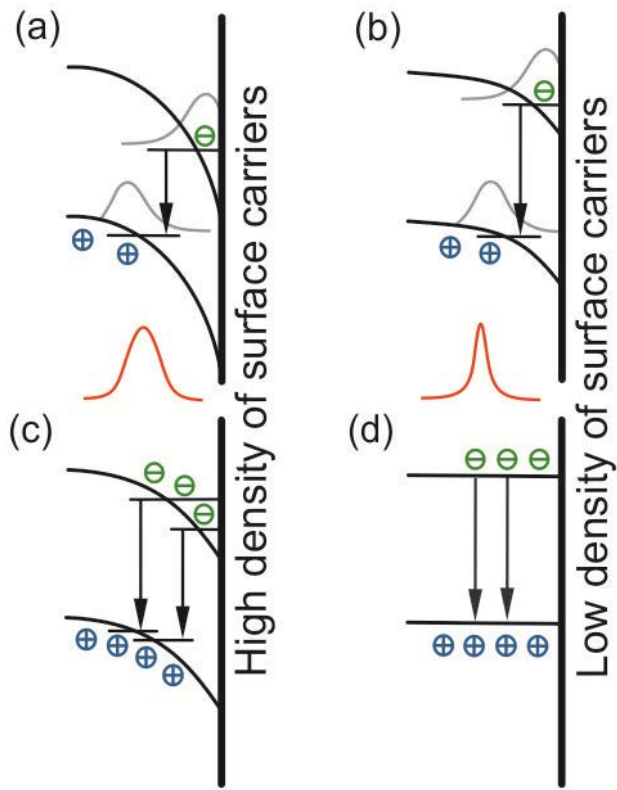


**Figure 4.13:** Scheme of the band bending at the NW/Substrate interface depending on the density of the surface carriers. Figures (a) and (b) represent the case of relatively low excitation power. The case of high excitation power is shown in figures (c) and (d).

The magnitude of the redshift is related to the number of carriers at the surface of the host-substrate (Figure 4.13.a and 4.13.b). When the excitation power is increased, in the case of high density of surface carriers (Figure 4.13.c), two phenomena take place: a reduction of the band bending due to a partial screening of the carriers and a state filling which explains the broadening of the PL emission. In the case of low density of surface carriers (Figure 4.13.d), the screening is easier to achieve while a smaller broadening of the PL emission is expected.

## 4.7 Conclusions.

The optical properties of WZ InP NWs grown at different temperatures were studied at low temperature by means of PL spectroscopy. Most of the samples showed the clear signs of type II recombination at the WZ/ZB interface, while only NWs grown at 420° C demonstrated a single peak attributed to WZ InP, which confirmed its quality. FWHM of this peak was found to be relatively close to the best values reported on single InP NWs at low temperature. The value of FWHM = 6 meV was also confirmed by  $\mu$ PL study on single InP NWs.

Next, the impact of the host-substrate on the optical properties was studied. It was shown that the influence of a host-substrate could have a significant impact on the optical properties of NWs. Namely, the optical properties may be affected by the substrate-induced strain created by the difference in the LTECs of the NWs and the host-substrate, and by some other surface effects. More specifically, the energy of  $\mu$ PL emission can be changed depending on the host-substrate material, while its shift as a function of excitation power and its FWHM can be related to the surface charges affecting the band bending and be different as from one host-substrate to another as from one day to another. Accordingly, consideration of these effects can serve for better understanding of some recently published results and should be taken into account whenever  $\mu$ PL results on transferred NWs are considered. For instance, in [4.12] and [4.9] the position of the  $\mu$ PL emission peak of InP NWs transferred on Si substrate has been found to be red-shifted from expected value or from value of PL emission of the as-grown sample. This shift could be explained, taking into account that the LTC of InP NWs is higher than that of the Si substrate and consequently, at low temperature, the NWs may be under a tensile strain which decreases the band gap. In addition, small differences in the positions of the peaks of different NWs [4.1, 4.2, 4.9] can be related to a difference in magnitude of the strain from one NW to another. Moreover, blueshift of  $\mu$ PL emission energy as the excitation power is increased is typically observed on single InP NWs [4.2, 4.9, 4.15] and sometimes attributed to the band filling effect [4.9]. It was shown that this blueshift may be a consequence of the transfer on a host-substrate and not an intrinsic property of NWs.

## 4.8 References.

- [4.1] A. Mishra, L. V. Titova, T. B. Hoang, H. E. Jackson, L. M. Smith, J. M. Yarrison-Rice, Y. Kim, H. J. Joyce, Q. Gao, H. H. Tan, and C. Jagadish, "Polarization and temperature dependence of photoluminescence from zincblende and wurtzite InP nanowires", *Applied Physics Letters*, vol. 91, p. 263104, 2007.
- [4.2] S. Perera, K. Pemasiri, M. a. Fickenscher, H. E. Jackson, L. M. Smith, J. Yarrison-Rice, S. Paiman, Q. Gao, H. H. Tan, and C. Jagadish, "Probing valence band structure in wurtzite InP nanowires using excitation spectroscopy", *Applied Physics Letters*, vol. 97, p. 023106, 2010.
- [4.3] J. Bao, D. C. Bell, F. Capasso, J. B. Wagner, T. Mårtensson, J. Trägårdh, and L. Samuelson, "Optical properties of rotationally twinned InP nanowire heterostructures", *Nano letters*, vol. 8, p. 836, 2008.
- [4.4] T. T. T. Vu, T. Zehender, M. a Verheijen, S. R. Plissard, G. W. G. Immink, J. E. M. Haverkort, and E. P. a M. Bakkers, "High optical quality single crystal phase wurtzite and zincblende InP nanowires", *Nanotechnology*, vol. 24, p. 115705, 2013.
- [4.5] J.-M. Jancu, K. Gauthron, L. Largeau, G. Patriarche, J.-C. Harmand, and P. Voisin, "Type II heterostructures formed by zinc-blende inclusions in InP and GaAs wurtzite nanowires", *Applied Physics Letters*, vol. 97, p. 041910, 2010.
- [4.6] S. Reitzenstein, S. Munch, C. Hofmann, A. Forchel, S. Crankshaw, L. C. Chuang, M. Moewe, and C. Chang-Hasnain, "Time resolved microphotoluminescence studies of single InP nanowires grown by low pressure metal organic chemical vapor deposition", *Applied Physics Letters*, vol. 91, p. 091103, 2007.
- [4.7] M. S. Gudiksen, J. Wang, and C. M. Lieber, "Size-Dependent Photoluminescence from Single Indium Phosphide Nanowires", *The Journal of Physical Chemistry B*, vol. 106, p. 4036, 2002.
- [4.8] J. Wang, M. S. Gudiksen, X. Duan, Y. Cui, and C. M. Lieber, "Highly polarized photoluminescence and photodetection from single indium phosphide nanowires", *Science*, vol. 293, p. 1455, 2001.
- [4.9] Y. Kobayashi, M. Fukui, J. Motohisa, and T. Fukui, "Micro-photoluminescence spectroscopy study of high-quality InP nanowires grown by selective-area metalorganic vapor phase epitaxy", *Physica E*, vol. 40, p. 2204, 2008.
- [4.10] M. H. Hadj Alouane, N. Chauvin, H. Khmissi, K. Naji, B. Ilahi, H. Maaref, G. Patriarche, M. Gendry, and C. Bru-Chevallier, "Excitonic properties of wurtzite InP nanowires grown on silicon substrate", *Nanotechnology*, vol. 24, p. 035704, 2013.
- [4.11] K. Pemasiri, M. Montazeri, R. Gass, L. M. Smith, H. E. Jackson, J. Yarrison-Rice, S. Paiman, Q. Gao, H. H. Tan, C. Jagadish, X. Zhang, and J. Zou, "Carrier Dynamics and Quantum Confinement in type II ZB-WZ InP Nanowire Homostructures", *Nano letters*, vol. 9, p. 648, 2009.

- [4.12] N. Chauvin, M. H. Hadj Alouane, R. Anufriev, H. Khmissi, K. Naji, G. Patriarche, C. Bruc-Chevallier, and M. Gendry, "Growth temperature dependence of exciton lifetime in wurtzite InP nanowires grown on silicon substrates", *Applied Physics Letters*, vol. 100, p. 011906, 2012.
- [4.13] S. Crankshaw, S. Reitzenstein, L. Chuang, M. Moewe, S. Münch, C. Böckler, A. Forchel, and C. Chang-Hasnain, "Recombination dynamics in wurtzite InP nanowires", *Physical Review B*, vol. 77, p. 235409, 2008.
- [4.14] E. Yablonovitch, C. J. Sandroff, R. Bhat, and T. Gmitter, "Nearly ideal electronic properties of sulfide coated GaAs surfaces", *Applied Physics Letters*, vol. 51, p. 439, 1987.
- [4.15] G. L. Tuin, M. T. Borgström, J. Trägårdh, M. Ek, L. R. Wallenberg, L. Samuelson, and M.-E. Pistol, "Valence band splitting in wurtzite InP nanowires observed by photoluminescence and photoluminescence excitation spectroscopy", *Nano Research*, vol. 4, p. 159, 2010.
- [4.16] L. V. Titova, T. B. Hoang, H. E. Jackson, L. M. Smith, J. M. Yarrison-Rice, Y. Kim, H. J. Joyce, H. H. Tan, and C. Jagadish, "Temperature dependence of photoluminescence from single core-shell GaAs-AlGaAs nanowires", *Applied Physics Letters*, vol. 89, p. 173126, 2006.
- [4.17] E. G. Gadret, G. O. Dias, L. C. O. Dacal, M. M. de Lima, C. V. R. S. Ruffo, F. Iikawa, M. J. S. P. Brasil, T. Chiaramonte, M. a. Cotta, L. H. G. Tizei, D. Ugarte, and a. Cantarero, "Valence-band splitting energies in wurtzite InP nanowires: Photoluminescence spectroscopy and ab initio calculations", *Physical Review B*, vol. 82, p. 125327, 2010.
- [4.18] J. Bao, D. C. Bell, F. Capasso, J. B. Wagner, T. Mårtensson, J. Trägårdh, and L. Samuelson, "Optical properties of rotationally twinned InP nanowire heterostructures", *Nano letters*, vol. 8, p. 836, 2008.
- [4.19] M. S. Gudiksen, J. Wang, and C. M. Lieber, "Size-Dependent Photoluminescence from Single Indium Phosphide Nanowires", *The Journal of Physical Chemistry B*, vol. 106, p. 4036, 2002.
- [4.20] T. Ba Hoang, A. F. Moses, L. Ahtapodov, H. Zhou, D. L. Dheeraj, A. T. J. van Helvoort, B.-O. Fimland, and H. Weman, "Engineering parallel and perpendicular polarized photoluminescence from a single semiconductor nanowire by crystal phase control", *Nano letters*, vol. 10, p. 2927, 2010.
- [4.21] G. Sallen, A. Tribu, T. Aichele, R. André, L. Besombes, C. Bougerol, S. Tatarenko, K. Kheng, and J. P. Poizat, "Exciton dynamics of a single quantum dot embedded in a nanowire", *Physical Review B*, vol. 80, p. 085310, 2009.
- [4.22] P. Mohan, J. Motohisa, and T. Fukui, "Fabrication of InP/InAs/InP core-multishell heterostructure nanowires by selective area metalorganic vapor phase epitaxy", *Applied Physics Letters*, vol. 88, p. 133105, 2006.
- [4.23] J. B. Schlager, N. A. Sanford, K. a. Bertness, J. M. Barker, A. Roshko, and P. T. Blanchard, "Polarization-resolved photoluminescence study of individual GaN nanowires grown by catalyst-free molecular beam epitaxy", *Applied Physics Letters*, vol. 88, p. 213106, 2006.

- [4.24] J. B. Schlager, K. A. Bertness, P. T. Blanchard, L. H. Robins, A. Roshko, and N. A. Sanford, "Steady-state and time-resolved photoluminescence from relaxed and strained GaN nanowires grown by catalyst-free molecular-beam epitaxy", *Journal of Applied Physics*, vol. 103, p. 124309, 2008.
- [4.25] F. Xu, J. W. Durham, B. J. Wiley, and Y. Zhu, "Strain-Release Assembly of Nanowires on Stretchable Substrates", *ACS nano*, vol. 5, p. 1556, 2011.
- [4.26] C. L. dos Santos and P. Piquini, "Diameter dependence of mechanical, electronic, and structural properties of InAs and InP nanowires: A first-principles study", *Physical Review B*, vol. 81, p. 075408, 2010.
- [4.27] S. Adachi, *Physical properties of III-V semiconductor compounds*. Mörrenbach: Wiley-VCH, 1992, p. 24.
- [4.28] M. Bordag, A. Ribayrol, G. Conache, L. E. Fröberg, S. Gray, L. Samuelson, L. Montelius, and H. Pettersson, "Shear stress measurements on InAs nanowires by AFM manipulation", *Small*, vol. 3, p. 1398, 2007.
- [4.29] F. Boxberg, N. Søndergaard, and H. Q. Xu, "Elastic and piezoelectric properties of zincblende and wurtzite crystalline nanowire heterostructures", *Advanced materials*, vol. 24, p. 4692, 2012.
- [4.30] F. Boxberg, N. Søndergaard, and H. Q. Xu, "Photovoltaics with piezoelectric core-shell nanowires", *Nano letters*, vol. 10, p. 1108, 2010.
- [4.31] M. W. Larsson, J. B. Wagner, M. Wallin, P. Håkansson, L. E. Fröberg, L. Samuelson, and L. R. Wallenberg, "Strain mapping in free-standing heterostructured wurtzite InAs/InP nanowires", *Nanotechnology*, vol. 18, p. 015504, 2007.
- [4.32] R. M. Martin, "Relation between Elastic Tensors of Wurtzite and Zinc-Blende Structure Materials", *Physical Review B*, vol. 6, p. 4546, 1972.
- [4.33] I. Vurgaftman, J. R. Meyer, and L. R. Ram-Mohan, "Band parameters for III–V compound semiconductors and their alloys", *Journal of Applied Physics*, vol. 89, p. 5815, 2001.
- [4.34] Z. Y. Zhai, X. S. Wu, Z. S. Jiang, J. H. Hao, J. Gao, Y. F. Cai, and Y. G. Pan, "Strain distribution in epitaxial SrTiO<sub>3</sub> thin films", *Applied Physics Letters*, vol. 89, p. 262902, 2006.
- [4.35] K. Harunai, H. Maeta, K. Ohashit, and T. Koiket, "The thermal expansion coefficient and Gruneisen parameter of InP crystal at low temperatures", *Solid State Physics*, vol. 20, p. 5275, 1987.
- [4.36] T. Soma, J. Satoh, and H. Matsuo, "Thermal expansion coefficients of GaAs and InP", *Solid State Communications*, vol. 42, p. 889, 1982.
- [4.37] S. Q. Wang, "First-principles study of the anisotropic thermal expansion of wurtzite ZnS", *Applied Physics Letters*, vol. 88, p. 061902, 2006.

- [4.38] G. Conache, S. M. Gray, A. Ribayrol, L. E. Fröberg, L. Samuelson, H. Pettersson, and L. Montelius, "Friction measurements of InAs nanowires on silicon nitride by AFM manipulation.", *Small*, vol. 5, p. 203, 2009.
- [4.39] B. F. Levine, C. J. Pinzone, S. Hui, C. a. King, R. E. Leibenguth, D. R. Zolnowski, D. V. Lang, H. W. Krautter, and M. Geva, "Ultralow-dark-current wafer-bonded Si/InGaAs photodetectors", *Applied Physics Letters*, vol. 75, p. 2141, 1999.
- [4.40] E. Kuokstis, J. W. Yang, G. Simin, M. A. Khan, R. Gaska, and M. S. Shur, "Two mechanisms of blueshift of edge emission in InGaN-based epilayers and multiple quantum wells", *Applied Physics Letters*, vol. 80, p. 977, 2002.
- [4.41] M. H. M. van Weert, O. Wunnicke, a. L. Roest, T. J. Eijkemans, a. Yu Silov, J. E. M. Haverkort, G. W. 't Hooft, and E. P. a. M. Bakkers, "Large redshift in photoluminescence of p-doped InP nanowires induced by Fermi-level pinning", *Applied Physics Letters*, vol. 88, p. 043109, 2006.

# **Chapter V**

---

## Spectroscopy of NW heterostructures

- 5.1 Introduction.
- 5.2 Spectroscopy of QWell-NWs.
- 5.3 Simulation of QWell-NWs.
- 5.4 Spectroscopy of QRod-NWs.
- 5.5 Simulation of QRod-NWs.
- 5.6 Conclusions.
- 5.7 Table of constants for InP and InAs of wurtzite type.
- 5.8 References.

## 5.1 Introduction.

In recent years semiconductor NW heterostructures have attracted considerable interest. Number of reports were published on fabrication and characterization of such types of heterostructures as QDot-NWs [5.1 – 5.4], QRod-NWs [5.5, 5.6] and QWell-NWs usually referred as core-shell [5.7 – 5.10] and core-multishell [5.11 – 5.14] NWs. Optical properties of these heterostructures are often studied by means of ( $\mu$ )PL spectroscopy. Core-shell structures usually exhibit relatively broad emission peaks or sometimes demonstrate multiple peaks of emission, attributed to the variations of the shell thickness [5.8, 5.11, 5.12]. As far as QDot-like structures are concerned, single sharp peaks with values of FWHM as small as 0.12 meV [5.4], 0.2 meV [5.1], and 0.05 – 0.2 meV [5.2] are typically reported for PL emission at low temperature and the peak is usually attributed to excitonic emission.

In this chapter, we present experimental and theoretical studies of the optical properties of InP/InAs/InP QWell-NWs and InAs/InP QRod-NWs grown on Si substrates. We aim to demonstrate that emission of radial QWell structures is controlled by thickness of the QWell. By the example of QRod-NWs we will demonstrate the impact of length and diameter of the QRod on the energy level structure. Finally, we hope to demonstrate that InAs/InP NW heterostructures can serve as efficient emitters with telecommunication wavelength at room temperature.

## 5.2 Spectroscopy of QWell-NWs.

We begin the present chapter with a study of the optical properties of the QWell-NWs grown on Si(001) substrate as described in Chapter 2. First, PL spectroscopy with excitation wavelength of 514 nm was conducted on the as-grown sample of QWell-NWs placed in the cryostat. The low temperature PL spectra were measured and kindly shared with the author by M. H. H. Alouane [5.15]. The obtained PL spectra measured at different temperatures, are shown in Figure 5.1. The low temperature spectrum consists of multiple peaks in the 0.8 – 1.3 eV range, whereas the room temperature spectrum demonstrates a single broad peak of emission.

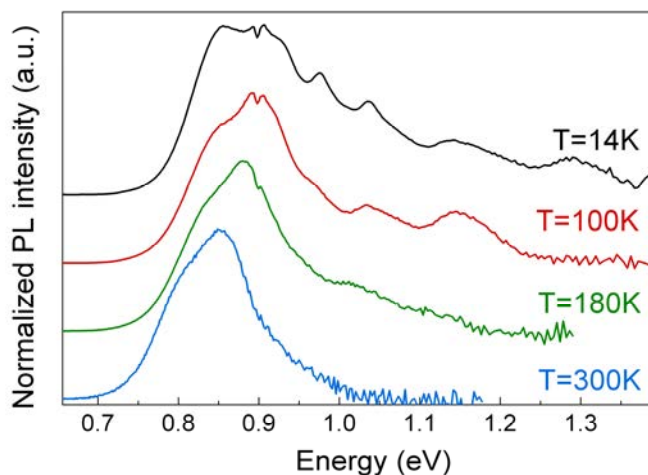


**Figure 5.1:** Changes in the PL spectrum of the QWell-NWs on Si(001) substrate with temperature.

The multiple peaks at low temperature may be attributed either to the state filling [5.7] or to ML fluctuation of thickness of the radial InAs QWell [5.12], as often observed in two dimensional InAs/InP QWells [5.16, 5.17]. In our case, positions of the peaks differs one from another by relatively large values of energy while the PL intensity as a function of the excitation power reveal linear dependences for all peaks. These facts left only the assumption of thickness fluctuations to consideration. Indeed, at low temperature thinner segments of a QWell cause stronger quantum confinement so the emission energy of these segments is higher as compared to that of thicker segments, as illustrated in Figure 5.2.a. In the work of Pal *et al* [5.12], the peaks of PL emission at 1.07, 1.17 and 1.32 eV were observed for the very similar InAs/InP QWell-NW structure at low temperature. These peaks were attributed to 3, 2 and 1 ML thicknesses of the radial QWell. Spectrum of our QWell-NWs contains similar peaks but shifted to lower energies

by 20 – 30 meV, which might be explained by differences in strain due to the different core size and different temperature of the measurements. Increase of the temperature results in carrier transfer to the thicker segments (Figure 5.2.b), so only low energy peaks are observed at room temperature. The emission of InAs QRod insertion is assumed to be negligible as compared to the emission of radial QWell, due to the huge difference in length.

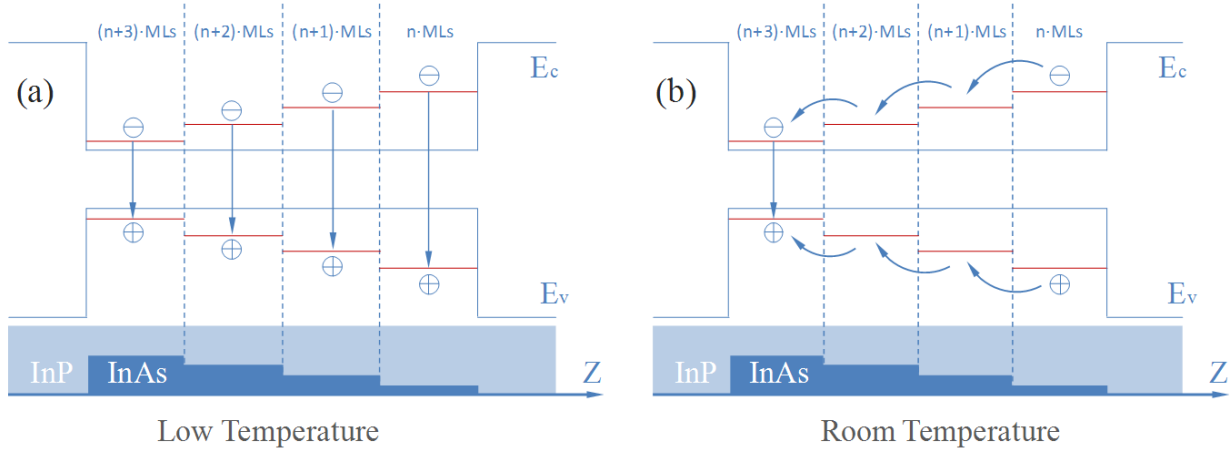


**Figure 5.2:** Schemes of carrier recombination in QWell-NWs at room and low temperatures.

For a better understanding of the recombination processes and their dependence on temperature, we present the analysis of the integrated PL intensity as a function of temperature (Figure 5.3) [5.15]. A 20-fold reduction of the PL intensity is measured between 14 K and 300 K.

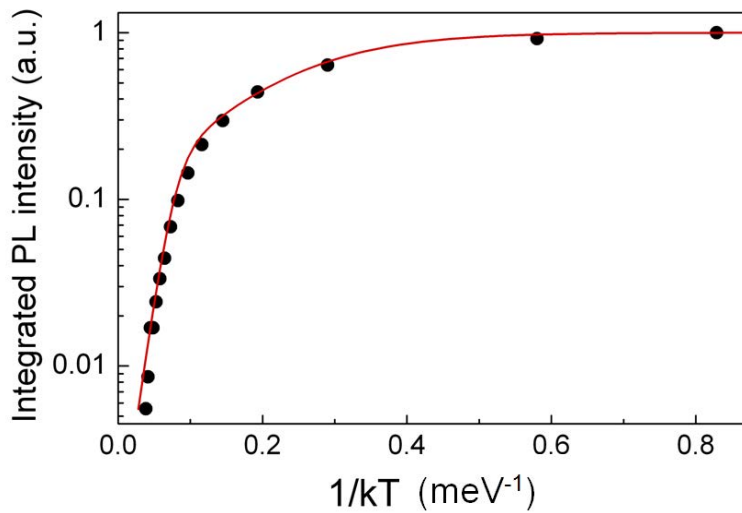


**Figure 5.3:** The Arrhenius plot of the integrated PL intensity of the whole emission band. Dots are the experimental points and the solid line is the corresponding fit.

To fit the experimental data the multi-channel Arrhenius equation was used [5.18]:

$$I = \frac{I_0}{1 + \sum_i c_i \exp(-E_i / k_b T)}$$

where index  $i$  represents the number of involved channels for carrier thermal escape,  $k_b$  is the Boltzmann constant,  $E_i$  is the thermal activation energy,  $I_0$  is the PL intensity at 0 K and  $c_i$  is a constant. The temperature dependence of integrated PL intensity can be perfectly fitted by considering two escape channels ( $i = 2$ ). The best fit was obtained using the following parameters:  $c_1 = 9$ ,  $E_1 = 10$  meV,  $c_2 = 1550$  and  $E_2 = 74$  meV. The smaller activation energy  $E_1$  can be attributed to the dissociation of the excitons trapped in the QWell followed by the nonradiative recombination of the carrier defects located in the QWell, as reported previously for the InAs(P)/InP QWells [5.19]. However, the high temperature activation energy ( $E_2$ ) is likely to be associated to the carrier thermionic emission through upper states of the QWell before escaping to the barrier material [5.20]. Our 20-fold reduction of the PL intensity is four times better than that obtained for InAsP/InP QWell monolithically grown on STO/Si substrates [5.21]. More details on the recombination processes in QWell-NWs will be presented in Chapter 8.

To improve our understanding of the optical properties, low temperature  $\mu$ PL experiments were conducted on single InP/InAs/InP QWell-NWs, transferred from Si (111) substrate onto a silicon host-substrate. Figure 5.4 shows  $\mu$ PL spectra of different single NWs on Si host-substrate and the PL spectrum of the NWs on the as-grown substrate. The peak observed at 1.1 eV in the  $\mu$ PL spectra is attributed to the silicon host-substrate. We assume that this peak is not observed in the PL spectra due to the high density of the NWs. The  $\mu$ PL spectra of the single NWs are complex: several peaks or groups of peaks are observed for each single NW. For instance, groups of peaks located around 0.88 eV, 0.92 eV, 0.98 eV and 1.05 eV are observed for NW2. The energies of these peaks are close to the energy positions of the PL peaks and shoulders associated to the monolayer (ML) fluctuations, and the one at 1.05 is also close to that observed in [5.12] and attributed to 3 ML InAs QWell. So each group of peaks can be associated with specific thickness of the radial QWell, as it is often concluded in literature [5.11 – 5.13].

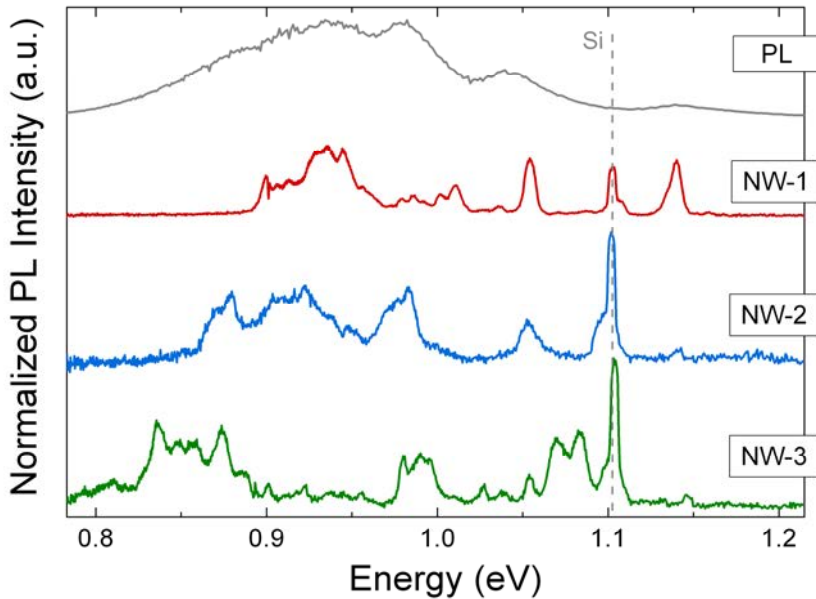


**Figure 5.4:** Low temperature  $\mu$ PL spectra of several NWs ( $P_{ex} = 150 \mu\text{W}$ ) compared to PL spectrum of the NWs on the as-grown Si (111) substrate.

This result is also confirmed by TEM studies. ML fluctuations of QWell thickness were observed comparing bottom and top parts of QWells and depending on the facets. The peaks within each group of peaks are attributed to the state filling as was already observed in core-shell NWs [5.7, 5.8].

### 5.3 Simulation of QWell-NWs.

To confirm the assumption about the peaks in PL spectra of the QWell-NWs the simulation of segments of QWell-NWs has been conducted. Here and elsewhere, simulation is performed with 3D nano device simulator “Nextnano<sup>3</sup>” [5.22]. The effective mass approximation model is used in the simulation process, taking into account strain, induced by substrate mismatch as well as effects of quantum confinement and piezoelectricity, unless otherwise is noted. Simulation of the electronic structure of WZ materials requires knowledge of many parameters such as lattice constants, effective masses, deformation potentials, and many others. Currently, not all the parameters of WZ InAs and InP are well known. For this reason our set of parameters contains values measured experimentally as well as those calculated theoretically or estimated from their ZB analogs. The elastic parameters were taken from [5.23] rather than from [5.24] in order to compare the results afterwards.

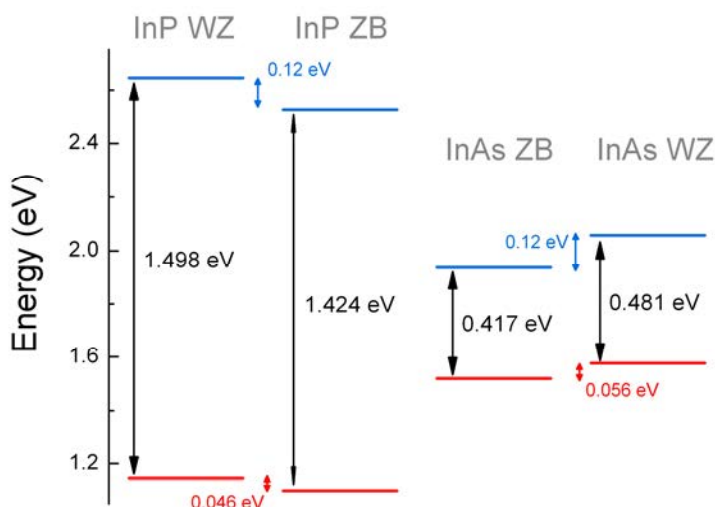


**Figure 5.5:** Band offset alignment for InAs and InP materials in ZB and WZ forms.

As far as the band offset between WZ InAs and WZ InP materials is concerned, the following method has been used: we started from the band offset between the InAs and InP material in the ZB phase as given by “Nextnano<sup>3</sup>” software and used few theoretical works investigating the band alignment between two polytypes of the same semiconductor material [5.25, 5.26]. Figure 5.5 shows the band offset alignment we have decided to use. In the case of WZ InP, we have assumed the band gap of 1.498 eV: we have observed a PL emission at 1.493

eV and we have added an estimated 5 meV exciton binding energy. The values of the band offset are estimated from [5.27]. In case of WZ InAs, we use the value of 0.481 eV obtained theoretically in [5.25, 5.26]. The values of InAs band offsets were estimated using [5.26]. The set of parameters used in this work is listed in section 5.7 of the present Chapter.

Now we proceed to a study of the quantum confinement effect and its role in the obtained experimental results. First we aim to demonstrate the effect of quantum confinement in radial QWell-NWs and how the emission energy depends on the QWell thickness. Figure 5.6 illustrates our assumption of correspondence of different PL emission peaks to different thicknesses of radial QWell. Taking into account PL results on both Si(001) and Si(111) substrates, we may obtain values of emission energy attributed to each number of MLs, though the integer constant  $n$  is not certain. Peak attributed to  $(n + 1)$  MLs is not present in these spectra, but was observed on other samples.

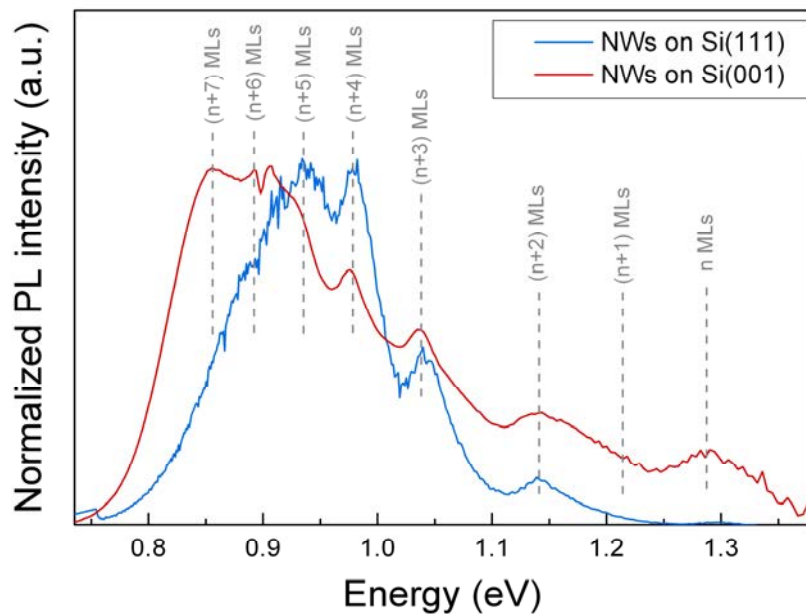


**Figure 5.6:** Low temperature PL spectra of QWell-NWs on Si(001) and Si(111) substrates. Dashed lines show the assumed positions of emission energy from segments with different thickness.

To check this assumption we simulate a planar WZ InAs/InP QWell (Figure 5.7). Changing the thickness of the QWell we may obtain the ground state energy in InAs QWell as a function of the QWell thickness.

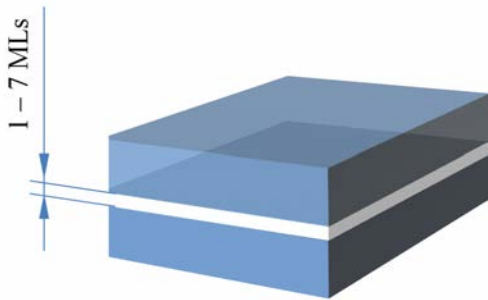


**Figure 5.7:** Scheme of the simulated WZ InAs/InP QWell.

To compare the simulation results with experimental points we need to calculate the size of one ML of WZ InAs. Since it is not certain to which crystallographic plane corresponds to the QWell facets, the ML thickness may be calculated for a ML either on m-plane or on a-plane:

$$ML^{(m\text{-plane})} = \sqrt{3} \cdot a_{WZ\ InAs} / 2 = 0.38 \text{ nm}$$

$$ML^{(a\text{-plane})} = a_{WZ\ InAs} / 2 = 0.214 \text{ nm}$$

To resolve this dilemma curves for both cases are shown in Figure 5.8 together with the positions of the peaks and shoulders extracted from experimental PL spectra (see Figure 5.6). It is also assumed that the peak at the highest energy ( $\approx 1.29$  eV) corresponds to emission from a radial QWell of 1 MLs (i.e.  $n = 1$ ), as it is sometimes assumed in literature [5.12].

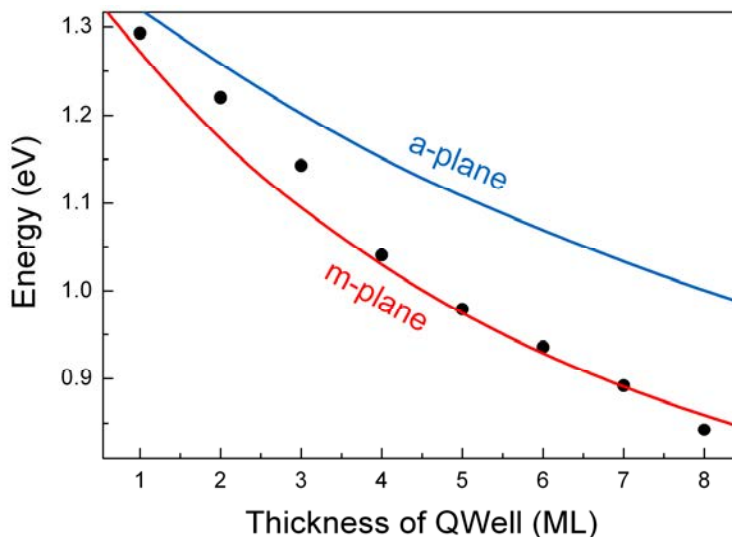


**Figure 5.8:** Peak positions in PL emission spectra of QWell-NWs as a function of assumed thickness of radial QWell. Dots represent experimental points and solid curve shows simulation result for a planar QWell.

The curve from m-plane is in relatively good agreement with the experimental points, and shows very similar behavior as a function of QWell thickness. Small difference may be explained by uncertainty in constants of WZ materials, which are not well known yet. Therefore, the assumption of different thickness of the radial QWell is justified by the theoretical simulation.

## 5.4 Spectroscopy of QRod-NWs.

We proceed to the investigation of the optical properties of QRod-NWs. PL emission of the QRod-NWs on the as-grown was studied as a function of the temperature from spectra 14 K to 300 K by M. H. H. Alouane [5.15] (Figure 5.9) using a 514 nm laser for the excitation. A single broad peak of PL emission is observed at 0.87 eV at low temperature. In contrast to QWell-NWs, in the absence of a radial QWell no multiple peaks are observed, and all the emission is attributed to the InAs QRod, confirming success in growth of QRod-NWs without parasitic radial QWell structures. The PL emission peak is shifting toward lower energy, as temperature is increased, reaching 0.8 eV (1.55  $\mu\text{m}$ ) at room temperature with the intensity of PL emission as much as 30% of its value at 14 K. This result is relatively close to the best values (50 – 67 %) reported for ZB InAs QDs or quantum dashes grown in a InP matrix [5.28, 5.29]. Such strong maintenance of the luminescence intensity has not been reported for III-V NW heterostructures grown on Si substrates yet.

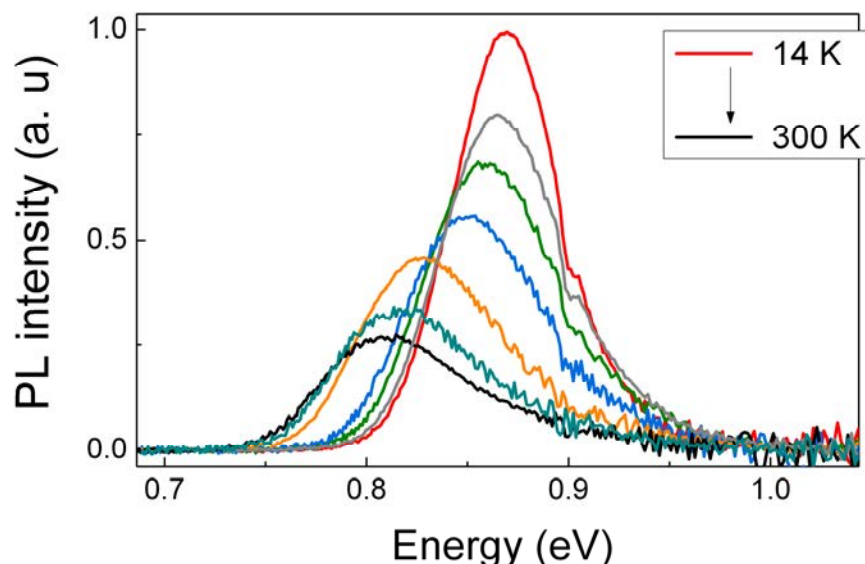


**Figure 5.9:** Changes in the PL spectrum of the QRod-NWs on as-grown substrate with temperature.

To confirm the good optical properties of this sample, time-resolved measurements have been performed at room temperature. Figure 5.10 shows the decay of the ground state emission at low excitation power (5  $\mu\text{W}$ ). The as-grown sample was used for this measurement, so approximately

50 – 200 NWs were excited by the pulsed laser. Analysis of the monoexponential decay curve gives a time constant of 7.5 ns.

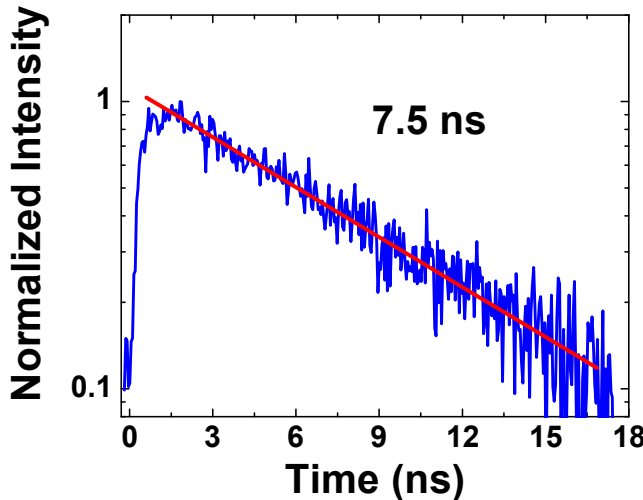


**Figure 5.10:** Lifetime decay curve for the ground state, measured at room temperature.

The measured decay time consists of the radiative and non-radiative recombination rates. To separate these two contributions, we use a standard approach assuming that the recombination is purely radiative at low temperature. Thus, we can write:

$$\frac{1}{\tau(T)} = \frac{1}{\tau_{\text{rad}}(T)} + \frac{1}{\tau_{\text{nrad}}(T)}$$

$$I(T) = I_0 \frac{\tau(T)}{\tau_{\text{rad}}(T)}$$

From Figure 5.9, using the measured lifetime ( $\tau$ ) we can calculate the room temperature radiative lifetime:

$$\tau_{\text{rad}}(\text{RT}) = I_0 \frac{\tau(\text{RT})}{I(\text{RT})} \approx 22 \text{ ns}$$

and the nonradiative lifetime:

$$\tau_{\text{nrad}}(\text{RT}) = \left( \frac{1}{\tau(\text{RT})} - \frac{1}{\tau_{\text{rad}}(\text{RT})} \right)^{-1} \approx 11 \text{ ns}$$

These long lifetimes at room temperature confirm the quality of the heterostructure.

To study the emission of QRod-NWs in more details the experiments on single NWs transferred on a host-substrate were conducted using the  $\mu$ PL setup. Figure 5.11 shows the room temperature  $\mu$ PL spectra of a single InAs/InP QRod-NW for various values of excitation power.

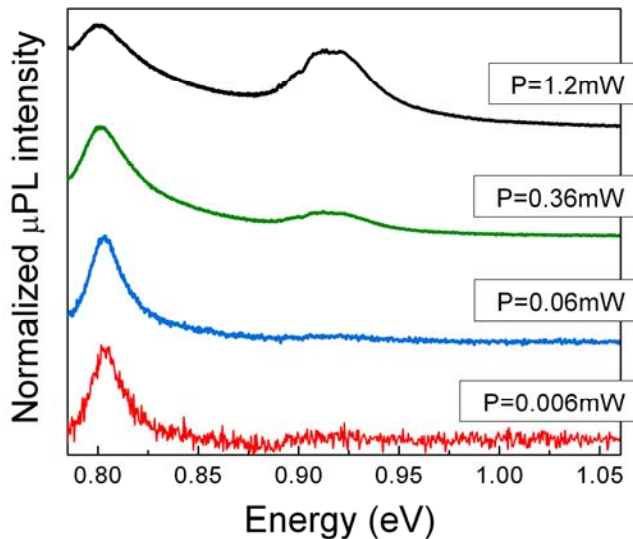


**Figure 5.11:** Room temperature  $\mu$ PL spectra of a single QRod-NW for various values of excitation power.

At low excitation power, a single peak is observed at 0.81 eV with a FWHM of 18 meV. Several QRod-NWs are studied and FWHM in the 17 – 22 meV range were measured. These values are close to those observed for single InAs QDots grown on GaAs substrates studied at room temperature (7 – 17 meV) [5.30]. When the excitation power is increased, a second peak arises at 0.92 eV. To understand the origin of these two peaks, we should consider the band structure of WZ material where the p-like valence band splits up into three bands labeled A, B and C, where A-band is the lowest energy state (see Chapter 1 for more details). Thereby, the peak at 0.81 eV appears to be the result of the recombination of electrons with holes in the A-band and the high energy peak may be attributed to a recombination between electrons in the ground state and holes in the B-band. Measurements performed on several QRods indicate a splitting in the 66 – 120 meV range. This assumption is in agreement with a theoretical calculation of the energy splitting between A and B-bands ( $\Delta E$ ) in bulk WZ InAs [5.25],

$$\Delta E = E(\Gamma_{7v}^1) - E(\Gamma_{9v}) = \frac{\Delta_{so} + \Delta_{cr}}{2} - \frac{\sqrt{(\Delta_{so} + \Delta_{cr})^2 - u^{-1}\Delta_{so}\Delta_{cr}}}{2}$$

where  $u$  is related to the lattice constants by  $u = (a / c)^2$  and takes the value of  $3/8$  for an ideal WZ structure as assumed here. Using values of  $\Delta_{so} = 0.379$  eV and  $\Delta_{cr} = 0.195$  eV calculated in [5.25], this calculation gives a value of  $\Delta E = 105$  meV. More recently, different values ( $\Delta_{so} = 0.356$  eV and  $\Delta_{cr} = 0.095$  eV) have been reported in [5.26], which gives the value of  $\Delta E = 57$  meV. The difference between experimental value of  $\Delta E$  and those calculated from the Eq. 5.1 is not surprising, taking into account the quantum confinement regime and the fact that the InAs QRods are strained in the NWs due to the lattice mismatch between InAs and InP.

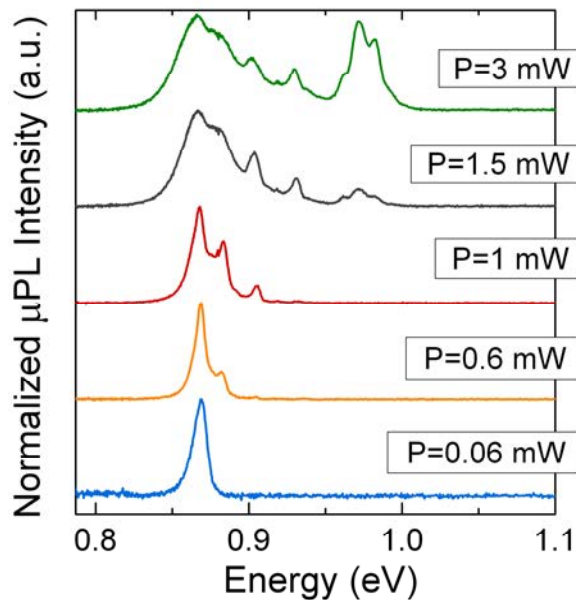
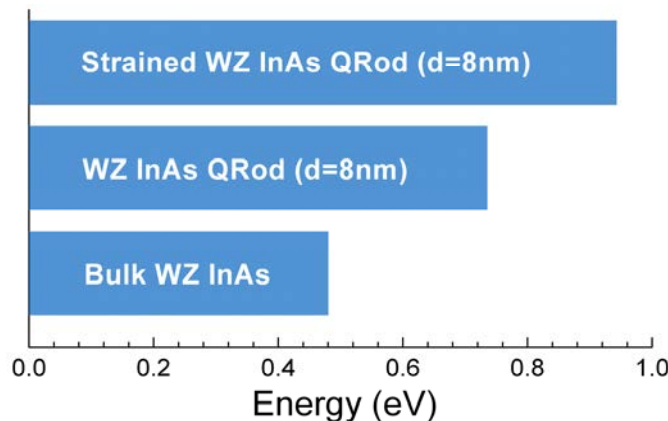


**Figure 5.12:** Low temperature  $\mu$ PL spectra of a single QRod-NW for various values of excitation power.

To demonstrate the energy level structure of the QRod we present the low temperature measurements on single QRod-NWs. Figure 5.12 shows low temperature  $\mu$ PL spectra of a single QRod-NW for various values of excitation power. A single peak of the ground state at 0.87 eV is observed at low excitation power. As the excitation power is increased the appearance of excited states is observed. At high excitation power the spectrum also demonstrates the emission of B-band at 0.96 eV, which, as well as A-band, consists of multiple peaks corresponding to different excited states. FWHM of the ground state peak at low temperature was measured on different NWs in 4 – 17 meV range. These values are clearly larger than those typically reported for QDot-NWs [5.1, 5.4]. Detailed investigation of the origin of this broadening and its excitation power dependence will be presented in Chapter 7.

## 5.5 Simulation of QRod-NWs.

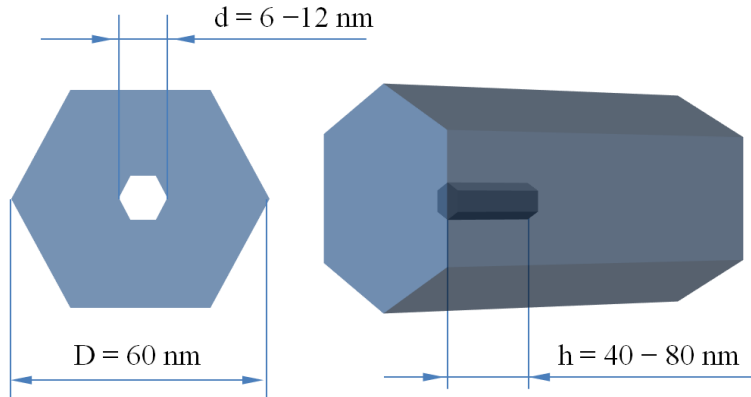
In order to understand the emission of these QRod-NWs we simulate these heterostructures for different values of length and diameters. To begin, we will consider the emission energy of WZ InAs material. The band gap of WZ InAs is known to be approximately 0.481 eV at low temperature [5.25, 5.26]. Despite this fact, PL experiments demonstrated PL emission energy higher than 0.85 eV at 14 K for both QWell-NWs and QRod-NWs. To explain this difference we consider the impacts of various factors on the emission energy.



**Figure 5.13:** Calculated energy of the ground state in three cases: bulk WZ InAs material, unstrained WZ InAs QRod of 8 nm diameter and the same QRod under the strain caused by lattice mismatch with WZ InP.

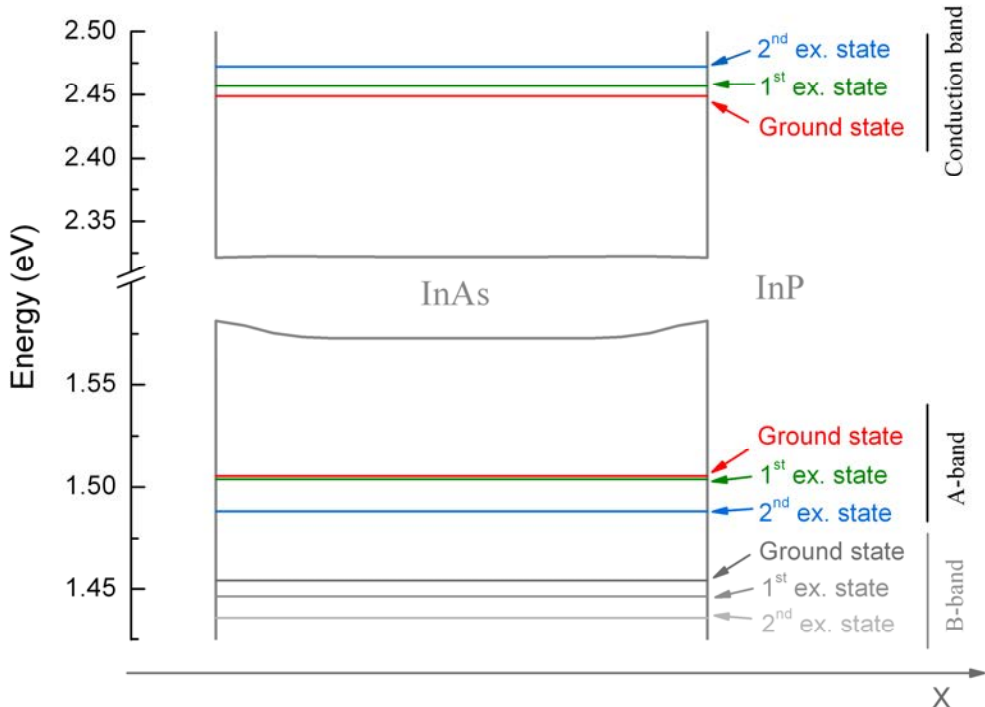
Figure 5.13 shows calculated energies of the ground state in three cases: bulk WZ InAs material, unstrained WZ InAs QRod of 8 nm in diameter and the same QRod under the strain caused by lattice mismatch with WZ InP. It is shown that the effect of quantum confinement may significantly increase the energy of the ground state. However, it is not enough for an 8 nm diameter InAs WZ QRod to reach energies higher than 0.85 eV. It was shown in Chapter 4, that strain applied to a semiconductor material may affect the ground state energy causing the shift of emission energy. In case of InAs/InP heterostructures we are concerned with a material pair of large lattice mismatch which is known to cause the strain fields in this kind of NW heterostructures [5.23]. As a consequence, this strain leads to increase of the emission energy, that may reach 0.88 eV in case of WZ InAs QRod of 8 nm in diameter embedded in WZ InP NW. We will return to the detailed study of the strain and stain-induced piezoelectricity in Chapter 7. Next, we study the quantum states in WZ InAs QRod embedded in WZ InP NW of the diameter

significantly larger than that of QRod (Figure 5.14). For the sake of simplicity, piezoelectric effects are not included in the calculation and will be considered in Chapter 7.



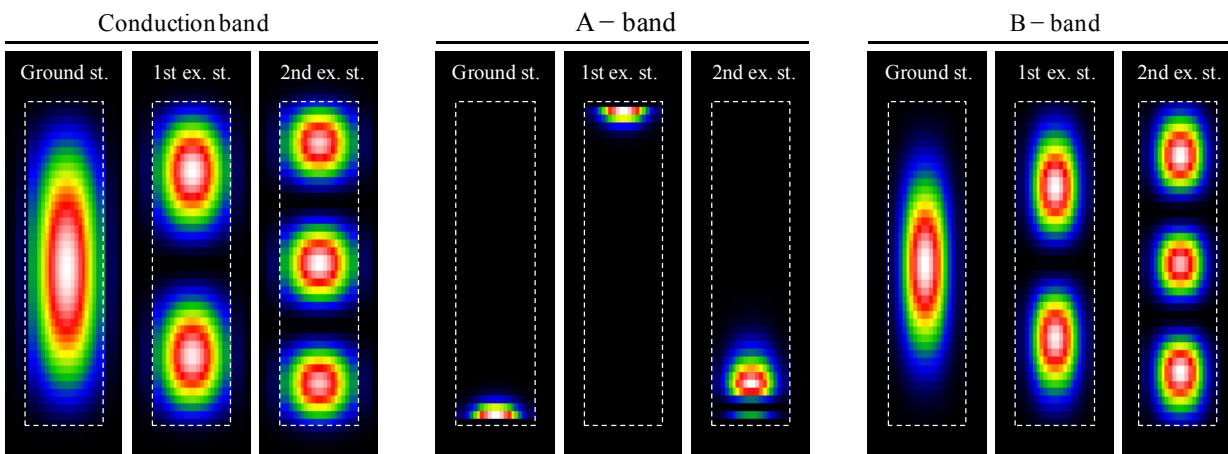
**Figure 5.14:** Scheme of the simulated QRod-NW.

In the present calculation only first conduction band and first two valence bands (A and B bands) are considered. Three energy levels are calculated for each band. We begin with the simulation of an 8 nm diameter WZ InAs QRod with a 40 nm length embedded in a WZ InP NW. The obtained band structure and energy values of the excited states are shown in Figure 5.15.



**Figure 5.15:** Simulated energy level structure of QRod-NWs.

It is important to note that InAs QRod is strained by the lattice mismatch and this strain affects the wavefunctions of the carriers. This strain impact is illustrated in Figure 5.16, where probability distribution of the carriers at each energy level are shown in vertical slices of the QRod. Carriers of conduction and B bands demonstrate the classical probability distributions, while the heavy holes (A-band), in contrast to unstrained QRod, are localized at the boundaries of the QRod. This localization results in a strong decrease of the electron - heavy hole recombination rate.



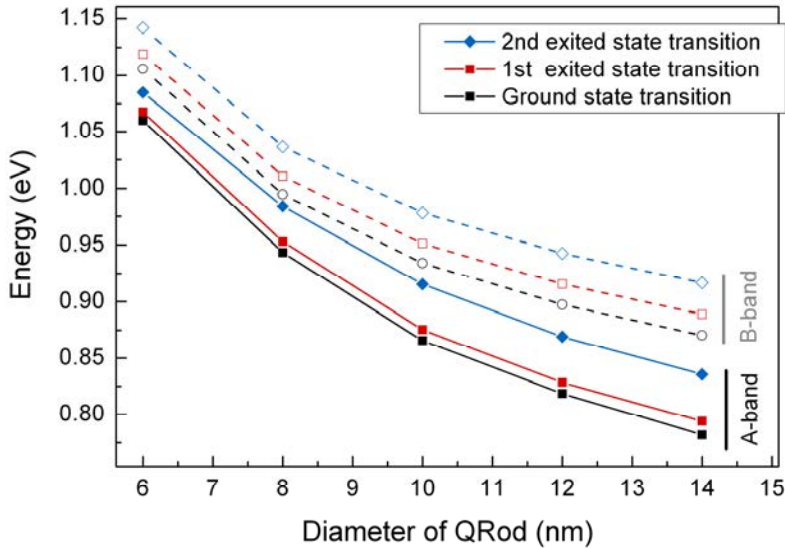
**Figure 5.16:** Probability distribution of carriers in different states at different bands for a strained InAs QRod ( $d = 8 \text{ nm}$ ,  $l = 40 \text{ nm}$ ) in an InP NW. Figure shows cross sections of the QRod (dashed line) in XZ plane.

Table 5.1 shows spatial overlap matrix elements for carriers in different. The B-band recombination takes place mainly in symmetrical levels (i.e. ground state to ground state, first excited state to first and so on), while probability of non-symmetrical transitions are either zero or very small (dark states). In the case of the A-band all the spatial overlap matrix elements are relatively small due to the carrier localization. Therefore, in the case of the A-band, it is highly uncertain, which transitions are responsible for the peaks in the PL spectra. However, for the sake of simplicity, in the following calculation the symmetrical transitions (i.e. ground state to ground state, first excited state to first and so on) will be used as if they were most probable.

**Table 5.1:** Spatial overlap matrix elements for carriers in different states.  $\Psi_{vb1}$ ,  $\Psi_{vb3}$  and  $\Psi_{vb3}$  are wavefunctions of ground, first and second excited states, respectively.

A-band	B-band
$ \langle \Psi_{vb\text{ gs}}   \Psi_{cb\text{ gs}} \rangle ^2 = 0.018$	$ \langle \Psi_{vb\text{ gs}}   \Psi_{cb\text{ gs}} \rangle ^2 = 0.830$
$ \langle \Psi_{vb\text{ gs}}   \Psi_{cb\text{ 1}} \rangle ^2 = 0.053$	$ \langle \Psi_{vb\text{ gs}}   \Psi_{cb\text{ 1}} \rangle ^2 = 0.000$
$ \langle \Psi_{vb\text{ gs}}   \Psi_{cb\text{ 2}} \rangle ^2 = 0.089$	$ \langle \Psi_{vb\text{ gs}}   \Psi_{cb\text{ 2}} \rangle ^2 = 0.022$
$ \langle \Psi_{vb\text{ 1}}   \Psi_{cb\text{ gs}} \rangle ^2 = 0.017$	$ \langle \Psi_{vb\text{ 1}}   \Psi_{cb\text{ gs}} \rangle ^2 = 0.000$
$ \langle \Psi_{vb\text{ 1}}   \Psi_{cb\text{ 1}} \rangle ^2 = 0.055$	$ \langle \Psi_{vb\text{ 1}}   \Psi_{cb\text{ 1}} \rangle ^2 = 0.833$
$ \langle \Psi_{vb\text{ 1}}   \Psi_{cb\text{ 2}} \rangle ^2 = 0.092$	$ \langle \Psi_{vb\text{ 1}}   \Psi_{cb\text{ 2}} \rangle ^2 = 0.000$
$ \langle \Psi_{vb\text{ 2}}   \Psi_{cb\text{ gs}} \rangle ^2 = 0.156$	$ \langle \Psi_{vb\text{ 2}}   \Psi_{cb\text{ gs}} \rangle ^2 = 0.023$
$ \langle \Psi_{vb\text{ 2}}   \Psi_{cb\text{ 1}} \rangle ^2 = 0.261$	$ \langle \Psi_{vb\text{ 2}}   \Psi_{cb\text{ 1}} \rangle ^2 = 0.000$
$ \langle \Psi_{vb\text{ 2}}   \Psi_{cb\text{ 2}} \rangle ^2 = 0.148$	$ \langle \Psi_{vb\text{ 2}}   \Psi_{cb\text{ 2}} \rangle ^2 = 0.809$

First we keep the length of the QRod constant (40 nm) and vary the diameter. Figure 5.17 shows the simulation results for the energies difference between excited states in conduction and valence bands (i.e. expected emission energies).



**Figure 5.17:** Energy difference between excited states in conduction and valence bands as a function of QRod diameter.

It is shown that the diameter of QRods plays an important role controlling quantum confinement and as a consequence increasing energy of the ground state transition in QRods of smaller diameter. Taking into account that the diameter of QRods in our NWs was measured in

the 8 – 11 nm range, the emission energy higher than 0.8 eV is in agreement with the simulation results. Moreover, the energy difference between ground states of A and B bands is shown to be diameter dependent and takes values in the 45 – 90 meV range for 6 – 14 nm diameter, which is in agreement with experimentally observed range of 66 – 120 meV.

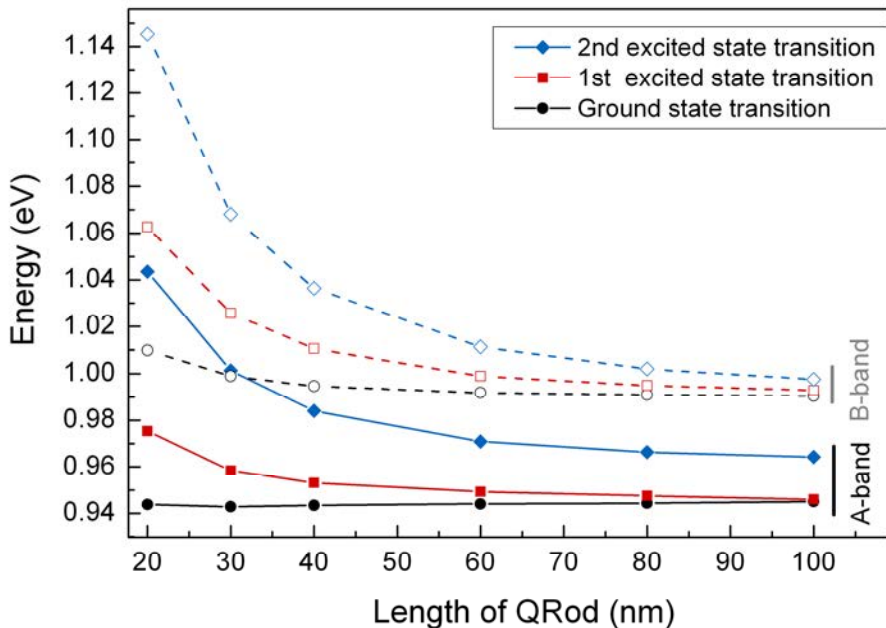


**Figure 5.18:** Energy difference between excited states in conduction and valence bands as a function of QRod length.

On the other hand, difference between the emission energies of different excited states does not change a lot with diameter. The difference between the peaks of different energy levels was found in 14 – 18 meV range for A-band and 9 – 11 meV for B-band (Figure 5.12). To compare this experimental data with simulation results, the impact of the QRod length on the electronical states is investigated (Figure 5.18). It is shown that the difference between the emission energies of the different levels strongly depends on the length of the QRod and may vary in the 4 – 30 meV range for A-band and in the 2 – 23 meV range for B-band.

## 5.7 Conclusions.

Summarizing, the optical properties of NW heterostructures have been studied by means of PL spectroscopy and theoretical simulation using the effective mass approximation. It was shown that QWell-NWs demonstrate the PL emission in the 0.8 – 1.3 eV range. The PL spectra contain multiple peaks, each of which may be attributed to a specific number of MLs of the radial QWell thickness.  $\mu$ PL spectra show groups of peaks which can be associated with the peaks and shoulders in the PL spectra. Simulation of planar QWells of various thicknesses shows that the theoretical dependence of the QWell emission energy is in agreement with that obtained experimentally.

As far as the QRod-NW heterostructures are concerned, it was demonstrated that intensity of room temperature PL emission remains as high as 30% of its value at 14 K.  $\mu$ PL measurements revealed presence of two peaks which were attributed to A and B-bands, in agreement with band splitting calculation. Low temperature spectra demonstrated peaks of excited states at each band. It was theoretically demonstrated that the energy difference between the excited states depends on the length of the QRod and is in agreement with the range of values obtained by simulation of the QRods. On the other hand, the diameter of QRods, was demonstrated to be the main factor controlling the emission energy. The values of emission energy for the ground state of simulated QRods were found to be in agreement with those measured experimentally. Finally, both QWell-NWs and QRod-NWs are able to reach the emission wavelength of 1.3 and 1.55  $\mu$ m which is particularly interesting for the fabrication of emitters in the telecommunication band.

## 5.7 Table of constants for InP and InAs of wurtzite type.

WZ InP	WZ InAs
<b>Lattice parameters [5.24]</b> a = 0.415 nm c = 0.6777 nm	<b>Lattice parameters [5.24]</b> a = 0.4284 nm c = 0.6996 nm
<b>Dielectric constant</b> $\epsilon_0 = 12.61$ (ZB)	<b>Dielectric constant</b> $\epsilon_0 = 15.15$ (ZB)
<b>CB Deformations potentials</b> For ZB InP [5.31]: $a_c = -6.0$ eV $a_v = -0.6$ eV We assume that the hydrostatic deformation is the same for the WZ material: $a_1 = -6.6$ eV $a_2 = -6.6$ eV	<b>CB Deformations potentials</b> For ZB InAs [5.31]: $a_c = -5.1$ eV $a_v = -1.0$ eV We assume that the hydrostatic deformation is the same for the WZ material: $a_1 = -6.1$ eV $a_2 = -6.1$ eV
<b>VB Deformations potentials</b> For ZB InP [5.31]: $a_v = -0.6$ eV $b = -0.2$ eV $d = -5.0$ eV and according to [5.32] $\delta_1 = -a_v = 0.6$ eV $\delta_2 = -b/2 = 0.1$ eV $\delta_3 = -d/3.46 = 1.445$ eV	<b>VB Deformations potentials</b> For ZB InAs [5.31]: $a_v = -1.0$ eV $b = -1.8$ eV $d = -3.6$ eV and according to [5.32] $\delta_1 = -a_v = 1$ eV $\delta_2 = -b/2 = 0.9$ eV $\delta_3 = -d/3.46 = 1.04$ eV
$D_1 = -\delta_1 - 4 \delta_3 = -6.38$ $D_2 = -\delta_1 + 2 \delta_3 = 2.29$ $D_3 = 6 \delta_3 = 8.67$ $D_4 = -3 \delta_3 = -4.335$ $D_5 = -\delta_2 - 2 \delta_3 = -3.49$ $D_6 = -1.414(2\delta_2 + \delta_3) = -2.33$	$D_1 = -\delta_1 - 4 \delta_3 = -5.16$ $D_2 = -\delta_1 + 2 \delta_3 = 1.08$ $D_3 = 6\delta_3 = 6.24$ $D_4 = -3\delta_3 = -3.12$ $D_5 = -\delta_2 - 2 \delta_3 = -2.98$ $D_6 = -1.414(2\delta_2 + \delta_3) = -4.016$

**Energy splitting**

$$\Delta_1 = \Delta_{\text{cr}} = 0.144 \text{ eV}$$

$$\Delta_2 = \Delta_3 = \Delta_{\text{so}}/3 = 0.026 \text{ eV}$$

**Energy splitting**

$$\Delta_1 = \Delta_{\text{cr}} = 0.195 \text{ eV}$$

$$\Delta_2 = \Delta_3 = \Delta_{\text{so}}/3 = 0.126 \text{ eV}$$

**Effective masses [5.25]**

$$m_e^\perp = 0.088$$

$$m_e^\parallel = 0.105$$

$$m_{hh}^\perp = 0.127$$

$$m_{hh}^\parallel = 1.58$$

$$m_{lh}^\perp = 0.836$$

$$m_{lh}^\parallel = 0.169$$

$$m_{cf}^\perp = 1.205$$

$$m_{cf}^\parallel = 0.097$$

**Effective masses [5.25]**

$$m_e^\perp = 0.042$$

$$m_e^\parallel = 0.060$$

$$m_{hh}^\perp = 0.084$$

$$m_{hh}^\parallel = 1.7$$

$$m_{lh}^\perp = 0.113$$

$$m_{lh}^\parallel = 0.101$$

$$m_{cf}^\perp = 0.319$$

$$m_{cf}^\parallel = 0.115$$

**Elastic parameters [5.23]**

$$C_{11} = 131.1 \text{ GPa}$$

$$C_{12} = 51.3 \text{ GPa}$$

$$C_{13} = 38.6 \text{ GPa}$$

$$C_{33} = 143.8 \text{ GPa}$$

$$C_{44} = 27.1 \text{ GPa}$$

**Elastic parameters [5.23]**

$$C_{11} = 110.3 \text{ GPa}$$

$$C_{12} = 42.8 \text{ GPa}$$

$$C_{13} = 32.1 \text{ GPa}$$

$$C_{33} = 120.8 \text{ GPa}$$

$$C_{44} = 27.3 \text{ GPa}$$

## 5.8 References.

- [5.1] N. Panev, A. I. Persson, N. Skold, and L. Samuelson, "Sharp exciton emission from single InAs quantum dots in GaAs nanowires", *Applied Physics Letters*, vol. 83, p. 2238, 2003.
- [5.2] M. H. M. van Weert, N. Akopian, F. Kelkensberg, U. Perinetti, M. P. van Kouwen, J. G. Rivas, M. T. Borgström, R. E. Algra, M. a Verheijen, E. P. a M. Bakkers, L. P. Kouwenhoven, and V. Zwiller, "Orientation-dependent optical-polarization properties of single quantum dots in nanowires", *Small*, vol. 5, p. 2134, 2009.
- [5.3] E. D. Minot, F. Kelkensberg, M. van Kouwen, J. A. van Dam, L. P. Kouwenhoven, V. Zwiller, M. T. Borgström, O. Wunnicke, M. A. Verheijen, and E. P. a M. Bakkers, "Single quantum dot nanowire LEDs", *Nano letters*, vol. 7, p. 367, 2007.
- [5.4] M. Tchernycheva, G. E. Cirlin, G. Patriarche, L. Travers, V. Zwiller, U. Perinetti, and J.-C. Harmand, "Growth and characterization of InP nanowires with InAsP insertions", *Nano letters*, vol. 7, p. 1500, 2007.
- [5.5] A. Sitt, A. Salant, G. Menagen, and U. Banin, "Highly emissive nano rod-in-rod heterostructures with strong linear polarization", *Nano letters*, vol. 11, p. 2054, 2011.
- [5.6] M. T. Borgström, V. Zwiller, E. Müller, and A. Imamoglu, "Optically bright quantum dots in single Nanowires", *Nano letters*, vol. 5, p. 1439, 2005.
- [5.7] Z. Zanolli, B. A Wacaser, M.-E. Pistol, K. Deppert, and L. Samuelson, "Core-shell InP-CdS nanowires: fabrication and study", *Journal of physics: Condensed matter*, vol. 19, p. 295218, 2007.
- [5.8] Z. Zanolli, M.-E. Pistol, L. E. Fröberg, and L. Samuelson, "Quantum-confinement effects in InAs-InP core-shell nanowires", *Journal of physics: Condensed matter*, vol. 19, p. 295219, 2007.
- [5.9] L. V. Titova, T. B. Hoang, H. E. Jackson, L. M. Smith, J. M. Yarrison-Rice, Y. Kim, H. J. Joyce, H. H. Tan, and C. Jagadish, "Temperature dependence of photoluminescence from single core-shell GaAs-AlGaAs nanowires", *Applied Physics Letters*, vol. 89, p. 173126, 2006.
- [5.10] G. Jacopin, L. Rigutti, S. Bellei, P. Lavenus, F. H. Julien, a V Davydov, D. Tsvetkov, K. A. Bertness, N. a Sanford, J. B. Schlager, and M. Tchernycheva, "Photoluminescence polarization in strained GaN/AlGaN core/shell nanowires", *Nanotechnology*, vol. 23, p. 325701, 2012.
- [5.11] Y. Masumoto, Y. Hirata, P. Mohan, J. Motohisa, and T. Fukui, "Polarized photoluminescence from single wurtzite InP/InAs/InP core-multishell nanowires", *Applied Physics Letters*, vol. 98, p. 211902, 2011.
- [5.12] B. Pal, K. Goto, M. Ikezawa, Y. Masumoto, P. Mohan, J. Motohisa, and T. Fukui, "Type-II behavior in wurtzite InP/InAs/InP core-multishell nanowires", *Applied Physics Letters*, vol. 93, p. 073105, 2008.

- [5.13] P. Mohan, J. Motohisa, and T. Fukui, "Fabrication of InP/InAs/InP core-multishell heterostructure nanowires by selective area metalorganic vapor phase epitaxy", *Applied Physics Letters*, vol. 88, p. 133105, 2006.
- [5.14] H. Khmissi, K. Naji, M. H. Hadj Alouane, N. Chauvin, C. Bru-Chevallier, B. Ilahi, G. Patriarche, and M. Gendry, "InAs/InP nanowires grown by catalyst assisted molecular beam epitaxy on silicon substrates", *Journal of Crystal Growth*, vol. 344, p. 45, 2012.
- [5.15] M. H. H. Alouane "Caracterisation optique de boites quantiques inserees dans des nanofils III-V sur silicium", INSA Lyon, 2013.
- [5.16] H. Folliot, S. Loualiche, B. Lambert, V. Drouot, and a. Le Corre, "Effects of interface-layers composition and strain distribution on the optical transitions of InAs quantum dots on InP", *Physical Review B*, vol. 58, p. 10700, 1998.
- [5.17] R. Leonelli, C. Tran, J. Brebner, J. Graham, R. Tabti, R. Masut, and S. Charbonneau, "Optical and structural properties of metalorganic-vapor-phase-epitaxy-grown InAs quantum wells and quantum dots in InP", *Physical review. B, Condensed matter*, vol. 48, p. 11135, 1993.
- [5.18] D. P. Popescu, P. G. Eliseev, A. Stintz, and K. J. Malloy, "Temperature dependence of the photoluminescence emission from InAs quantum dots in a strained Ga 0.85 In 0.15 As quantum well", *Semiconductor Science and Technology*, vol. 19, p. 33, 2004.
- [5.19] H. P. Lei, H. Z. Wu, Y. F. Lao, M. Qi, A. Z. Li, and W. Z. Shen, "Difference of luminescent properties between strained InAsP/InP and strain-compensated InAsP/InGaAsP MQWs", *Journal of Crystal Growth*, vol. 256, p. 96, 2003.
- [5.20] B. Ilahi, L. Sfaxi, and H. Maaref, "Optical investigation of InGaAs-capped InAs quantum dots: Impact of the strain-driven phase separation and dependence upon post-growth thermal treatment", *Luminescence*, vol. 27, p. 741, 2007.
- [5.21] B. Gobaut, J. Penuelas, J. Cheng, a. Chettaoui, L. Largeau, G. Hollinger, and G. Saint-Girons, "Direct growth of InAsP/InP quantum well heterostructures on Si using crystalline SrTiO<sub>3</sub>/Si templates", *Applied Physics Letters*, vol. 97, p. 201908, 2010.
- [5.22] "Nextnano.de", 2013. [Online]. Available: <http://www.nextnano.de/nextnano3/index.htm>. [Accessed: 20-Jun-2013].
- [5.23] F. Boxberg, N. Søndergaard, and H. Q. Xu, "Elastic and piezoelectric properties of zincblende and wurtzite crystalline nanowire heterostructures", *Advanced materials*, vol. 24, p. 4692, 2012.
- [5.24] M. W. Larsson, J. B. Wagner, M. Wallin, P. Håkansson, L. E. Fröberg, L. Samuelson, and L. R. Wallenberg, "Strain mapping in free-standing heterostructured wurtzite InAs/InP nanowires", *Nanotechnology*, vol. 18, p. 015504, 2007.
- [5.25] A. De and C. E. Pryor, "Predicted band structures of III-V semiconductors in the wurtzite phase", *Physical Review B*, vol. 81, p. 155210, 2010.

- [5.26] A. Belabbes, C. Panse, J. Furthmüller, and F. Bechstedt, "Electronic bands of III-V semiconductor polytypes and their alignment", *Physical Review B*, vol. 86, p. 075208, 2012.
- [5.27] M. Murayama and T. Nakayama, "Chemical trend of band offsets at wurtzite/zinc-blende heterocrystalline semiconductor interfaces", *Physical Review B*, vol. 49, p. 4710, 1994.
- [5.28] R. Hostein, A. Michon, G. Beaudoin, N. Gogneau, G. Patriache, J.-Y. Marzin, I. Robert-Philip, I. Sagnes, and A. Beveratos, "Time-resolved characterization of InAsP/InP quantum dots emitting in the C-band telecommunication window", *Applied Physics Letters*, vol. 93, p. 073106, 2008.
- [5.29] B. Salem, T. Benyattou, G. Guillot, C. Bru-Chevallier, G. Bremond, C. Monat, G. Hollinger, and M. Gendry, "Strong carrier confinement and evidence for excited states in self-assembled InAs quantum islands grown on InP(001)", *Physical Review B*, vol. 66, p. 193305, 2002.
- [5.30] K. Matsuda, K. Ikeda, and T. Saiki, "Homogeneous linewidth broadening in a In(0.5)Ga(0.5)As/GaAs single quantum dot at room temperature investigated using a highly sensitive near-field scanning optical microscope", *Physical Review B*, vol. 63, p. 121304, 2001.
- [5.31] I. Vurgaftman, J. R. Meyer, and L. R. Ram-Mohan, "Band parameters for III–V compound semiconductors and their alloys", *Journal of Applied Physics*, vol. 89, p. 5815, 2001.
- [5.32] Y. M. Sirenko, J. Jeon, K. W. Kim, and M. A. Littlejohn, "Envelope-function formalism for valence bands in wurtzite quantum wells", *Physical Review B*, vol. 53, p. 53, 1997.

# **Chapter VI**

---

## Polarization properties of nanowires

- 6.1 Introduction.
- 6.2 State of the art.
- 6.3 Mechanisms responsible for polarization anisotropy.
- 6.4 Polarization properties of InP nanowires.
- 6.5 Polarization properties of QWell nanowires.
- 6.6 Polarization properties of single QRod nanowires.
- 6.7 Polarization anisotropy of nanowire ensembles.
- 6.8 Ensemble polarization model.
- 6.9 Wavelength and temperature dependences of polarization anisotropy.
- 6.10 Conclusions.
- 6.11 References.

## 6.1 Introduction.

Polarization anisotropy of both emission and absorption is one of the unique features of semiconductor NWs. In the present chapter, the mechanisms responsible for this polarization anisotropy will be considered theoretically and studied experimentally. We will begin the investigation with polarization properties of single InP NWs to understand the mechanisms responsible for the polarization of emission. Then we will continue with the polarization properties of NW heterostructures: InAs/InP QWell-NWs and QRod-NWs. We aim to demonstrate the factors that affect the degree of linear polarization (DLP) in case of both absorption and emission. Once the situation is clear for single NWs, we will try to demonstrate the polarization anisotropy of NW ensembles. For this purpose we will study polarization of QRod-NWs on as-grown substrates of different types (Si(001) and Si(111)) by means of PL spectroscopy. We aim to demonstrate that the polarization properties on single NWs and NW ensembles may be correlated via a proposed model, so that knowing all necessary parameters, the polarization anisotropy of NWs may be studied on NW ensembles. Similar idea has already been used in the works of A. Balocchi et al. [6.1] and Yu. I. Mazur et al. [6.2], where a population of vertically standing NWs and an ordered array of quantum dots were used for polarization measurements. This approach may provide certain convenience. As an example, we will show how excitation wavelength and temperature dependences of DLP can be measured on NW ensemble using the proposed method. The obtained results will be compared to the predictions of existing models so that the conclusions about the efficiency of this approach can be drawn. Since the possible fabrication of polarization sensitive devices based on NW ensembles (randomly oriented or not) has been demonstrated [6.2, 6.3], the knowledge of the polarization properties of NW ensembles may have a potential application.

## 6.2 State of the art.

Polarization properties of semiconductor NWs, have been studied experimentally in a number of works for many years. The polarization anisotropy is usually studied on a single NW, that is transferred onto a clean host-substrate and then the PL emission from the NW is analyzed with various angles of polarizer, which may be placed in front of the monochromator [6.4 – 6.7], laser [6.4, 6.5] or even both [6.8]. In particular, several works were published on polarization properties of InP NWs [6.7, 6.9 – 6.11]. As far as NW heterostructures are concerned, only few works were published on polarization anisotropy of core-shell (QWell) [6.5, 6.6, 6.12], quantum dot (QDot) [6.13, 6.14] and QRod [6.15] NWs.

The commonly used value reflecting the polarization anisotropy is the degree of linear polarization (DLP). DLP of emission (DLP<sup>e</sup>) is defined as

$$\text{DLP}^e = \frac{I_{||}^e - I_{\perp}^e}{I_{||}^e + I_{\perp}^e} \quad (6.1)$$

where  $I_{||}^e$  and  $I_{\perp}^e$  are the emission intensities (index “e”) with the polarization parallel and perpendicular to the NW growth axis. On the analogy with DLP of emission, DLP of absorption (index “a”) is defined as:

$$\text{DLP}^a = \frac{I_{||}^a - I_{\perp}^a}{I_{||}^a + I_{\perp}^a} \quad (6.2)$$

where  $I_{||}^a$  and  $I_{\perp}^a$  are the emission intensities measured when the excitation was parallel and perpendicular to the NW axis, respectively. It is assumed that the number of absorbed photons is proportional to the number of emitted photons, so measuring the PL emission of the sample we can calculate DLP of absorption.

The main results obtained on InP NWs are summarized in Table 6.1. In the literature ZB InP NWs were found to be strongly polarized parallel to NW axis, with DLP<sup>e</sup> in 0.7 – 0.92 range [6.7, 6.9, 6.10]. This anisotropy is generally attributed to dielectric confinement effect. On the other hand negative values of –0.42 and –0.49 of DLP<sup>e</sup> were observed on WZ InP NWs [6.7, 6.11] and were attributed to the selection rule of WZ material.

**Table 6.1:** DLP of absorption and emission measured on InP NWs.

<b>Work</b>	<b>Phase</b>	<b>Dimensions</b>	<b>Substrate</b>	$\lambda_{\text{ex}}$	<b>DLP<sup>a</sup></b>	<b>DLP<sup>e</sup></b>
[6.9]	ZB	D $\approx$ 10 - 15 nm	Quartz	488/514 nm	0.91	0.91
[6.10, 6.16]	ZB	D $\approx$ 30 nm, L $\approx$ 2 $\mu\text{m}$	SiO <sub>2</sub> on Si	457.9 nm	0.89	0.73
[6.10, 6.16]	ZB	D $\approx$ 30 nm, L $\approx$ 2 $\mu\text{m}$	Au on SiO <sub>2</sub>	457.9 nm	0.89	0.7
[6.7]	WZ	Tapered L $\approx$ 1 $\mu\text{m}$	Si	780 nm		-0.49
[6.7]	ZB	D $\approx$ 80 nm, L $\approx$ 2 - 7 $\mu\text{m}$	Si	780 nm		0.82
[6.11]	WZ	D $\approx$ 100 nm, L $\approx$ 4 $\mu\text{m}$	Au on Si	532 nm		-0.42

Furthermore, few studies of polarization anisotropy of InAs/InP NW heterostructures were reported (Table 6.2). Emission and absorption of QDot (or axial QWell) NWs were found to be highly polarized parallel to the NW axis, while DLP of type II PL emission from radial QWell-NWs was negative.

**Table 6.2:** DLP of absorption and emission measured on InAs/InP NW heterostructures.

<b>Work</b>	<b>Phase</b>	<b>Type and dimensions</b>	<b>Substrate</b>	$\lambda_{\text{ex}}$	<b>DLP<sup>a</sup></b>	<b>DLP<sup>e</sup></b>
[6.13]	WZ	QDot (D $\approx$ 30 nm, h $\approx$ 10 nm) NW (D $\approx$ 30 nm, L $\approx$ 3 $\mu\text{m}$ )	SiO <sub>2</sub> on Si	532 nm	0.78	0.72 (at 980 nm)
[6.6]	WZ	QWell (1 & 2 ML thickness) NW (D $\approx$ 140 nm, L $\approx$ 2 $\mu\text{m}$ )	SiO <sub>2</sub> on Si	532 nm		-0.41 (at 1050 nm) -0.45 (at 980 nm)

### 6.3 Mechanisms responsible for polarization anisotropy.

In general, there are three major mechanisms responsible for the phenomenon of polarization anisotropy in both emission and absorption.

#### Selection rule

The first mechanism is known as the “selection rule” of WZ material [6.7, 6.17 – 6.19]. According to this rule in NWs with WZ type of crystallographic structure the emission from recombination of electrons in the conduction band with holes from A-band is expected to be polarized perpendicularly to the NW axis, whereas both perpendicular and horizontal polarizations are allowed for the recombination with holes from B and C bands. This selection rule has been experimentally demonstrated, for the A-band, in a number of works on NWs of large diameter ( $> 80\text{nm}$ ) [6.7, 6.17, 6.19, 6.20]. Chuang and Chang [6.21] developed a model to obtain the momentum-matrix elements for the optical transition from the conduction band edge to the three valence-subband edges of WZ material, when the optical polarization is parallel or perpendicular to the c-axis (Table 6.3).

**Table 6.3:** Interband momentum-matrix elements for polarizations along the c-axis and perpendicular to the c-axis. Here,  $P_1$  and  $P_2$  are the Kane’s parameters, and  $a$  and  $b$  are parameters depending on  $\Delta_1$ ,  $\Delta_2$  and  $\Delta_3$  (see [6.21] for more details)

	$\hat{\mathbf{e}} \parallel \mathbf{c} \text{ axis}$	$\hat{\mathbf{e}} \perp \mathbf{c} \text{ axis}$
$E_1$ (A-band)	0	$m_0^2 P_2^2 / 2^{-2}$
$E_2$ (B-band)	$b^2 m_0^2 P_1^2 / 2^{-2}$	$a^2 m_0^2 P_2^2 / 2^{-2}$
$E_3$ (C-band)	$a^2 m_0^2 P_1^2 / 2^{-2}$	$b^2 m_0^2 P_2^2 / 2^{-2}$

According to this model, in WZ NWs we may expect only perpendicular polarization from A-band and both polarizations from B and C-bands. However, it is important to note that the polarization ratio can be significantly changed by strain. More details on the selection rule and energy band structure can be found in Chapter 1.

## Quantum confinement

The second mechanism takes place in case of strong quantum confinement regime, when the size of 1D structure is smaller than the exciton Bohr radius. A giant anisotropy of the optical polarization was predicted in very thin InP NWs on the basis of a tight-binding model [6.22]. It was shown that the optical absorption or luminescent emission will be 100% polarized along the NW. Such a high degree of polarization is in contrast to the results of a simple  $k \cdot p$  model of Sercel and Vahala [6.23], which predicts a much more modest value of anisotropy. However, this result was obtained by considering only the heavy and light hole couplings in a typical ZB semiconductor such as GaAs. Maslov *et al* [6.24] tried to resolve this discrepancy between the tight-binding and envelope function theories by including band mixing into  $k \cdot p$  calculation. Strong diameter dependence of polarization anisotropy in this case was shown, demonstrating smooth transition between two regimes: that of moderately thin quantum wires, in which only the heavy and light holes are sufficient to describe the band-edge properties [6.23] and that of extremely thin nanowires, for which a tight-binding model has been applied [6.22].

## Dielectric confinement

On the other hand, in NWs of the diameter larger than Bohr radius, the third mechanism is often dominating [6.8, 6.9]. In this case, known as dielectric confinement, the polarization anisotropy is caused by dielectric mismatch between NW and its environment. This difference in dielectric constants favors the parallel component of the electric field causing anisotropy of the electric field distribution [6.13, 6.25, 6.26]. Usually, to estimate the polarization anisotropy cased by this effect, a simple case of infinite cylinder is considered. According to Landau theory of dielectric media [6.27], when the incident field ( $E_e$ ) is polarized parallel to the cylinder, the electric field inside the cylinder is not reduced. But when polarized perpendicular to the cylinder, the electric field amplitude ( $E_{\perp}$ ) is attenuated according to

$$E_{\perp} = \frac{2\epsilon_0}{\epsilon + \epsilon_0} E_e \quad (6.3)$$

where  $\epsilon$  and  $\epsilon_0$  are dielectric constants of the cylinder and vacuum, respectively. However, this is only true for NWs of the diameter much smaller than the wavelength ( $D/\lambda \ll 1$ ) and decrease of polarization ratio with increase of the diameter was clearly demonstrated in [6.8] (Figure 6.1).

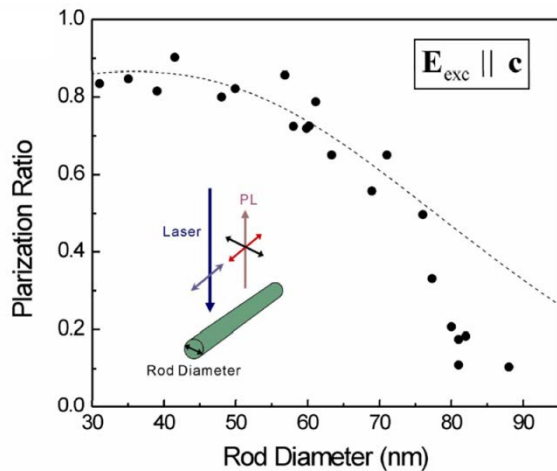


**Figure 6.1:** Image from [6.8]. The polarization ratio of μPL emission from single GaN nanorods with different diameters.

To clarify this mechanism H. Ruda and A. Shik [6.25, 6.26] suggested a theoretical model, which explains the dependence of the polarization ratio on  $D/\lambda$  ratio for both absorption and emission. This model has been used in the [6.8] to fit the diameter dependents of polarization ratio illustrated in Figure 6.1. It is important to mention that in the work of H. Ruda and A. Shik [6.26] a limiting case of a non-absorbing (or weakly absorbing) NW was considered, while in the work of J. Giblin *et al.* [6.28, 6.29] the complex, frequency dependent NW dielectric constant is used to consider the case of a strongly absorbing NW. In this model, named local field approximation (LFA) model, the parallel/perpendicular polarization energy absorption rates may be obtained for cylindrical NWs as follows:

$$I^a = \frac{\pi a}{Z} |E_0|^2 \operatorname{Re} \left[ -i \sum_{n=-\infty}^{\infty} \sqrt{\epsilon(\omega)^*} |c_n|^2 J_n(ka) J_n^*(ka) \right] \quad (6.4.a)$$

$$I_{\perp}^a = \frac{\pi a}{Z} |E_{0\perp}|^2 \operatorname{Re} \left[ -i \sum_{n=-\infty}^{\infty} \sqrt{\epsilon(\omega)^*} |d_n|^2 J'_n(ka) J_n^*(ka) \right] \quad (6.4.b)$$

where  $H_n(ka)$  are complementary Hankel functions of the first kind,  $k_0 = 2\pi\sqrt{\epsilon_0(\omega)}/\lambda$  is the wavenumber in the surrounding medium,  $a$  is the NW radius and coefficients  $c_n$  and  $d_n$  are

$$c_n = \frac{\sqrt{\varepsilon_M(\omega)}H'_n(k_0a)J_n(k_0a) - \sqrt{\varepsilon_M(\omega)}H_n(k_0a)J'_n(k_0a)}{\sqrt{\varepsilon_M(\omega)}H'_n(k_0a)J_n(ka) - \sqrt{\varepsilon_M(\omega)}H_n(k_0a)J'_n(ka)} \quad (6.5.a)$$

$$d_n = \frac{\sqrt{\varepsilon_M(\omega)}H_n(k_0a)J'_n(k_0a) - \sqrt{\varepsilon_M(\omega)}H'_n(k_0a)J_n(k_0a)}{\sqrt{\varepsilon_M(\omega)}H_n(k_0a)J'_n(ka) - \sqrt{\varepsilon_M(\omega)}H'_n(k_0a)J_n(ka)} \quad (6.5.b)$$

This last LFA model will be used to fit the experimental results of the present chapter.

## Experimental conditions

Moreover, the experimental conditions can have an impact on the measured value of the polarization anisotropy. One key parameter is the numerical aperture (NA) of the microscope objective [6.30], as shown in Figure 6.2.

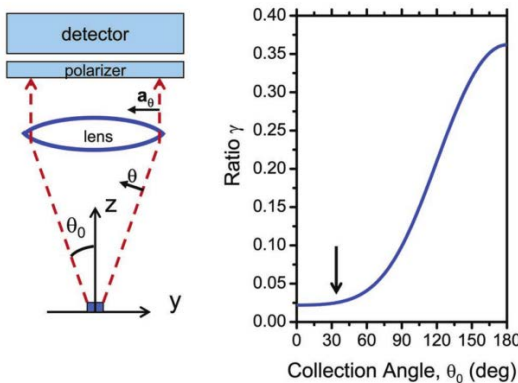


**Figure 6.2:** Image from [6.30]. Scheme of a collection system and calculated angular dependence of the ratio of emission intensities ( $\gamma$ ).

We see that the ratio  $\gamma(\theta_0) = I_{\perp} / I_{\parallel}$  is NA dependent: the ratio is nearly constant for  $\theta \leq 40^\circ$ , and then increases for higher values of NA. This is explained by the fact that the approximations  $I_{\perp} \approx W_{x \rightarrow \perp} \cdot n_x$  and  $I_{\parallel} \approx W_{y \rightarrow \parallel} \cdot n_y$  (where  $W$  is the energy absorption rate and  $n$  in number of photons) are valid only for relatively small NA.

Since the polarization anisotropy is also dependent on dielectric constant of the media, it is important to mention that polarization ratio measured on NWs transferred onto a host-substrate may be affected by the refractive index of the substrate [6.13]. However, rather similar polarization results are observed on NWs transferred on the host-substrates of different materials [6.7], [6.11], so we suppose that the host-substrate has minor impact on the polarization properties.

## 6.4 Polarization properties of InP nanowires.

To begin, we study the polarization anisotropy of emission from WZ InP NWs. To measure DLP<sup>e</sup> we performed room temperature μPL measurements, using non-polarized excitation, while the polarization of emission is selected with a polarizer at the collection.

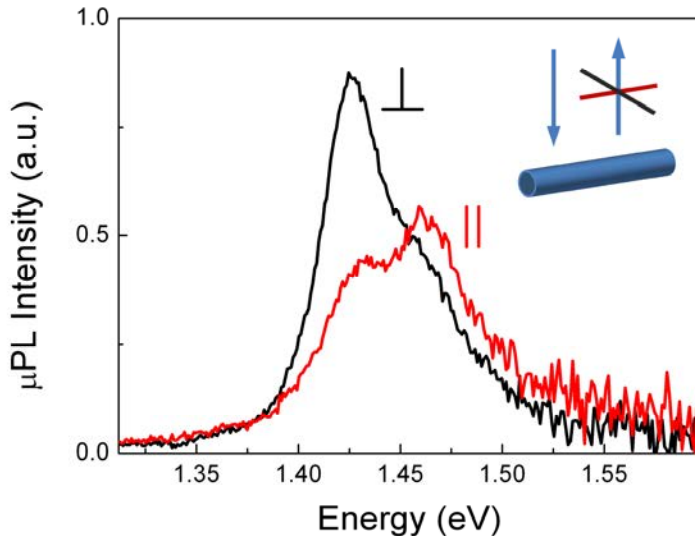


**Figure 6.3:** Room temperature μPL spectra of a single InP NW with different polarization of emission.

Figure 6.3 shows room temperature μPL spectra of a typical single InP NW for different polarizations of emission. Fitting these spectra with two Gaussians (one for each band), the values of DLP<sup>e</sup> for A and B bands were found to be -0.62 and 0.11, respectively. The negative value on A-band and low value on B-band shows that in this NW the WZ selection rule seems to be dominating. On the other hand, according to the model of Chuang and Chang [6.21], using the parameters of WZ InP ( $\Delta_1 = 0.144$ ,  $\Delta_2 = \Delta_3 = 0.026$ ,  $m_{e\parallel} = 0.105$ ,  $m_{e\perp} = 0.088$  and  $E_g = 1.49$  eV) and assuming absence of strain in our free standing NWs, the following values of DLP<sup>e</sup> for the different bands may be obtained from Table 6.3:  $DLP^{A\text{-band}} = -1$ ,  $DLP^{B\text{-band}} = -0.74$  and  $DLP^{C\text{-band}} = 0.93$ . So the strong negative values of DLP<sup>e</sup> for both A and B bands are expected in theory. In practice, different results were obtained on different InP NWs, and even positive DLP values of both A and B bands were observed on some of them. This difference is attributed to variations of NW diameter. The diameter of the InP NWs ranges from 80 to 120 nm. So we assume that the dielectric confinement effect may overcome the impact of the selection rule for NWs of smaller diameter.

## 6.5 Polarization properties of QWell nanowires.

We continue with a study of the polarization anisotropy of emission from NW heterostructures. In the literature, the polarization of ZB GaAs/AlGaAs core-shell NWs was found to be strongly parallel to the NW axis [6.5], which is attributed to the dielectric confinement. On the contrary, WZ InP/InAs/InP core-multishell NWs, similar to our WZ InP/InAs/InP QWell NWs, were found to be highly polarized in the direction perpendicular to NW axis with  $DLP^e = -0.48$  [6.6]. Despite the similarity of the structure, results obtained on our QWell-NWs are the opposite.

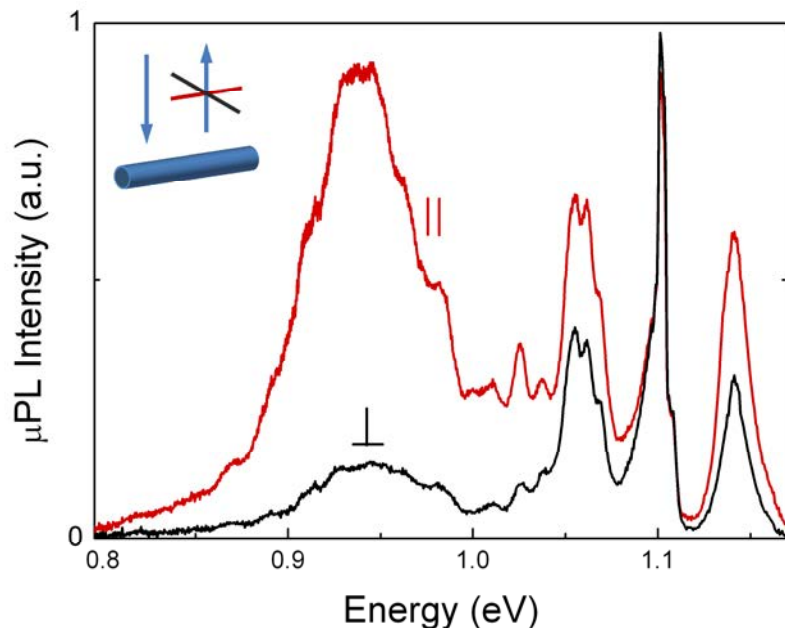


**Figure 6.4:** Emission of a single NW as a function of the linear polarization: red dashed (blue solid) line polarization parallel (perpendicular) to the NW axis.

Figure 6.4 shows the  $\mu$ PL emission of a single QWell-NW for two polarization configurations: parallel and perpendicular to the NW axis. The maximum of  $\mu$ PL intensity is obtained for the linear polarization parallel to the NW axis. The values of  $DLP^e$  are equal to 0.73 (for the peak at 0.94 eV), 0.24 (at 1.06 eV) and 0.3 (at 1.14 eV), whereas the peak from Si host-substrate (1.1 eV) remains non-polarized. This result is similar to the  $DLP^e$  obtained for ZB InAs(P)/InP quantum wires and dashes where emission polarized along the wire/dash axis was reported with DLP in the 0.2 – 0.5 range [6.31, 6.32], but is in contradiction with the selection rule for the A-band of the WZ phase. So, we have to assume, that the shape of the NW, has more

impact on the polarization anisotropy than the selection rules of bulk WZ. Polarization resolved measurements performed on several NWs revealed that the NW emission was mainly parallel to the NW axis and that the DLP seems to be independent of the emission energy (Figure 6.5).

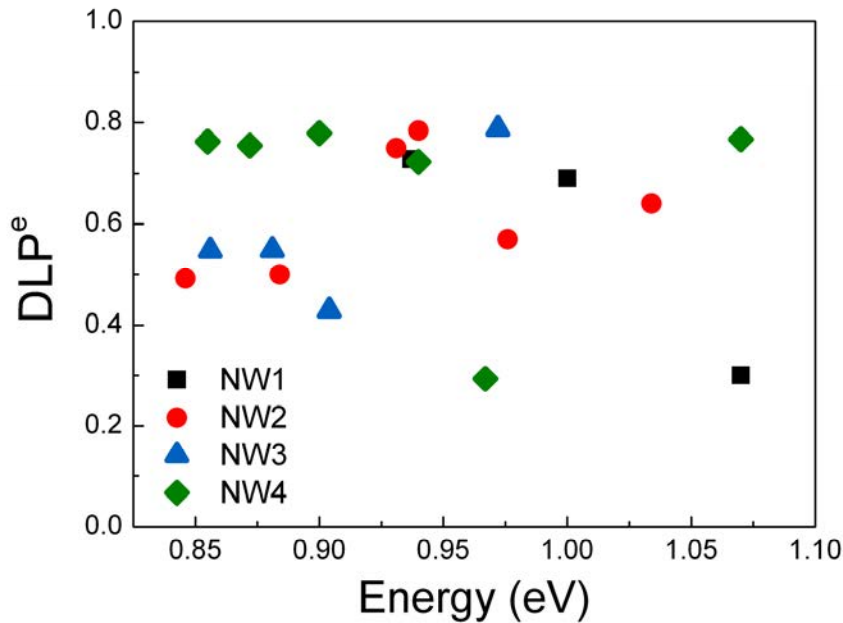


**Figure 6.5:** Degree of linear polarization as a function of the emission energy.

This result confirms the hypothesis of a DLP driven by the NW geometry, so  $DLP^e$  should depend on the ratio of NW diameter to emission wavelength. In our case, due to the relatively small NW diameter ( $\approx 80$  nm), this ratio is  $\ll 1$  for the entire QWell emission range (1100 – 1500 nm). Using this result we can reconstruct the value of  $DLP^e$  without the impact of dielectric confinement. So, taking the average measured values of  $DLP^e$  from 0.5 to 0.7, and assuming that the perpendicular component was attenuated according to Eq. 6.3, we may recover the original intensity of perpendicularly polarized emission from the radial QWell. In this case  $DLP^e$  will be in the range from -0.88 to -0.68, which is in agreement with the selection rule of WZ material.

However, the complicated spectra of QWell-NWs (see Chapter 5) make it difficult to understand the origins of polarization anisotropy of each peak and explain the difference between them. For this reason we proceed to the sample of heterostructures of simpler type: QRod-NWs.

## 6.6 Polarization properties of single QRod nanowires.

In the following section, the polarization anisotropy of QRod-NWs will be studied for both emission and absorption. In the literature, polarization properties of WZ InAsP/InP QDot NWs [6.13] and CdSe/CdS QRod-NWs [6.15] were reported. Despite the selection rule, the QDot-NWs exhibited high values of both DLP<sup>a</sup> and DLP<sup>e</sup> in the 0.7 – 0.9 range, so the anisotropy was attributed to dielectric confinement. QRod-NWs demonstrated similar behavior showing values of DLP<sup>a</sup> in the 0.63 – 0.82 range depending on the excitation wavelength and value of DLP<sup>e</sup> about 0.82. We, in our turn, obtained similar results on WZ QRod-NWs.

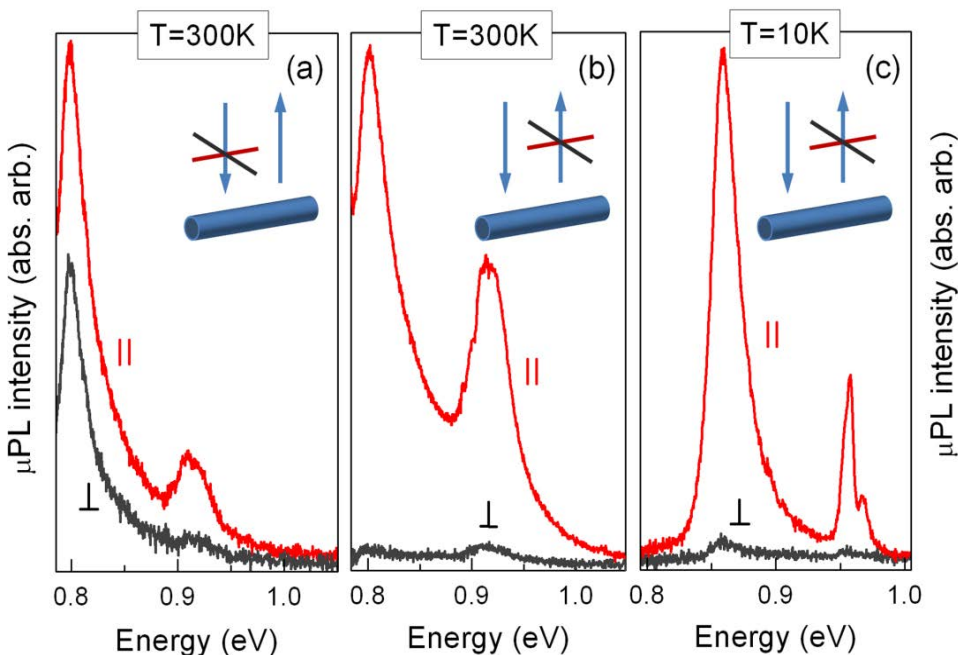


**Figure 6.6:** μPL spectra of a single InAs/InP QRod-NW for different polarizations of absorption (a) and emission measured at room (b) and low (c) temperatures.

Figure 6.6.a shows μPL emission spectra measured using different polarization of excitation at room temperature, while no selection made for collection. The measured DLP<sup>a</sup> varies from one NW to another, but on the average is equal to 0.5. This distribution can be explained by the difference in diameter from one NW to another. On the contrary, when polarization anisotropy of emission was investigated under non-polarized excitation at room temperature, the DLP<sup>e</sup> was found to be the same for all measured NWs and equal to 0.94 (Figure 6.6.b). This value is similar to that observed for InAsP QDot-NWs with very different QDot

dimensions: a 10 nm height and a 30 nm diameter [6.13]. The DLP<sup>a</sup> is not surprising. It is known that the efficiency of the NW absorption is favored when the excitation is polarized parallel to the NW axis [6.5, 6.8, 6.13], and may be considered as purely classic phenomenon of dielectric confinement. Indeed, using the LFA model we may obtain DLP<sup>a</sup> from Eq. 6.2 using Eq. 6.4 and 6.5. For the excitation wavelength of 632 nm and the average diameter of NW (100 nm), for an InP cylinder DLP<sup>a</sup> = 0.48 is obtained, which is close to the experimental value. Here and elsewhere, since InAs QRods are located at the bottom of NWs, we neglect a possible impact of top tapering part of NWs and assume the diameter to be uniform, or at least consider the average diameter.

The situation is more complex as far as the DLP<sup>e</sup> is concerned. The valence band ground state of the WZ InAs material is expected to be the A-band, which, according to the selection rule, only allows emission perpendicular to the NW axis [6.7, 6.17]. To explain the polarization anisotropy of emission, we can assume that the ground state of the QRod is not a pure A-band state but a mixing of A and B bands. Similar kind of mixing has already been predicted and observed for WZ nitride QDots [6.33] and for ZB quantum posts or rods (with, in this case, the mixing between the HH and LH bands) [6.34]. Then, we have to take into account the inhibition of the PL emission perpendicular to the NW as a consequence of the small NW diameter as compared to the PL emission wavelength. To describe this situation, we consider a system where the exciton can be polarized parallel to the NW (z-axis) or perpendicular to the NW (x and y axes). The equations to describe such a system are:

$$\frac{dn_i}{dt} = -(\gamma_i + 2\gamma_s)n_i + \sum_{j \neq i} \gamma_s n_j + G \quad i = x, y, z \quad (6.6)$$

Where G is the photogeneration rate, n<sub>z</sub> (n<sub>x</sub>, n<sub>y</sub>) is the state population emitting in parallel (perpendicular) to the NW, γ<sub>z</sub> (γ<sub>x</sub>, γ<sub>y</sub>) is the oscillator strength parallel (perpendicular) to the NW c-axis, and γ<sub>s</sub> the longitudinal spin relaxation rate between two states. Under a continuous wave excitation, the intensities are equal to:

$$I_z = \gamma_z n_z = \frac{G \gamma_z (\gamma_y + 3\gamma_s)}{(\gamma_z + 2\gamma_s)(\gamma_y + \gamma_s) - 2\gamma_s^2}$$

$$I_y = I_x = \gamma_y n_y = \frac{G\gamma_y(\gamma_z + 3\gamma_s)}{(\gamma_z + 2\gamma_s)(\gamma_y + \gamma_s) - 2\gamma_s^2}$$

So DLP<sup>e</sup> may be written as:

$$DLP^e = \frac{I_z - I_y}{I_z + I_y} = \frac{\gamma_z - \gamma_y}{\gamma_z + \gamma_y + 2\gamma_z\gamma_y/3\gamma_s}$$

At room temperature, we can assume that  $\gamma_s \gg \gamma_z$  and  $\gamma_s \gg \gamma_y$ , consequently:

$$DLP^e \approx \frac{\gamma_z - \gamma_y}{\gamma_z + \gamma_y}$$

In our case, we have very small ratio  $D/\lambda \approx 0.06$  and the inhibition factors are equal to  $\gamma_{\perp} = 4\gamma_{\perp}^0/n(n^2 + 1)$  and  $\gamma_{\parallel} = \gamma_{\parallel}^0/n$ , where  $\gamma_{\perp}$  ( $\gamma_{\parallel}$ ) is the recombination rate of the dipole perpendicular (parallel) to the NW axis and  $\gamma_{\perp}^0$  ( $\gamma_{\parallel}^0$ ) is the intrinsic recombination rates of the dipole without the NWs [6.35]. Taking into account the refractive index of InP and assuming an isotropic recombination rate, the DLP<sup>e</sup> may be estimated as:

$$DLP^e = \frac{\gamma_{\parallel} - \gamma_{\perp}}{\gamma_{\parallel} + \gamma_{\perp}} = \frac{(n^2 + 1)^2 - 4}{(n^2 + 1)^2 + 4} \approx 0.95$$

This theoretical value is very close to the experimental one and means that the intrinsic QRod dipole is almost isotropic in the NWs, therefore the detected anisotropy is mainly due to the inhibition of the PL emission perpendicular to the NW. To confirm this fact,  $\mu$ PL at low temperature (10 K) has been performed on the same single NWs. As shown in Figure 6.6.c the DLP<sup>e</sup> remains the same even at low temperature. Moreover, the DLP<sup>e</sup> is very strong for all the observed lines of the single QRod (ground and excited states) which confirms that the strong polarization anisotropy is not related to a specific selection rule of the ground state.

Moreover, this value of DLP<sup>e</sup> means a very strong anisotropy in the oscillator strengths  $\gamma_z/\gamma_y \approx 30$ . Using the lifetime measured in Chapter 5, the absolute values of the oscillator strength may be extracted. Now the Eq. 6.6 are used to calculate the theoretical decay rate. Using the relationship  $\gamma_z \gg \gamma_y$ , the PL intensity collected in a time-resolved PL setup may be represented as:

$$I(t) = \gamma_z n_z(t) + \gamma_y n_y(t) \approx \gamma_z n_z(t)$$

Introducing  $n_{\perp} = n_x + n_y$ , and using Eq. 6.6 with  $G = 0$ , a system of two coupled equations may be obtained:

$$\frac{dn_z}{dt} = -(\gamma_z + 2\gamma_s) n_z + \gamma_s n_{\perp}$$

$$\frac{dn_{\perp}}{dt} = -(\gamma_y + \gamma_s) n_{\perp} + 2\gamma_s n_z$$

This system is equivalent to the coupled equations studied in [6.36]. When the conditions  $\gamma_s \gg \gamma_z$  and  $\gamma_s \gg \gamma_y$  are applied, the decay is defined as [6.36]:

$$n_z(t) \approx \exp(-\gamma_z t/2)$$

The lifetime of 7.5 ns was measured in Chapter 5. Therefore, from the relations  $\gamma_z / 2 = 7.5 \text{ ns}^{-1}$  and  $\gamma_z / \gamma_y \approx 30$ , we obtain the oscillator strength values of  $\gamma_z = 3.75 \text{ ns}^{-1}$  and  $\gamma_y = 110 \text{ ns}^{-1}$ . The lifetime of 110 ns at room temperature for the polarization perpendicular to the NW confirms the strong inhibition due to the geometry of the NW.

## 6.7 Polarization properties of nanowire ensembles.

Due to the strong polarization anisotropy found on QRod-NWs, it is possible to investigate the optical properties of QRod-NW ensembles on the as-grown substrates. For this purpose two samples with different orientations of NWs on the substrate are used: one with NWs grown on Si(001) substrate and another with NWs grown on Si(111) substrate.

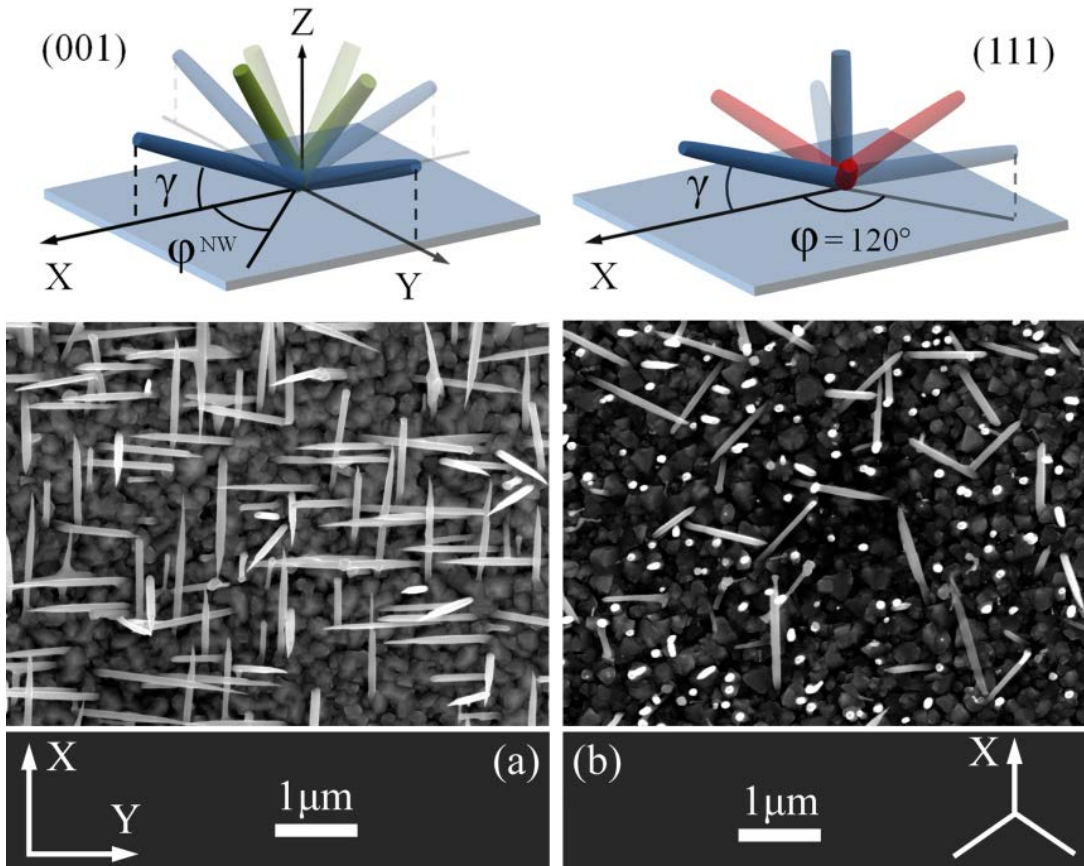


**Figure 6.7:** Scheme of axes and angles relative to NWs and SEM images of the surface of the as-grown (001) (a) and (111) samples (b).

For the Si(001) substrate, the SEM image demonstrates that the NWs are mainly oriented along X and Y axes (Figure 6.7.a). It was shown by X-ray diffraction pole figures that the NWs mainly grow in the four [111] directions of the Si(001) substrate at an angle of  $\gamma = 35^\circ$  to the surface. Moreover, a certain amount of short NWs grow in the [115] directions of the Si(001) substrate at  $\gamma = 74^\circ$  angle (shown by green color in Figure 6.7.a), due to the twin formation at the first stage of the NW growth. Thus the QRod-NWs on Si(001) substrate exhibit a clear four-fold symmetry.

On the contrary, SEM image of NWs grown on the Si(111) substrate demonstrates that the NWs are grown vertically and in three different directions ( $\varphi^{\text{NW}} = 0^\circ, 120^\circ$  and  $240^\circ$ ) at a  $\gamma = 19.5^\circ$  angle as shown in the Figure 6.7.b. This is also evidenced by Figure 6.8.a that shows the X-ray diffraction pole figure of the NWs grown on Si(111) substrate. The pole figure exhibits six clear spots located at the angle  $\gamma = 19.5^\circ$  (see black arrows). An azimuthal cross section of the intensity was performed in order to compare the relative intensity of each peak (Figure 6.8.b).

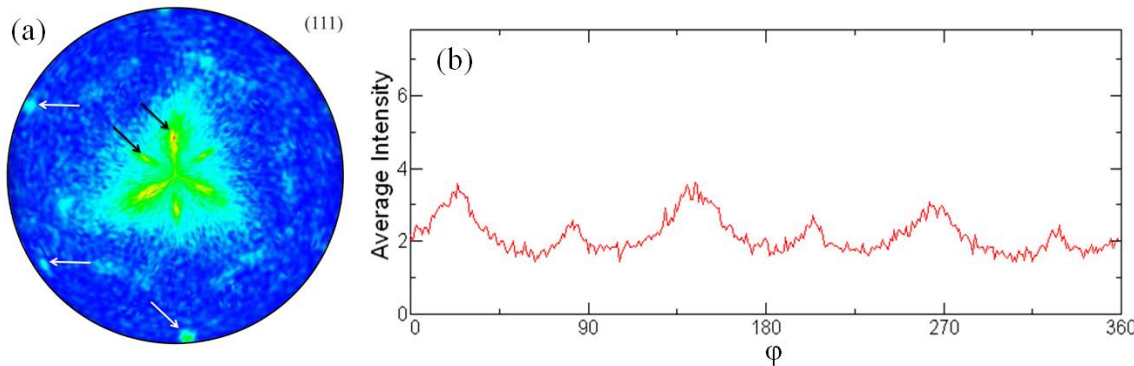


**Figure 6.8:** (a) X-ray diffraction pole figure of the NWs on (111) sample. Black and white arrows show the spots located at  $\gamma = 19.5^\circ$  and  $\gamma = 90^\circ$  respectively. (b) Azimuthal cross section of the intensity.

The cross section shows the six peaks can be seen as two tripods shifted by  $60^\circ$  (shown by red and blue colors in Figure 6.7.b). However, this fact does not make difference for the following calculation so we simplify the model assuming NWs to be only each  $120^\circ$ . In addition, another set of spots (see white arrows) are visible at  $\gamma = 90^\circ$  which corresponds to the border of the pole figure and can be attributed to vertical NWs. These results are in agreement with NWs growing in the [111] directions of the Si(111) substrate. Thereby, using the knowledge of the NW growth directions on a given sample and the parameters of the single NWs, the ensemble may be studied as a well defined system.

The optical experiments are performed on a standard PL setup (see Chapter 3.2) using a non-polarized 20 mW He-Ne laser (632.8 nm) focused on the sample with a spot size of  $\approx 0.2$  mm, which means that  $\approx 15 \cdot 10^4$  and  $\approx 3 \cdot 10^4$  QRod-NWs are excited on the (001) and (111) samples, respectively. Contrary to the single QRod-NW studies, two polarizers are used: one to control the linear polarization of the laser and another to control the polarization of the emission. So, the intensity was measured as a function of the excitation polarization ( $\varphi^{\text{ex}}$ ) for different

values of polarization of collection ( $\varphi^{\text{col}}$ ). The polarization anisotropy observed on (001) sample is shown in the Figure 6.9.a, where the PL intensity demonstrates oscillations when  $\varphi^{\text{col}}$  is either equal to  $0^\circ$  or to  $90^\circ$ , but maintains constant at  $\varphi^{\text{col}} = 45^\circ$  and  $135^\circ$ .

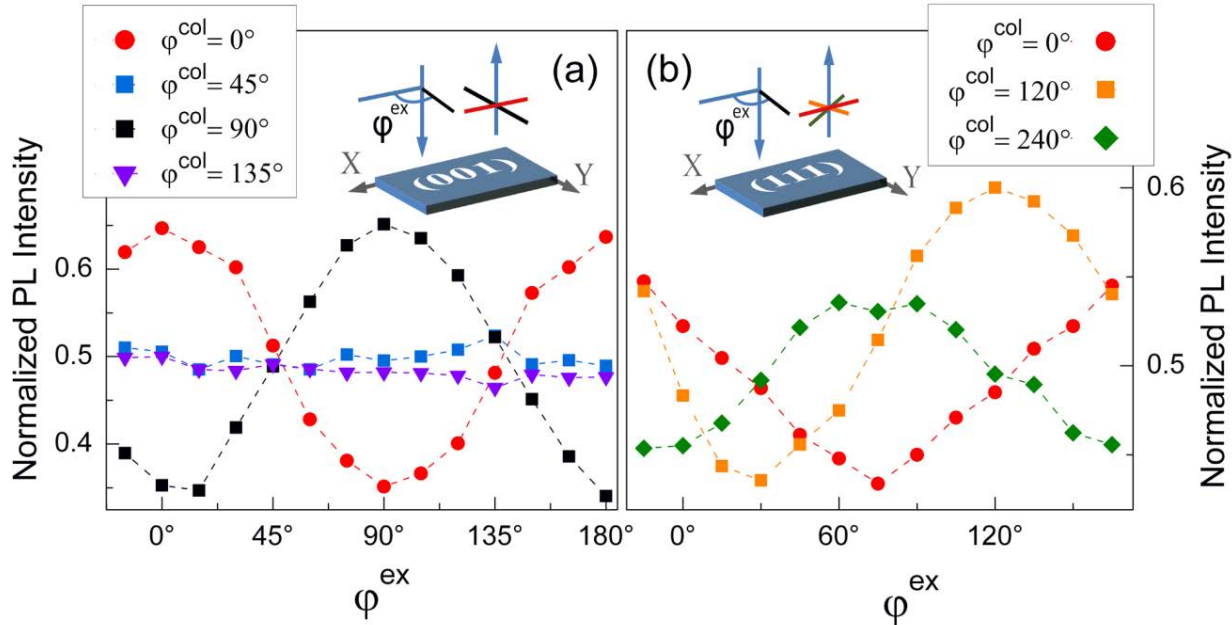


**Figure 6.9:** Intensity of emission of QRod-NW ensembles as a function of the polarization of the absorption and collection. For (001) sample (a) and (111) sample (b).

Figure 6.9.b demonstrates the results of the same experiment but performed on the Si(111) sample. In this geometry, as it was already observed for a “NW tripod” [6.37], the intensity shows oscillations as a function of  $\varphi^{\text{ex}}$  at any  $\varphi^{\text{col}}$ , having maximums when these angles are equal. Slightly different oscillation amplitudes at different values of  $\varphi^{\text{col}}$  and positions of the peaks indicate disproportion in distribution of NWs along different directions and that is one of the reasons why we prefer to focus on the (001) substrate in the following study.

## 6.8 Ensemble polarization model.

Let us now introduce the model that will be used to correlate the polarization properties, particularly DLP, of NW ensembles with the optical properties of single NWs. The emission intensity of a single NW can be represented as a product of absorption (Abs) and emission (Em) functions:

$$I(\varphi^{\text{NW}}, \varphi^{\text{ex}}, \varphi^{\text{col}}, \gamma) = C \cdot \text{Abs}(\varphi^{\text{NW}}, \varphi^{\text{ex}}, \gamma) \cdot \text{Em}(\varphi^{\text{NW}}, \varphi^{\text{col}}, \gamma) \quad (6.7)$$

where  $C$  is a proportional coefficient,  $\varphi^{\text{NW}}$  is the azimuthal angle between X axis and projection of the NW on XY plane (see the Figure 6.7.a),  $\varphi^{\text{ex}}$  and  $\varphi^{\text{col}}$  are the azimuthal angles between X axis and axes of polarizers at excitation and collection, correspondingly. Due to the fact that the NW diameter is much less than the emission wavelength, we assume that we can describe the NWs on the substrate as an assembly of dielectric ellipsoids [6.38]. First, we will consider the absorption function. Assuming that the NW is parallel to X axis ( $\varphi^{\text{NW}} = 0^\circ$ ) the absorption function can be written as [6.38]:

$$\text{Abs}(\varphi^{\text{ex}}, \gamma) = k^2 \cdot \cos^2(\varphi^{\text{ex}}) \cos^2(\gamma) + k_{\perp}^2 \cdot [\sin^2(\varphi^{\text{ex}}) + \cos^2(\varphi^{\text{ex}}) \sin^2(\gamma)] \quad (6.8)$$

where  $k_{\parallel}$  ( $k_{\perp}$ ) is the ratio of the longitudinal (transverse) electric field inside to that outside of a NW. Or it can be rewritten as:

$$\text{Abs}(\varphi^{\text{ex}}, \gamma) = a + b \cdot \cos^2(\varphi^{\text{ex}}) \cdot \cos^2(\gamma) \quad (6.9)$$

where coefficients  $a$  and  $b$  are defined as  $a = k_{\perp}^2$  and  $a + b = k_{\parallel}^2$ . These coefficients can be written as functions of the DLP using the Eq. 6.9 with  $\gamma = 0^\circ$ ;  $\varphi^{\text{ex}} = 0^\circ, 90^\circ$  and the condition of normalization  $2 \cdot a + b = 1$ . Indeed:

$$\text{DLP}^a = \frac{\text{Abs}_{\perp} - \text{Abs}_{\parallel}}{\text{Abs}_{\perp} + \text{Abs}_{\parallel}} = \frac{\text{Abs}(\varphi^{\text{ex}} = 0^\circ) - \text{Abs}(\varphi^{\text{ex}} = 90^\circ)}{\text{Abs}(\varphi^{\text{ex}} = 0^\circ) + \text{Abs}(\varphi^{\text{ex}} = 90^\circ)} \quad (6.10)$$

and consequently:

$$a = (1 - \text{DLP}^a) / 2; \quad b = \text{DLP}^a \quad (6.11)$$

Therefore Eq. 6.8 can be written containing DLP<sup>a</sup> of a single NW as:

$$\text{Abs}(\varphi^{\text{ex}}, \gamma) = (1 - \text{DLP}^a) / 2 + \text{DLP}^a \cdot \cos^2(\varphi^{\text{ex}}) \cdot \cos^2(\gamma) \quad (6.12)$$

The same procedure can be applied to emission, so the emission function can be written as:

$$\text{Em}(\varphi^{\text{col}}, \gamma) = (1 - \text{DLP}^e) / 2 + \text{DLP}^e \cdot \cos^2(\varphi^{\text{col}}) \cdot \cos^2(\gamma) \quad (6.13)$$

Knowing the absorption and emission functions of a single NW, the intensity of a NW ensemble (index “\*”) can be written as a sum of functions for each of n NWs in the ensemble:

$$I^*(\varphi^{\text{ex}}, \varphi^{\text{col}}, \gamma) = \sum_{k=1}^n I(\varphi_k^{\text{NW}}, \varphi^{\text{ex}}, \varphi^{\text{col}}, \gamma) = C \cdot \sum_{k=1}^n \text{Abs}(\varphi^{\text{ex}} + \varphi_k^{\text{NW}}, \gamma) \cdot \text{Em}(\varphi^{\text{col}} + \varphi_k^{\text{NW}}, \gamma) \quad (6.14)$$

Or for simple cases of ordered ensembles, where only few preferential directions exist:

$$I^*(\varphi^{\text{ex}}, \varphi^{\text{col}}, \gamma) = C \cdot \sum_{k=1}^N \text{Abs}(\varphi^{\text{ex}} + 2\pi(k-1)/N, \gamma) \cdot \text{Em}(\varphi^{\text{col}} + 2\pi(k-1)/N, \gamma) \quad (6.15)$$

where N is the number of opposite directions in a given NW ensemble (i.e. N = 3 for Si(111), N = 4 for Si(001), N = 1 for a single NW and N → ∞ for a random distribution).

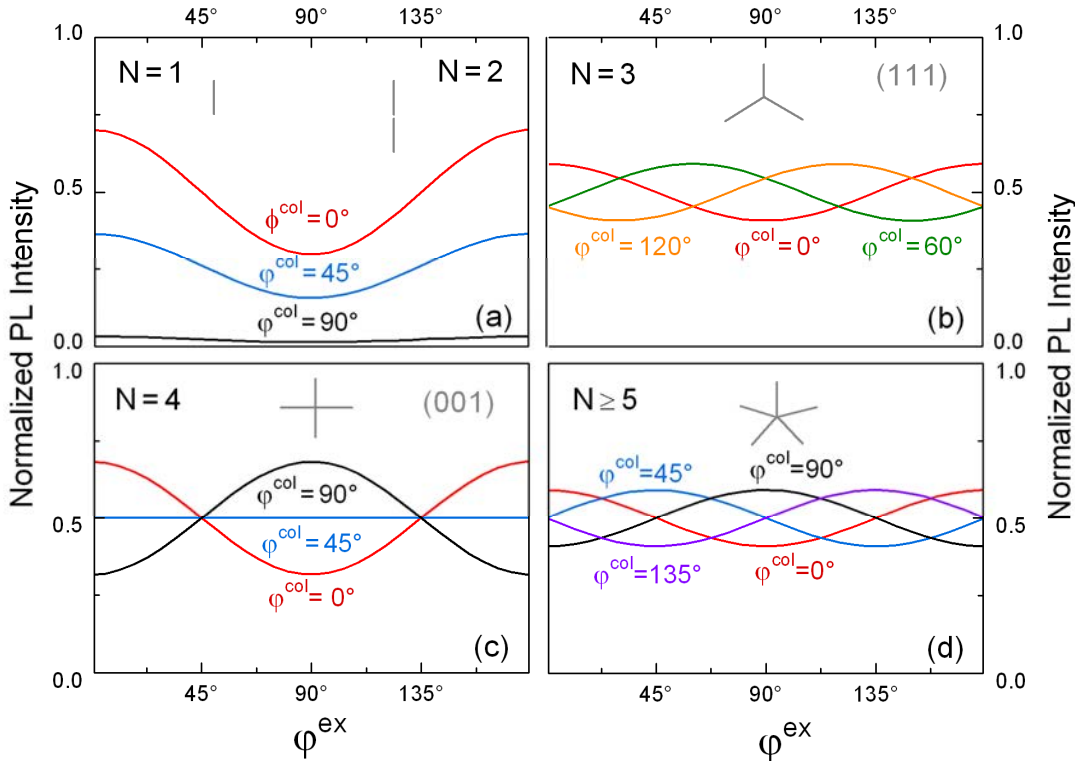


**Figure 6.10:** Calculated polarization anisotropies of QRod-NW ensembles of different kind.

In this equation we assumed that the number of NWs along each preferential direction is the same. Moreover, in this model, due to the relatively low density of NWs on the substrates, we

neglect the effect of multiple scattering in the NW layer. Intensities calculated from Eq. 6.15 (using the following values  $DLP^a = 0.5$ ,  $DLP^e = 0.94$  and  $\gamma = 35^\circ$ ) for various values of  $\phi$  and  $N$  are shown in Figure 6.10. It is important to note that for  $N \geq 3$  DLP of absorption and emission are equal, indeed:

$$DLP^{*a} = \frac{I^*(0,0) - I^*(90,0)}{I^*(0,0) + I^*(90,0)} = \frac{I^*(0,0) - I^*(0,90)}{I^*(0,0) + I^*(0,90)} = DLP^{*e} \quad (6.16)$$

This fact brings a certain convenience, proposing a way to avoid some technical problems, as we will see further. However, in the reality these  $DLP^*$  dependences might actually be slightly different, if the amount of NWs in different directions is not the same. Such difference would be indicated by different amplitudes of oscillations and in case of Si(001) substrate ( $N = 4$ ) also by the presence of oscillations in case of  $\phi^{col} = 45^\circ$ . Absence of such oscillations in our results leads us to the conclusion that the amount of NWs oriented along X and Y axes on Si(001) substrate is the same, and consequently  $DLP^{*a}$  and  $DLP^{*e}$  are equal for this sample. The case of multiple directions ( $N \geq 5$ ) shows the same polarization anisotropy for any values of  $N$ , including  $N \rightarrow \infty$ , which represents the case of randomly oriented NW. In this case the effect of “polarization memory” [6.25] can be described and one can qualitatively study the polarization properties even on an array or randomly oriented NWs.

Figure 6.11 represents the agreement of the theory explained above and the data of the Figure 6.9. The dots represent the measured values of emission intensity, polarized at  $\phi^{col} = 0^\circ$  and  $\phi^{col} = 120^\circ$  for Si(001) and Si(111) substrates correspondingly, as a function of the polarization of excitation. Solid lines show the result predicted from the model, where the parameters were taken from measurements of single NWs ( $DLP^a = 0.48$  and  $DLP^e = 0.94$ ). The parameter  $\xi_{(001)} = N_{\gamma=35^\circ} / N_{\gamma=74^\circ}$ , which reflects the ratio between the amounts of NWs inclined at different angles, remains uncertain, and is used as a degree of freedom. To obtain the best fit,  $\xi_{(001)} = 4$  was taken (Figure 6.10.a). This value seems to be reasonable being in agreement with SEM images.

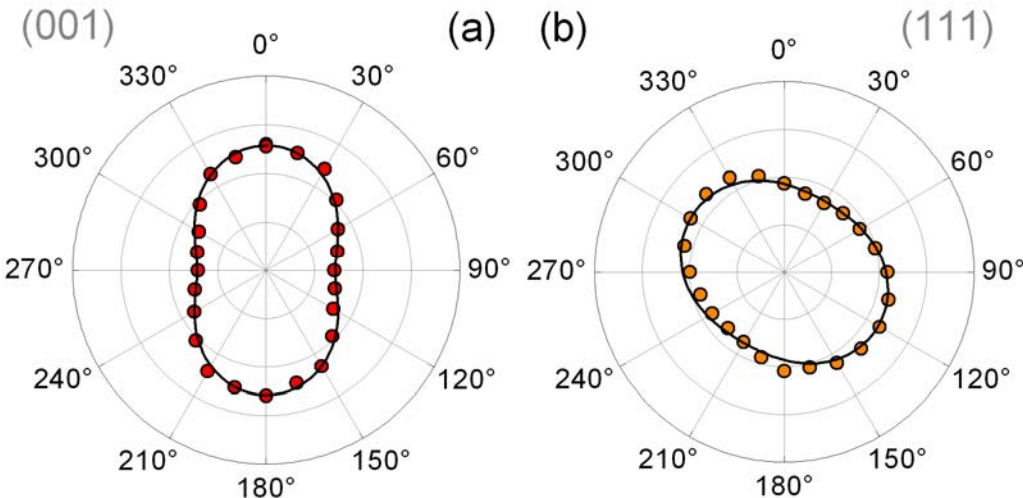


**Figure 6.11:** Dependence of the PL intensity on the angle  $\varphi^{\text{ex}}$  for  $\varphi^{\text{col}} = 0^\circ$  and  $\varphi^{\text{col}} = 120^\circ$  for the Si(001) (a) and Si(111) (b) substrates correspondingly, fitted by the theoretical curve.

As for the Si(111) substrate, the parameter  $\xi_{(111)} = N_{\gamma=19.5^\circ} / N_{\gamma=90^\circ}$  was found to be equal to 2 for the best fit (Figure 6.11.b). In fact, the amount of vertically standing NWs is clearly larger than the amount of inclined ones, so  $\xi_{(111)}$  should actually be below 1. This discrepancy can be explained taking into account that vertical NWs absorb light mostly by the upper part while the QRod is situated at the bottom of NWs, therefore these NWs probably almost do not participate in photoluminescence. However, due to the higher quality of the Si(001) sample and the better agreement of the results obtained on it with the theory, we use only this sample for the following investigation.

## 6.9 Wavelength and temperature dependences of polarization anisotropy.

As was already mentioned, it had been shown theoretically [6.25, 6.26] that DLP<sup>a</sup> depends on the ratio of the diameter to the excitation wavelength ( $D/\lambda$ ), but only few works were published on the experimental confirmation of this statement [6.8, 6.28, 6.29]. Our approach provides us a possibility to investigate this issue studying the ensemble of NWs under the excitation with various wavelengths.

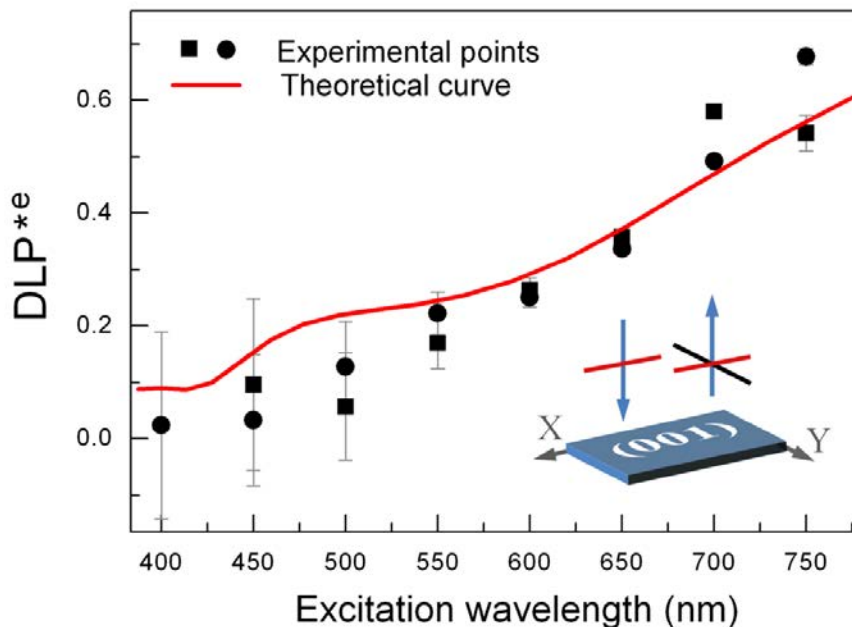


**Figure 6.12:** DLP\*<sup>e</sup> as a function of excitation wavelength. The results from 2 different places on the sample are presented by dots of different shapes. Solid line represents simulation result for a NW with the diameter of 100 nm. The sample was excited by the light with the width of spectral line of about 50 nm, thus each dot should be considered as an average value in  $\pm 25$  nm range.

For this purpose the laser in  $\mu$ PL setup has been replaced by a monochromator coupled with a white lamp. The spot size of the light beam was tuned to be as large as the laser spot size in the PL measurements. So, the QRod-NWs on Si(001) were excited by the light polarized parallel to X-axis, while the emission was collected through a polarizer, first parallel and then perpendicular to X-axis, therefore we measured the DLP\*<sup>e</sup>. It is important to note, that though we are interested in the DLP<sup>a</sup>, in the present experiment it is more convenient to measure the DLP\*<sup>e</sup>, and as it was shown above (Eq. 6.15), they in fact are equal. As a result, measuring the DLP\*<sup>e</sup> = DLP\*<sup>a</sup> on the ensemble of the NWs, we observed a clear increasing trend as the excitation

wavelength is increased from 400 nm up to the band gap of InP (Figure 6.12). This result can be explained by the suppression of the perpendicular component of the incident electric field inside the NWs, and its dependence on ratio  $D / \lambda_{\text{ex}}$ . Such increasing trend has already been demonstrated in 480 – 680 nm range for different types of CdSe based NWs [6.28, 6.29]. To compare this experimental data with a theory describing the electromagnetic field behavior on a dielectric cylinder, the LFA model was used [6.28, 6.29]. Within the bounds of this model the dependence of the DLP<sup>a</sup> on the excitation wavelength for a single InP NW with a 100nm diameter was obtained and then introduced in our model, to obtain the same dependence for the NW ensemble. In this calculation we used the  $\text{DLP}^e = 0.94$  measured experimentally on single QRod-NWs and the parameter  $\xi_{(001)} = 4$  obtained from the fitting in Figure 6.11.b, so we had no degree of freedom to modify the obtained curve. Nevertheless, this curve is in agreement with the experimental data (solid line in Figure 6.11).

Another interesting, but yet not well studied, question is the temperature dependence of DLP. Although the  $\text{DLP}^e$  of the single QRod-NWs at room temperature was found to be the same as at low temperature, there are, however, different temperature dependent mechanisms that may control DLP. For instance the thermal activation of nonradiative defects can take place and play a role in this question as well as temperature dependence of spin relaxation rate. Moreover, dielectric constant of the material changes with temperature, though we can safely assume that this dependence is negligible. In addition, the ratio between recombination rates along different axes can be changed with temperature. In a word, even having the same DLP at room and at low temperatures, it is not absolutely improbable to find a surprising behavior in between. So to check possible impacts of these phenomena, the  $\text{DLP}^{*a}$  was studied as a function of temperature using PL setup. The ensemble of QRod-NWs, placed into the cryostat, was excited with the laser beam (632nm) polarized parallel to X-axis and then parallel to Y-axis, while only the emission polarized parallel to X-axis was collected.

Surprisingly, increasing temperature, we observed a decrease of  $\text{DLP}^{*a}$ , but reaching room temperature, we noticed an increase of  $\text{DLP}^{*a}$  as some time passed. Finally, in few hours, the  $\text{DLP}^{*a}$  returned to the same value as it was at low temperature (Figure 6.12).

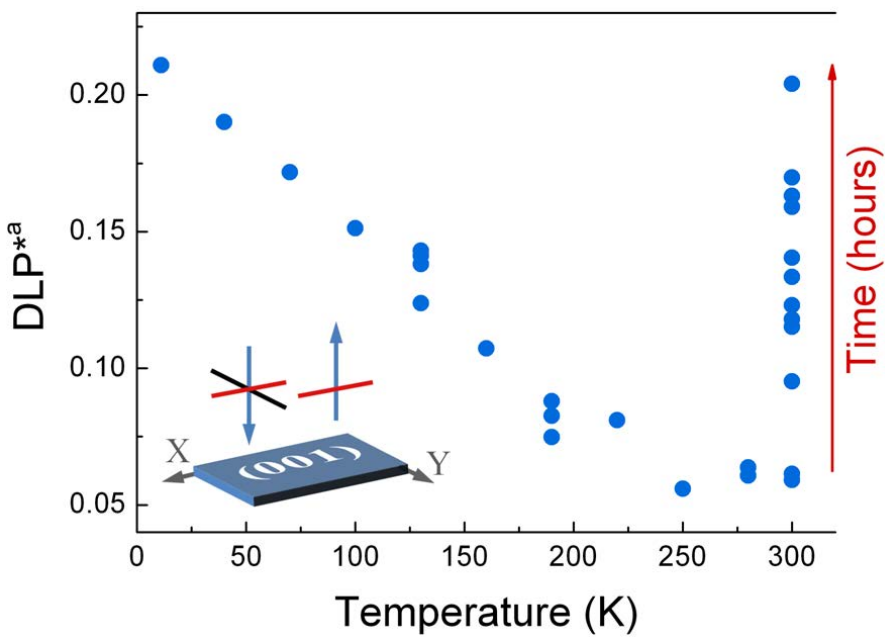


**Figure 6.12:** Temperature dependence of  $DLP^{*a}$ . The increase of the DLP with time is shown at 300K.

Obviously, none of the above mentioned temperature dependent mechanisms could be responsible for such behavior, so we may conclude that DLP itself probably does not depend on temperature. This conclusion is also supported by J. B. Schlager *et al* [6.39] for GaN NWs, by A. Balocchi *et al.*[6.1] for GaN/AlN quantum dot NWs and by theoretical calculations of InAs/InP QDot-NWs when the inhibition of the PL emission perpendicular to the NW is taken into account [6.34]. But observed behavior of  $DLP^{*a}$  can probably be explained as a phenomenon of precipitation of molecules onto the surface of NWs as the temperature is increased and following detachment at room temperature and normal pressure. That would cause increase of the diameter of the NWs, and lead to decrease of  $DLP^{*a}$ . However, the exact origin of this temperature dependence remains uncertain.

## 6.10 Conclusions.

In conclusion, polarization properties of single InP NWs, InAs/InP QWell-NWs, InAs/InP QRod-NWs and ensemble of the InAs well ordered NWs have been studied by means of PL spectroscopy. It was shown that polarization anisotropy of absorption may be attributed to the dielectric confinement that results in inhibition of the perpendicular component of PL emission. Theoretical calculation demonstrates that DLP<sup>a</sup> estimated from LFA model is in agreement with that obtained from the experiments on InAs/InP QRod-NWs. Polarization anisotropy of emission is the matter of higher diversity. For InP NWs the polarization of emission was shown to be determined mostly by selection rule of WZ material. However, it does not seem to be the case for NW heterostructures. QWell-NWs demonstrate maximum emission polarized parallel to the NW axis with DLP in 0.4 – 0.8 range. QRod-NWs demonstrate very strong polarization anisotropy of emission ( $DLP^e = 0.94$ ). This value is in agreement with that expected due to the small  $D/\lambda$  ratio, so we conclude that the anisotropy is mainly caused by the inhibition of the PL emission perpendicular to the NW.

Moreover, it was demonstrated that the polarization properties of the single QRod-NWs, being independent on temperature, was in agreement with theoretical predictions and could be correlated with the properties of ensembles of these NWs in the scopes of the proposed model. Furthermore, using this approach, the polarization anisotropy of the NWs was investigated as a function of excitation wavelength and temperature on the NW ensemble. A clear increase of the polarization ratio is observed as the excitation wavelength is increased in agreement with the theoretical prediction. So it was shown that the NW ensembles may be used to study the polarization properties of NWs.

## 6.11 References.

- [6.1] A. Balocchi, J. Renard, C. T. Nguyen, B. Gayral, H. Mariette, B. Daudin, G. Tourbot, X. Marie, and B. Columbia, "Temperature insensitive optical alignment of the exciton in nanowire embedded GaN Quantum Dots", *Physical Review B*, vol. 84, p. 235310, 2011.
- [6.2] Y. I. Mazur, W. Q. Ma, X. Wang, Z. M. Wang, G. J. Salamo, M. Xiao, T. D. Mishima, and M. B. Johnson, "InGaAs/GaAs three-dimensionally-ordered array of quantum dots", *Applied Physics Letters*, vol. 83, p. 987, 2003.
- [6.3] Y. Yu, V. Protasenko, D. Jena, H. G. Xing, and M. Kuno, "Photocurrent polarization anisotropy of randomly oriented nanowire networks", *Nano letters*, vol. 8, p. 1352, 2008.
- [6.4] X. Chen, A. Nazzal, D. Goorskey, M. Xiao, Z. Peng, and X. Peng, "Polarization spectroscopy of single CdSe quantum rods", *Physical Review B*, vol. 64, p. 245304, 2001.
- [6.5] L. V. Titova, T. B. Hoang, H. E. Jackson, L. M. Smith, J. M. Yarrison-Rice, Y. Kim, H. J. Joyce, H. H. Tan, and C. Jagadish, "Temperature dependence of photoluminescence from single core-shell GaAs-AlGaAs nanowires", *Applied Physics Letters*, vol. 89, p. 173126, 2006.
- [6.6] Y. Masumoto, Y. Hirata, P. Mohan, J. Motohisa, and T. Fukui, "Polarized photoluminescence from single wurtzite InP/InAs/InP core-multishell nanowires", *Applied Physics Letters*, vol. 98, p. 211902, 2011.
- [6.7] A. Mishra, L. V. Titova, T. B. Hoang, H. E. Jackson, L. M. Smith, J. M. Yarrison-Rice, Y. Kim, H. J. Joyce, Q. Gao, H. H. Tan, and C. Jagadish, "Polarization and temperature dependence of photoluminescence from zincblende and wurtzite InP nanowires", *Applied Physics Letters*, vol. 91, p. 263104, 2007.
- [6.8] H.-Y. Chen, Y.-C. Yang, H.-W. Lin, S.-C. Chang, and S. Gwo, "Polarized photoluminescence from single GaN nanorods: effects of optical confinement", *Optics express*, vol. 16, p. 13465, 2008.
- [6.9] J. Wang, M. S. Gudiksen, X. Duan, Y. Cui, and C. M. Lieber, "Highly polarized photoluminescence and photodetection from single indium phosphide nanowires", *Science*, vol. 293, p. 1455, 2001.
- [6.10] O. L. Muskens, J. Treffers, M. Forcales, M. T. Borgström, E. P. A. M. Bakkers, and J. G. Rivas, "Modification of the photoluminescence anisotropy of semiconductor nanowires by coupling to surface plasmon polaritons", *Optics Letters*, vol. 32, p. 2097, 2007.
- [6.11] G. L. Tuin, "Master Thesis: "Optical characterization of Wurtzite Indium Phosphide", Lund University, 2010.
- [6.12] G. Jacopin, L. Rigutti, S. Bellei, P. Lavenus, F. H. Julien, A. V Davydov, D. Tsvetkov, K. A. Bertness, N. A. Sanford, J. B. Schlager, and M. Tchernycheva, "Photoluminescence polarization in strained GaN/AlGaN core/shell nanowires", *Nanotechnology*, vol. 23, p. 325701, 2012.

- [6.13] M. H. M. van Weert, N. Akopian, F. Kelkensberg, U. Perinetti, M. P. van Kouwen, J. G. Rivas, M. T. Borgström, R. E. Algra, M. a Verheijen, E. P. a M. Bakkers, L. P. Kouwenhoven, and V. Zwiller, "Orientation-dependent optical-polarization properties of single quantum dots in nanowires", *Small*, vol. 5, p. 2134, 2009.
- [6.14] G. Bulgarini, M. E. Reimer, and V. Zwiller, "Optical polarization properties of a nanowire quantum dot probed along perpendicular orientations", *Applied Physics Letters*, vol. 101, p. 111112, 2012.
- [6.15] A. Sitt, A. Salant, G. Menagen, and U. Banin, "Highly emissive nano rod-in-rod heterostructures with strong linear polarization", *Nano letters*, vol. 11, p. 2054, 2011.
- [6.16] J. Treffers, "Optical properties of single indium phosphide nanowires on flat surfaces and metallic gratings", 2007.
- [6.17] E. G. Gadret, G. O. Dias, L. C. O. Dacal, M. M. de Lima, C. V. R. S. Ruffo, F. Iikawa, M. J. S. P. Brasil, T. Chiaramonte, M. a. Cotta, L. H. G. Tizei, D. Ugarte, and a. Cantarero, "Valence-band splitting energies in wurtzite InP nanowires: Photoluminescence spectroscopy and ab initio calculations", *Physical Review B*, vol. 82, p. 125327, 2010.
- [6.18] C. Wilhelm, A. Larrue, X. Dai, D. Migas, and C. Soci, "Anisotropic photonic properties of III-V nanowires in the zinc-blende and wurtzite phase", *Nanoscale*, vol. 4, p. 1446, 2012.
- [6.19] B. Ketterer, M. Heiss, E. Uccelli, J. Arbiol, and A. Fontcuberta i Morral, "Untangling the electronic band structure of wurtzite GaAs nanowires by resonant Raman spectroscopy", *ACS nano*, vol. 5, p. 7585, 2011.
- [6.20] D. Spirkoska, A. L. Efros, W. R. L. Lambrecht, T. Cheiwchanchamnangij, A. Fontcuberta i Morral, and G. Abstreiter, "Valence band structure of polytypic zinc-blende/wurtzite GaAs nanowires probed by polarization-dependent photoluminescence", *Physical Review B*, vol. 85, p. 045309, 2012.
- [6.21] S. Chuang and C. Chang, "K-P Method for Strained Wurtzite Semiconductors", *Physical Review B*, vol. 54, p. 2491, 1996.
- [6.22] M. Persson and H. Xu, "Giant polarization anisotropy in optical transitions of free-standing InP nanowires", *Physical Review B*, vol. 70, p. 161310, 2004.
- [6.23] P. C. Sercel and K. J. Vahala, "Polarization dependence of optical absorption and emission in quantum wires", vol. 44, p. 5681, 1991.
- [6.24] A. V. Maslov and C. Ning, "Radius-dependent polarization anisotropy in semiconductor nanowires", *Physical Review B*, vol. 72, p. 161310, 2005.
- [6.25] H. Ruda and A. Shik, "Polarization-sensitive optical phenomena in semiconducting and metallic nanowires", *Physical Review B*, vol. 72, p. 115308, 2005.

- [6.26] H. Ruda and A. Shik, "Polarization-sensitive optical phenomena in thick semiconducting nanowires", *Journal of Applied Physics*, vol. 100, p. 024314, 2006.
  - [6.27] L. D. Landau and E. M. Lifshitz, *Electrodynamics of Continuous Media*. Moscow: Nauka, 1992.
  - [6.28] J. Giblin, V. Protasenko, and M. Kuno, "Wavelength Sensitivity of Single Nanowire Excitation Polarization Anisotropies Explained through a Generalized Treatment of Their Linear Absorption", *ACS nano*, vol. 3, p. 1979, 2009.
  - [6.29] J. Giblin and M. Kuno, "Nanostructure Absorption: A Comparative Study of Nanowire and Colloidal Quantum Dot Absorption Cross Sections", *The Journal of Physical Chemistry Letters*, vol. 1, p. 3340, 2010.
  - [6.30] T. B. Hoang, L. V Titova, J. M. Yarrison-Rice, H. E. Jackson, A. O. Govorov, Y. Kim, H. J. Joyce, H. H. Tan, C. Jagadish, and L. M. Smith, "Resonant excitation and imaging of nonequilibrium exciton spins in single core-shell GaAs-AlGaAs nanowires", *Nano letters*, vol. 7, p. 588, 2007.
  - [6.31] H. Yang, X. Mu, I. B. Zotova, Y. J. Ding, and G. J. Salamo, "Self-assembled InAs quantum wires on InP(001)", *Journal of Applied Physics*, vol. 91, p. 3925, 2002.
  - [6.32] B. Salem, J. Olivares, G. Guillot, G. Bremond, J. Brault, C. Monat, M. Gendry, G. Hollinger, F. Hassen, and H. Maaref, "Optical properties of self-assembled InAs quantum islands grown on InP(001) vicinal substrates", *Applied Physics Letters*, vol. 79, p. 4435, 2001.
  - [6.33] M. Winkelnkemper, A. Schliwa, and D. Bimberg, "Interrelation of structural and electronic properties in  $\text{In}_{(x)}\text{Ga}_{(1-x)}\text{N}/\text{GaN}$  quantum dots using an eight-band  $k \cdot p$  model", *Physical Review B*, vol. 74, p. 155322, 2006.
  - [6.34] Y.-M. Niquet and D. Mojica, "Quantum dots and tunnel barriers in InAs/InP nanowire heterostructures: Electronic and optical properties", *Physical Review B*, vol. 77, p. 115316, 2008.
  - [6.35] J. Bleuse, J. Claudon, M. Creasey, N. S. Malik, J.-M. Gérard, I. Maksymov, J.-P. Hugonin, and P. Lalanne, "Inhibition, enhancement, and control of spontaneous emission in photonic nanowires", *Physical Review Letters*, vol. 106, p. 103601, 2011.
  - [6.36] G. Narvaez, G. Bester, A. Franceschetti, and A. Zunger, "Excitonic exchange effects on the radiative decay time of monoexcitons and biexcitons in quantum dots", *Physical Review B*, vol. 74, p. 205422, 2006.
  - [6.37] A. Lan, J. Giblin, V. Protasenko, and M. Kuno, "Excitation and photoluminescence polarization anisotropy of single CdSe nanowires", *Applied Physics Letters*, vol. 92, p. 183110, 2008.
  - [6.38] P. Lavallard and R. A. Suris, "Polarized photoluminescence of an assembly of non cubic microcrystals in a dielectric matrix", *Solid State Communications*, vol. 95, p. 267, 1995.
  - [6.39] J. B. Schlager, N. A. Sanford, K. a. Bertness, J. M. Barker, A. Roshko, and P. T. Blanchard, "Polarization-resolved photoluminescence study of individual GaN nanowires grown by catalyst-free molecular beam epitaxy", *Applied Physics Letters*, vol. 88, p. 213106, 2006.
-

# **Chapter VII**

---

## Piezoelectricity of wurtzite nanowire heterostructures

- 7.1      Introduction.
- 7.2      Experimental results: piezoelectric field observation.
- 7.3      Experimental results: impact of temperature.
- 7.4      Simulation of piezoelectric field in nanowire heterostructures.
- 7.5      Simulation results.
- 7.6      Conclusions.
- 7.7      References.

## 7.1 Introduction.

Advances in epitaxial growth technology provide possibilities for growth of nanowire (NW) heterostructures with well controlled dimensions, position [7.1] and crystal structure [7.2], offering various types of piezoelectric structures for piezo-mechanical [7.3, 7.4] and photovoltaic applications [7.5 – 7.7]. However, only few works were published on experimental studies of the piezoelectric field influence on the optical properties of InAs/InP NW heterostructures. It is known that the epitaxial NW heterostructures grown of materials with dissimilar lattice constant, acquire the elastic strain fields [7.8]. Such strain fields were demonstrated experimentally and theoretically for WZ InAs/InP NW QDots [7.9]. Under the applied stress certain crystals develop an electric moment whose magnitude is proportional to the stress. This phenomenon is known as direct piezoelectric effect [7.10]. In ZB materials, due to the symmetry of the strain tensor, the piezoelectric effect is negligible, while in the WZ materials strong built-in fields can be generated under applied strain [7.11]. This effect was shown for such WZ semiconductor structures as QWells [7.12], QDots [7.13] and NWs [7.14, 7.15]. This piezoelectric field in its turn can affect the optical properties of the heterostructures grown from piezoelectric materials, as it was experimentally shown for one-dimensional structures such as AlGaAs/GaAs quantum wires [7.16], GaN based axial QWell-NWs [7.17, 7.18] and theoretically demonstrated for InAs/InP core-shell NWs [7.6].

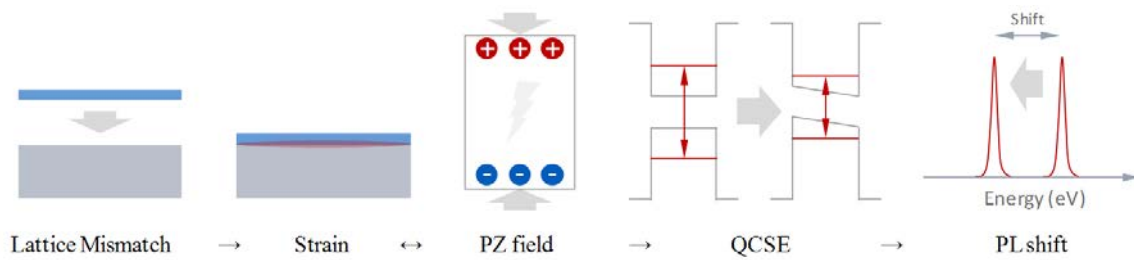


**Figure 7.1:** Scheme of processes leading from lattice mismatch to the PL emission shift.

Recently, the elastic and piezoelectric properties of WZ and ZB InAs/InP NW heterostructures have been studied using electroelastically coupled continuum elasticity theory [7.19]. In that work, authors show that the strain-induced piezoelectric field of few mV/nm can appear in InAs QDots of various dimensions, especially in the WZ type. In the present chapter, we describe the experimental confirmation of presence of the piezoelectric field in InAs/InP QRod-NWs and its impact on the optical properties of the structure.

## 7.2 Experimental results: piezoelectric field observation.

To study the NWs by means of  $\mu$ PL, the NWs were ultrasonically removed from the as-grown substrate and transferred onto a TEM copper grid, served as a host-substrate. The sample was mounted in a He-flow cryostat and cooled to 10 K. The excitation was provided by a continuous wave He-Ne laser beam (632.8 nm) focused by a microscope objective to a spot size of  $\approx 4 \mu\text{m}$ .

A dozen of single InAs/InP QRod-NWs was studied.  $\mu$ PL emission of each NW was measured as a function of laser power. Typical evolution of spectrum with the excitation power is shown in Figure 7.2.a. The analysis of the  $\mu$ PL emission peak position and its FWHM as a function of excitation power clearly revealed two types of dependences.

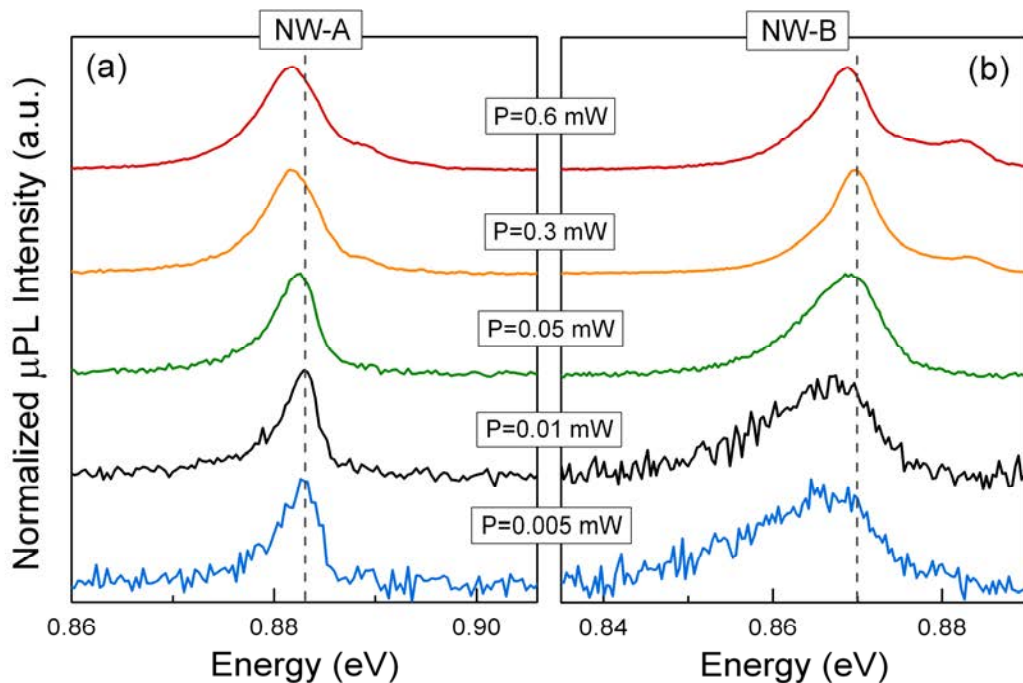


**Figure 7.2:** Normalized spectra of  $\mu$ PL emission at different values of excitation power measured on NW-A (a) and NW-B (b) at temperature of 10K. Dashed lines are guides to the eye.

The first type, represented by NW-A, shows classical redshift and broadening of the peak as the excitation power is increased (Figure 7.2.a), while the second type, represented by NW-B, demonstrates a different dependence. Being broad and redshifted at low excitation power, the peak is blueshifting and reducing its FWHM as the excitation power is increased up to 3 mW (Figure

7.2.b). At high excitation power both types demonstrate similar broadenings and redshifts. Figures 7.3.a and 7.3.b show positions of the  $\mu$ PL emission peaks of NW-A and NW-B as functions of the excitation power. While NW-A demonstrates a small redshift, NW-B shows significant blueshift as the laser power is increased. The blueshift and narrowing of the PL emission with the excitation power increase are typically related to an electric field screening and explained in terms of quantum confinement Stark effect (QCSE). In the present case, due to the lattice mismatch between InAs and InP materials, the InAs QRods are strained, so the strain-induced piezoelectric polarization inducing an electric field may indeed be expected.

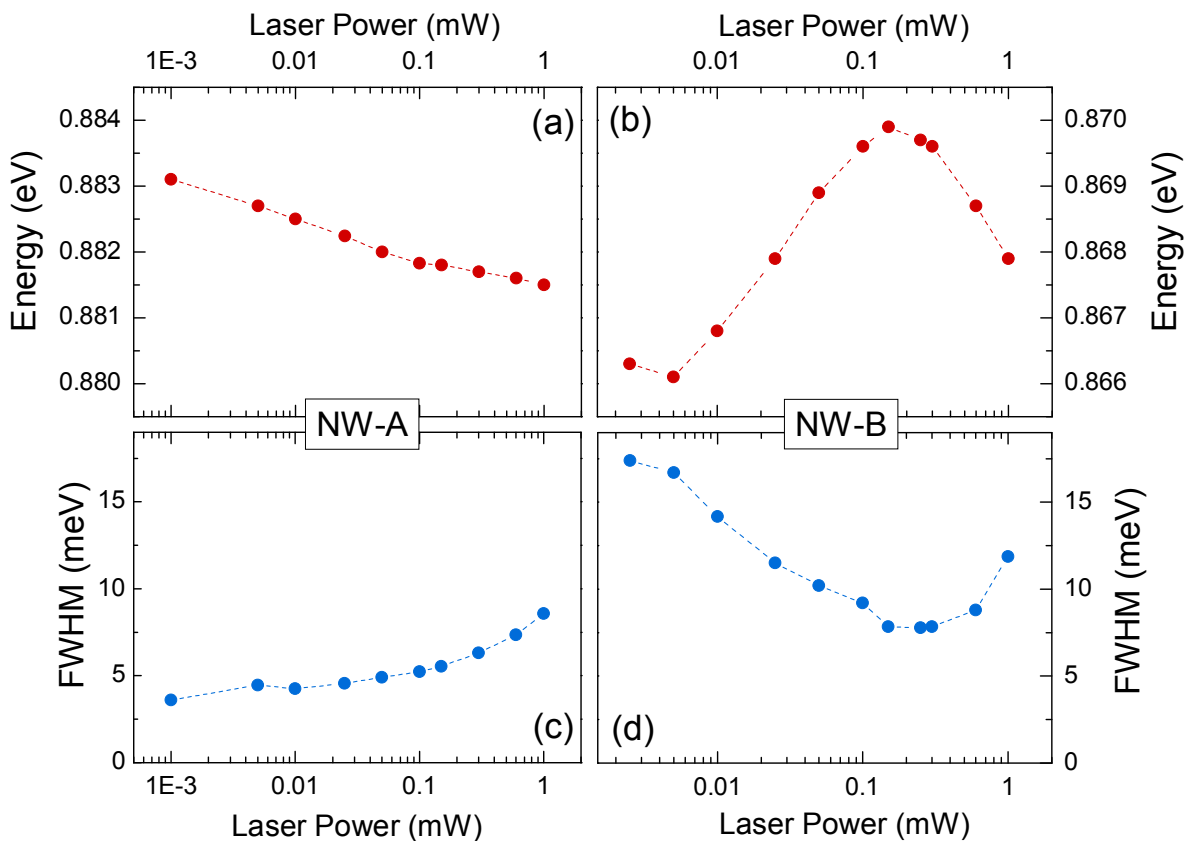


**Figure 7.3:** Position of the  $\mu$ PL emission peak (a, b) and FWHM (c, d) as functions of excitation power, measured on NW-A and NW-B at temperature of 10 K.

Therefore, the QCSE, caused by this piezoelectric field, can affect the optical properties. It is known, that the piezoelectric field depends on dimensions of the structure [7.25 – 7.27], so the value of the piezoelectric field can vary from one NW to another, depending on the size of QRod.

So assuming a weak piezoelectric field (or absence of the field) for NW-A, but strong for NW-B, the results on NW-B can be explained in terms of the QCSE. Indeed, at low excitation power the energy of  $\mu$ PL emission is decreased due to the carrier separation, but increasing the laser power the piezoelectric field can be screened by photogenerated carriers, so the QCSE is getting weaker as the laser power is increased leading to the blueshift of  $\mu$ PL emission (Figure 7.3.b). As the excitation power is reaching 0.2 mW the piezoelectric field is completely screened, and the following increase of the power is leading to the standard redshift. On the other hand, the QCSE causes broadening of the peak. Since the increase of the excitation power reduces the QCSE, the FWHM is decreasing too as the laser power is increased (Figure 7.3.d). When the piezoelectric field is screened at 2 mW, the FWHM starts to increase with laser power due to the band filling effect, coming to agreement with the normal peak broadening of NW-A in the absence of the field (Figure 7.3.c). Similar piezoelectric effects have already been observed in QWell [7.20] and quantum wire [7.16, 7.21] structures.

### 7.3 Experimental results: impact of temperature.

To check the impact of temperature on the piezoelectric field, the measurements were repeated at different temperatures. Figures 7.4.a and 7.4.b show the evolution of FWHM with temperature. For the NW-A, where no piezoelectric field was observed, the dependence is linear, and the difference between the values of FWHM, measured at different values of excitation power, remains small (Figure 7.4.a).

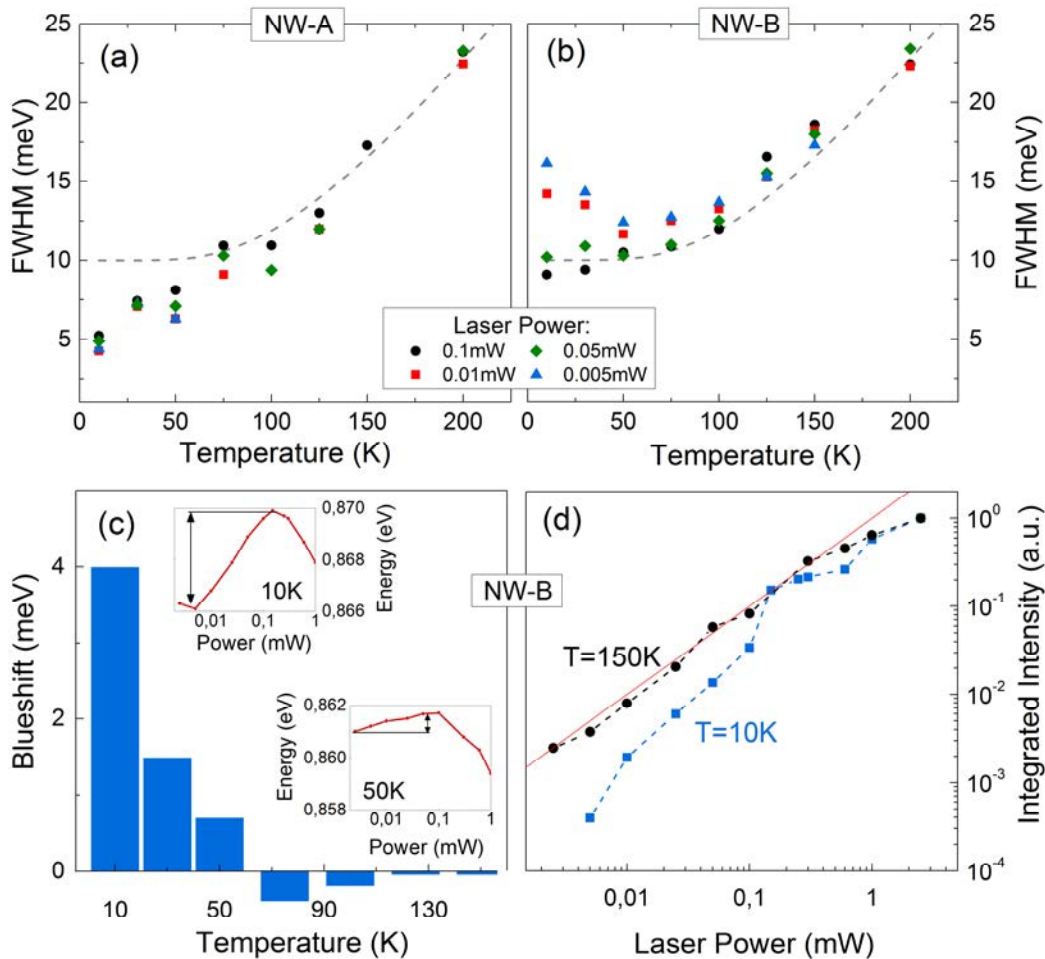


**Figure 7.4:** FWHM, measured on NW-A (a) and NW-B (b) at different values excitation power, as a function of temperature. Dashed lines represent theoretical fit. (c) Blueshift of the emission peak of NW-B in 0.005 – 0.2 mW range as a function of temperature. The inner plots show the position of the peak dependence on the excitation power at 10 K and 50 K. (d) Normalized integrated  $\mu$ PL intensity as a function of the excitation power. The red line shows the linear dependence proportional to one.

NW-B, on the contrary, demonstrates as broader peak as lower is the excitation power, at low temperature, but as the temperature is increased up to 75 K, this excitation power dependence vanishes (Figure 7.4.a). At this temperature the carriers are thermally activated so that their energy is  $\approx kT = 6.5$  meV, which presumably overcomes the energy of the piezoelectric field and the field effect is diminished. Homogeneous broadening of the FWHM with temperature, when the piezoelectric field is screened, can be explained by LO phonon scattering. The red curves in Figures 7.4.a and 7.4.b represent the Bose-Einstein statistics:

$$\Gamma = \Gamma_0 + \frac{\Gamma_{ph}}{e^{h\Omega_{LO}/kT} - 1}$$

where  $\Gamma_0$  is an inhomogeneous term accounting for interface roughness and  $\Gamma_{ph}$  represents the homogeneous broadening due to scattering by phonons. To obtain the best fit the values  $\Gamma_0 = 10$  meV and  $\Gamma_{ph} = 60$  meV were used.

Moreover, the blueshift of  $\mu$ PL emission, observed on NW-B at low temperature, is also decreasing with temperature due to the thermal carrier activation, and vanishes at 75 K (Figure 7.4.c). At this temperature the carriers obtain enough energy to overcome the field, so they can recombine with the energy of the band gap. In other words, the probability of recombination is highest in the place where overlap of their wavefunctions is the most, which corresponds to the case of direct transitions, if the carriers are not separated by an electric field.

On the other hand, in case of carrier separation (i.e. at low temperature and weak excitation power) the overlap of the carrier wavefunctions, separated by the electric field, is decreased. The overlap decrease means low probability of recombination and consequently low intensity of the emission. This effect is demonstrated in Figure 7.4.d. At relatively high temperature (150 K) the piezoelectric field can not separate carriers and we see nearly linear dependence of the intensity, while at low temperature, the dependence is linear only above 0.2 mW, where the piezoelectric field is screened. Below this value, the field is not screened and the carriers are separated, as it was concluded above, so we see faster decrease of intensity with laser power as compared to the case of high temperature.

## 7.4 Simulation of piezoelectric field in nanowire heterostructures.

To fully understand the piezoelectric phenomena taking place in the QRods and to check the impact of the QRod geometry on the field, we present the calculation of the expected piezoelectric field inside our QRod-NWs. Recently, simulation results on piezoelectric effects in WZ InAs/InP NW heterostructures have been published by F. Boxberg *et al* [7.19]. It was shown that a significant electric field may be induced in WZ InAs/InP QDot-NWs due to the lattice mismatch. If the strain profile is not difficult to approximate (lattice parameters and elastic coefficients are known), the situation is different for the calculation of the piezoelectric field. The piezoelectric polarization ( $P_{\text{piezo}}$ ) is proportional to the strain tensor ( $\epsilon_{ijk}$ ) as  $P_{\text{piezo}} = e_{ijk} \epsilon_{ijk}$ , where  $e_{ijk}$  is a tensor of piezoelectric constants. In WZ material there are only three non-zero components:  $e_{31}$ ,  $e_{33}$  and  $e_{15}$ . However, the piezoelectric coefficients and the spontaneous polarization are not well known for the InAs and InP in WZ crystallographic phase. A first strategy to estimate the piezoelectric coefficients would be to use the quasi cubic approximation which allows us to calculate the WZ piezo constants from the piezo coefficient  $e_{14}$  of the ZB phase [7.22]:

$$e_{15} = e_{31} = -e_{14}/\sqrt{3}, \quad e_{33} = 2e_{14}/\sqrt{3}$$

More recently, the coefficients have been calculated by first-principle calculations [7.23]. As shown in Table 7.1, the obtained values differ strongly from those estimated using the quasi-cubic approximation. We have decided to choose the values given by the first-principle calculations (taken from [7.19]) for our simulations.

**Table 7.1:** Piezoelectric constants of InAs and InP materials of WZ type calculated by first-principle calculations. The values estimated from quasi-cubic approximation are given in brackets.

	<b>WZ InP</b>	<b>WZ InAs</b>
$e_{33}$	0.086 ( 0.069 )	-0.028 (-0.057)
$e_{31}$	0.101 (-0.034)	-0.045 ( 0.028 )
$e_{15}$	0.071 (-0.034)	0.040 ( 0.028 )

As far as the spontaneous polarization is concerned, no specific value has been found in the literature. However, this parameter is usually neglected in the calculation of InP WZ/ZB

superlattices [7.24] or InAs/InP NWs [7.19]. The spontaneous polarization is assumed to be rather small for WZ InP: the value is expected to be weaker than that of InN ( $-0.03 \text{ C/m}^2$ ) [7.24]. Thus, we will neglect the spontaneous polarization in the calculation.

To check the validity of the ‘‘Nextnano<sup>3</sup>’’ software, calculations are first performed using the same material parameters and NW geometry as in [7.19]. In the present calculation, by contrast with the simulation in Chapter 5, the piezoelectricity of the materials is included. For the sake of comparison we assume the round shape of NWs (instead of hexagonal). First, we compare the strain distribution in a WZ InP NW (18 nm in diameter) containing a cylindrical InAs QDot of 8 nm in diameter and in height.

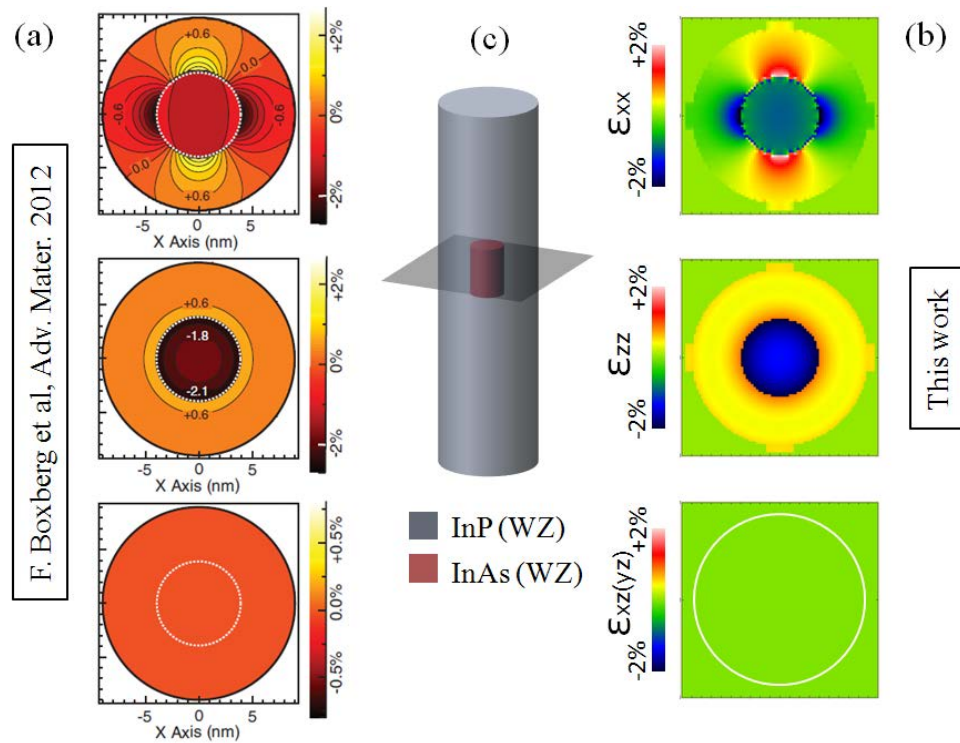


**Figure 7.5:** Calculated strain distribution in WZ InAs/InP QDot-NWs. (a) Results from [7.19]. (b) Results obtained in this work. (c) Schematic illustration of QDot-NW geometry.

Figure 7.5 shows calculated strain distribution in WZ InAs/InP QDot-NWs. In case of diagonal strain components, nearly 2% strain is induced by the lattice mismatch, whereas no strain is observed for  $xz$  or  $yz$  components. These results are in good agreement with the strain distribution calculated by F. Boxberg *et al* [7.19] (Figures 7.5.a and 7.5.b). This strain applied to piezoelectric material leads to the carrier separation along Z axis and the resulted potential in

QDot is shown in Figure 7.6. The potential obtained in our simulation is slightly lower than that obtained in [7.19], but in general the shapes of the potentials are very close.

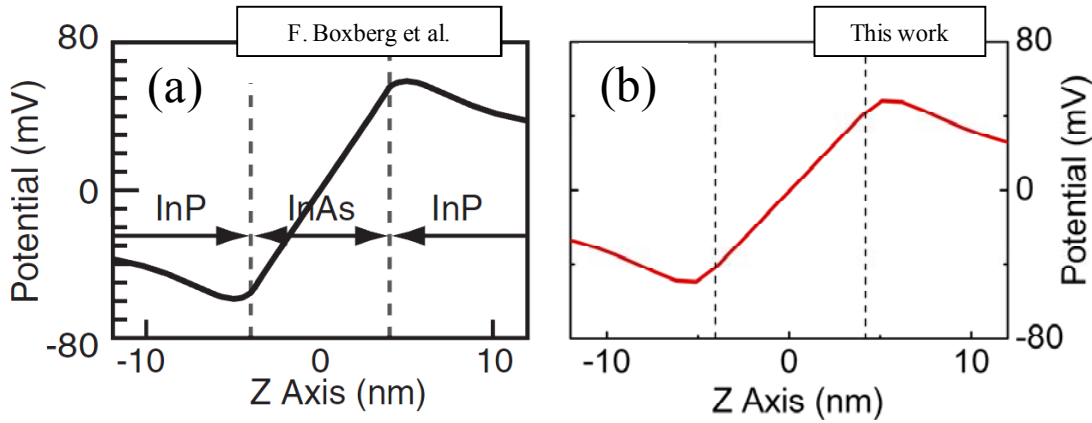


**Figure 7.6:** Potential in WZ InAs/InP QDot-NWs calculated in [7.19] (a) and in this work (b).

It was also shown by Boxberg *et al* [7.19] that the piezoelectric field strongly depends on the dimensions of the QDot. To confirm this dependence we simulated QDots of various dimensions, so that the radius ( $r_1$ ) and height (h) of the InAs QDot were varied in 4 – 16 nm range. The electric field is defined by the potential difference between the bottom and the top of the QDot divided by the distance between these points.

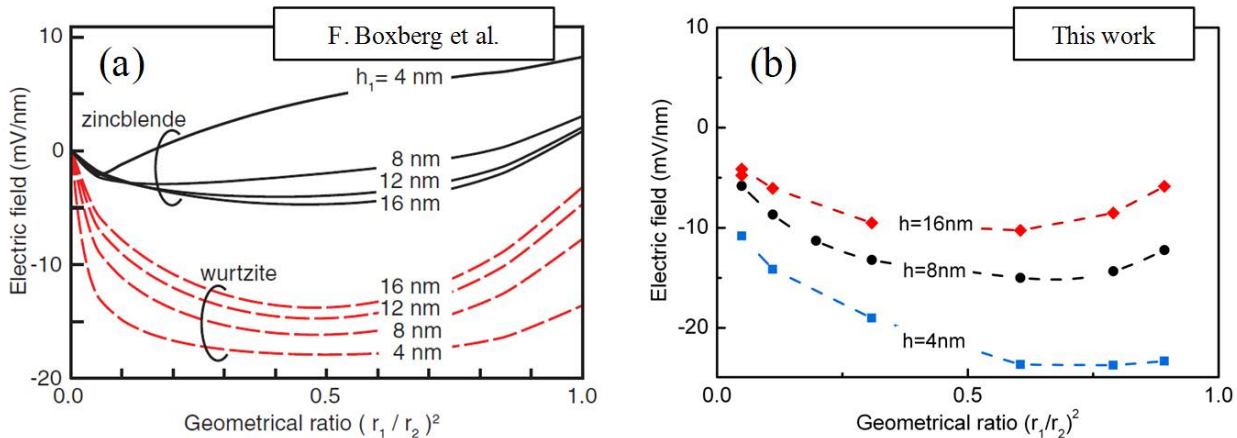


**Figure 7.7:** Electric field in a QDot as a function of its dimensions (h is height of QDot,  $r_1$  and  $r_2$  are radii of QDot and NW correspondingly).

Figure 7.7 shows principal agreement of electric field dependence on the QDot dimensions between that calculated in this work and in [7.19]. So we may conclude that the piezoelectric field, being dependent on the strain, depends on the QDot dimensions as a consequence.

## 7.5 Simulation results.

Once the simulation is verified we may proceed to the investigation of the electric field in our QRod-NWs. In this case, height of QRod is much larger than the radius, the ratio of  $r_1 / r_2$  is small and the hexagonal cross section in accordance with a wurtzite NW grown along the [0001] axis is assumed. Figure 7.8 shows the simulated geometry of a WZ InAs/InP QRod-NW and the calculated strain distribution in it.

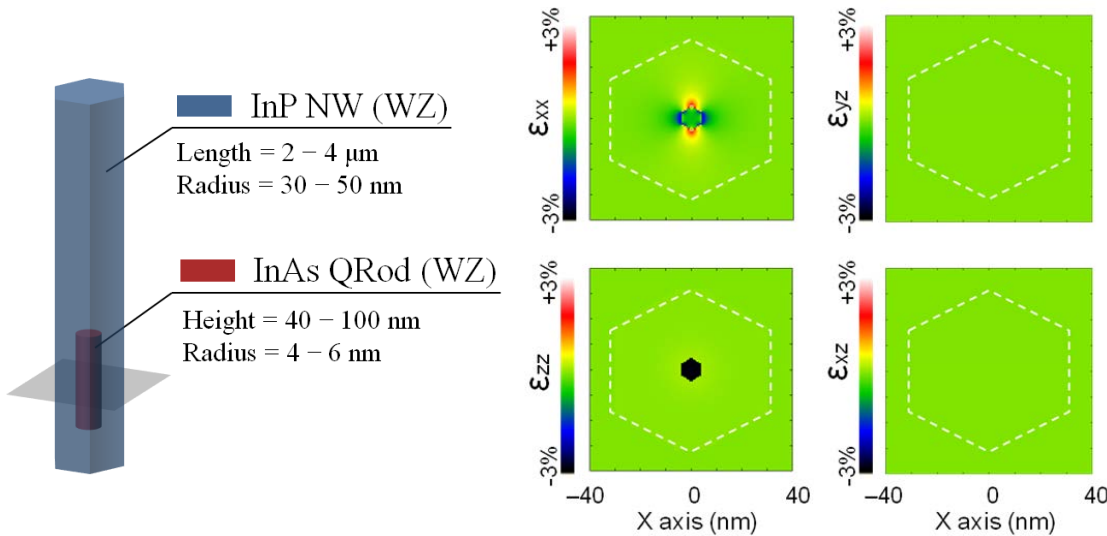


**Figure 7.8:** Schematic illustration of QRod-NW geometry and calculated strain distribution in a WZ InAs/InP QRod-NW.

Despite the difference in geometry the strain distribution remains nearly the same as in case of QDot-NWs described previously. However, the spatial potential distribution caused by this strain, is slightly different from that in QDot-NWs (Figure 7.9.a). The minimum and maximum of the potential are localized along the z-axis, close to the InAs/InP interfaces. Contrary to the result obtained in [7.19], the potential profile is not a linear slope inside the QRod. This is a consequence of the big length of the QRod as compared to its diameter. An averaged electric field can be calculated using the potential difference between the two QRod extremities and a field of 40 kV/cm is obtained. The impact of the QRod length and diameter on the electric field is shown in Figure 7.9.b. The average electric field is increasing as the diameter is increased and the length is decreased.

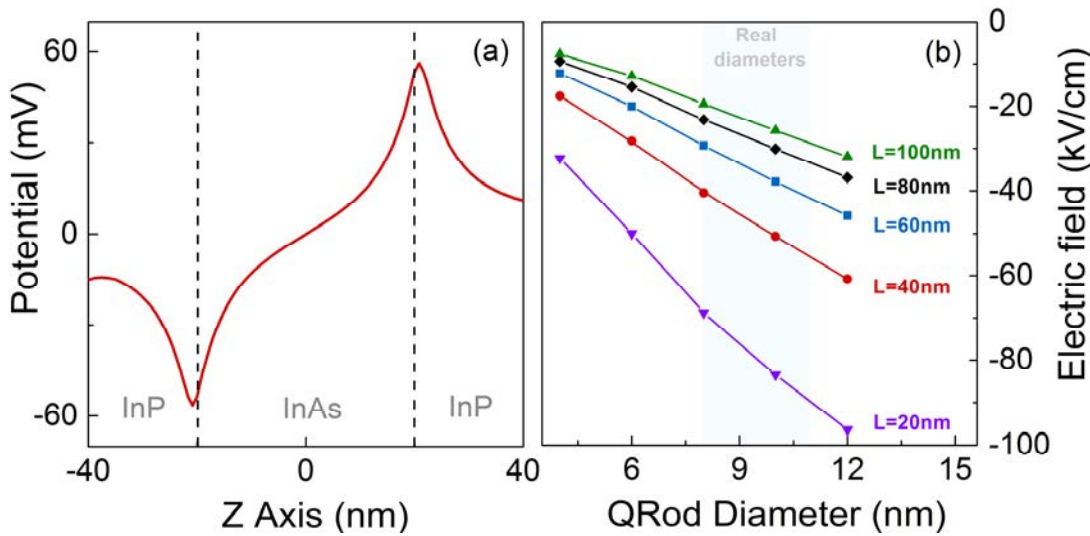


**Figure 7.9:** (a) Calculated potential in WZ InAs/InP QRod-NW NW along the NW axis and (b) the electric field in a QRod as a function of its dimensions. The blue region shows the range of diameters measured in our QRod-NWs.

This fact is very important for understanding of the existence of the two types of QRod-NWs. Indeed, NWs containing QRods of smaller radius and/or larger length must have smaller piezoelectric field and as a consequence smaller PL emission shift due to the QCSE. On the other hand, it is known that QCSE itself depends on the quantum confinement and becomes negligible for QDots of a small radius [7.25 – 7.27].

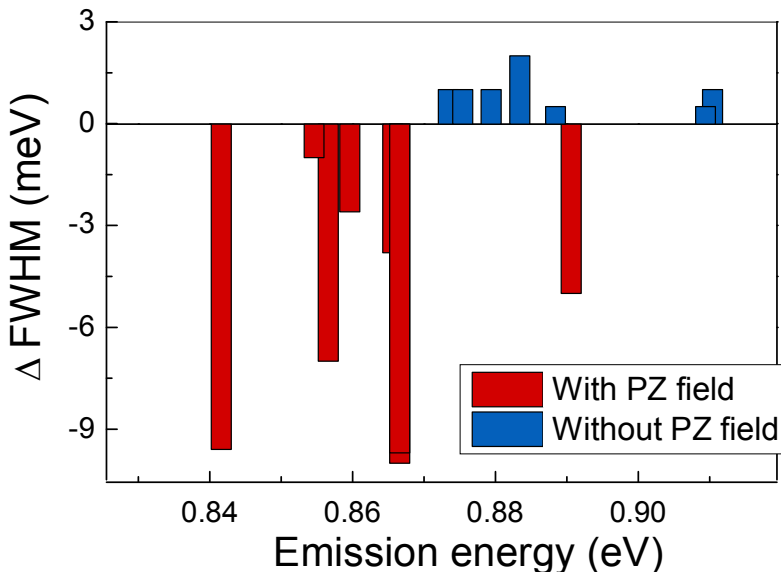


**Figure 7.10:** Narrowing of the PL emission peak as a function of the emission energy for the NWs of the two types.

In any event, PL emission shift caused by the piezoelectric field may be radius dependent one way or the other. This explanation is confirmed by our experimental results. Several QRods have been investigated and the linewidth narrowing (measured between 0.002 mW and 0.2 mW) is reported in Figure 7.10 as a function of the QRod emission energy. The FWHM narrowing, which is directly related to the presence of a piezoelectric field, is mainly observed for QRod emitting below 0.87 eV. In these NW heterostructures, the QRod diameter is smaller than the QRod length which means that the emission of the ground state is controlled by the QRod diameter. Therefore, the correlation observed between the linewidth narrowing and the emission energy means that the piezoelectric field is mainly driven by the diameter and increases for bigger diameters. This observation is in agreement with the fact that the QCSE itself depends on the size of a structure and becomes negligible for QDs of a small diameter. It is however not clear which of the two effects is responsible for this phenomenon, strain dependence on radius, QCSE dependence or both.

The second key result is the difference between the theoretical electric field and the measured blueshift of PL emission. Although the measured value is not directly related to the electric field, but controlled by QCSE, its value however is much smaller than expected for such field. This result can be explained assuming that the electric field is already partly screened when we start to see PL emission. Indeed, when the electric field is unscreened, the carriers should be strongly separated along the length of the QRod and, as a consequence, no PL emission is expected. To provide a qualitative explanation of the screening phenomena, we should consider the electric field in a QRod. The spatial distribution of the electric field along the QRod axis in the absence of excitation is illustrated in Figure 7.11.a. When the laser excitation is provided, the electrons and holes are separated in space, and will induce a partial screening of the piezoelectric field.

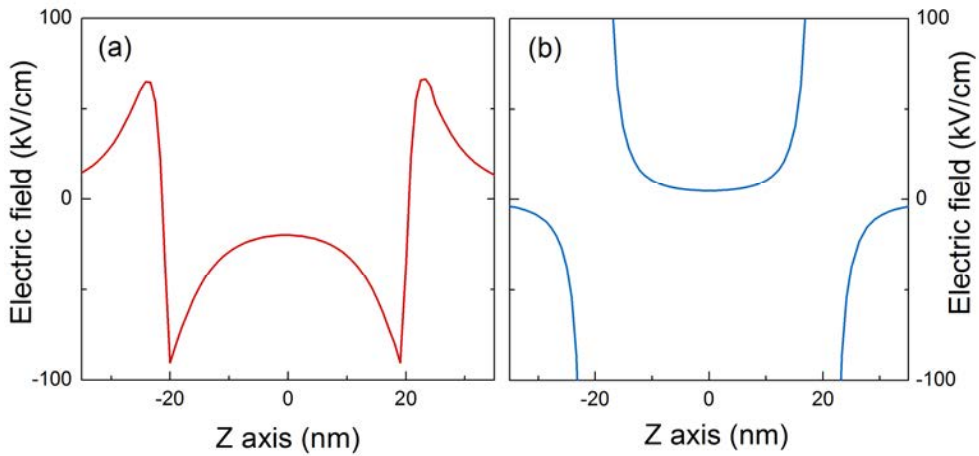


**Figure 7.11:** Calculated electric field profile in WZ InAs/InP QRod-NW (a) and the electric field profile of an electric dipole (b).

In the following part, we will describe this laser induced electron-hole pair as a dipole where charges are located at the boundaries of the QRod. According to the principle of superposition, the electric field of a dipole is  $E_{\text{dipole}} = E_+ + E_-$ , where  $E_+$  and  $E_-$  are the electric fields of charges  $q$  and  $-q$ . So according to Coulomb's law the electric field of a dipole can be calculated as:

$$E_{\text{dipole}} = E_+ + E_- = \frac{1}{4\pi\epsilon_0\epsilon_{\text{InAs}}} \left( \frac{q}{(z+h/2) \cdot |z+h/2|} + \frac{-q}{(z-h/2) \cdot |z-h/2|} \right)$$

where  $z$  is the coordinate along  $z$  axis and  $h$  is distance between the charges (i.e. QRod length in our case). The electric field of an electric dipole ( $h = 40$  nm) is shown in Figure 7.11.b.

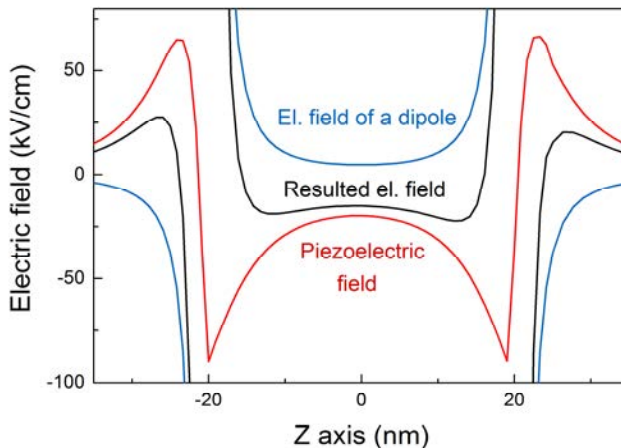


**Figure 7.12:** Electric field screening by an electric dipole.

So the superposition of the piezoelectric and dipole electric fields results in screening of the piezoelectric field (Figure 7.12). An increase of the number of electron-hole pairs, leads to further screening of the electric field, and several electron-hole pairs are enough to screen the field completely (Figure 7.13.a).

Previously we have concluded that a noticeable piezoelectric field exists only in NWs with QRods of relatively large radius. The simulation of QRod emission energy as a function of its radius, presented in Chapter 5.5, showed that the emission in 0.84 – 0.87 eV and 0.87 – 0.91 eV ranges should be related to 5.5 nm and 4.5 nm radius QRods, respectively. Consequently, we may expect faster screening in the QRods of lower radius. This situation is demonstrated in Figure 7.13.b, where clearly several electron-hole pairs are needed to screen the electric field in QRod of large diameter, while only few electron-hole pair is enough to screen the field in a thinner QRod.

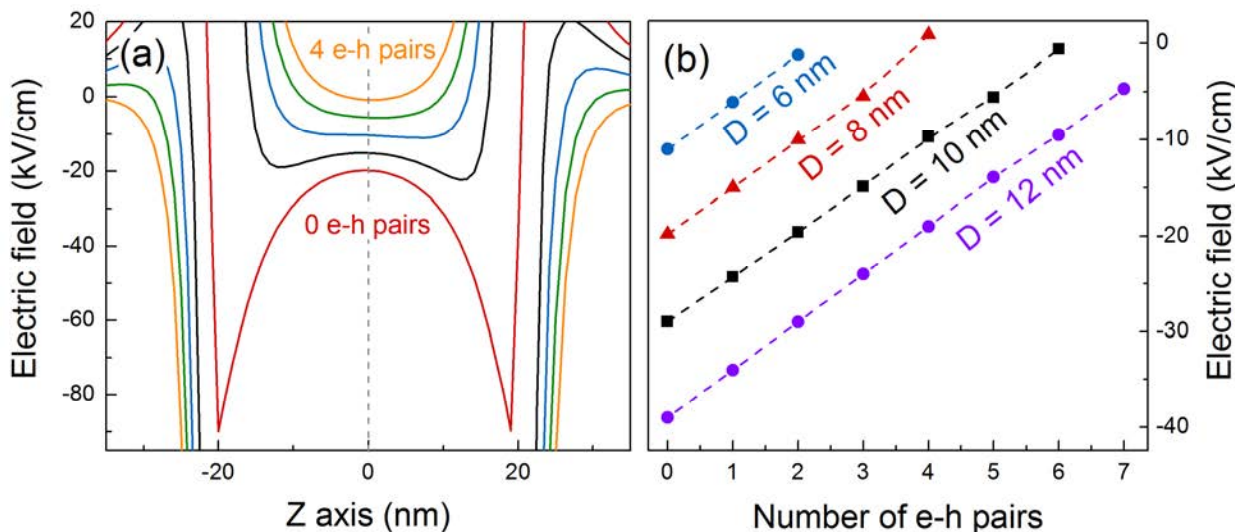


**Figure 7.13:** Screening of a piezoelectric field by e-h pairs. (a) Spatial distribution of the electric field for different number of e-h pairs in a QRod of 4 nm in radius and (b) electric field in the center of QRods of various radii as a function of the number of electron-hole pairs.

However, these simulation results only aim to explain the phenomenon of screening qualitatively. Here, we have considered only the electric field in the center of QRods, though the matter may be more complicated since the field is not uniform and the values of potential at the edges of QRods may differ from the values in the center.

## 7.6 Conclusions.

We report on the evidences of the strain-induced piezoelectric field in WZ InAs/InP QRod-NWs. This electric field caused by the lattice mismatch between the InAs and InP results in a QCSE and, as a consequence, affects the optical properties of the structure. Namely, PL emission blueshift and peak narrowing are observed in one group of NWs as the excitation power is increased, in contrast to the other group where no such effects were observed. It was shown that this piezoelectric field could be screened by photogenerated carriers or its impact could be removed by increasing temperature. In this case, above certain values of the excitation power or temperature PL peak position and FWHM were showing the dependences indistinguishable from those of NWs showing no piezoelectric field.

Moreover, the piezoelectric effect was theoretically demonstrated in WZ InAs/InP QRod(QDot)-NW structures and was shown to be in good agreement with the similar results in the literature [7.19]. Summarizing, it is shown that lattice mismatch between NW and QRod materials leads to a considerable strain, which generates a piezoelectric field and carrier separations along the QRod. In this case, the potential depends on the dimensions of the QRod, especially the radius, so that the PL emission shift may be radius dependent. This assumption was confirmed by statistical analysis of the experimental results. It was shown that the NWs exhibiting the piezoelectric field emit at lower energy than those showing no signs of piezoelectric field, so the existence of two groups of NWs may be attributed to the difference in radius of QRods.

In conclusion, it was shown that piezoelectric effect in WZ NW heterostructures could affect the optical properties, decreasing the intensity of PL emission and broadening the emission peak. This effect however can if needed be avoided by designing NW heterostructures with QRods (QDots) of lower dimensions. On the contrary, if the effect is desirable for carrier separation in photovoltaic applications [7.6] the design of heterostructures should suggest the larger possible strain between the components.

## 7.7 References.

- [7.1] T. Mårtensson, M. T. Borgström, L. Samuelson, W. Seifert, and B. J. Ohlsson, "Fabrication of individually seeded nanowire arrays by vapour–liquid–solid", *Nanotechnology*, vol. 14, p. 1255, 2003.
- [7.2] A. Fuhrer, L. E. Fröberg, J. N. Pedersen, M. W. Larsson, A. Wacker, M.-E. Pistol, and L. Samuelson, "Few electron double quantum dots in InAs/InP nanowire heterostructures", *Nano letters*, vol. 7, p. 243, 2007.
- [7.3] X. Wang, K. Kim, Y. Wang, M. Stadermann, A. Noy, A. V Hamza, J. Yang, and D. J. Sirbuly, "Matrix-Assisted Energy Conversion in Nanostructured Piezoelectric Arrays", *Nano letters*, vol. 10, p. 4901, 2010.
- [7.4] Z. Wang, J. Hu, A. P. Suryavanshi, K. Yum, and M.-F. Yu, "Voltage generation from individual BaTiO(3) nanowires under periodic tensile mechanical load.", *Nano letters*, vol. 7, p. 2966, 2007.
- [7.5] R. R. LaPierre, a. C. E. Chia, S. J. Gibson, C. M. Haapamaki, J. Boulanger, R. Yee, P. Kuyanov, J. Zhang, N. Tajik, N. Jewell, and K. M. a. Rahman, "III-V nanowire photovoltaics: Review of design for high efficiency", *Physica Status Solidi (RRL)*, vol. 16, 2013.
- [7.6] F. Boxberg, N. Søndergaard, and H. Q. Xu, "Photovoltaics with piezoelectric core-shell nanowires", *Nano letters*, vol. 10, p. 1108, 2010.
- [7.7] C. Colombo, M. Heiß, M. Gratzel, and A. Fontcuberta i Morral, "Gallium arsenide p-i-n radial structures for photovoltaic applications", *Applied Physics Letters*, vol. 94, p. 173108, 2009.
- [7.8] J. Gronqvist, N. Sondergaard, F. Boxberg, T. Guhr, S. Aberg, and H. Q. Xu, "Strain in semiconductor core-shell nanowires", *Journal of Applied Physics*, vol. 106, p. 053508, 2009.
- [7.9] M. W. Larsson, J. B. Wagner, M. Wallin, P. Håkansson, L. E. Fröberg, L. Samuelson, and L. R. Wallenberg, "Strain mapping in free-standing heterostructured wurtzite InAs/InP nanowires", *Nanotechnology*, vol. 18, p. 015504, 2007.
- [7.10] J. F. Nye, *Physical Properties of Crystals*. Oxford: Oxford University Press, 1985, p. 110.
- [7.11] I. Vurgaftman, J. R. Meyer, and L. R. Ram-Mohan, "Band parameters for III–V compound semiconductors and their alloys", *Journal of Applied Physics*, vol. 89, p. 5815, 2001.
- [7.12] S. Park and S. Chuang, "Crystal-orientation effects on the piezoelectric field and electronic properties of strained wurtzite semiconductors", *Physical Review B*, vol. 59, p. 4725, 1999.
- [7.13] V. a. Fonoberov and A. a. Balandin, "Excitonic properties of strained wurtzite and zinc-blende GaN/Al<sub>x</sub>Ga<sub>1-x</sub>N quantum dots", *Journal of Applied Physics*, vol. 94, p. 7178, 2003.
- [7.14] W. S. Su, Y. F. Chen, C. L. Hsiao, and L. W. Tu, "Generation of electricity in GaN nanorods induced by piezoelectric effect", *Applied Physics Letters*, vol. 90, p. 063110, 2007.

- [7.15] J. Song, J. Zhou, and Z. L. Wang, "Piezoelectric and semiconducting coupled power generating process of a single ZnO belt/wire. A technology for harvesting electricity from the environment.", *Nano letters*, vol. 6, p. 1656, 2006.
- [7.16] X.-Q. Liu, X.-L. Wang, M. Ogura, T. Guillet, V. Voliotis, and R. Grousson, "Modification of optical properties by strain-induced piezoelectric effects in ultrahigh-quality V-groove AlGaAs/GaAs single quantum wire", *Applied Physics Letters*, vol. 80, p. 1894, 2002.
- [7.17] L. F. Zagonel, S. Mazzucco, M. Tencé, K. March, R. Bernard, B. Laslier, G. Jacopin, M. Tchernycheva, L. Rigutti, F. H. Julien, R. Songmuang, and M. Kociak, "Nanometer scale spectral imaging of quantum emitters in nanowires and its correlation to their atomically resolved structure", *Nano letters*, vol. 11, p. 568, 2011.
- [7.18] J. Lähnemann, O. Brandt, C. Pfüller, T. Flissikowski, U. Jahn, E. Luna, M. Hanke, M. Knelangen, A. Trampert, and H. T. Grahn, "Coexistence of quantum-confined Stark effect and localized states in an (In,Ga)N/GaN nanowire heterostructure", *Physical Review B*, vol. 84, p. 155303, 2011.
- [7.19] F. Boxberg, N. Søndergaard, and H. Q. Xu, "Elastic and piezoelectric properties of zincblende and wurtzite crystalline nanowire heterostructures.", *Advanced materials*, vol. 24, p. 4692, 2012.
- [7.20] T. Wang, D. Nakagawa, J. Wang, T. Sugahara, and S. Sakai, "Photoluminescence investigation of InGaN/GaN single quantum well and multiple quantum wells", *Applied Physics Letters*, vol. 73, p. 3571, 1998.
- [7.21] P. Lefebvre and B. Gayral, "Optical properties of GaN/AlN quantum dots", *Comptes Rendus Physique*, vol. 9, p. 816, 2008.
- [7.22] F. Bernardini, V. Fiorentini, and D. Vanderbilt, "Spontaneous polarization and piezoelectric constants of III-V nitrides", *Physical Review B*, vol. 56, p. R10024, 1997.
- [7.23] J. Xin, Y. Zheng, and E. Shi, "Piezoelectricity of zinc-blende and wurtzite structure binary compounds", *Applied Physics Letters*, vol. 91, p. 112902, 2007.
- [7.24] L. Zhang, J.-W. Luo, A. Zunger, N. Akopian, V. Zwiller, and J.-C. Harmand, "Wide InP Nanowires with Wurtzite/Zincblende Superlattice Segments Are Type-II whereas Narrower Nanowires Become Type-I: An Atomistic Pseudopotential Calculation", *Nano letters*, vol. 10, p. 4055, 2010.
- [7.25] G. W. Wen, J. Y. Lin, H. X. Jiang, and Z. Chen, "Quantum-confined Stark effects in semiconductor quantum dots", *Physical Review B*, vol. 52, p. 5914, 1995.
- [7.26] K. Chang and J. Xia, "Asymmetric Stark shifts of exciton in InAs/GaAs source pyramidal quantum dots", *Solid State Communications*, vol. 104, p. 351, 1997.
- [7.27] Y. Wang, H. S. Djie, and B. S. Ooi, "Quantum-confined Stark effect in interdiffused quantum dots", *Applied Physics Letters*, vol. 89, p. 151104, 2006.

# **Chapter VIII**

---

## **Quantum efficiency of nanowire heterostructures**

- 8.1      Introduction.
- 8.2      Sample description.
- 8.3      Experimental method.
- 8.4      Results and discussion.
- 8.5      Conclusions.
- 8.6      References.

## 8.1 Introduction.

Semiconductor NW heterostructures are potential building blocks for nanoscale electronics and optoelectronic devices. In recent years, the increasing interest in the use of NW heterostructures for solar cell applications and photonics has been observed [8.1, 8.2]. For these potential applications understanding of recombination processes and the knowledge of such important parameter as the quantum efficiency (QE) are required. Recently some successful results on the former issue were reported [8.3, 8.4]. However, only few works have been published so far on the NW QE. Studies of PL QE of ZnO NWs demonstrated value of the QE in 10 – 20% range [8.5, 8.6]. Initial studies on individual CdSe NWs reveal values of emission QE on the order of 0.1% ( $d = 10 \text{ nm}$ ,  $I_{\text{exc}} = 150 \text{ W/cm}^2$ ) [8.7]. Occasionally, values up to 20% are reported ( $d = 7 \text{ nm}$ ,  $I_{\text{exc}} = 25 \text{ W/cm}^2$ ) [8.8]. This suggests a wide variability of CdSe NW QEs. Generally, though the values QE are small, their magnitude can be attributed to the numerous defects that NWs possess on their surface. As a point of comparison, CdSe quantum belts, with well-defined surfaces, exhibit the QE up to 30% [8.9]. Moreover, it was demonstrated that QE depends of the NW environment and may be affected by the substrate [8.10]. However, no studies of QE of NW heterostructures were published so far. In this context we study the QE of InAs/InP QWell and QRod NWs grown on Si substrates. In this chapter we present the comparative study where QE and internal QE (IQE) of these NW heterostructures will be investigated at various values of excitation power and compared to the QE of planar analogues.

## 8.2 Sample description.

In the present chapter we investigate the QE of both QWell and QRod NW heterostructures, studied in preceding chapters. The former consist of an InP core surrounded by a few monolayer InAs shell which is capped by a thick InP shell, while the later contains only a single InAs QRod in each InP NW (see Chapter 2). It is important to remind that HAADF-STEM imaging, carried out on both NW samples, showed that QWell-NWs consisted of a few monolayer thick InAs QWell with an inner 14 nm-thick InP core and an outer 30 nm-thick InP shell formed during the subsequent InP growth (Figure 8.1.a). A QRod-NW contains an InAs QRod of the 8 – 11 nm diameter and 45 – 135 nm length (Figure 8.1.b).

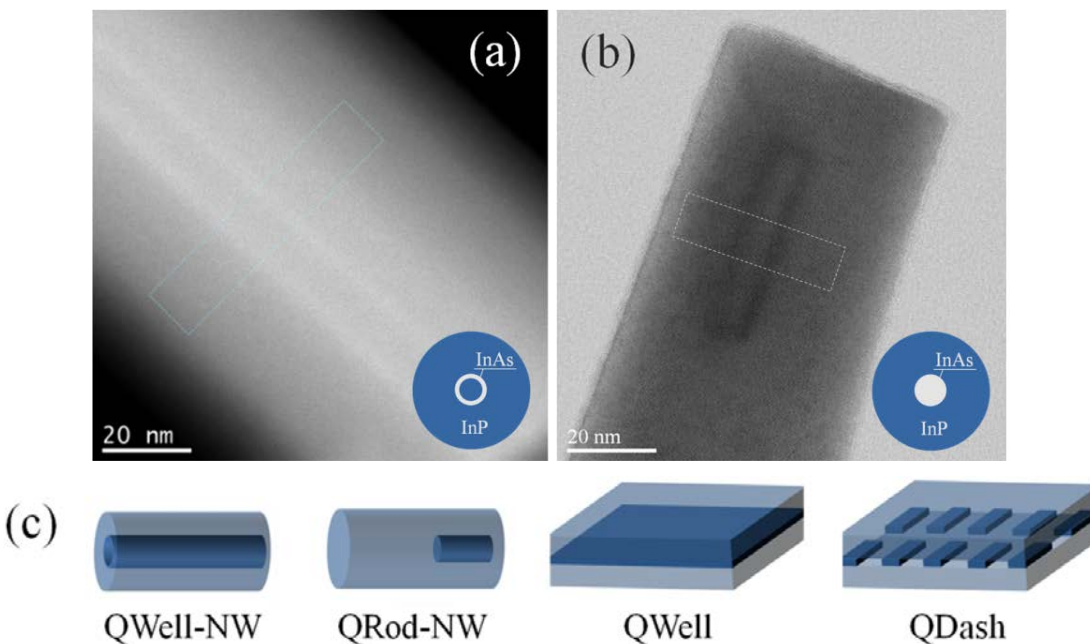


**Figure 8.1:** HAADF-STEM images of InAs/InP radial QWell (a) and QRod (b) NWs and corresponding cross-sectional schemes. (c) Schematically illustrated samples of different types.

For the sake of comparison, we have chosen the closest planar analogues of our NW samples: an InAsP/InP QWell and an InAs/InP quantum dash (QDash) sample, which consists of a high density of quantum dots elongated along the [1-10] axis. A schematic illustration of the samples chosen for comparison is shown in Figure 8.1.c

### 8.3 Experimental method.

In this section we briefly remind the experimental technique for PL QE measurements that was explained in Chapter 3 in details. The PL QE ( $\eta$ ) is defined as the ratio of the number of emitted photons to the number of absorbed photons. A standard technique for measuring PL QE involves the use of an integrating sphere [8.6, 8.11 – 8.14], where the light is isotropically redistributed over the sphere surface, due to the high reflectance material of the internal surface, so that the possible angular anisotropy of emission [8.15] does not affect the results.

To calculate the QE, it is important to know the absorption of the incident laser beam by the sample. Measurements on NWs freestanding on their as-grown substrate pose a problem of undesirable absorption by the Si substrate. Moreover presence of the substrate may affect the absorption in NWs [8.10]. To avoid these problems, the NWs were transferred onto a sticky tape, transparent for both laser light and near infrared emission of the NWs, and emitting no light in considered range of wavelengths (see Chapter 3.6). As explained in Chapter 3.4, the method similar the one developed by de Mello *et al* [8.12] is used for the PL QE measurements. In this case experiments in three different configurations, illustrated in Figure 8.2, are required.

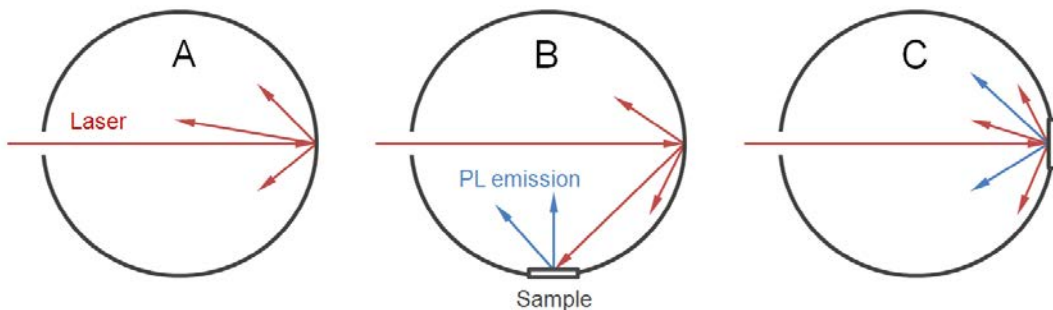


**Figure 8.2:** Schemes illustrating three configurations of the sphere typically used for the QE measurement.

In the first experiment (Configuration A) the entire laser intensity ( $L_a$ ) is measured with an empty sphere. In Configuration B, the reflected laser intensity ( $L_b$ ) and emission of the sample ( $P_b$ ) are measured for an indirect excitation. And finally (Configuration C), the reflected laser intensity ( $L_c$ ) and emission of the sample ( $P_c$ ) are measured under the direct excitation. Then, the QE of the sample can be calculated from the equation [8.12]:

$$\eta = \frac{P_c - (1-A)P_b}{L_a A} \quad (8.1)$$

where  $A = 1 - L_c / L_b$  is the absorption coefficient of the sample. Due to the fact, that A and B configurations are indistinguishable for our samples (i.e.  $P_b = 0$  and  $L_a = L_b$ ), in the present study we only use A and C configurations. In this case the Eq. 8.1 can be simplified as

$$\eta = P_c / L_a A, \quad (8.2)$$

where the absorption coefficient is now defined as  $A = 1 - L_c / L_a$ . For all the samples the condition of zero-overlap between absorption and emission spectra is satisfied, since the laser light is absorbed in the InP layers, while InAs active regions are emitting in the 0.8 – 1.1 eV range. On this account we can neglect the effects of reabsorption and reemission [8.16, 8.17].

## 8.4 Results and discussion.

To illustrate this technique, the PL spectra obtained on QWell and QWell-NWs in A and C configurations are shown in Figure 8.3.

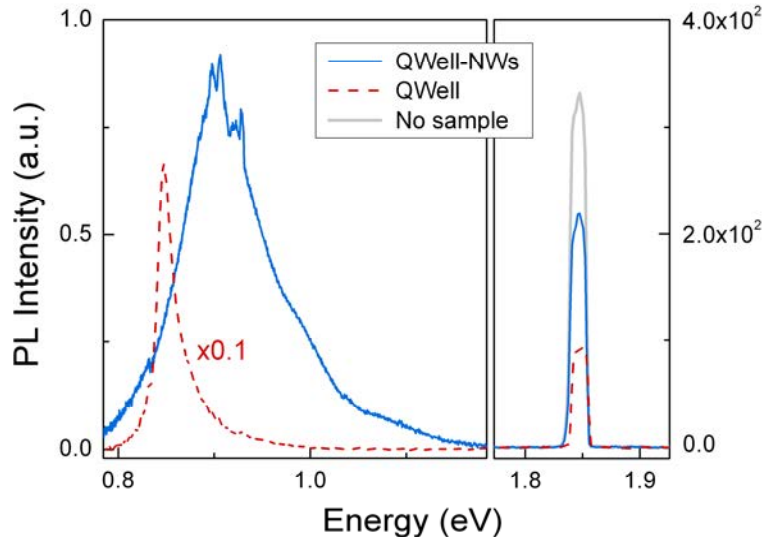


**Figure 8.3:** Laser lines and emission spectra of QWell (dashed line) and QWell-NWs (solid line) in C configuration and laser line in the A configuration.

The same procedure has been carried out for QRod-NWs and QDash samples (Figure 8.4).

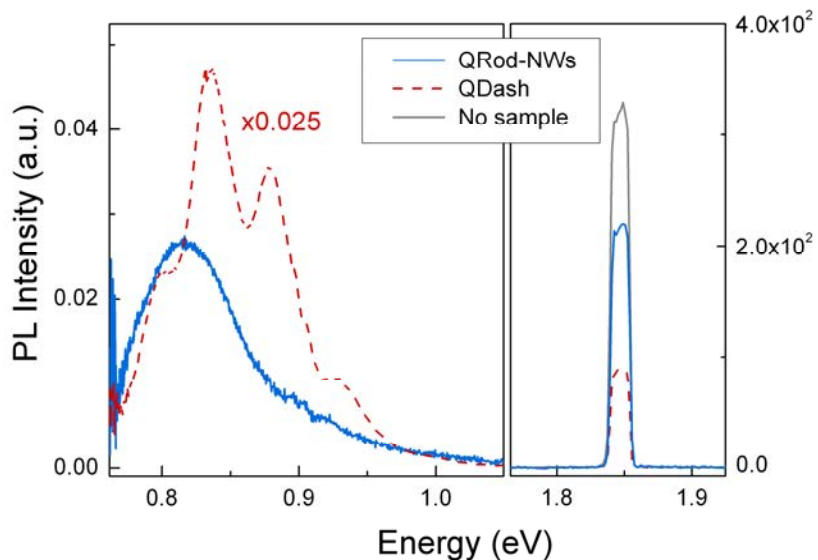


**Figure 8.4:** Laser lines and emission spectra of QRod-NWs (solid line) and QDash (dashed line) samples in C configuration and laser line in the A configuration.

In both cases emission intensity of planar samples is much higher than that of NW samples. On the other hand this high intensity is certainly related to a much stronger absorption in these samples. To calculate the QE of the samples, it is necessary to measure the area under the laser profiles ( $L_a$  and  $L_c$ ) and PL profile ( $P_c$ ). The values of absorption and QE calculated from Eq. 8.2 are presented in the Table 1.

**Table 8.1:** Values of absorption (A) and QE ( $\eta$ ).

Sample	A	$\eta$
QWell-NWs	0.35	0.9% $\pm$ 0.1%
QRod-NWs	0.34	0.2% $\pm$ 0.06%
QWell	0.71	0.8% $\pm$ 0.6%
QDash	0.72	5.3% $\pm$ 1%

It is difficult to assess the scale of any systematic errors, so to estimate the error we used the difference between the results obtained on different spots of the samples. The values of absorption (A) demonstrate a remarkable similarity among both NW samples ( $A = 0.34 - 0.35$ ) and planar structure samples ( $A = 0.71 - 0.72$ ). This is not surprising, taking into account that the outer structure, responsible for the absorption, is the same for both samples of each class. Moreover, the absorption values of 0.71 – 0.72 is in good agreement with the fact that a 31% reflection can be estimated for a normal laser beam at the air/InP interface. Both QWell-NWs and QRod-NWs are based on WZ InP NWs while QWell and QDash samples are both covered by ZB InP capping layers. The values of  $\eta$  show that QWell-NWs have QE comparable to that of the planar QWell (0.8 – 0.9%). The QRod-NWs, however, demonstrate significantly lower QE (0.2%), while the QDash sample has the highest QE of all investigated samples (5.3%).

In order to explain these values, the PL spectroscopy has been conducted at various values of excitation power and temperatures. Figure 8.5 shows PL intensity and QE of the samples as a function of the excitation power, while the ratio of the PL intensity at low temperature (10 K) to intensity at room temperature is reported in Table 8.2 for above (671 nm laser) and below (1064 nm laser) InP band gap excitation. These values may be considered as parameter reflecting the quality of the active regions. The small difference between the values in the Table 8.2 and those obtained in Chapter 5 is explained by the difference in power and wavelength of the used lasers.

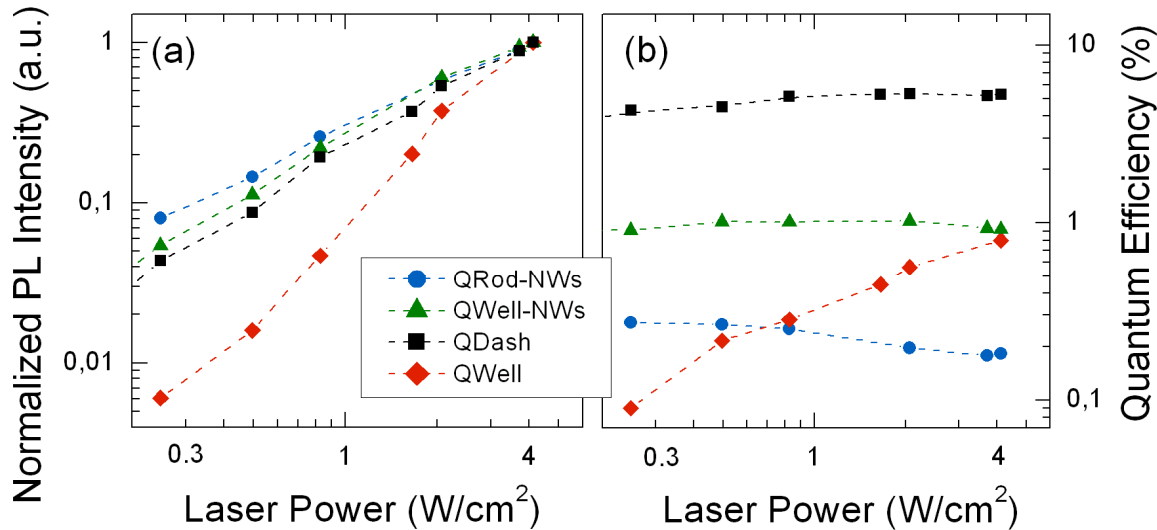


**Figure 8.5:** PL intensity (a) and PL QE (b) as a function of the excitation power. Dashed lines are guide to the eye.

For the QWell sample the slope of the PL intensity dependence on the excitation power is close to 2 (Figure 8.5.a). This value means that the nature of the PL recombination in this QWell is dominated by nonradiative recombination of uncorrelated electron-hole pairs [8.18]. This is in agreement with the small value (as compared to  $kT$ ) of the exciton binding energy, which is around 1 meV in bulk InAs and thus in the 1 – 4 meV range for an InAs QWell [8.19]. In case of QWell-NWs, the slope is closer to one and, as a consequence, should be related to radiative recombination of uncorrelated electron-hole pairs. However, when the sample is excited below the WZ InP band gap, a strong decrease of the PL intensity with increase of temperature ( $I_{10K} / I_{300K} = 50$ ) is observed (Table 8.2) and we have to conclude that, at room temperature, the emission is dominated by nonradiative processes related to excitonic recombination. The difference between the values for below and above InP band gap excitation is explained by weaker excitation density in the former case, so we assume that in the case of the QWell-NWs not all the defect states are saturated at below band gap excitation.

The observation of an excitonic recombination at room temperature could be explained if the recombination process take place in localized states of the radial QWell [8.20] where the exciton binding energy would be bigger. If 100% internal quantum efficiency (IQE) is assumed at 10 K, the 50-fold decrease of the PL intensity with temperature means that the maximum IQE at

room temperature is 2%. Thus, the measured QE of the QWell-NWs (0.9% at room temperature) is limited by the low value of the IQE. Indeed, as was demonstrated earlier in Chapter 5, the thickness of a radial QWell is not uniform, but may vary from the bottom to the top, or depending on the facet. When the NWs are removed from the Si substrate, the bottom section of the QWell is directly in contact with the bottom interface. This bottom part is probably where the thickness of the QWell is the biggest because the probability for the adatoms to reach the catalyst during the growth is weaker. Thus, we can assume that a part of the registered emission takes place very close to the surface and are impacted by nonradiative processes. Therefore, the PL emission at room temperature is mainly related to nonradiative excitonic recombination, process which is compatible with a slope equal to one [8.18]. On the contrary, the low QE of the QWell sample is explained by the relatively low excitation power: an increase of the excitation power will favor the radiative bimolecular recombination over the nonradiative processes and increase the QE as observed in Figure 8.5.b.

**Table 8.2:** Ratios of the PL intensity at 10 K to that at 300 K for different excitation wavelengths.

Sample	$I_{10K} / I_{300K}$ ( $\lambda_{ex}=671\text{nm}$ )	$I_{10K} / I_{300K}$ ( $\lambda_{ex}=1064\text{nm}$ )
QWell-NWs	$15.7 \pm 0.5$	$50 \pm 15$
QRod-NWs	$3.7 \pm 0.7$	$2.2 \pm 0.1$
QWell	$2.2 \pm 0.5$	$2.7 \pm 0.3$
QDash	$2.6 \pm 0.6$	$1 \pm 0.1$
InP NWs	$22 \pm 2.1$	—

As far as the QDash and QRod-NW samples are concerned, the situation is different. Both samples show a linear dependence of the PL intensity with the excitation power (Figure 8.5.a). Moreover these samples reveal good optical properties at room temperature. For above band gap excitation, the ratio  $I_{10K} / I_{300K}$  was found to be equal to 2.6 and 3.7 for the QDash and QRod-NW samples, correspondingly. These values are close to the best reported values for InAs(P)/InP quantum dots and dashes [8.21, 8.22]. Below InP band-gap excitation confirms the good quality of these emitters: nearly no PL decrease is recorded for the QDash sample and a 2.2 ratio is obtained for the QRod-NW sample. Thus, the strong difference of QE between these two samples

can not be explained by low IQE in the QRod-NWs. The weak QE of the QRod-NWs is probably a consequence of carrier losses in the InP NWs. Indeed, as shown on pure WZ InP NWs without any InAs heterostructures, the PL intensity is strongly decreasing ( $I_{10K} / I_{300K} = 22$ ) as the temperature is changed from 10 to 300 K, which indicates significant amount of defects in these unpassivated NWs. Since the InAs QRods are localized at the bottom part of InP NWs (see Chapter 2), which have a length in the  $1 - 4 \mu\text{m}$  range, we assume that only a part of the carriers can reach the active region, which leads to the relatively low QE. Therefore we conclude that reducing the length of the QRod-NWs may increase their QE. In this context, it would be interesting to conduct the QE measurements with 1064 nm laser, to demonstrate the enhanced QE, which we unfortunately were unable to do.

## 8.5 Conclusions.

In conclusion, PL QE of NW heterostructures and their planar analogues are measured by means of a PL setup coupled to an integrating sphere. It is shown that, at relatively low excitation power, the QWell-NWs have a QE comparable to that of the planar QWell. However, it is demonstrated that the QE of QWell-NWs is decreased by the low quality of its active region, as shown by the low IQE. On the other hand, despite the high quality of the active region in QRod-NW, its QE is relatively low because of the low quality of InP NWs themselves. On this account, we may conclude that quality of both InAs insertion and InP NW itself has impact on the QE of NW heterostructures, and thus should be improved to obtain light emitting devices of high efficiency.

## 8.6 References.

- [8.1] Z. Fan, D. J. Ruebusch, A. a. Rathore, R. Kapadia, O. Ergen, P. W. Leu, and A. Javey, "Challenges and prospects of nanopillar-based solar cells", *Nano Research*, vol. 2, p. 829, 2009.
- [8.2] F. Boxberg, N. Søndergaard, and H. Q. Xu, "Photovoltaics with piezoelectric core-shell nanowires", *Nano letters*, vol. 10, p. 1108, 2010.
- [8.3] O. Demichel, M. Heiss, J. Bleuse, H. Mariette, and A. Fontcuberta i Morral, "Impact of surfaces on the optical properties of GaAs nanowires", *Applied Physics Letters*, vol. 97, p. 201907, 2010.
- [8.4] C. K. Yong, K. Noori, Q. Gao, H. J. Joyce, H. H. Tan, C. Jagadish, F. Giustino, M. B. Johnston, and L. M. Herz, "Strong Carrier Lifetime Enhancement in GaAs Nanowires Coated with Semiconducting Polymer", *Nano letters*, vol. 12, p. 6293, 2012.
- [8.5] Y. Zhang, R. E. Russo, and S. S. Mao, "Quantum efficiency of ZnO nanowire nanolasers", *Applied Physics Letters*, vol. 87, p. 043106, 2005.
- [8.6] Daniel J. Gargas, H. Gao, H. Wang, and P. Yang, "High Quantum Efficiency of Band-Edge Emission from ZnO Nanowires", *Nano letters*, vol. 11, p. 3792, 2011.
- [8.7] V. V. Protasenko, K. L. Hull, and M. Kuno, "Disorder-Induced Optical Heterogeneity in Single CdSe Nanowires", *Advanced Materials*, vol. 17, p. 2942, 2005.
- [8.8] J. J. Glennon, W. E. Buhro, and R. A. Loomis, "Simple Surface-Trap-Filling Model for Photoluminescence Blinking Spanning Entire CdSe Quantum Wires", *Journal of Physical Chemistry*, vol. 112, p. 4813, 2008.
- [8.9] Y.-H. Liu, V. L. Wayman, P. C. Gibbons, R. A. Loomis, and W. E. Buhro, "Origin of High Photoluminescence Efficiencies in CdSe Quantum Belts", *Nano letters*, vol. 10, p. 352, 2010.
- [8.10] M. Heiss and A. Fontcuberta i Morral, "Fundamental limits in the external quantum efficiency of single nanowire solar cells", *Applied Physics Letters*, vol. 99, p. 263102, 2011.
- [8.11] D. Braun, E. G. J. Staring, R. C. J. E. Demandt, G. L. J. Rikken, Y. A. R. R. Kessener, and A. H. J. Venhuizen, "Photo- and electroluminescence efficiency in poly(dialkoxy-p-phenylenevinylene)", *Synthetic Metals*, vol. 66, p. 75, 1994.
- [8.12] J. C. de Mello, H. F. Wittmann, and R. H. Friend, "An Improved Experimental Determination of External Photoluminescence Quantum Efficiency", *Advanced materials*, vol. 9, p. 230, 1997.
- [8.13] N. C. Greenham, I. D. W. Samuel, G. R. Hayes, R. T. Phillips, A. B. Holmes, and R. H. Friend, "Measurement of absolute photoluminescence quantum efficiencies in conjugated polymers", *Chemical Physics Letters*, vol. 241, p. 89, 1995.

- [8.14] H. Mattossi, H. Murata, C. D. Merritt, Y. Iizumi, J. Kido, and Z. H. Kafafi, "Photoluminescence quantum yield of pure and molecularly doped organic solid films", *Journal of Applied Physics*, vol. 86, p. 2642, 1999.
- [8.15] Y. Fontana, G. Grzela, E. P. A. M. Bakkers, and J. G. Rivas, "Mapping the directional emission of quasi-two-dimensional photonic crystals of semiconductor nanowires using Fourier microscopy", *Physical Review B*, vol. 86, p. 245303, 2012.
- [8.16] J. N. Demas and G. A. Crosby, "The Measurement of Photoluminescence Quantum Yields", *The Journal of Physical Chemistry*, vol. 75, p. 991, 1971.
- [8.17] T.-S. Ahn, R. O. Al-Kaysi, A. M. Müller, K. M. Wentz, and C. J. Bardeen, "Self-absorption correction for solid-state photoluminescence quantum yields obtained from integrating sphere measurements", *The Review of scientific instruments*, vol. 78, p. 086105, 2007.
- [8.18] C. Netzel, V. Hoffmann, T. Wernicke, a. Knauer, M. Weyers, M. Kneissl, and N. Szabo, "Temperature and excitation power dependent photoluminescence intensity of GaInN quantum wells with varying charge carrier wave function overlap", *Journal of Applied Physics*, vol. 107, p. 033510, 2010.
- [8.19] B. G., M. E., L. L. Chang, and E. L., "Exciton binding energy in quantum wells", *Physical Review B*, vol. 26, p. 1974, 1982.
- [8.20] M. H. H. Alouane, R. Anufriev, N. Chauvin, H. Khmissi, K. Naji, B. Ilahi, H. Maaref, G. Patriarche, M. Gendry, and C. Bru-Chevallier, "Wurtzite InP/InAs/InP core-shell nanowires emitting at telecommunication wavelengths on Si substrate", *Nanotechnology*, vol. 22, p. 405702, 2011.
- [8.21] B. Salem, T. Benyattou, G. Guillot, C. Bru-Chevallier, G. Bremond, C. Monat, G. Hollinger, and M. Gendry, "Strong carrier confinement and evidence for excited states in self-assembled InAs quantum islands grown on InP(001)", *Physical Review B*, vol. 66, p. 193305, 2002.
- [8.22] R. Hostein, A. Michon, G. Beaudoin, N. Gogneau, G. Patriache, J.-Y. Marzin, I. Robert-Philip, I. Sagnes, and A. Beveratos, "Time-resolved characterization of InAsP/InP quantum dots emitting in the C-band telecommunication window", *Applied Physics Letters*, vol. 93, p. 073106, 2008.

# General conclusions

---

In this general conclusion we will briefly summarize the main results presented in this thesis. In the beginning we described the optimization of the growth conditions in order to obtain InP NWs with a pure WZ crystallographic structure. After that, growth technique was modified. Adding growth interruption to allow a flux switching, we obtained a procedure to grow NW heterostructures. Then the growth conditions were optimized to obtain QRod-NWs without parasitic heterostructures, such as radial QWell. Finally, three types of WZ NW samples were obtained: pure InP NWs, InAs/InP radial QWell-NWs and InAs/InP QRod-NWs.

The investigation of the optical properties was started with low temperature PL spectroscopy of WZ InP NWs grown at various temperatures. Most of the samples showed clear signs of type II recombination at the WZ/ZB interface, while only NWs grown at 420° C demonstrated a single peak attributed to WZ InP, which confirmed quality of this sample. FWHM of this peak was found to be relatively close to the best values reported on single InP NWs at low temperature. The value of FWHM = 6 meV was also confirmed by  $\mu$ PL study on single InP NWs.

The next part of Chapter IV was mostly devoted to a study of the impact of the host-substrate on the optical properties of InP NWs. It was shown that the influence of a host-substrate could have significant impacts on the optical properties of NWs, due to the strain, created by the difference in the thermal expansion coefficients of the NWs and the host-substrate, and due to some other surface effects. More specifically, the  $\mu$ PL emission energy may be changed depending on the host-substrate material, while the shift of the emission energy as a function of excitation power and its FWHM may be related to the surface charges affecting the band bending and be different from one substrate to another and from one day to another. Accordingly, consideration of these effects may serve for a better understanding of some recently published results and should be taken into account whenever  $\mu$ PL results on transferred NWs are considered.

Chapter V is focused on the optical properties of NW heterostructures studied by means of PL spectroscopy and simulated theoretically. PL spectra of WZ InAs/InP QWell-NWs revealed multiple peaks, each of which was attributed to a specific thickness of the radial QWell,

while  $\mu$ PL spectra showed groups of peaks which could be associated with the peaks and shoulders in the PL spectra. This attribution was confirmed by theoretical calculations, where the QWell emission energy was simulated as a function of the QWell thickness.

As far as QRod-NW heterostructures are concerned, it was demonstrated that intensity of room temperature PL emission remains as high as 30% of its value at 14 K.  $\mu$ PL measurements revealed the presence of two peaks which were attributed to A and B-band emission energies, in agreement with the band splitting calculation. Low temperature spectra demonstrated that each band is composed of several peaks. It was theoretically shown that the energy difference between these states, observed at low temperature, depends on the length of the QRod. On the other hand, the diameter of QRods, was demonstrated to be the main factor that controls the energy of PL emission and the splitting between A and B bands. The calculated energy of the QRod ground state was found to be in agreement with the experimental value. Finally, both QWell-NWs and QRod-NWs were demonstrated to be particularly interesting for III-V emitters on silicon due to their ability to reach 1.3 and 1.55  $\mu$ m emission wavelengths.

The polarization properties of single InP NWs, InAs/InP QWell-NWs, InAs/InP QRod-NWs and ensembles of the InAs/InP QRod-NWs were studied by means of PL spectroscopy in Chapter VI. Polarization anisotropy of absorption was attributed to the dielectric confinement that results in the inhibition of the perpendicular component of PL emission. This assumption was found to be in agreement with theoretical calculation which demonstrated that DLP<sup>a</sup>, estimated from LFA model, is in agreement with that obtained from experiments on InAs/InP QRod-NWs. On the contrary, the polarization of emission was shown to be determined mostly by selection rule of WZ material for InP NWs. On the other hand, it does not seem to be the case for NW heterostructures. QWell-NWs demonstrated maximum emission polarized parallel to the NW axis with DLP<sup>e</sup> in 0.4 – 0.8 range, while QRod-NWs demonstrated very strong polarization anisotropy of emission (DLP<sup>e</sup> = 0.94). Due to the small “NW diameter / Emission wavelength” ratio of the InAs/InP heterostructure NWs, we concluded that the anisotropy was mainly caused by the inhibition of the PL emission perpendicular to the NW axis. Moreover, it was demonstrated that the polarization properties of the single QRod-NWs can be studied directly on a NW ensemble still on its as-grown substrate. Polarization anisotropy of the NW ensembles was in agreement with theoretical predictions and could be correlated with the properties of single NWs in the

scope of the proposed model. Furthermore, using this approach, the polarization anisotropy of the NWs was investigated as a function of excitation wavelength and temperature. A clear increase of the polarization ratio was observed as the excitation wavelength was increased in agreement with the theoretical prediction. So it was shown that the NW ensembles may be used to study the polarization properties of NWs.

The next chapter was devoted to the experimental observation of strain-induced piezoelectric field in WZ InAs/InP QRod-NWs, and theoretical calculations confirming this assumption. The piezoelectric field, caused by the strain due to the lattice mismatch between InAs and InP, results in a quantum confined Stark effect and affects the optical properties of the structure. Namely, PL emission blueshift and peak narrowing are observed in one group of NWs as the excitation power is increased in contrast to the other group where no such effects were observed. It was shown that this piezoelectric field could be screened by photogenerated carriers or removed by increasing temperature. In this case, above certain values of the excitation power or temperature, PL peak position and FWHM were showing the same dependences as NWs showing no piezoelectric field. Theoretical calculations showed that the piezoelectric field was indeed expected in WZ InAs/InP QRod-NW heterostructures. It was demonstrated that in agreement with theoretical predictions in the literature the significant strain, caused by the lattice mismatch, results in a piezoelectric field. The potential was demonstrated to be strongly dependent on the dimensions of the QRod. On this account we assumed the presence of two groups of NWs (with and without signs of piezoelectric field) may be attributed to the difference in QRod diameter. This assumption was confirmed by the statistical study of all the measured NWs. Indeed, NWs with no signs of the piezoelectric field had higher emission energy (lower diameter of QRod) than those showing clear signs of the piezoelectric field. In conclusion, it was shown that piezoelectric effect in WZ NW heterostructures could affect the optical properties, decreasing the intensity of PL emission and broadening the emission peak. This effect however can, if needed, be avoided by designing NW heterostructures with QRods (QDots) of lower dimensions. On the contrary, if the effect is desirable for carrier separation in photovoltaic applications the design of heterostructures should suggest the larger possible strain between the components.

Finally, in Chapter VIII, the PL quantum efficiency (QE) of NW heterostructures and their planar analogues were measured by means of a PL setup coupled to an integrating sphere. It was shown that the QWell-NWs had a QE comparable to that of the planar QWell at relatively low excitation power. In addition, it was demonstrated that the QE of QWell-NWs is decreased by the low quality of its active region, as shown by the low internal quantum efficiency. On the other hand, despite the high quality of the QRod-NW active region, its QE is relatively low because of the low quality of InP NWs themselves. On this account, we concluded that quality of both InAs insertion and InP NW itself has impact on the QE of NW heterostructures, and thus should be improved to obtain light emitting devices of high efficiency.

In general, the obtained knowledge of the optical and mechanical properties of pure InP NWs and InAs/InP NW heterostructures will improve understanding of the electrical and mechanical processes taking place in semiconductor NW heterostructures and will serve for the future nanodevice applications.

# List of publications

---

Portions of this thesis have appeared in the following publications:

- R. Anufriev, N. Chauvin, H. Khmissi, K. Naji, G. Patriarche, M. Gendry, and C. Bru-Chevallier, “*Piezoelectric effect in InAs/InP quantum rod nanowires*”, to be submitted, 2013
- R. Anufriev, N. Chauvin, H. Khmissi, K. Naji, G. Patriarche, M. Gendry, and C. Bru-Chevallier, “*Quantum efficiency of InAs/InP nanowire heterostructures grown on silicon substrates*”, Physica Status Solidi (RRL), vol. 7, p.878, 2013.
- R. Anufriev, N. Chauvin, H. Khmissi, K. Naji, J.-B. Barakat, J. Puelas, G. Patriarche, M. Gendry, and C. Bru-Chevallier, “*Polarization properties of single and ensembles of InAs/InP quantum rod nanowires emitting in the telecom wavelengths*”, Journal of Applied Physics, vol. 113, p. 193101, 2013.
- R. Anufriev, N. Chauvin, H. Khmissi, K. Naji, M. Gendry, and C. Bru-Chevallier, “*Impact of substrate-induced strain and surface effects on the optical properties of InP nanowires*”, Applied Physics Letters, vol. 101, p. 072101, 2012.
- N. Chauvin, M. H. H. Alouane, R. Anufriev, H. Khmissi, K. Naji, G. Patriarche, C. Bru-Chevallier, and M. Gendry, “*Growth temperature dependence of exciton lifetime in wurtzite InP nanowires grown on silicon substrates*”, Applied Physics Letters, vol. 100, p. 011906, 2012.
- M. H. H. Alouane, R. Anufriev, N. Chauvin, H. Khmissi, K. Naji, B. Ilahi, H. Maaref, G. Patriarche, M. Gendry, and C. Bru-Chevallier, “*Wurtzite InP/InAs/InP core-shell nanowires emitting at telecommunication wavelengths on Si substrate*”, Nanotechnology, vol. 22, p. 405702, 2011.

# Appendix

---

## Résumé détaillé de la thèse en français

- A.1 Introduction.
- A.2 Fabrication et propriétés structurales des nanofils.
- A.3 Nanofils InP contraints par le substrat.
- A.4 Propriétés optiques des hétérostructures InAs/InP en géométrie nanofil.
- A.5 Etude de la polarisation des nanofils InP et InAs/InP.
- A.6 Etude de la piézoélectricité dans les nanofils InAs/InP.
- A.7 Etude de l'efficacité quantique.
- A.8 Bibliographie.

## A.1 Introduction.

Ce travail de thèse porte sur l'étude des propriétés optiques de nanofils InP et d'hétérostructures nanofils InAs/InP épitaxiés sur substrat silicium.

Les nanofils de semiconducteurs III-V sont très étudiés depuis quelques années en raison de leur fort potentiel d'applications aussi bien en photonique intégrée, en (opto-) électronique que dans le domaine du photovoltaïque. La possibilité de les épitaxier sur différents types de substrat, et en particulier de pouvoir les intégrer sur substrat de silicium, a motivé l'implication de l'INL dans ce domaine de recherche pour mener une activité sur la croissance par épitaxie par jet moléculaire de nanofils III-V (filière In(As)P et GaAs) sur substrat de silicium par la méthode vapeur-liquide-solide (VLS), dans l'objectif général de l'intégration de fonctions photoniques et optoélectroniques.

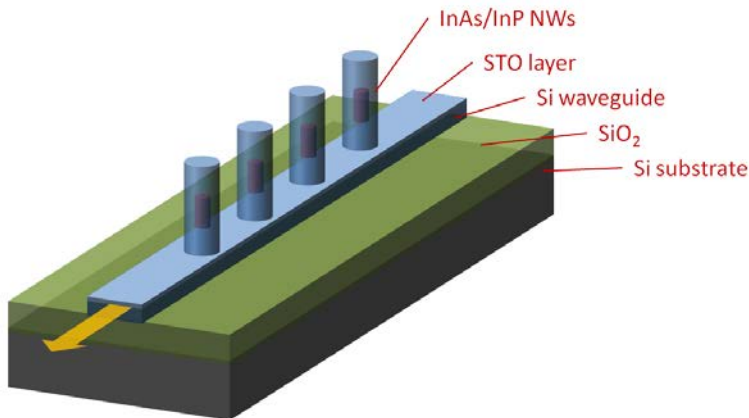


**Figure A.1:** Schéma de principe de la source III-V sur silicium.

Ce travail de thèse a été réalisé principalement dans le cadre du projet ANR «INSCOOP». Ce projet propose une stratégie originale pour intégrer une source de lumière efficace à la filière SOI (silicium sur isolant). Pour ce faire un guide d'onde optique en silicium doit être fabriqué à partir d'un substrat SOI. La source optique compacte fonctionnant aux longueurs d'onde télécom (fenêtre 1,3 µm ou 1,55 µm) sera fabriquée directement sur le guide d'onde silicium de manière monolithique en utilisant l'approche nanofils. L'émetteur sera constitué d'un segment d'InAs(P) inséré dans un nanofil d'InP. Une contrainte supplémentaire sera de former un réseau régulier de nanofils afin de former un cristal photonique actif résonant. Le mode de cette structure doit ensuite se coupler au mode du guide d'onde en silicium pour permettre le transfert des photons émis par le III-V dans le guide d'onde silicium.

## A.2 Fabrication et propriétés structurales des nanofils.

La fabrication des échantillons a été réalisée par l'équipe Hétéroépitaxie et Nanostructures de l'INL. Le principe général de la croissance VLS est détaillé dans la Figure A.2. La croissance débute par le démouillage d'une fine couche d'or ou d'un mélange or-indium sur le substrat de départ (dans notre cas un substrat silicium orienté 001 ou 111).

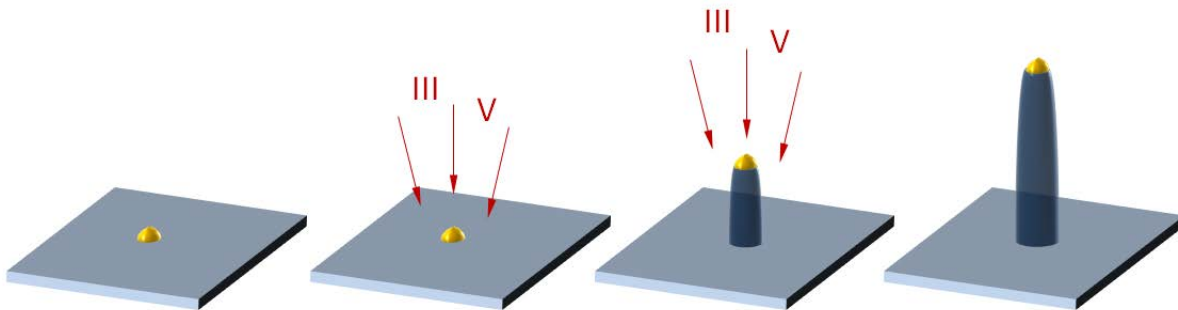


**Figure A.2:** Principales étapes de la croissance VLS.

Ce démouillage permet d'obtenir des gouttes de tailles nanométriques qui vont jouer le rôle de catalyseur et se transformer en alliage avec l'injection des flux d'éléments III et V. La croissance des nanofils démarre lorsque les gouttes sont sursaturées ce qui provoque une nucléation dans la partie inférieure de la goutte, à l'interface liquide solide.

### Optimisation des conditions de croissance des nanofils InP.

---

Une particularité de la méthode de croissance VLS est la difficulté de stabiliser une phase cristalline précise tout au long de la croissance des nanofils. Si les conditions de croissance ne sont pas optimisées, on observe le plus souvent des nanofils présentant un mélange de phases cristallines hexagonale (wurtzite) et cubique (blende de zinc) tel que montré sur la Figure A.3.a. Il faut donc optimiser les conditions de croissance pour obtenir des nanofils InP de bonne qualité structurale. Pour ce faire deux paramètres ont été étudiés : le rapport entre les flux d'élément V et d'élément III puis la température de croissance. Ces études ont révélé qu'un fort rapport V sur III et une température de croissance comprise entre 380 – 420°C favorisent la formation de nanofils InP purement wurtzite (Figure A.3.b) [A.1].

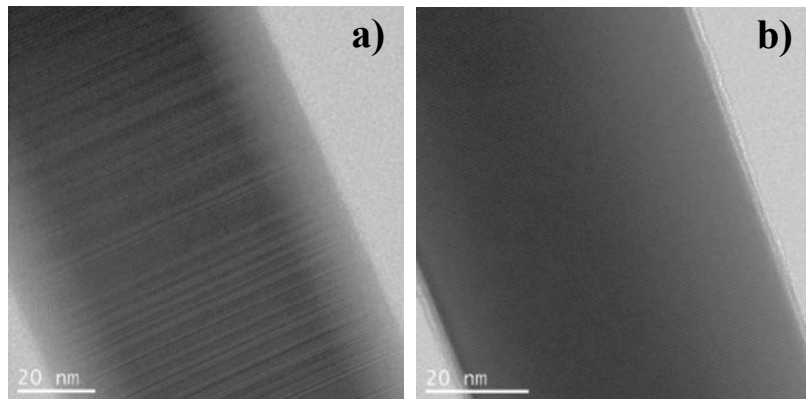


**Figure A.3:** (a) Insertions de plans cubiques dans un nanofil wurtzite. (b) Nanofils purement wurtzite.

### Insertion d'hétérostructures d'InAs dans les nanofils InP.

---

Après avoir optimisé les conditions de croissance des nanofils d'InP, plusieurs processus de croissance ont été testés pour insérer un segment d'InAs dans ces nanofils [A.2]. Dans la première approche testée (Figure A.4.a), la température de croissance est maintenue à 400° C tout au long de la croissance. Cette croissance a permis la synthèse d'un segment d'InAs (Figure A.5.a) mais un puits quantique radial s'est aussi formé sur les facettes du nanofil en raison d'une croissance radiale non désirée.

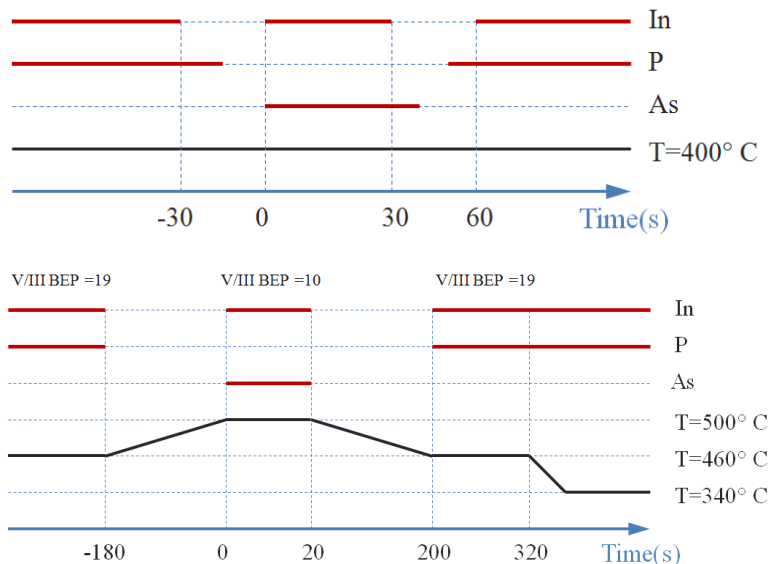


**Figure A.4:** 1<sup>ère</sup> procédure de croissance (a) et procédure de croissance optimisée (b).

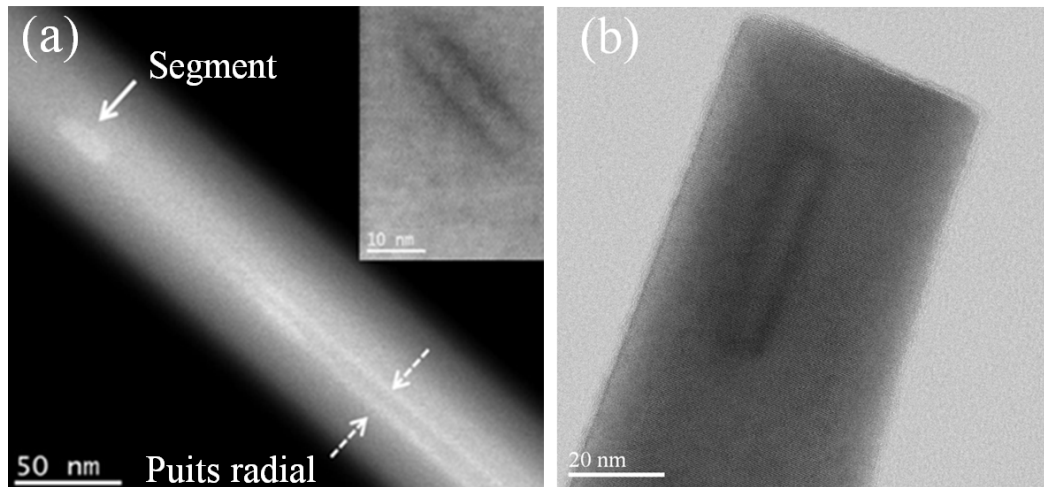


**Figure A.5:** Images TEM de nanofils (a) 1<sup>ère</sup> procédure de croissance et (b) procédure de croissance optimisée.

Une nouvelle méthode de croissance a ensuite été testée, impliquant une variation de la température de croissance pour améliorer le contrôle des croissances axiales et radiales. Pour cet échantillon, il a été décidé de positionner le segment dans la partie inférieure du nanofil. Cette nouvelle méthode a permis d'insérer un segment d'InAs tout en réduisant voire supprimant complètement la croissance radiale (Figure A.5.b).

### A.3 Nanofils InP contraints par le substrat.

Pour réaliser l'étude optique d'un nanofil unique, il est nécessaire de le transférer sur un nouveau substrat. Nous avons décidé d'étudier un phénomène qui avait déjà été observé par J. B. Schlager *et.al.* [A.3] pour des nanofils GaN: les nanofils reportés sur substrat peuvent être légèrement contraints à basse température s'il existe une différence entre les coefficients d'expansion thermique du nanofil et du substrat.

Il faut bien comprendre que les nanofils ne sont pas «collés» sur le substrat mais simplement posés et que le contact entre le substrat et les nanofils transférés doit être lié à la force de van der Waal. Les nanofils sont capables d'accommorder la contrainte induite en raison de leur géométrie 1D. En effet, la déformations que peut accommader une nanostructure est déterminée par l'équation suivante [A.4]:

$$|\varepsilon_{\max}| = \frac{\tau}{3\sqrt{3}E} \frac{L_0}{w} \quad (\text{A.1})$$

où  $\tau$  est la force de friction,  $E$  le module d'Young,  $L_0$  la longueur du nanofil et  $w$  la largeur de contact entre le nanofil et le substrat. Dans le cas d'une nanostructure de géométrie isotrope, la déformation maximale serait de l'ordre du ratio  $\tau / E$  soit de l'ordre de  $10^{-5}$ . Mais dans le cas des nanofils ce ratio doit être multiplié par le rapport  $L_0/w$  qui est de l'ordre de 100 pour nos nanofils InP. On peut donc supposer que nos nanofils sont capables d'accommader des déformations de l'ordre de  $10^{-4}$  à  $10^{-3}$ , valeurs suffisamment grandes pour être détectables en μPL.

Nous avons décidé de faire une étude plus approfondie de ce problème en essayant de contrainte en tension mais aussi en compression des nanofils InP. Nous avons transféré des nanofils d'InP provenant d'une même épitaxie sur trois substrats différents :

- Un substrat silicium, substrat assez standard dans la littérature pour le transfert de nanofils, dont le coefficient d'expansion thermique à 300 K est de  $2,6 \cdot 10^{-6} \text{ }^{\circ}\text{C}^{-1}$ .
- Un substrat InP en phase cubique dont le coefficient d'expansion à 300 K est de  $4,6 \cdot 10^{-6} \text{ }^{\circ}\text{C}^{-1}$ . En raison de la différence de gap de l'ordre de 70 meV entre la phase hexagonale et la phase cubique, il n'y a pas de risque que la PL du substrat ne recouvre le signal provenant des nanofils.
- Un substrat SrTiO<sub>3</sub> (STO) dont le coefficient d'expansion à 300 K est de  $9,4 \cdot 10^{-6}$ . Ce type de substrat ne semble pas utilisé dans la littérature pour transférer des nanofils mais son très

fort coefficient d'expansion en fait un candidat intéressant pour contraindre le nanofil en compression.

La Figure A.6 montre des résultats obtenus en  $\mu$ PL à température ambiante (a) et à basse température (b). A température ambiante les spectres sont similaires. Deux pics sont observés, le pic situé à basse énergie est associé à la recombinaison des porteurs entre le niveau fondamental de la bande de conduction et la bande A (trous lourds) de la bande de valence. Un second niveau est aussi observé qui est associé à la recombinaison entre les électrons de cette même bande de conduction et les trous de la bande B (trous légers). Cette dernière bande a été activée thermiquement. L'écart énergétique entre les deux bandes est en accord avec des résultats expérimentaux complémentaires.

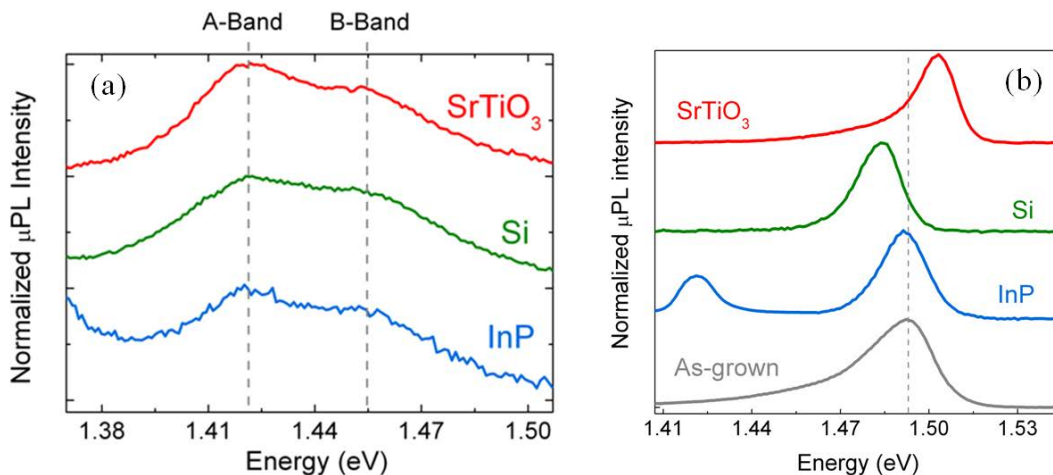


**Figure A.6:** Spectres de nanofils InP sur différents substrats mesurés à température ambiante (a) et à basse température (b).

A basse température, on voit clairement que les nanofils n'émettent plus à la même énergie : si l'émission des nanofils d'InP sur substrat d'InP est très proche de l'échantillon de référence (échantillon as-grown), on voit un décalage vers le rouge pour le nanofil transféré sur substrat silicium et un décalage vers le bleu pour le nanofil sur substrat STO. Les décalages sont en accord qualitatif avec ce qui est attendu : les nanofils sont censés être contraints en tension sur le substrat silicium et en compression sur le substrat STO. Nous avons étudié une douzaine de nanofils sur chaque substrat pour étudier la distribution statistique (Figure A.7).

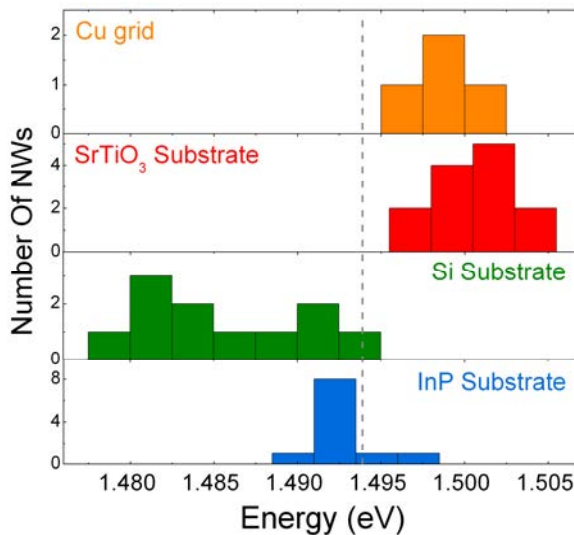


**Figure A.7:** Distribution statistique de l'énergie d'émission des nanofils en fonction du substrat utilisé.

On remarque, tout d'abord la très faible distribution statistique pour les nanofils InP sur substrat InP : plus de 75% des nanofils émettent à la même énergie. En ce qui concerne les deux autres substrats on observe une forte distribution statistique. Les nanofils sur Si émettent tous en dessous du gap de l'InP non contraint alors que les nanofils sur STO émettent tous au dessus du gap de l'InP. A titre d'illustration, on montre aussi sur cette figure l'énergie d'émission de quelques nanofils d'InP reportés sur le maillage d'une grille TEM constituée essentiellement de cuivre. Cette grille présente une forte valeur du coefficient d'expansion thermique et l'on observe, là encore, une émission supérieure au gap non contraint.

La distribution en énergie semble donc se produire lorsque les nanofils sont contraints. Elle peut s'expliquer par l'équation (A.1) qui détermine la déformation maximale qu'un nanofils peut accommoder. Cette déformation va dépendre de la force de friction qui peut varier d'un nanofil à l'autre et de la géométrie du nanofil (longueur, largeur de contact). La distribution en énergie est alors liée à une distribution de contrainte entre différents nanofils.

Ce résultat montre que le choix du substrat peut influencer de manière importante les propriétés d'émission des nanofils : on a mesuré des pics associés à l'InP wurtzite émettant sur une gamme de 20 meV. Des études complémentaires ont été menées (étude de photoluminescence en fonction de la température, étude par cathodoluminescence) qui confirment ce phénomène de contrainte dans le nanofil induite par le substrat.

## A.4 Propriétés optiques des hétérostructures InAs/InP en géométrie nanofil.

Les propriétés optiques des puits quantiques radiaux et des segments d'InAs ont été étudiées par PL et  $\mu$ PL après avoir été transférés sur différents substrats.

### Puits quantiques radiaux.

Des études à 10 K ont été réalisées sur une population de nanofils (Figure A.8.a) et sur des nanofils uniques (Figure A.8.b). Les spectres de PL de la Figure A.8.a montrent que ces nanofils émettent sur une large gamme spectrale et que cette émission est constituée de nombreux pics. Des études de PL complémentaires ont été effectuées pour démontrer que ces nombreux pics ne sont pas des états excités. Nous supposons que le signal de PL provient du puits quantique radial et que les nombreux pics observés sont la conséquence de la fluctuation de l'épaisseur du puits. L'étude de  $\mu$ PL montre que les spectres d'émission restent toujours aussi complexes à l'échelle du nanofils unique. Ceci indique que la fluctuation de l'épaisseur du puits se fait au sein d'un même nanofil.

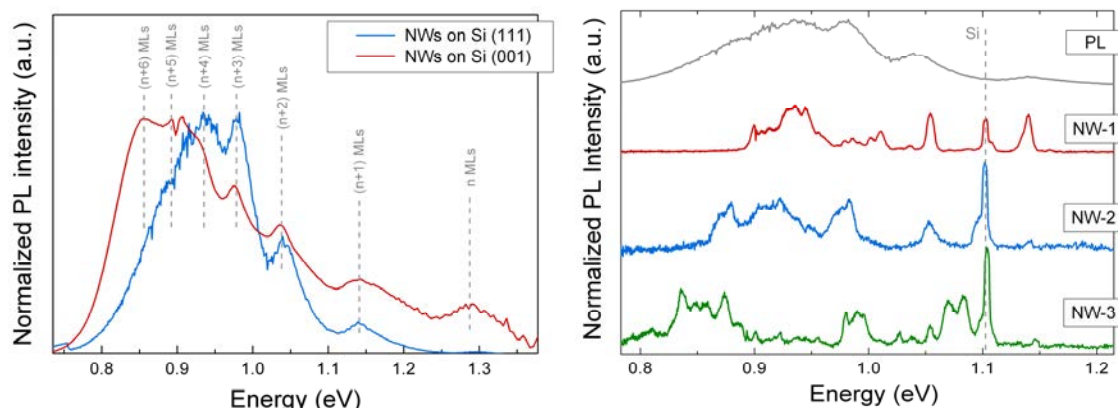


**Figure A.8:** Spectres de PL de nanofils (a) et de  $\mu$ PL de nanofils uniques (b) à basse température.

Une simulation a été réalisée en utilisant le logiciel Nextnano<sup>3</sup> [A.5, A.6]. Ce logiciel permet de calculer en 3D les champs de contraintes, les répartitions de charges, le diagramme de bandes et les états électroniques dans l'approximation de la masse effective. Les états électroniques présents dans un puits quantique radial inséré dans un nanofil d'InP sont calculés en fonction de l'épaisseur du puits en partant de la géométrie donnée par la Figure A.9.a. Le calcul a été effectué pour deux orientations cristallines différentes.

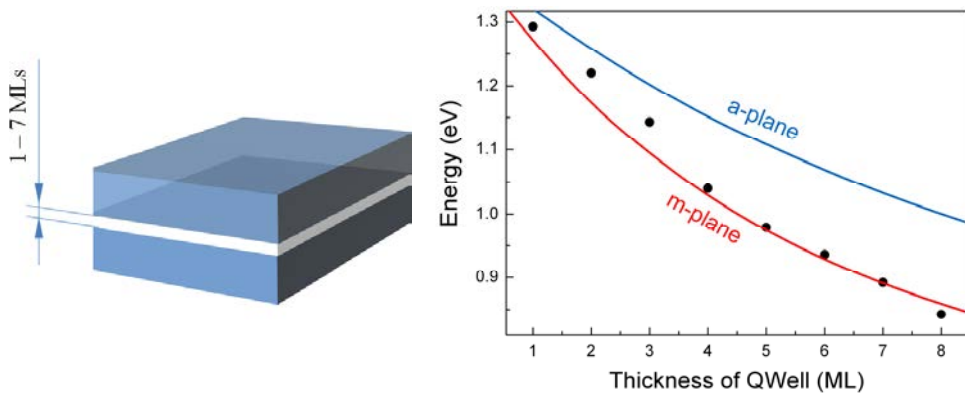


**Figure A.9:** Géométrie modélisée pour le calcul (a). Résultats expérimentaux (points) et calculs théoriques (courbe rouge) (b).

En effet les facettes d'un nanofil wurtzite peuvent être soit des plans « m » soit des plans « a ». Le résultat obtenu pour le plan-m (courbe rouge sur la Figure A.9.b) est en bon accord avec nos résultats expérimentaux. Il faut noter la difficulté de ce genre de calcul car il nécessite de connaître de nombreux paramètres de l'InP et l'InAs en phase cristalline wurtzite, phase peu connue car rencontrée uniquement dans la géométrie nanofil.

### Nanofils d'InP contenant un segment d'InAs.

La bonne tenue en température d'un nanofil unique nous permet d'étudier l'intensité de PL d'un segment unique à température ambiante (Figure A.10.a). On observe un niveau fondamental qui émet autour de 1,5  $\mu\text{m}$  et l'apparition, à plus forte puissance d'excitation, d'un niveau excité situé à environ 0,1 eV du niveau fondamental.

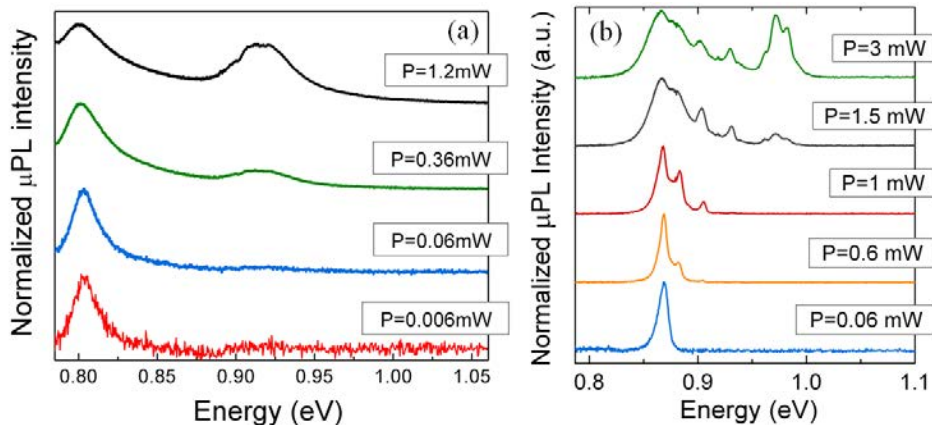


**Figure A.10:** Propriétés optiques d'un nanofil unique en fonction de la puissance d'excitation, à température ambiante (a) et à basse température (b).

Lorsque l'on étudie un segment similaire à basse température (Figure A.10.b) on observe que le niveau fondamental ( $\approx 0,87$  eV) et le niveau excité ( $\approx 0,97$  eV) sont en réalité composés de plusieurs états électroniques. On a utilisé le logiciel Nextnano<sup>3</sup> pour étudier les niveaux des états électroniques en fonction du diamètre et de la longueur des segments d'InAs (Figure A.11.a). La Figure A.11.b montre l'évolution des transitions en fonction du diamètre du segment.

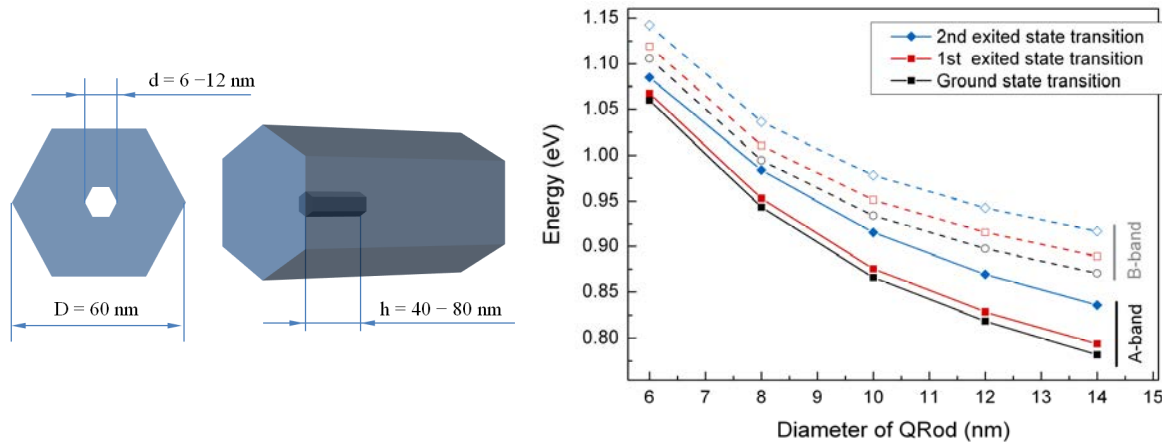


**Figure A.11:** (a) Géométrie utilisée pour les calculs. (b) Evolution théorique des niveaux électroniques en fonction du diamètre.

D'après les résultats théoriques, le niveau fondamental ( $\approx 0,87$  eV) est associé à la bande A : recombinaison des électrons situés sur le niveau de plus basse énergie de la bande de conduction avec des trous situés dans la bande A (bande trous-lourds). Le niveau excité ( $\approx 0,97$  eV) observé dans la Figure A.10.a semble être associé à la recombinaison entre des électrons situés sur le niveau de plus basse énergie de la bande de conduction et des trous situés dans la bande B (trous-légers).

Les résultats obtenus avec la simulation sont assez cohérents avec nos résultats expérimentaux si on tient en compte le fait que nos segments mesurent entre 8 et 12 nm de diamètre :

- Le niveau fondamental de la boîte varie entre 0,9 et 0,8 eV à basse température.
- L'écart entre la bande A et la bande B varie entre 50 et 70 meV.
- Chaque bande est constituée de plusieurs niveaux. Des calculs complémentaires ont montré que l'écart d'énergie entre ces niveaux varie avec la longueur du segment.

## A.5 Etude de la polarisation des nanofils InP et InAs/InP.

L'étude des propriétés optiques des nanofils en jouant sur la polarisation est un sujet qui a été étudié par de nombreux groupes. L'étude de la polarisation dans un nanofil (en émission ou en absorption) est un sujet complexe car de nombreux paramètres peuvent entrer en ligne de compte : le confinement quantique, les règles de sélection de la phase hexagonale, les propriétés photoniques du nanofils.

Dans cette thèse, pour décrire la polarisation d'un nanofil, nous utilisons le degré de polarisation linéaire (DLP). Dans le cas de l'absorption, le DLP est défini par la relation:

$$DLP^a = \frac{I_{\parallel}^a - I_{\perp}^a}{I_{\parallel}^a + I_{\perp}^a}$$

où  $I_{\parallel}^a$  ( $I_{\perp}^a$ ) est l'intensité de PL collectée lorsque la polarisation du laser est parallèle (perpendiculaire) à l'axe du nanofils. Dans le cas d'une étude de la DLP en émission, l'équation utilisée est la suivante :

$$DLP^e = \frac{I_{\parallel}^e - I_{\perp}^e}{I_{\parallel}^e + I_{\perp}^e}$$

où  $I_{\parallel}^e$  ( $I_{\perp}^e$ ) est l'intensité de la PL qui est polarisée parallèlement (perpendiculairement) à l'axe du nanofil.

### Le nanofil : une structure photonique.

---

Lorsque l'on étudie la polarisation d'une nanostructure InAs dans un nanofils InP, il faut être capable de distinguer ce qui relève des règles de sélection propres aux états quantiques de la nanostructure et de ce qui est une conséquence de la géométrie nanofil. En effet, selon la théorie de Landau sur les milieux diélectriques, lorsqu'un champ électrique incident est polarisé parallèlement au cylindre, le champ électrique à l'intérieur du cylindre n'est pas réduit. Par contre, quand ce champ est polarisé perpendiculairement au cylindre, l'amplitude du champ électrique dans le cylindre ( $E_{\perp}$ ) est atténué selon la formule :

$$E_{\perp} = \frac{2\epsilon_0}{\epsilon + \epsilon_0} E_e$$

où  $\epsilon$  est la constante diélectrique du nanofil. Dans cette thèse, nous avons décidé de modéliser l'impact de la géométrie du nanofil sur le champ électromagnétique en utilisant un modèle développé par J. Giblin *et al* [A.7, A.8].

### Etude de l'impact de la géométrie nanofils sur l'absorption.

Nous avons étudié l'impact de la géométrie nanofil sur l'absorption à partir d'une nanofil contenant une nanostructure InAs. L'intensité du segment est collectée en fonction de la polarisation du laser.

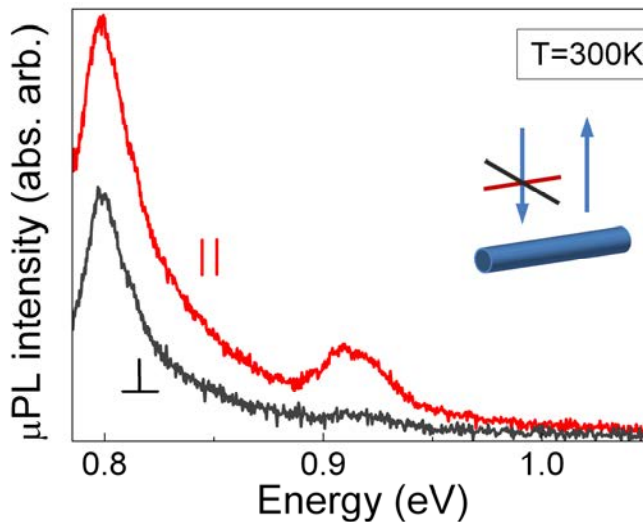


**Figure A.12:** Spectre d'un nanofil en fonction de la polarisation du laser.

On a trouvé un DLP en absorption de l'ordre de 0.5 ce qui est en accord avec le modèle théorique de Giblin qui prédit un DLP de l'ordre de 0.48 pour un nanofils de 100 nm de diamètre à la longueur d'onde du laser de 632.8 nm.

### Etude de la polarisation en émission.

#### Nanofil InP.

Nous nous intéressons maintenant à la DLP en émission d'un nanofil InP. L'émission d'un nanofil en fonction de la polarisation est montrée sur la Figure A.13. L'émission du nanofil se décompose en deux pics associés aux bandes A et B de l'InP wurtzite. L'émission associée à la

bande A est fortement anisotrope avec une émission principalement perpendiculaire au nanofil. On obtient des DLP en émission de  $-0.62$  pour l'émission depuis la bande A et  $0.11$  pour l'émission depuis la bande B.

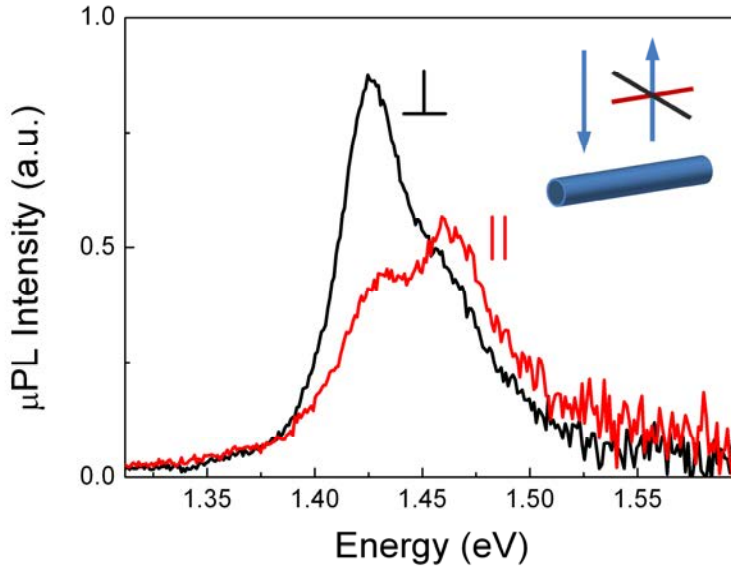


**Figure A.13:** Spectre de PL d'un nanofil d'InP résolu en polarisation

Dans le cas d'un matériau hexagonal massif non contraint d'InP, la théorie prévoit des valeurs de  $-1$  et  $-0.83$ , pour les bandes A et B respectivement. Dans la littérature des valeurs de l'ordre de  $-0.4$  à  $-0.5$  ont été reportées en ce qui concerne la bande A [A.9, A.10]. A notre connaissance, il n'y a pas de valeur dans la littérature en ce qui concerne la bande B.

#### Segment d'InAs dans nanofil InP.

Nous avons aussi étudié l'émission des segments d'InAs en fonction de la polarisation. Cette étude a été menée à température ambiante (Figure A.14.a) et à basse température (Figure A.14.b).

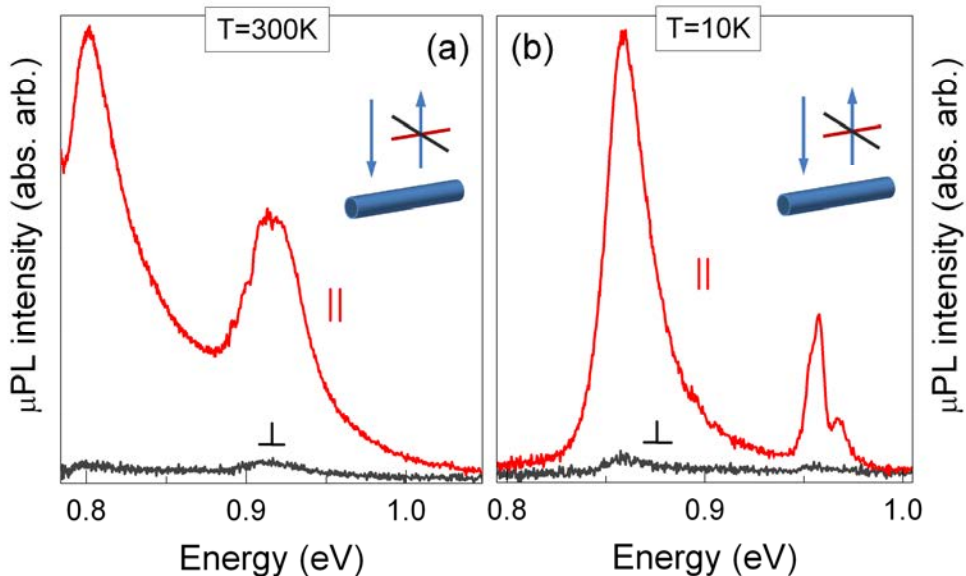


**Figure A.14:** Emission d'un segment à température ambiante (b) et à 10 K (c) en fonction de la polarisation.

Contrairement au nanofil d'InP wurtzite, l'émission du niveau fondamental est polarisée parallèlement au nanofil et non perpendiculairement avec un DLP extrêmement grand ( $DLP > 0.9$ ). Nous expliquons ce résultat par la conjonction de deux phénomènes:

- Le niveau fondamental n'est pas constitué à 100% de trous lourds mais est en réalité un mélange trous lourds-trous légers. Ceci permet au niveau fondamental d'avoir une composante parallèle au nanofil.
- L'émission perpendiculaire au nanofil est très fortement atténuée en raison du caractère photonique du nanofil [A.11].

#### Etude sur une population de nanofils.

Des études ont ensuite été réalisées sur une population de nanofils. En effet, un nanofil présente un DLP à la fois à l'absorption et en émission. On peut donc réaliser une étude sur un ensemble de nanofils en contrôlant la polarisation du laser exciteur et la polarisation de l'émission qui est analysée. On a réalisé cette étude sur un échantillon de nanofils contenant des segments d'InAs en raison du très grand DLP en émission de ces segments.

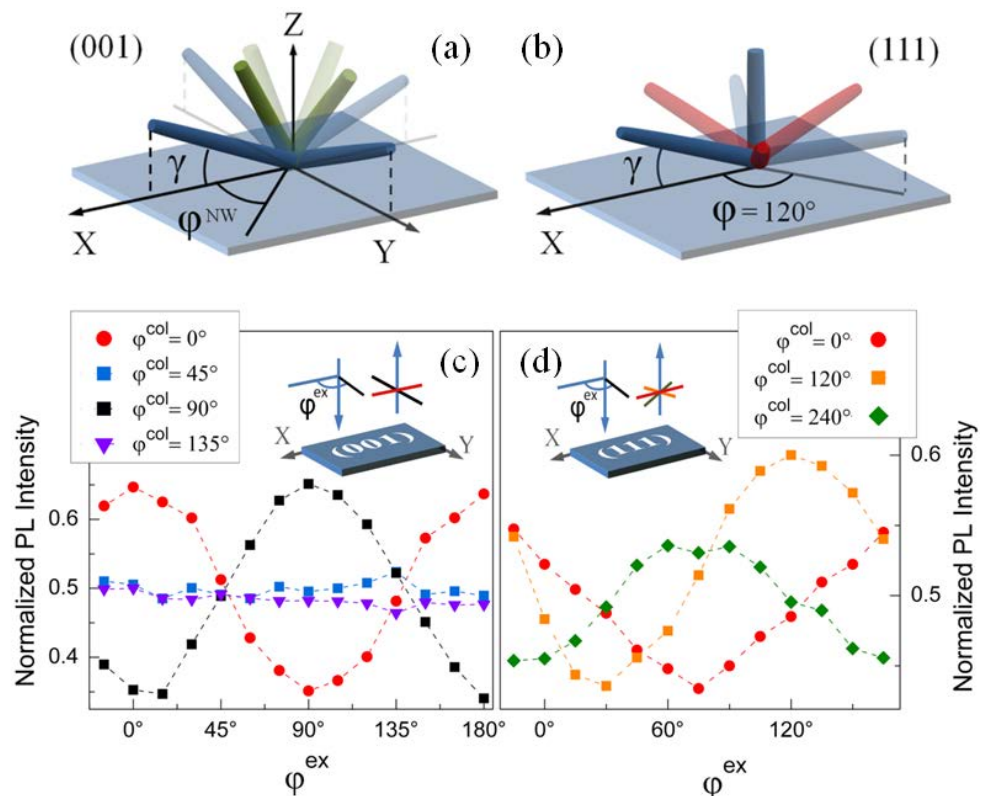


**Figure A.15:** (a), (b) Orientation des nanofils en fonction du substrat. Intensité de PL en fonction de la polarisation (b), (c).

L'orientation des nanofils sur le substrat est connue et elle varie en fonction du substrat utilisé pour la croissance : silicium (001) ou silicium (111). Les orientations observées en microscopie électronique à balayage sont détaillées sur les Figures A.15.a et A.15.b. Les Figures A.15.c et A.15.b montrent l'intensité du signal collecté en fonction de la polarisation en excitation et en collection. Les résultats dépendent fortement du substrat utilisé pour la croissance. Ces résultats sont en accord avec un modèle que nous avons développé qui prend en compte l'orientation des nanofils sur le substrat et les DLP mesurés sur nanofils uniques.

## A.6 Etude de la piézoélectricité dans les nanofils InAs/InP.

Lorsque l'on a étudié les segments d'InAs insérés dans des nanofils InP en fonction de la puissance d'excitation, on a constaté un comportement assez original pour certains nanofils (NW-B de la Figure A.16.b). Lorsque l'on augmente la puissance d'excitation, un léger décalage vers le bleu ainsi qu'une forte réduction de la largeur à mi-hauteur sont observés. Ces phénomènes ne s'observent pas pour tous les nanofils : le nanofil NW-A (Figure A.16.a) a un comportement plus typique avec un élargissement de la largeur à mi-hauteur et un léger décalage vers le rouge.

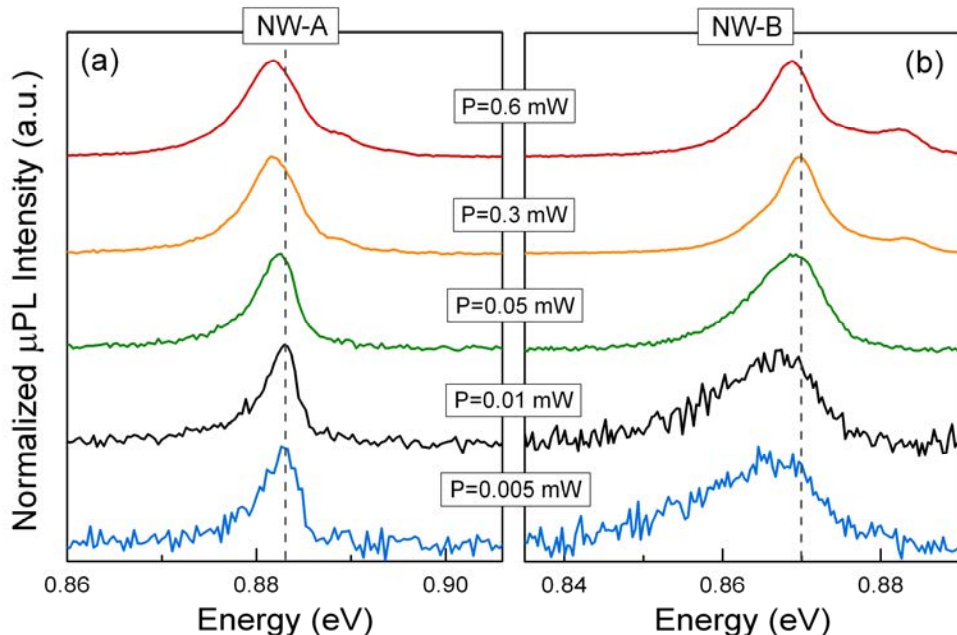


**Figure A.16:** Spectres de  $\mu$ PL en fonction de la puissance d'excitation pour deux segments différents.

Lorsque que l'on étudie ces deux nanofils en fonction de la température (Figure A.17), on voit que le phénomène de réduction de la largeur à mi-hauteur avec la puissance de pompe diminue lorsque la température augmente et disparaît pour des températures supérieures à 50 K (Figure A.17.b). Au dessus de cette température, les nanofils A et B présentent des largeurs à mi-hauteurs similaires.

Les résultats obtenus sur le nanofil de type B sont typiques d'un écrantage de champs électrique induit par la puissance de pompe (Figure A.16.b) ou par l'activation thermique de porteurs (Figure A.17.b).

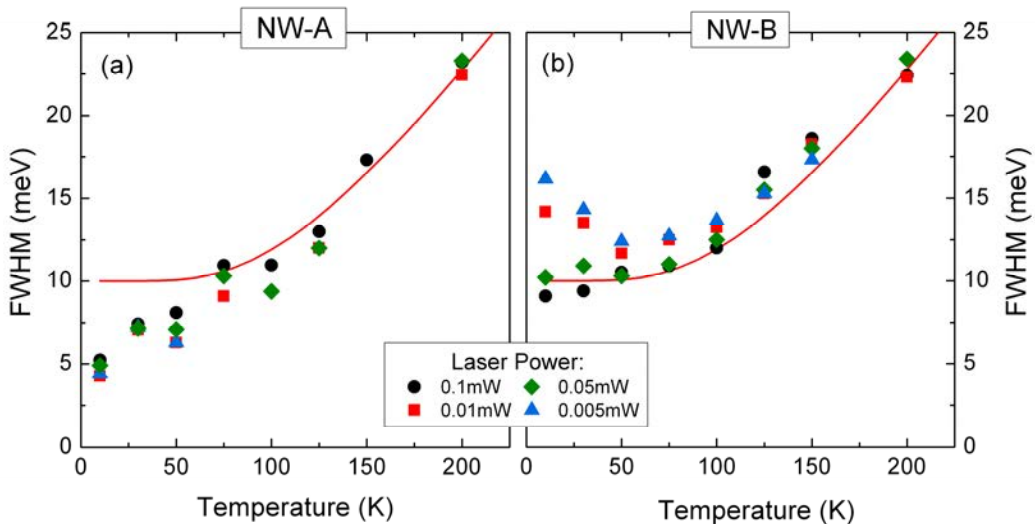


**Figure A.17:** Evolution de la largeur à mi-hauteur en fonction de la température pour les nanofils de type A (a) et de type B (b)

Si un champ électrique est écranté, il reste à déterminer l'origine de ce champ. Comme les nanofils sont en phase wurtzite et que les segments sont contraints, nous faisons l'hypothèse qu'il y a un champ piézoélectrique à l'intérieur des segments. L'étude de la piézoélectricité est importante car dans le cadre du projet INSCOOP, on souhaite des émetteurs de lumière efficace. La piézoélectricité qui provoque une séparation des porteurs est donc contre productive par rapport à l'objectif visé.

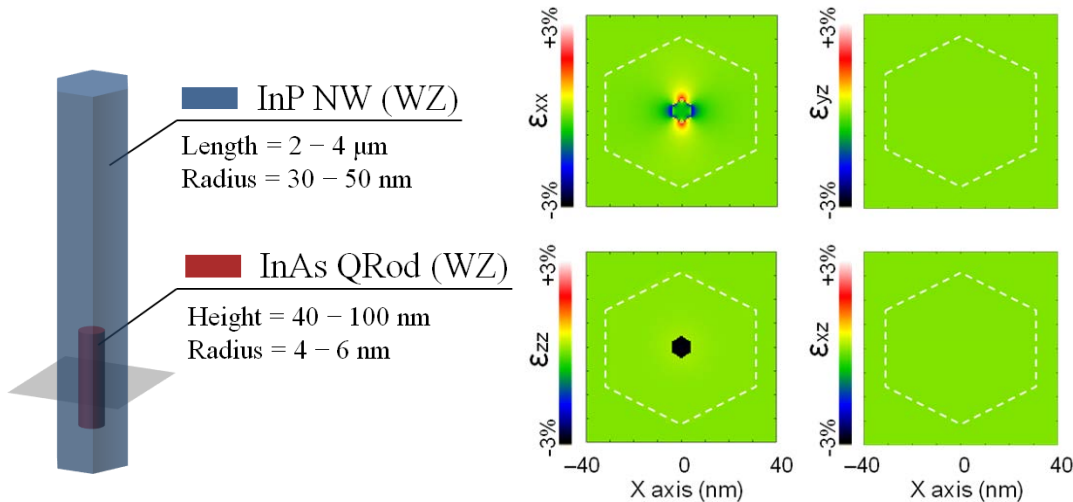


**Figure A.18:** Structure simulée dans Nextnano<sup>3</sup> et déformations obtenues.

Nous avons utilisé le logiciel Nextnano<sup>3</sup> pour calculer le champ électrique induit par la contrainte dans le segment. Nous avons simulé un nanofils InP wurtzite contenant un segment d'InAs. Dans une première étape, nous avons calculé les déformations (Figure A.18), puis le champ piézoélectrique présent dans le segment d'InAs (Figure A.19).

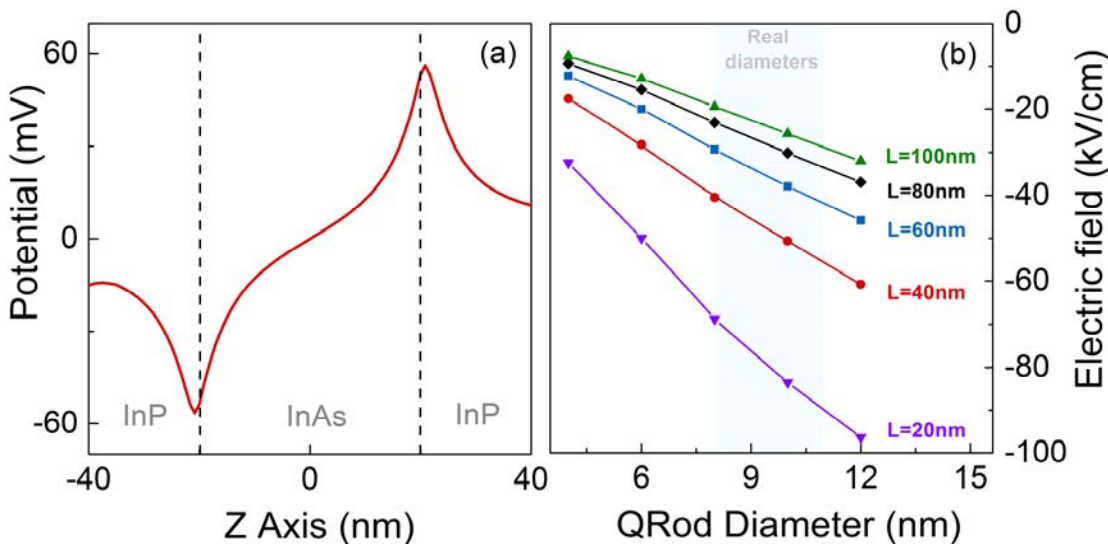


**Figure A.19:** Potentiel et champ électrique théorique en fonction du rayon et de la longueur du segment d'InAs.

D'après les calculs des champs électriques de plusieurs dizaines de kV/cm sont attendus dans ce type de nanostructures. Les champs obtenus sont nettement plus grands que ce que nous avons mesurés. Nous expliquons cela par le fait qu'à basse puissance d'excitation, les porteurs sont fortement séparés par le champ piézoélectrique ce qui réduit fortement la probabilité de recombinaison et donc la probabilité d'observer un signal de μPL. On peut donc supposer que lorsque l'on voit le signal de PL, le champ a déjà été fortement écranté par les premières charges injectées.

## A.7 Etude de l'efficacité quantique.

Connaître l'efficacité quantique de nos nanofils est quelque chose d'important au vu des applications visées. A l'exception de quelques études effectuées sur des nanofils en solution (essentiellement des nanofils semiconducteurs II-VI [A.12]), il existe très peu de résultats sur le sujet. Dans ce chapitre, l'efficacité quantique de nanofils a été étudiée à température ambiante à l'aide d'une sphère intégratrice. Nous avons étudiés les deux géométries de nanofils déjà présentées dans le second chapitre : un échantillon avec un puits quantique radial et un échantillon contenant des segments d'InAs.

Nous avons décidé de comparer ces échantillons avec deux hétérostructures purement III-V (sans substrat silicium) de la même filière de matériaux : un échantillon constitué d'un puits quantique InAsP/InP et un échantillon constitué de bâtonnets quantiques d'InAs/InP.

## Méthode expérimentale

---

Pour mesurer l'efficacité quantique, nous utilisons une méthode relativement standard en effectuant des mesures dans trois configurations différentes [A.13] (Figure A.20):

- Configuration A : l'intensité du laser ( $L_a$ ) est mesurée lorsqu'il n'y a pas d'échantillon dans la sphère.
- Configuration B : l'intensité du laser ( $L_b$ ) et de la photoluminescence de l'échantillon ( $P_b$ ) sont collectées lorsque le laser excite l'échantillon de manière indirecte.
- Configuration C : l'intensité du laser ( $L_c$ ) et de la photoluminescence de l'échantillon ( $P_c$ ) sont collectées lorsque le laser excite l'échantillon de manière directe.

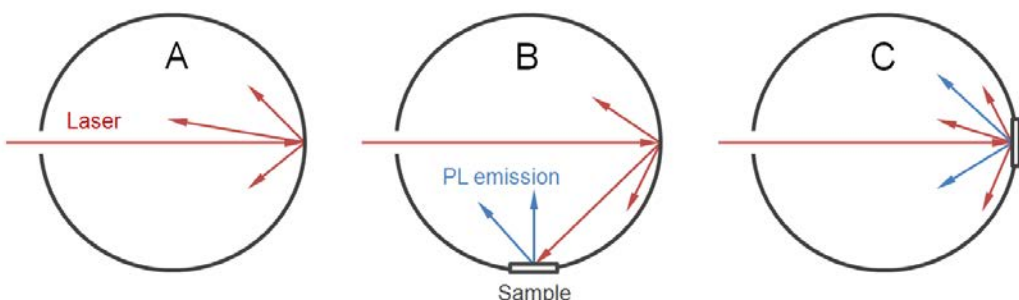


**Figure A.20:** Les trois configurations utilisées pour la mesure d'efficacité quantique.

L'efficacité quantique de l'échantillon étudié est égale à :

$$\eta = \frac{P_c - (1 - A) P_b}{L_a A}$$

où,  $A = 1 - L_c / L_b$  est le coefficient d'absorption de l'échantillon. Dans notre cas, aucune émission n'a été mesurée lorsque l'échantillon est excité de manière indirecte. Les résultats sont donc identiques pour les configurations A et B. L'efficacité quantique peut donc se résumer à la formule :

$$\eta = P_c / L_a A$$

Un autre aspect important à prendre en compte est le fait que les nanofils sont épitaxiés sur un substrat silicium qui peut absorber une partie du signal laser et provoquer une sous estimation de l'efficacité quantique. Pour contourner ce problème nous avons décidé de transférer les nanofils sur un ruban adhésif, ruban dont l'absorption du signal laser est négligeable et qui n'émet aucune luminescence dans la gamme étudiée.

## Résultats expérimentaux.

---

La Figure A.21 montre les résultats obtenus pour les puits quantiques en géométrie nanofil et planaire.

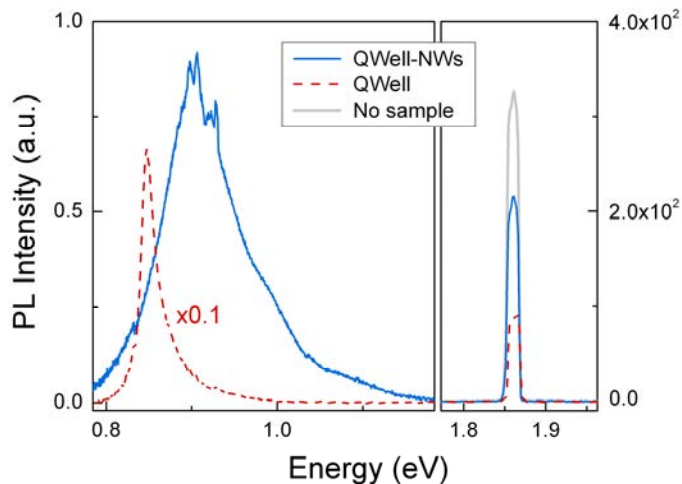


**Figure A.21:** Spectres du puits quantique planaire (courbe rouge), du puits quantique radial (bleue) et du laser de pompe (rouge et bleue) obtenus en configuration C. Le spectre « gris » montre le signal laser en configuration A.

Le tableau suivant résume les résultats obtenus pour nos différents échantillons. En ce qui concerne l'absorption (A), on constate que les structures planaires absorbent d'avantage de signal laser. La valeur d'absorption mesurée, autour 0.71 – 0.72, implique une réflexion de 0.28 – 0.29 qui est en bon accord avec la valeur théorique pour une couche d'InP excitée à la normale (0.3)

Sample	A	$\eta$
QWell-NWs	0.35	0.9% $\pm$ 0.1%
QRod-NWs	0.34	0.2% $\pm$ 0.06%
QWell	0.71	0.8% $\pm$ 0.6%
QDash	0.72	5.3% $\pm$ 1%

Nous obtenons une efficacité quantique à température ambiante de 0,9% pour le puits quantique radial. Cette valeur est comparable à l'efficacité quantique mesurée pour une structure planaire III-V. L'efficacité des segments est plus faible (0,2%) et nous expliquons cette faible valeur par le fait que beaucoup de porteurs générés dans le nanofil InP sont dans l'incapacité de relaxer dans le segment.

## A.8 Bibliographie.

- [A.1] M. H. Hadj Alouane, N. Chauvin, H. Khmissi, K. Naji, B. Ilahi, H. Maaref, G. Patriarche, M. Gendry, and C. Bru-Chevallier, "Excitonic properties of wurtzite InP nanowires grown on silicon substrate", *Nanotechnology*, vol. 24, p. 035704, 2013.
- [A.2] H. Khmissi, K. Naji, C. M.H. Hadj Alouane, N. Chauvin, C. Bru-Chevallier, B. Ilahi, G. Patriarche, and M. Gendry, "InAs/InP nanowires grown by catalyst assisted molecular beam epitaxy on silicon substrates", *Journal of Crystal Growth*, vol. 344, p. 45, 2012.
- [A.3] J. B. Schlager, K. A. Bertness, P. T. Blanchard, L. H. Robins, A. Roshko, and N. A. Sanford, "Steady-state and time-resolved photoluminescence from relaxed and strained GaN nanowires grown by catalyst-free molecular-beam epitaxy", *Journal of Applied Physics*, vol. 103, p. 124309, 2008.
- [A.4] F. Xu, J. W. Durham, B. J. Wiley, and Y. Zhu, "Strain-Release Assembly of Nanowires on Stretchable Substrates", *ACS nano*, vol. 5, p. 1556, 2011.
- [A.5] "Nextnano.de", 2013. [Online]. Available: <http://www.nextnano.de/nextnano3/index.htm>. [Accessed: 20-Jun-2013].
- [A.6] S. Birner, S. Hackenbuchner, M. Sabathil, G. Zandler, J. A. Majewski, T. Andlauer, T. Zibold, R. Morsch, A. Trellakis, and P. Vogl, "Modeling of semiconductor nanostructures with nextnano<sup>3</sup>", *Acta Physica Polonica A*, vol. 110, p. 111, 2006.
- [A.7] J. Giblin, V. Protasenko, and M. Kuno, "Wavelength Sensitivity of Single Nanowire Excitation Polarization Anisotropies Explained through a Generalized Treatment of Their Linear Absorption", *ACS nano*, vol. 3, p. 1979, 2009.
- [A.8] J. Giblin and M. Kuno, "Nanostructure Absorption: A Comparative Study of Nanowire and Colloidal Quantum Dot Absorption Cross Sections", *The Journal of Physical Chemistry Letters*, vol. 1, p. 3340, 2010.
- [A.9] A. Mishra, L. V. Titova, T. B. Hoang, H. E. Jackson, L. M. Smith, J. M. Yarrison-Rice, Y. Kim, H. J. Joyce, Q. Gao, H. H. Tan, and C. Jagadish, "Polarization and temperature dependence of photoluminescence from zincblende and wurtzite InP nanowires", *Applied Physics Letters*, vol. 91, p. 263104, 2007.
- [A.10] G. L. Tuin, "Master Thesis: "Optical characterization of Wurtzite Indium Phosphide", Lund University, 2010.
- [A.11] J. Bleuse, J. Claudon, M. Creasey, N. S. Malik, J.-M. Gérard, I. Maksymov, J.-P. Hugonin, and P. Lalanne, "Inhibition, enhancement, and control of spontaneous emission in photonic nanowires", *Physical Review Letters*, vol. 106, p. 103601, 2011.
- [A.12] V. V. Protasenko, K. L. Hull, and M. Kuno, "Disorder-Induced Optical Heterogeneity in Single CdSe Nanowires", *Advanced Materials*, vol. 17, p. 2942, 2005.
- [A.13] J. C. de Mello, H. F. Wittmann, and R. H. Friend, "An Improved Experimental Determination of External Photoluminescence Quantum Efficiency", *Advanced materials*, vol. 9, p. 230, 1997.